UNIVERSIDADE FEDERAL DO PARANÁ

RAFAEL DE CARVALHO BUENO

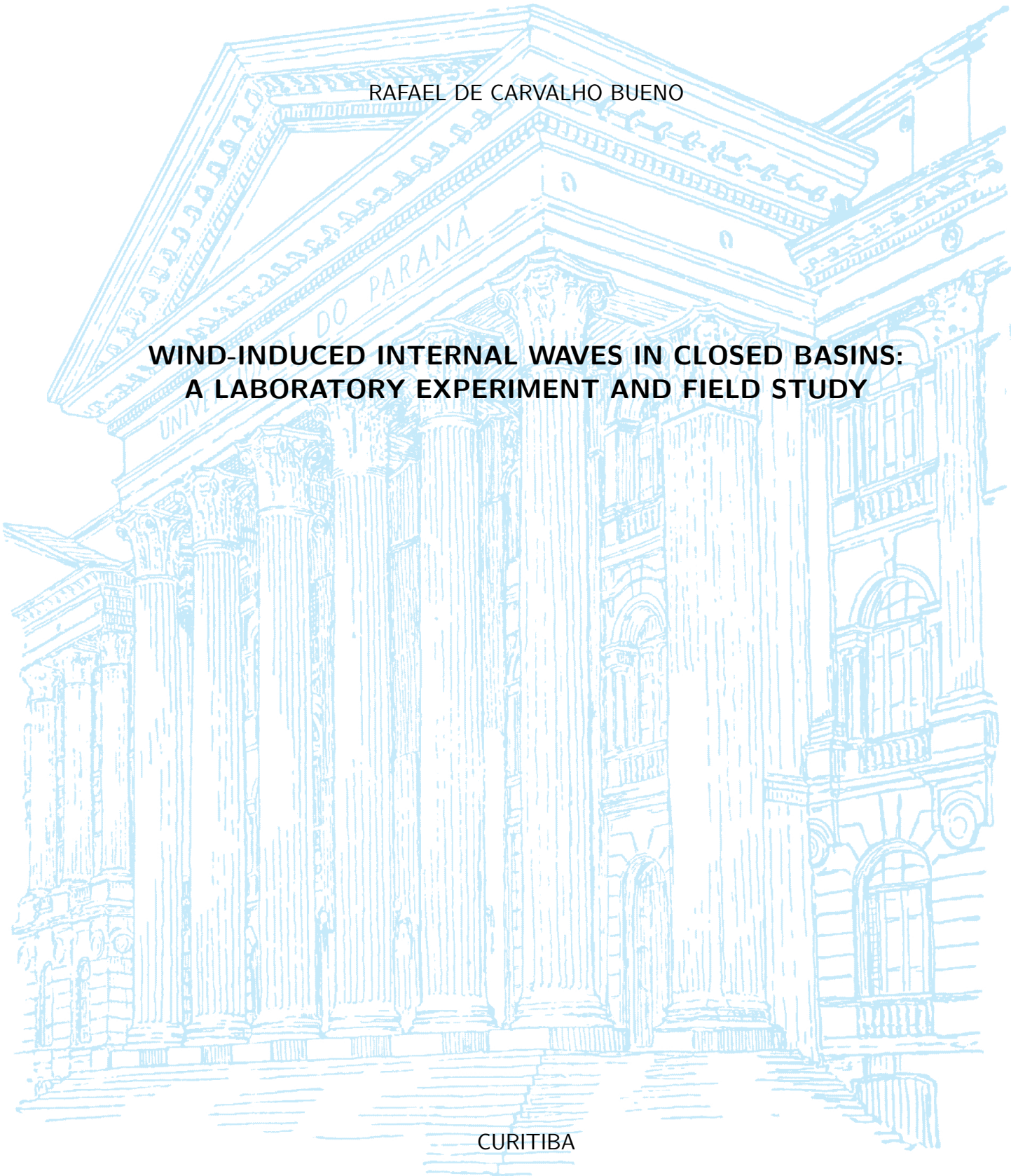

WIND-INDUCED INTERNAL WAVES IN CLOSED BASINS: A LABORATORY EXPERIMENT AND FIELD STUDY

CURITIBA

2018

RAFAEL DE CARVALHO BUENO

Wind-induced internal waves in closed basins:

A laboratory experiment and field study

Dissertação apresentada ao Programa de Pós-Graduação em Engenharia de Ambiental da Universidade Federal do Paraná, como requisito parcial à obtenção do grau de Mestre

Supervisor: Dr.-Ing Tobias Bleninger

CURITIBA

2018

Rafael de Carvalho Bueno
Wind-induced internal waves in closed basins:
A laboratory experiment and field study/ Rafael de Carvalho Bueno. – Curitiba, 2018.
154 p. : il. (algumas color.) ; 30 cm.

Supervisor: Dr.-Ing Tobias Bleninger

Dissertation (Master) – Universidade Federal do Paraná, Setor de Tecnologia, Programa de Pós-Graduação em Engenharia Ambiental, 2018.

1. Internal Seiches 2. Lake Classification 3. Wedderburn Number 4. Lake Modeling I. Universidade Federal do Paraná II. Tobias Bleninger III. Wind-induced internal waves in closed basins: A laboratory experiment and field study

CDD: 000.00

Approval

RAFAEL DE CARVALHO BUENO

WIND-INDUCED INTERNAL WAVES IN CLOSED BASINS:
A LABORATORY EXPERIMENT AND FIELD STUDY

Dissertação apresentada ao Programa de Pós-Graduação em Engenharia de Ambiental da Universidade Federal do Paraná, como requisito parcial à obtenção do grau de Mestre

---

Dr.-Ing Tobias Bleninger
Orientador

Ph.D. Maurício Felga Gobbi
UFPR – PPGEA

Ph.D. Ailin Ruiz de Zarate Fabregas
UFPR – PPGM

Curitiba, February 2019

For my mother, Maria José de Carvalho Bueno.
Her support, encouragement, and constant love have sustained me throughout my life

Acknowledgements

Writing this thesis has been fascinating and extremely rewarding. This dissertation thesis is the result not only of my passion for science but also of the valuable support of many individuals.

First and foremost, I would like to express my sincere gratitude to my advisor, Dr.-Ing professor Tobias Bleninger, for guiding me and reach my potential. His constant enthusiasm for research fueled me during all these years, always encouraging me. It is an honor and a privilege to do this work with him. He has been supportive and has given me the freedom to pursue various projects without any objection and always with some valuable advices. I appreciate his recognition of my efforts, and all this motivate me to the right track to seek perfection. My thanks to him that introduced me to this project and gave me the opportunity to keep studying this topic that I am so fascinated. It is a honor for me to have him as my advisor. I hope have him always as my advisor, not just now and in my Ph.D, but even in the future as a professor.

My gratitude goes out as well to a professor and an inspiration, DSc. Professor Michael Mannich. His support has helped me in countless way. He is one of the models of professor and researcher I hope one day to become.

I would also like to thank my examination board for spending much time reading and evaluating my master thesis. A special thanks goes to Ph.D. Professor Mauricio Gobbi, that evaluated not just this work, but also my undergraduate thesis, I hope you could see the improvement of my academic performance.

I would like to present my sincere thankfulness to my dear mom. I can barely find the words to express all the love and support she has given to me. She has been a constant source of encouragement, and definitely she is my hero. She bravely raised me alone after my father passed out, when I was just 12 years old. She truly is the most amazing person I know and I am so honored to learn from her everyday. Knowing her support my dreams motivates me to work harder every day. It is more than thanks, It is more than saying "I love her with all my hearts" because that is not enough. I hope that one day I could be half the parent that she is.

I can replay over and over in my mind every moment with him. He has been and always will be my constant source of inspirations. *Pai, te amo. Você sempre estará comigo..*

I would like to thank my girlfriend Milena Hofmann, for all her love and support, without any complaint or regret. Her understanding of my passion for science allows me to reach my potential.

My special regards to all my teachers who have taught me since my childhood, at various stages.

I would also like to acknowledge financial support provided by CAPES – Brazilian Federal Agency for Support and Evaluation of Graduate Education within the Ministry of Education of Brazil. In addition, I would like to express my sincere appreciation to the graduate program of Environmental Engineering (PPGEA) of the Federal University of Paraná (UFPR). I feel home here, and this is due to the amazing students, professors, and all staff. We are a family, we will be bigger, stronger, and bolder. I would like to thank Huaxia Yao and James Rusak from the Dorset Environmental Science Centre, Ontario Ministry of Environment, Conservation and Parks, to provide the data from Harp Lake. I also want to thank Professor S. Geoffrey Schladow, Director of Tahoe Environmental Research Center, from University of California, Davis, that provided some data from Lake Tahoe which I used to validate my algorithm. I kindly thank all MuDak partners, It is a honor to work with world-renowned researchers in my research

field.

Collective thanks go to all friends and colleagues from UFPR that provided me moral support for my academic pursuits. A special thank to some friends and collaborators, Lediane Marcon, Liége Wosiacki, Lucas Hoeltgebaum, and Geovana Colombo. I am indebted to Bruna Arcie Polli, that provided me her numerical model and answered all my doubts sent in extremely long e-mails. There were also some people outside of academia that I want to thank for the continuous support and the after-hours entertainment. I am particularly grateful to Marcelo Kamei, Filipi Mello, and Willian Kamei. I would like to especially thank my dear Finnish friend, Iita-Mari Ruponen, and French one, Alicia Videau for helping on abstract translation. All abstracts of this Master thesis, written in five languages, are ways to thank different cultures that I have experienced and has expanded on my peripheral vision and contributed to my outlook on life.

Last, but not least, all people, students, professors, workers, managers, poor and rich, that truly believe that science and education are the cornerstones that move our country and the world towards stability, equality and prosperity.

Curitiba, February 2019

"Mas a ciência tem o inefável dom de curar todas as mágoas; (...)"
– Machado de Assis;
O Alienista,
1882

Abstract

Internal wave is a oscillating disturbance within a stable density-stratified fluid. In stratified water basins, these waves have been detected and pointed as one of the most important process of water movements and vertical mixing. Most part of wind momentum and energy that cross the water surface is responsible to generate large standing internal waves, also called basin-scale internal seiches, in stratified basins. These waves are responsible for large scale motion, in which up to 40% of hypolimnetic volume may be exchanged after its passage. The baroclinic activity has important effects on nutrients, microorganisms, and chemical compounds fluxes, affecting strongly the water quality of these ecosystems. This research paid particular attention to the importance of the shear velocity as a source of turbulent kinetic energy available to excite internal seiches in small stratified basins. We compared in which condition the amplitude growth deviates from linear and nonlinear mathematical descriptions. To analyze all factors we used a set of methods, that included auto- and cross-correlations, spectral analysis of time-series records, and mathematical models of internal waves. We based our analysis on data, underwater temperature and meteorological conditions, obtained in two distinct small-stratified water basins, Vossoroca reservoir and Harp Lake. In addition, we also performed 13 laboratory experiments in a rectangular tank considering different stratification conditions to be incorporated in our analysis. We observed that for $W < 1$ and $h_e/H < 0.25$, the mathematical solutions overestimated the internal seiche amplitude, since it does not account the energy transference to generate instabilities, in which W is the Wedderburn number and h_e/H is the ratio between the epilimnion thickness and the total water depth. In addition, considering field observation, we detected that the wind forcing frequency and the natural frequency of internal seiche enable the resonance phenomenon, and consequently the internal seiche amplitude growth. We inferred that the contribution of the amplitude growth is not based directly on the wind frequency that matches exactly the internal wave frequency, but the whole higher frequency spectrum of the wind. Finally, we also concluded that the available turbulent kinetic energy plays an important role on the longitudinal internal seiche evolution. For most values of the parameter W, the internal wave excited presents a constant interfacial displacement along the basin with a strong variation just near the internal seiche node. However, considering $1 < W < 3$, we observed a exponential growth as the distance from the node increases.

Key-words: Internal Seiche. Lake Classification. Wedderburn Number. Lake Modeling.

Resumo

Ondas internas são perturbações propagantes que ocorrem no interior de um fluido estratificado. Estas ondas tem sido frequentemente detectadas e apontadas como um dos processo hidrodinâmico mais importante em bacias estratificadas, influenciando diretamente na dinâmica e mistura vertical do sistema. Grande parte da energia proveniente de ventos que cruzam a superfície de lagos e reservatórios é responsável pela formação de ondas internas longas e estacionárias, também conhecidas como seichas internas. Estas ondas são responsáveis por movimentos de grande escala, onde mais de 40% do volume proveniente do hipolímnio pode ser transportado para as camadas mais rasas do sistema após a sua passagem. Os movimentos baroclínicos afetam diretamente a qualidade da água destes ecossistemas, afetando os fluxos de nutrientes, microrganismos e compostos químicos. Esta pequisa tem como principal interesse a investigação da importância da velocidade de cisalhamento do vento como fonte da energia cinética turbulenta disponível para a formação de seichas internas em pequenas bacias estratificadas, avaliando em quais condições de instabilidades a amplitude das ondas internas não é satisfatoriamente modelado pela teoria matemática linear e não linear proposta. Para analisar todos estes fatores, foram empregados diversos métodos de identificação, nos quais incluem auto correlações, correlações cruzadas, análise espectral de séries temporais e modelos matemáticos de ondas internas. A análise foi baseada em dados obtidos em duas pequenas bacias, o reservatório do Vossoroca e o Lago de Harp. Ainda foram executados 13 experimentos em laboratório através de um tanque retangular considerando diferentes condições de estratificação para incorporar às análises de campo. Foi observado que para $W < 1$ e $h_e/H < 0.25$, os modelos matemáticos, tanto o linear quanto o não linear, superestimam as amplitudes das ondas internas, visto que ambos não incorporam a transferência de energia devido às instabilidades do sistema, onde W é o número de Wedderburn e h_e/H representa a razão entre a espessura do epilímnio e a profundidade total da bacia. Também foi observado que, para os dados de campo, a presença de componentes espectrais do vento, acompanhado com movimentos baroclínicos, permitem a ocorrência do fenômeno de resonância, contribuindo para um aumento acima do previsto da amplitude da onda interna. Foi observado que o efeito de resonância não está ligado diretamente ao espectro do vento que coicede com a frequência natural da onda, mas com todo o espectro do vento com maior frequência. Finalmente, foi também concluído que a energia cinética turbulenta disponivel tem também um papel fundamental na evolução longitudinal da onda. Para uma larga faixa de W, a onda interna apresenta variação constante ao longo da bacia, com abrupta variação apenas próximo ao nó da onda, primeiro terço. No entanto, considerando $1 < W < 3$, a amplitude local da onda aumenta exponencialmente com a distância ao nó.

Palavras-chaves: Seicha interna. Classificação de lagos. Número de Wedderburn. Modelagem de lagos.

Résumé

Une onde interne est une perturbation qui se propage au sein d'une densité stratifiée fluide. Dans des bassins d'eau stratifiés, ces ondes ont été détectées et considérées parmi les plus importants processus de mouvements d'eau et de mélange vertical. La majorité de la force du vent et de l'énergie qui traverse la surface de l'eau est la cause de grandes onde internes stationnaire, aussi appelées seiches internes, dans des bassins stratifiés. Ces ondes sont responsables de mouvements à grande échelle, dans lesquels jusqu'à 40% de volume d'hypolimnion peuvent être modifiés après leur passage. L'activité barocline a des effets notoires sur les flux de nutriments, microorganismes et composés chimiques, affectant ainsi fortement la qualité de l'eau de ces écosystèmes. Cette recherche a particulièrement prêté attention à l'importance de la vitesse de cisaillement en tant que source d'énergie cinétique turbulente disposée à stimuler les seiches internes de petits bassins stratifiés, comparant dans quelles conditions la croissance d'amplitude dévie des descriptions mathématiques linéaires et non-linéaires. Pour analyser tous les facteurs, nous avons eu recours à un ensemble de méthodes qui comprenait de l'autocorrélation, des corrélations croisées, de l'analyse des séries chronologiques et des modèles mathématiques d'ondes internes. Nous avons basé notre analyse sur des données concernant la température sous-marine et les conditions météorologiques, obtenues dans deux bassins d'eau distincts à faible stratification: le réservoir de Vossoroca et le lac Harp. De plus, nous avons également effectué 13 tests de laboratoires dans un réservoir rectangulaire prenant en compte différentes conditions de stratification à incorporer à notre analyse. Nous avons observé que pour $W < 1$ et $h_e/H < 0.25$, les solutions mathématiques surestimaient l'amplitude de la seiche interne, puisqu'elles ne prennent pas en compte le transfert d'énergie pour générer des instabilités. Aussi, compte tenu des observations faites sur le terrain, nous avons noté que la fréquence de forçage du vent et la fréquence naturelle de la seiche interne conduisent au phénomène de résonance, et par conséquent à la croissance de l'amplitude de la seiche interne. Nous avons remarqué que la contribution de la croissance de l'amplitude ne repose pas directement sur la fréquence du vent qui correspond exactement à la fréquence de l'onde interne, mais à tout le spectre de fréquence supérieure du vent. Enfin, nous sommes également arrivés à la conclusion que l'énergie cinétique turbulente disponible joue un rôle essentiel dans l'évolution de la seiche interne longitudinale. Pour la plupart des W, l'onde interne stimulée présente un déplacement interfacial constant le long du basin avec une forte variation juste à côté du nodule de la seiche interne. Cependant, compte tenu de $1 < W < 3$, nous avons observé une croissance exponentielle lorsque la distance du nodule augmente.

Mots-clés: Seiche interne. Classification des lacs. Nombre de Wedderburn. Modélisation de lacs.

Kurzfassung

Interne Wellen sind Instabilitäten in dichtestratifizierten Fluiden, die sich wellenförmig ausbreiten. In stratifizierten geschlossenen Gewässer, wie zum Beispiel Seen, sind interne Wellen eines der dominanten Prozesse für vertikale Mischung. Ein großer Teil des windinduzierten Impulses an der Wasseroberfläche ist für die Entstehung von großen stehenden internen Wellen verantwortlich. Diese werden in Seen auch Seiches genannt. Diese Wellen können bis zu 40% des Wasservolumens im Hypolimnion austauschen. Dieser Effekt ist wichtig für den Nährstoffaustausch und für Mikroorganismen und somit wichtig für die Wasserqualität. In dieser Arbeit wurde die Scherzone und die dort entstehende turbulente kinetische Energie zur Erzeugung von internen Wellen in kleinen Seen untersucht. Hierbei wurden die Bedingungen für linearen oder nicht-linearen Wachstum der Wellenamplitude analysiert. Hierfür wurden insbesondere Kreuzkorrelationen und Spektralanalysen von gemessen Zeitreihen durchgeführt, sowie vereinfachte mathematische Modelle herangezogen. Die genutzten Datensätze stammen von der Stauhaltung Vossoroca, in Curitiba, Brasilien, sowie vom Harp See in Nordamerika, wo kontinuierliche Temperaturprofilmessungen und meteorologische Datenreihen zur Verfügung standen. Zusätzlich wurden in dieser Arbeit 13 Laborexperimente in einem rechteckigen Tank durchgeführt. Die Ergebnisse zeigen, dass für $W < 1$ und $h_e/H < 0.25$ die mathematischen Ansätze die Wellenamplituden überschätzten. Dies, da die mathematischen Ansätze den Energietransfer zur Erzeugung von Instabilitäten nicht beinhalten. Die Ergebnisse der Feldmessungen zeigen, dass die Windfrequenz und die natürliche Eigenschwingungsfrequenz des Sees einen Resonanzeffekt erzeugen und damit die Amplitude der internen Wellen vergrößern. Hierbei ist nicht nur die Windfrequenz verantwortlich, die der Eigenfrequenz des Sees entspricht, jedoch das ganze höhere Frequenzspektrum des Windes. Für die Langzeitentwicklung der Wellen spielt die vorhandene turbulente kinetische Energie eine wichtige Rolle. Für die meisten W -Nummern wird eine Welle erzeugt, welche einer konstanten Schwankung der Zwischenschicht entspricht, mit großen Änderungen am Seiche Knotenpunkt. Andererseits, für $1 < W < 3$ wurde mit wachsendem Abstand zum Knotenpunkt ein exponentielles Wachstum beobachtet.

Schlüsselworte: interne Wellen. Seenklassifikation. Wedderburn Nummer. Seenmodellierung.

Tiivistelmä

Vedenpinnan alla tapahtuva sisäinen aalto on etenevää häiriötä vakaan tiheyden nesteessä. Kerrostuneissa vesialtaissa nämä aallot on todettu ja osoitettu yhdeksi tärkeimmäksi tapahtumasarjaksi, joka liikuttaa vettä ja sekoittaa sitä pystysuuntaisesti. Suurin osa tuulen liikemäärästä ja energiasta, joka ylittää veden pinnan, saa aikaan suuria sisäisiä seisovia aaltoja. Tällaisia aaltoja kutsutaan suljetuissa kerrostuneissa vesialtaissa seisovaksi aalloksi eli pinnanalaiseksi seicheksi. Nämä aallot aiheuttavat suuren mittaluokan liikettä, jonka seurauksena jopa 40% alusveden tilavuudesta voi olla vaihtunut aaltojen ohimentyä. Barokliinisella aktiivisuudella on suuri vaikutus ravinteille, pienelijöille ja kemiallisen seoksen vaihteluille ja virtauksille, ja se vaikuttaa vahvasti veden laatuun ekosysteemeissä. Tämä tutkimus kiinnitti erityistä huomiota liikenopeuden tärkeyteen turbulenttisen kineettisen energian lähteenä ja sen vaikutuksesta kiihdyttää pinnan alaisia seichejä pienissä kerrostuneissa altaissa verraten olosuhteita, joissa äärivälien kasvu poikkeaa lineaarisesta ja epälineaarisesta matemaattisista kuvauksista. Analysoidaksemme kaikki muuttujat, käytimme eri metodeja. Metodimme sisälsivät autokorrelaatioita ja ristikorrelaatioita, aikasarjatallenteiden spektrianalyysejä ja matemaattisia mallinnuksia sisäisistä aalloista. Perustimme analyysimme aineistoon, vedenalaiseen lämpötilaan ja meteorologisiin olosuhteisiin, joita tutkimme kahdesta erilaisesta vähäkerrostuneesta vesialtaasta, Vossorocan tekojärveltä ja Harp-järveltä. Suoritimme myös 13 laboratoriokoetta suorakulmaisessa vesisäiliössä ottaaksemme huomioon erilaiset kerrostumisolosuhteet ja liittääksemme ne analyysiimme. Huomasimme, että matemaattiset ratkaisut $W < 1$ ja $he/H < 0.25$ yliarvioivat pinnanalaisen seichen värähtelytaajuuden, sillä kaavat eivät pidä sisällään energian siirtymistä epävakauden muodostuessa. Lisäksi, ottaen huomioon kenttätutkimuksen, me havaitsimme, että tuulen voiman frekvenssi ja pinnanalaisen seichen ominaistaajuus mahdollistavat resonanssi-ilmiön, joka kasvattaa pinnanalaisen seichen laajuutta. Havaitsimme, että värähtelytaajuuden kasvu ei perustu suoraan tuulen frekvenssiin, joka vastaa täysin sisäisen aallon frekvenssiä, vaan kokonaan korkeampaa tuulen frekvenssispektriä. Lisäksi lopuksi teimme johtopäätelmän, että turbulenssisella kineettisella energialla on tärkeä rooli pitkittäisen pinnanalaisen seichen kehityksessä. Ennen kaikkea W esittää sisäisen aallon kiihtymistä jatkuvana rajapinnan syrjäytymisenä allasta pitkin suurella variaatiolla aivan pinnanlaisen seichen risteyskohdassa. Kuitenkin, ottaen huomioon $1 < W < 3$, havaitsimme ekspotentiaalisen kasvun, kun etäisyys risteyskohdasta kasvaa.

Asiasanat: : Sisäinen aalto (seiche). Järviluokitus. Wedderburn kaava. Järvimallinnus.

List of Figures

List of Tables

List of abbreviations and acronyms

WKB	Wentzel-Kramers-Brillouin method
DFT	Discrete Fourier transform
FFT	Fast Fourier transform
STFT	Short-time Fourier transform
WDT	Windowed Fourier transform
PSD	Power spectral density
CPSD	Cross power spectrum
TEDM	Two layer equivalent depth model
TVDM	Two layer variable depth model
SAR	Synthetic-aperture radar

List of symbols

N	Brunt-Väisälä frequency
g	Gravitational acceleration
ρ_i	Density of the fluid i
κ_ϵ	Conductivity at the reference temperature ϵ
f_ϵ	temperature correction factor for natural waters
z	Depth scale
δ_{min}	Density gradient threshold
h_i	Thickness of layer i
g'	Reduced gravity
S	Instability frequency
w_*	Wind friction velocity
κ	Von Kármán constant
σ_w	Wind stress at water surface
C_D	Surface drag coefficient
w_{10}	Wind velocity at 10 meters above the surface
K	Universal constant
Ri	Richardson number
Fr	Froude number
W	Wedderburn number
L	Reservoir length
L_p	Reservoir length at pycnocline depth
L_N	Lake number
H	Total depth/thickness of the basin
A_s	Reservoir surface area
S_t	Schmidt stability
ζ	Interfacial wave displacement
f_i	Internal wave linear frequency
f_d	Damping frequency-scale
α	e-folding energy decay frequency
δ_b	Turbulent boundary layer thickness
δ_ρ	Pycnocline thickness

ν	Water kinematic viscosity
c_p	Non-rotating internal wave phase speed
k_o	Nonlinear coefficient
k_u	Dispersion coefficient
c_p	Internal wave phase speed (two-layer system)
f_s	Nonlinear frequency-scale
f_{kh}	Kelvin-Helmholtz frequency-scale
f_b	Supercritical frequency-scale
$\mathscr{F}\{f(n)\}$	Fourier transform of function $f \equiv \hat{f}$
ω_t	Parameter of frequency transformation
M	Signal length
ϕ_{ff}	Power spectral density of function f
ϕ^*_{ff}	Mean-square power spectral density of function f
T_s	Sampling period
ϕ^*_{fg}	Cross power spectrum of function f and g
$\bar{\mu_f}$	Signal mean of function f
C_{fg}	Coherence between signals f and g
P_{fg}	Phase shift between signal f and g
W_f	Wavelet transform of function f
υ	Translating parameter of the mother wavelet
s	Scaling parameter of the mother wavelet
ψ	Wavelet function
$\bar{W_f}$	Global wavelet spectrum
u_i	Velocity vector -
P	Total thermodynamic pressure
Λ	Viscosity coefficient (First term)
ν_u	Viscosity coefficient (Second term)
S_{ij}	Rate of strain tensor in $i-j$ direction
$\overline{\omega_o \hat{j}}$	Inertial frequency
$\bar{\phi}$	Mean latitude
ε	Angular frequency of the Earth $\equiv 7.27\ 10^{-5}$ rad/sec
U^*	Ursell number
λ	Wavelength
h_w	Wave height

Bu	Burger number
Ld	Rossby deformation radius
L'	Length scale $= 2\overline{\omega_o j}/L_p$
Ω	Vorticity
Π	Non-dimensional quantity of q
Re	Reynolds number
S_p	Gravity current velocity
Δt	Time step
σ^2	Variance
$U(s\omega_t)$	Heavyside step function
k_ϕ	Wave-vector of function ϕ
K_{cell}	Cell constant (conductivity meter)
ϕ_i	Velocity potential of layer i
k	Wavenumber
ω	Angular frequency of the internal wave
η	Surface displacement
ζ	Internal wave displacement
$T_{n,m}$	Internal wave period of mode VnHm
n	Number of vertical mode
m	Number of horizontal mode
β_n	Eigenvalue of a multi-layer system
c_n	Internal wave phase speed for β_n (multi-layer system)
$\bar{H}$	Parametrization of total water depth of a two-layer system
T	Water temperature
T_{wind}	Duration of a wind event
Ψ_{dur}	Filtering parameter (Wind duration)
Ψ_{dir}	Filtering parameter (Wind duration + direction)
r^2	Coefficient of determination

Contents

1 Introduction

Internal gravity waves are oscillating disturbances within a stable density-stratified fluid. One of the first scientific observations[1] of internal waves on natural environment were made by Nansen (1897) during an expedition to the North Pole in 1893. The Norwegian explorer Fridtjof Nansen feels an extra drag on his boat Fram due to internal waves as the ship passed the Nordenskiold Archipelago, north of Siberia. He called the phenomenon "dead water", reporting that it slowed his boat to a quarter of its normal speed.

> *"Fram appeared to be held back, as if by some mysterious force, and she did not always answer the helm. In calm weather, with a light cargo, Fram was capable of* 6 *to* 7 *knots. When in dead water she was unable to make* 1.5 *knots*[2]*."*
>
> F. Nansen (1897)

Ekman (1904), as a Ph.D. student motivated by the observations made by Nansen (1897), was the first researcher to study in detail the dead-water effect. He explained that energy from ships is transmitted to internal waves which occur between layers of different densities. An important loss of steering power is experienced by the boat, and consequently the ship speed decreases dramatically. The interest in investigations involving internal waves grew up after 1965, when the most tragic incident involving a USA submarine with an crew of 129 on board fell down to deep water due to a passage of a large internal wave. The US Thresher submarine was going along the thermocline, when an internal wave took it down quickly to really deep waters. The U-boat lost orientation and had problems due to high pressure, killing all 129 people on board (GOVORUSHKO, 2011).

Recently, Alford et al. (2015) pointed out that solitary internal waves of 170 meters of amplitude produced in the Luzon Strait, between Taiwan and the Philippines, are a key for understanding climate change, and are an important missing piece of the puzzle in climate modeling. Internal waves in the ocean influence ocean turbulence and consequently affects the ocean currents that carry heat and salinity around the globe. This phenomenon may increase the mixing of sea, which transfer heat from the upper ocean to the depths and lead to ice loss.

Internal waves occur in every perturbed stratified system. As the energy needed to increase a water layer in the air is greater than energy needed to rise a water layer in the lower water density, internal waves normally are much bigger than surface waves generated by the same energy input. These waves have been reported in different scientific areas, from cosmology to limnology. The scientific community have observed internal waves in ocean, atmosphere, thermal stratified basins, stellar interiors. The formation of internal waves depend on the system and the perturbation source. The Dead Water phenomenon described by Nansen (1897) was caused essentially by the friction caused by the boat Fram. Conversely, internal waves observed in the South China Sea by Alford et al. (2015) are generated primarily by tidal flow past seafloor topography and wind blowing on the ocean surface. As the internal waves propagate

[1] There are some evidences that a similar phenomenon have been describe by Publius Cornelius Tacitus, a senator and historian of the Roman Empire, on his books The Germania (latin: *De Origine et situ Germanorum*) written 98 AD. He mentioned a flat sea on which one could not row a boat

[2] The knot is a unit of speed equal to one nautical mile per hour, 1 knot $\equiv$ 1.852 km/h

west from the Luzon Strait they steepen, producing a package of internal solitary waves with 150 meters of amplitude. Similarly, as observed by Mortimer (1952), the formation of internal waves in closed basins is caused by many sources, but the wind action over the basin surface is the most important source of energy for wavefields. However, since the basin is closed, the long wave formed by the wind creates a basin-scale internal wave called internal seiches, as shown in Figure 1.

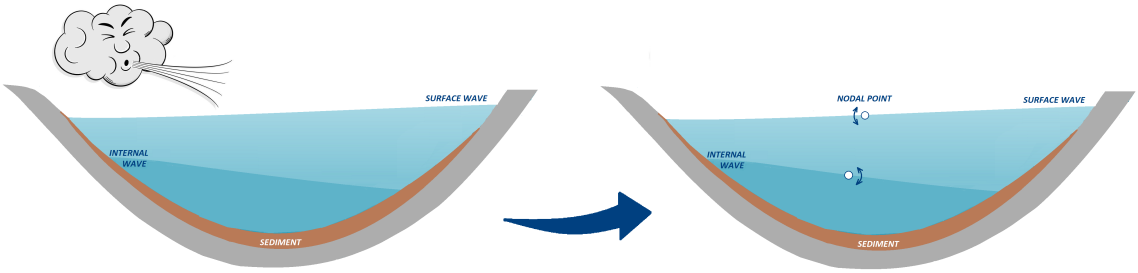

Figure 1 – Wind-induced stationary internal wave in a stratified basin.

The first observation of internal seiches in thermally stratified lakes was provided by Thoulet (1894 apud MORTIMER, 1952), Watson (1903) nonetheless was the first limnologist to provide the right interpretation of these gravity waves in closed basins. Watson (1903) concluded that the temperature oscillation observed during a campaign in Lake Loch Ness was due to an uninodal baroclinc internal wave caused by the wind action on the lake surface. Since the beginning of 20th century, internal waves on closed basins have been extensively studied. Wedderburn and Williams (1911) and Mortimer (1952) defended the importance of internal waves in lakes and reservoirs, spreading the knowledge of their existence and importance. New technologies have provided better understanding of internal waves patterns in basins, revealing their strong influence on the system dynamic. The spectral analysis and the improvement on water temperature measurements have improved the detection of internal waves in lakes. A phenomenon that initially appeared to exist just in some rare cases, actually is frequently in lakes and reservoirs of different sizes and shapes.

Recent research has addressed the importance of internal waves in reservoirs and lakes. According to Bruce et al. (2008), wind-induced internal waves are responsible for large scale motions in the benthic boundary layer, and consequently leading to episodes of sediment re-suspension. Umlauf and Lemmin (2005) observed in Lake Geneva that up to 40% of hypolimnetic volume was exchanged after a passage of a large internal seiche. The energy deposited into such long internal waves is eventually transformed through a down-scale energy cascade across the spectrum of internal waves due to the strong turbulence production in the benthic boundary layer. As observed by Boegman, Ivey and Imberger (2005b), it allows that fundamental internal seiches degenerate into a train of solitary waves, increasing the system mixing. Although in closed basins baroclinic motion does not present a global-scale effect as observed by Alford et al. (2015) in the Luzon Strait, these motions in lakes and reservoirs affect strongly the water quality of these ecosystems. Many recent studies have pointed out the ecological effects due to passage of internal seiches on nutrients (MACINTYRE; JELLISON, 2001), microorganisms (PANNARD; BORMANS; LAGADEUC, 2008), and chemical compounds fluxes (BOUFFARD; ACKERMAN; BOEGMAN, 2013). According to Mortimer (1952), internal waves have been considered the most important process of water movements and vertical mixing in closed stratified basins.

Globally, Downing et al. (2006) estimated the existence of more than 304 million "standing" water bodies[3] covering an area of approximately 4.5 million km^2, which is equivalent to half the area of Brazil.

[3] Even though many studies call lakes, ponds, impoundments as "standing water bodies", these water

Even though the understanding of internal wave effect has been largely studied since the 20th century, the large majority of scientific studies have been conduced for large lakes (> 10 km^2), which represents 0.07% of all water basins worldwide. According to Downing et al. (2006), the 99.93% of fresh water basins with area lower than 10 km^2 cover an area of 2.5 million km^2, which correspond to 52% of the total area of all "standing" water bodies. Even though baroclinic motion is an ubiquitous feature of closed basins, as LaZerte (1980) pointed out, their occurrence in small lakes has seldom been investigated. According to Pannard et al. (2011), the restricted surface area of small basins and the relatively shallow system allows strong stratification. Thus, even weak wind events can excite internal waves. The ecological consequence may be amplified due to the shallow system.

In this research we analyze the development of basin-scale internal waves formed in fresh water closed small basins during the summer months of thermal stratification. We identify the amplitude, frequency, and vertical and horizontal baroclinic modes in two different "standing" water bodies, a small dendritic reservoir with predominant easterly wind events (Vossoroca reservoir) and a regular elliptic lake with no predominant wind events in one specific direction (Harp Lake). We also characterize the thermal stratification and the degeneration of long internal waves. We compare the results of different periods and basins to highlight the importance of the shear velocity along the basin as a source of turbulent kinetic energy available for mixing during an internal wave event considering different meteorological and underwater temperature conditions. Moreover, we observe the importance of wind resonance to increase the internal wave energy. Finally, we compare results and methods from field observations with laboratory experiments.

In light of the foregoing discussion, we work toward several specific objectives:

- Identification of internal waves in Vossoroca reservoir and Harp Lake;
- Classification of generation and disintegration of long internal seiches according to the nonlinear and linear theory;
- Improve some variables to better predict the internal wave occurrence;
- Classification and identification of probability to excite internal wave for each seasons and basins based on internal wave formation and its main patterns;
- Compare the internal wave energy cascade along the basin with the system stability;
- Evaluate how wind resonance affects the increase of wave energy;
- Observe through field observations and laboratory experiments the importance of the shear velocity as a source of turbulent kinetic energy available for mixing during an internal wave event.

bodies are not completely stagnant. Lakes and reservoirs may present internal water movement, and as seen in this study, the motion may be predictable and influence strongly the water quality.

2 Literature Review

" I conclude from these observations, and others taken at different parts of the loch, that is an internal oscillation in the waters – an internal seiche [1] [...]"
E. R. Watson (1903)

2.1 Thermal stratification of closed basins

Stratification occurs in most lakes and reservoirs and has important effects on these ecosystems with chemical, physical, and biological consequences, playing an important role in the water quality. For example, stratification can have an important effect on pollutant transport. There are many factors that can affect stratification in this kind of environment. One of the most common cases is when the density stratification is caused by temperature differences. This density stratification is referred to as thermal stratification. As Alloway and Ayres (1997) point out, in regions with warm and cold seasons lakes are likely to have thermal stratification.

Solar radiation, the main source for thermal stratification, strikes the water surface, and portion of this radiation is reflected, whilst other penetrates the water surface. Because of the low conductivity of water, the amount of absorbed solar radiation decreases with depth. Therefore, the water near the surface becomes warmer than that at the bottom. As Ji (2017) stated, in a summer with high solar radiation, the lake becomes stratified into three distinct vertical zones: epilimnion, metalimnion, and hypolimnion, as shown in Figure 2(a). If the density gradient falls abruptly through the metalimnion, the system can be approximated by a two-layer system, epilimnion and hypolimnion. The metalimnion becomes just an interface between these layers. The epilimnion is the top layer of the reservoir where the water temperature is more influenced by solar radiation and by the atmosphere exchange between air and water. It is defined as the warmer and oxygen-rich upper layer. This zone can be well mixed depending on the exposure of the reservoir to wind. Thus, the larger the reservoir and the higher the intensity of the wind, the larger is the well mixed depth. The temperature of this layer may vary according to the region of the water body and can be influenced by many other factors, such as wind intensity, reservoir size, suspended materials, and reservoir location. The hypolimnion is the bottom, coldest, and densest layer (Figure 2(a)). This zone is often anoxic and inhabited by only few species.

The metalimnion is defined as the zone where water temperature drops very fast. The surface within the metalimnion through the point of greatest water temperature change is called thermocline. Many books and papers use the term "thermocline" as a synonym for metalimnion. However, in order to avoid misunderstanding, we consider "thermocline" just the point where temperature drops fastest. Thus, thermocline is just a single interface within the metalimnion, as seen in Figure 2. The metalimnion is located bellow the epilimnion and above the hypolimnion, its thickness can vary from one body of water to another. Usually, in small impoundments, the thermocline may be located approximately 3 metres below the surface of the reservoir, and the metalimnion can have a thickness of approximately 30 cm. In

[1] Watson (1903) observed these oscillation in a field campaign in Lake Loch Ness. His conclusion was the first right interpretation of internal waves in lakes. He also supposed in that paper that these oscillations were created by strong wind events, supposition that would be properly identified by Birge (1916) years late.

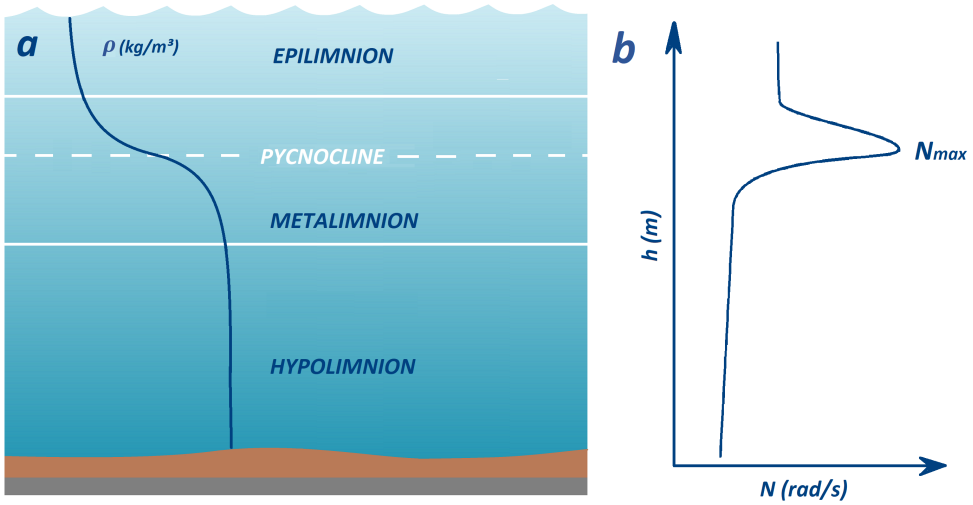

Figure 2 – a) Temperature stratification in a typical reservoir/lake during summer and b) the vertical profile of buoyancy frequency.

large reservoirs, the thermocline may be 10 m deep and the metalimnion may have several centimeters. In fresh water basins, the thermocline matches with the pycnocline since the system is essentially just thermally stratified. The pycnocline is a region of the water column with strongest vertical change in density (DENNY; GAINES, 2007). When stratification is based only on salinity, the pycnocline matches with the halocline, the zone where water salinity drops fastest. However, in ocean and large reservoirs, such as those formed from strip mining excavations, both temperature and salt may affect the density stratification, and consequently the pycnocline does not match with any other cline.

According to Serreze and Barry (2014), the density of most substances decreases when thermal energy is removed. However, water increases its density just until 4 °C, where density reaches its maximum at 1 atm, 1,000 kg/m^3. When the water temperature is reduced further, an unusual phenomenon is observed. Water starts to decrease in density. This phenomenon is referred to as the water anomaly and is responsible for ice floats at the water surface. In this circumstances, the system becomes stable and the stratification increases. The intensity and duration of this stratification depends on many factors, such as solar radiation, wind, topography, and dissolved or suspended substances. Although stratification in lakes is mainly modified by solar radiation, water density is a function of temperature, salinity, and pressure. Thus, the water density may be based on weight of a carefully measured volume of solution, avoiding series of individual measurements. These measurements can be done with a pycnometer or a densimeter. Direct water density measurements are difficult to be obtained for long periods and large depths. Since the end of 19th century researches have focused to establish an empirical equation that could be used to determine water density based on pressure, temperature and salinity measurements. The effort to establish an equation that covers an entire range of all these three variables is a result of a series of experimental analysis. One of the first equations of state was formulated for pure and sea water by, respectively, Tait (1888) and Knudsen Martin e Forch (1901). Mamaev (1964) formulated an equation based in Knudsen equation and obtained a nonlinear equation of state covering a salinity range of 0 to 40 ppt and a temperature range of 0 to 30 °C. Kell (1975) found a polynomial form for the equation of state valid for pure water in a range of 0 – 150 °C, and pressure less than 10^8 Pa. Applying the same procedure, but using the thermal and saline gradients calculated by IESS-1980, a new form of Mamaev (1964)'s formula covering a maximum temperature of 40 °C was obtained. Pruppacher and Klett (1980) have shown that, in atmospheric pressure range, the isothermal compressibility of water

is very small, and consequently water density is not strongly influenced by pressure. Thus, under this circumstances, water may be classified as an incompressible fluid. Millero and Poisson (1981) proposed an 1-atm expression for seawater density with accuracy of 0.01%. The algorithm was implemented by Fofonoff and Millard (1983), and uses the density of the reference pure water formulated by Craig (1961). The equation proposed by Fofonoff and Millard (1983) covers ranges of many parameters, including conductivity to salinity conversion; specific heat of seawater, and potential temperature. Recently, a new standard formulation based in Fofonoff and Millard (1983) was introduced. The new formulation proposed by Commission et al. (2015) updated thermodynamic description. The new approach is totally consistent with thermodynamic Maxwell cross-differentiation relations and incorporate the new thermodynamic description of pure water that has been developed by Wagner and Pruß (2002). Many internal wave studies have used the formulation proposed by Fofonoff and Millard (1983), even for fresh water lakes, and neglecting other effects on water density.

An important characteristic of a stratified ambient with density distribution is the buoyancy frequency, or also called as Brunt-Väisälä frequency. The buoyancy frequency is a measure of the static stability. The higher the density difference, the higher is the Buoyancy frequency, and consequently, the greater is the system stability (Figure 2(b)). For that reason, the metalimnion layer is an obstacle to transfer heat, aquatic micro-organisms, chemical compounds, and nutrients. They also contribute to decrease the velocity of the currents, and reflection of lights (IMBERGER, 1998b). Mathematically, the Brunt-Väisälä frequency, N, is given by

$$N \equiv \sqrt{-\frac{g}{\rho_o}\frac{\partial \bar{\rho}}{\partial z}}, \tag{2.1}$$

in which g is gravitational acceleration, $\bar{\rho}$ is the potential density, ρ_o is the characteristic density of the fluid, and the z is the vertical coordinate pointing upwards. When $\partial\bar{\rho}/\partial z$ is negative, the ambient is called stable, corresponding to a denser fluid below the lower one. Physically, the implication of this is that when a part of a fluid is displaced upward being heavier, it tends to return down to its stable position. In this process, this part of fluid acquires a vertical velocity; upon reaching its original level the particle's inertia causes it to go further downward. So, the portion is recalled upward by a buoyant force and an oscillation persist about the equilibrium level (CUSHMAN-ROISIN; BECKERS, 2011). This idea is further explored in section 2.3, when internal waves theory is presented.

2.1.1 Salinity and temperature measurements

As mentioned before, water density is a function of temperature, pressure, and salinity. These parameters need to be measured to yield a satisfactory water density, and consequently a precise representation of the environmental conditions. Temperature can be measured by many devices, such as thermocouples, resistive temperature devices (RTDs), and thermistors. Thermocouples are devices to measure temperature by measuring a change in voltage. Whenever there is a temperature difference along two wires, there is also a electric potential difference that generates a magnetic field, and consequently the compass is moved to indicate the temperature. The magnitude of this electric pressure depends on the wires material. The relationship between voltage created by the conductors and temperature is known for a large number of conductor pair, and have been largely documented (TAYLOR, 1997). Even though thermocouples have a very fast response to temperature changes, voltage signal in a majority of cases is nonlinear. They are susceptible to corrosion and have worse long-term stability and accuracy than the resistive devices.

Resistive temperature devices (RTDs), also called resistance thermometers, are devices to measure temperature based in resistance change, and have a positive temperature coefficient. Most RTDs

devices consist of fine coiled wire wrapped around a ceramic core. Usually, the wire is made of pure metals such as nickel, platinum, and copper. These devices are classified according to metal that are used in their composition. In the same way of thermocouples, RTDs have been largely documented according to a large range of wires. Their elements are relatively fragile. Therefore, RTDs are typically protected by a sheathed probe. RTDs provide an excellent long-term stability and repeatability, ability for sensors to repeat the same behavior under the same conditions for any given temperature. In the similarly way of thermocouples, resistance thermometers can be affected by corrosion, converting the metal element from its pure form to a metal oxide, which will tend to increase the wire resistance. When RTDs are made with platinum, they are not affected by corrosion or oxidation. However, Platinum resistance thermometers may be really more expensive. Although RTDs show an almost linear resistance-temperature relationship, the temperature coefficient is really low (HERMAN, 2011). As a result, it does exhibit a low change in resistance over a large change of temperature.

The second type of resistive device used to measure temperature is known as a thermistor. Thermistors have much higher temperature coefficients than RTDs. Their resistance varies dramatically over some temperature range, and are considered one of the most sensitive devices to measure temperature, with sensitivities in the range of 3 to 6%. Thermistors are ceramic semiconductors made from metal oxides which have an electrical resistance that decrease with temperature (BUERK, 1995). These type of sensors are extremely nonlinear.

All types of temperature sensors may be used as static or dynamic. Static temperature sensor need to have a temporal resolution required for the phenomenon that is investigated. Generally, the recommended sample frequency is twice the maximum Brunt-Väisälä frequency, N_{max}, and 4 times the average N at the sensor depth. This kind of sensors is often coupled in an anchored buoy station, also called mooring or chain. Moorings keep instruments in a specific submerged position. The surface buoy is usually equipped with a data logger, which is responsible to recover sensors data. To avoid movements and rotations due to internal and external forces, ball-bearing swivels, anchors and rope are often used on the surface and near the basin bottom. In terms of internal wave investigation, essentially the mooring is equipped with a thermistor chain. The thermistor chain is a long electrical cable containing temperature sensors and connected to batteries and a host logger systems. Since internal waves can be excited in different depths, a several quantity of temperature sensor along the vertical coordinate is essential, as shown in Figure 3(b). In spite of the fact that a good spatial resolution is crucial for internal waves investigation, for low-frequency waves, temporal resolution is not so important. It can have order of minutes, since basin-scale internal waves generally has order of several hours. On the other hand, to investigate high-frequency internal waves ($\sim 10^{-}3\ Hz$), internal wave breaking, and shear instabilities ($\sim 10^{-}2\ Hz$) high temporal resolution along the reservoir is crucial to capture these thermal oscillations.

Dynamic temperature sensors need to have a fast response. Generally, this type of temperature sensors are coupled with others devices. As a result, this combination of devices are called as multi-parametric sensors. One of the most famous instruments developed for determining water properties in lakes, reservoir, and oceans is known as CTD – an acronym for conductivity, temperature, and depth. Usually, CTDs use a fast response Platinum RTD to measure temperature. CTD device has a pressure sensor that measures the equivalent hydrostatic pressure of the water above the sensor to calculate the total water depth. CTDs are also equipped with a conductivity sensor that measures true or specific conductivity. A profiling CTD measurement is made when this device travels vertically though the water. Therefore, this device is submerged until it hits the bottom. Many multi-parametric sensors can make an average between the travel up and down to measure the profile parameters. Although CTDs have a good spatial resolution, as shown in Figure 3(a), a good temporal resolution is difficult to obtain for long time of measurements, mainly because this device usually is operated manually. Even though a reasonable

temporal resolution could be reached, submersion time could be a problem for temporal resolution since only one sensor is responsible to make all spatial measurements. Definitely, the temperature sensors used in this multi-parametric devices can be used as static sensors to obtain a high temporal resolution. However, generally CTDs temperature sensor are made with platinum resistance thermometers. They present a high temporal resolution with high accuracy. Therefore, considering that they would work as static sensors, more sensors should be deployed at different depths to obtain water temperature profiles. Nevertheless, only one Platinum resistance thermometer can be coast more than 60 times of a common Cooper thermocouples.

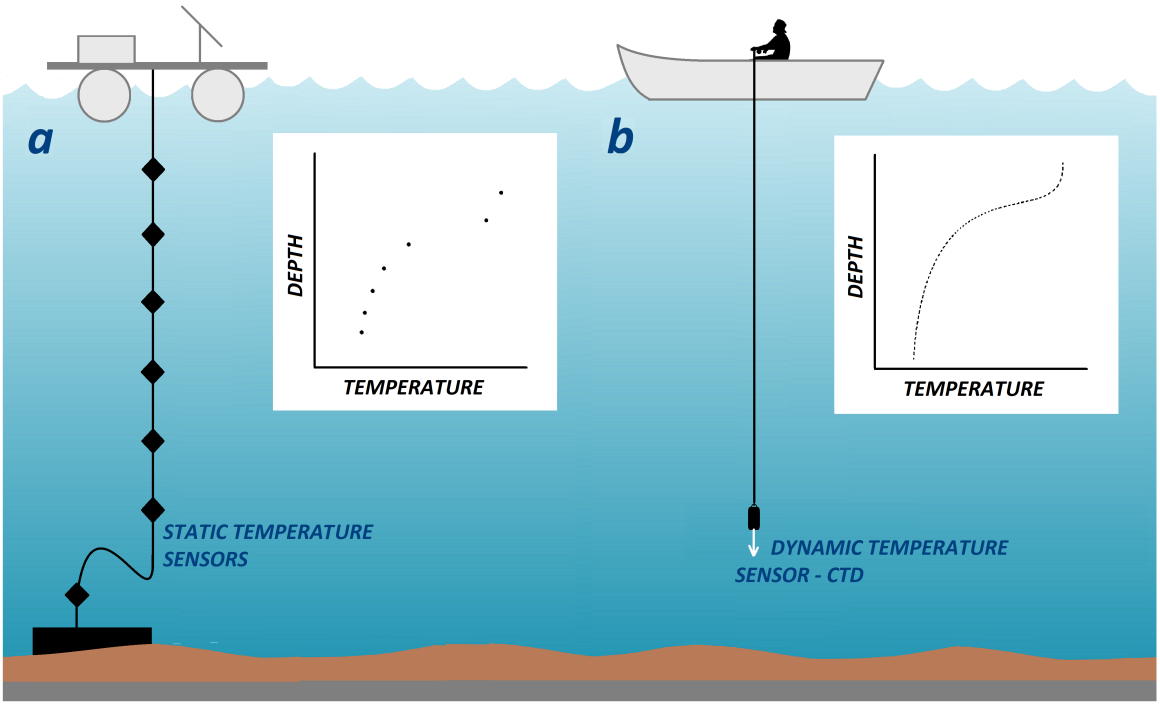

Figure 3 – Difference between dynamic and static temperature sensor, considering 7 static temperature sensors deployed equidistantly.

In most impoundments, density stratification is dominated by thermal stratification, and consequently water density is dominated by temperature change. However, in most hydrodynamic experiments, it is difficult to control heat transport, and consequently the temperature of the water. Thus, in most cases, experimental analysis of stratified flow is conducted in a channel where stratification is caused by a salinity difference. As Perkin and Walker (1972) stated, salinity could be defined as a conductivity ratio. The water conductivity depends on the number of dissolved ions per volume and their mobility. Thus, temperature can affect directly the ions mobility, but may also cause an increase in the number of ions solution due to dissociation of molecules. According to Gray (2005), the relationship between temperature and conductivity follows a extremely nonlinear behavior for natural waters, such as sea, rivers, reservoirs, and lakes. Thus, the higher the temperature and number of ions, the higher will be the water conductivity. That is why seawater has high conductivity, and consequently higher density than the fresh water. Although the number of the ions increase in seawater, the system remains electrically neutral. This phenomenon occurs when electrolytes dissolve in water, they split into cations and anions, but the concentration of each atoms remains the same.

Conductivity can be measured by conductivity meter and usually is displayed with units μS/cm or mS/cm. Most conductivity meters are delivered with certified cell constants. The cell constant, K_{cell},

is defined as the distance between the probe's electrodes divided by the surface of the electrodes. The determination of the cell constant depends on the conductance readings and the conductivity results. The conductance, the ability of the solution to conduct electric, is affected by the distance and area that the electrodes act. Thus, for a sample with low conductivity, the electrodes can be placed closer or the surface area of electrodes can be raised. Nowadays, conductivity meter have been developed to operate on a four ring principle, where one only probe can have more than one cell constant. Nonetheless, the cell constant needs to be selected appropriately for each application. Figure 4 shows standard conductivity values for a set of samples and the range of recommended cell constants for a given conductivity meters.

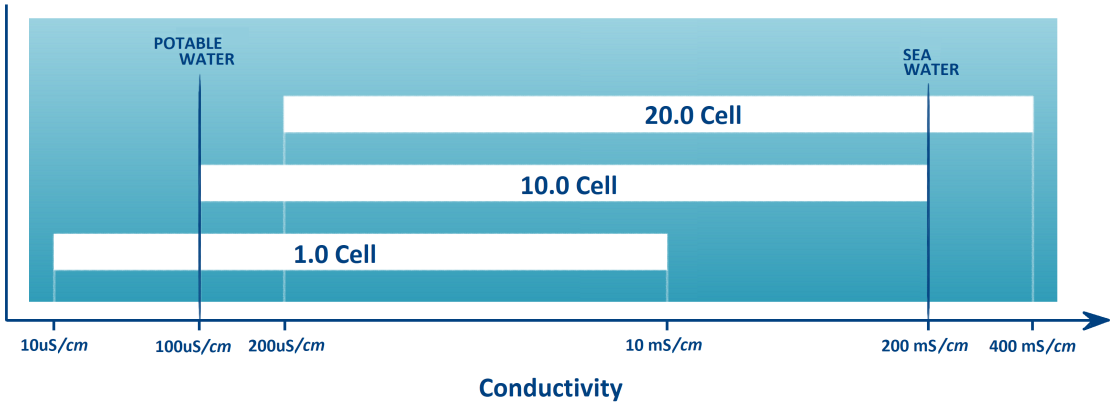

Figure 4 – Range of conductivity for three different cell constant.

As mentioned before, the extremely nonlinear behavior of conductivity implies that a nonlinear temperature compensation method should be used. Different methods of temperature correction have been developed to simplify the relationship between these variables. In this case, a nonlinear temperature compensation is required. According to Barron and Ashton (2005), the results should be referenced to a specified temperature, to allow the comparison between conductivity measurements. Thus, the conductivity is measured by using a temperature compensation at a reference temperature, 20 °C or 25 °C (HAYNES, 2014):

$$\kappa_{\tau-\epsilon} = f_\epsilon \kappa_\tau, \tag{2.2}$$

in which $\kappa_{\tau-\epsilon}$ is the conductivity at the reference temperature ϵ, κ_τ is the measured conductivity, and f_ϵ is the temperature correction factor for natural waters (nonlinear correction). A list of temperature correction factors for a range of 0.0 °C to 35 °C is provided by Mattler-Toledo AG, Analytical (2013). Many current conductivity meters make this correction automatically. Some conductivity meters also offer a specific temperature correction method.

As previously stated, salinity is a function of conductivity. Therefore, as Knudsen Martin e Forch (1901) observed, salinity can be measured using electrical conductivity. A useful summary of equations used to calculate salinity from electrical conductivity was presented by Fofonoff and Millard (1983). However the application of these equations is restricted to a range 2 to 42 psu.

Pressure is the third and last variable in a complete form of an equation of state. As stated previously, in many applications water is considered an incompressible fluid since under atmospheric pressure range, the isothermal compressibility of water is very small. Therefore, we do not need to consider pressure as a function of density since in reservoirs and lakes the pressure changes are too low to cause a significant change in density. Clearly, the pressure may affect water density in case of high pressure systems. In nature the effect of pressure in water may be important in abyss zone, the relative density change is $\approx 4.5\%$ in that really deep ocean zone.

2.1.2 Pycnocline depth and thickness

One of the most important indicators of energy budget, nutrient recycling, primary production dynamic, and mixing dynamic in impoundments is the pycnocline depth and also the metalimnion thickness (WETZEL, 2001). The pycnocline is the point where density changes most rapidly with depth, but the pycnocline depth and the metalimnion thickness are not easy to obtain as illustrated in Figure 2. Most of the time the reservoir is thermally stratified, temperature measurements are taken at large discrete depth spacing as shown in Figure 3(b). Therefore, the pycnocline depth and the metalimnion thickness are influenced by the spatial measurement resolution. Clearly, the pycnocline region is located within the bounds of two depths at which the discrete measurements presents the highest density gradient, where $i = \varphi$.

$$\left.\frac{\partial \rho}{\partial z_{i\delta}}\right|_{i=\varphi} = \frac{\rho_{\varphi+1} - \rho_{\varphi}}{z_{\varphi+1} - z_{\varphi}}. \tag{2.3}$$

Nevertheless, we cannot guarantee that the pycnocline is located exactly at the midpoint depth of these measurements. Thus, Read et al. (2011) proposed a new approach to improve the initial guess that the pycnocline is located at the midpoint depth between measurements that have the highest density gradients, $z_p \approx z_{\varphi\delta}$. This technique adds a weight to adjacent measurements, and is given by

$$z_p \approx z_{\varphi+1}\left(\frac{\Delta_{\rho+1}}{\Delta_{\rho-1} + \Delta_{\rho+1}}\right) + z_{\varphi}\left(\frac{\Delta_{\rho-1}}{\Delta_{\rho-1} + \Delta_{\rho+1}}\right), \tag{2.4}$$

in which $\Delta_{\rho+1} = (z_{\varphi\delta+1} - z_{\varphi\delta})/(\partial\rho/\partial z_{\varphi\delta} - \partial\rho/\partial z_{\varphi\delta+1})$, $\Delta_{\rho-1} = (z_{\varphi\delta} - z_{\varphi\delta-1})/(\partial\rho/\partial z_{\varphi\delta} - \partial\rho/\partial z_{\varphi\delta-1})$, and z_p is the pycnocline depth. Figure 5 shows a schematic view of the technique and all variables that are used in this weight method to estimate the pycnocline depth. This method can be used to estimate the thermocline and halocline depth too. Certainly, as aforementioned, in a thermally stratified environment, the highest density gradient matches with the maximum change in temperature.

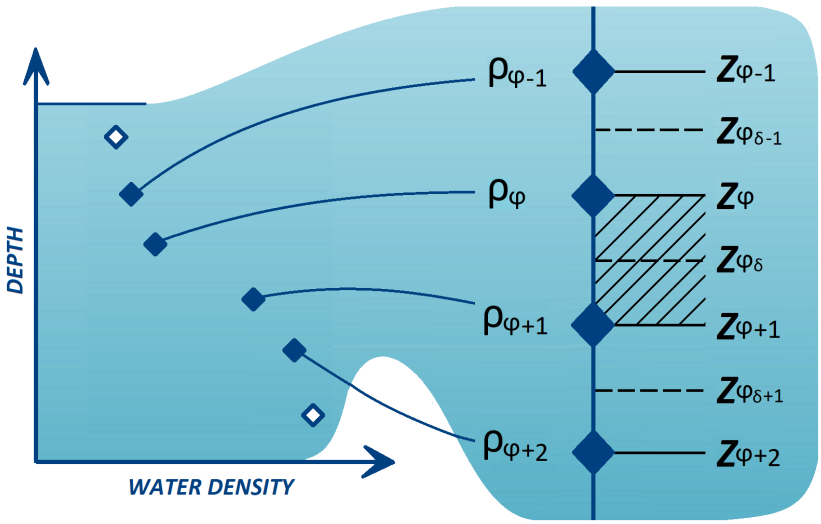

Figure 5 – Weighting scheme to find the pycnocline depth.

The metalimnion thickness can be estimated with the same analogy. The estimation can be based on derivatives of the discrete density measurements. The algorithm presented by Read et al. (2011) relies on a density gradient threshold, δ_{min}, to define the metalimnion thickness. According to Lamont et al. (2004), the epilimnion region is defined as the region above the metalimnion where the density gradient is lower than 0.5 kg/m^3/m. Similar to the pycnocline depth calculation, the density gradient is based on

discrete temperature measurements, and the depth of the epilimnion end can be estimated by a linear interpolation of the slopes derived from equation 2.3. However, i starts at φ and goes to $i = 1$, the loop operation stops when $\partial\rho/\partial z_{i\delta} \leq \delta_{min}$. Thus the depth of the end of the epilimnion region, z_e, can be estimated by

$$z_e = z_{i\delta} + \left(\delta_{min} - \frac{\partial\rho}{\partial z_{i\delta}}\right) \frac{|z_{i\delta} - z_{i\delta+1}|}{\frac{\partial\rho}{\partial z_{i\delta}} - \frac{\partial\rho}{\partial z_{i\delta+1}}}. \tag{2.5}$$

Likewise, for the depth of the metalimnion base, z_h, i starts at φ and goes to $i = k-1$. The loop operation stops when $\partial\rho/\partial z_{i\delta} \leq \delta_{min}$ and is predicted by

$$z_h = z_{i\delta-1} + \left(\delta_{min} - \frac{\partial\rho}{\partial z_{i\delta-1}}\right) \frac{|z_{i\delta} - z_{i\delta-1}|}{\frac{\partial\rho}{\partial z_{i\delta}} - \frac{\partial\rho}{\partial z_{i\delta-1}}} \tag{2.6}$$

The metalimnion thickness can be obtained by subtracting equation 2.6 from 2.5. Another approach to determine the pycnocline depth and also the metalimnion thickness is a method developed by Gorham and Boyce (1989). They related the pycnocline depth with reservoir surface area, the maximum depth of the reservoir, and the wind friction velocity, turbulent velocity caused by the speed of the wind at water surface. Naturally, for internal wave investigation, a temperature sensor chain is an essential part for internal waves investigation. Nevertheless, this method demonstrates that wind velocity plays an import role in the dynamic of reservoirs, and consequently shows that lentic water bodies are not a lentic ecosystem influenced just by the solar radiation. Stratification can be strongly affected by transport and mixing in impoundments and lakes.

2.2 Transport and mixing in water basins

Although reservoirs and lakes do not contain visible currents and are often classified as standing waters, the reservoir water is not motionless. There are countless forces that can create motion on the water of impoundments, such as wind, water density difference, inflow and outflow currents, landslides, earthquakes, and geothermally induced convection currents (OSBORNE, 2000). There are many parameters that are important to understand the transport and mixing in water basins. Then, before we introduce the motion that can be created by external forces, some important parameters related with stability of the system are presented. The Brunt-Väisälä frequency is related with the static stability. Equation 2.1 can be discretized as

$$N = \sqrt{\frac{g'}{z_{\hat{i}}}}, \tag{2.7}$$

where $g' \equiv g(\rho_{i+1} - \rho_i)/\rho_{i+1}$ is the reduced gravity, ρ_{i+1} is the water density at z_{i+1} depth, and $z_{\hat{i}}$ is the average depth between i and $i+1$. The opposite parameter of stability frequency is the square of the vertical shear of the horizontal velocity. When the instability is caused by the friction velocity of the wind, the shear is related with the wind stress at water surface, and it can be expressed as

$$S \equiv \frac{\partial w}{\partial z} \approx \frac{w_*}{\kappa h_i}, \tag{2.8}$$

in which S is the instability frequency in Hz, w_* is the friction velocity of the wind in m/s, h_i is the distance between the water surface and the region i, and $\kappa \approx 0.4$ is the Von Kármán constant. According to Imberger and Patterson (1989), the friction velocity can be calculated by

$$w_* = \sqrt{\frac{\sigma_w}{\rho_e}}, \tag{2.9}$$

where ρ_e is the average density of the epilimnion and σ_w is the wind stress at water surface. The action of the wind along the water surface results in a transfer of frictional momentum from the wind to the water surface, a downward eddy-transport of horizontal momentum from the atmosphere. This transport takes place in the form of stress applied at the reservoir surface. The wind stress may be parameterized as

$$\sigma_w = C_D \rho_a w_{10}^2, \tag{2.10}$$

in which w_{10} is the wind velocity at 10 meters above the surface of the reservoir, ρ_a is the air density, and C_D is the surface drag coefficient. Due to surface gravity wave action, part of the wind stress at the water surface is consumed by the generation and maintenance of surface gravity waves. In this case, just part of the momentum is transferred into the water. As a result, the wind stress depends not only on the wind speed, w_{10}, but also the effect of the surface gravity waves. Thus, the total wind stress is parameterized by the surface drag coefficient, C_D, which depends on the wind speed and the wave development state. Generally, there are two regimes to describe the drag coefficient. Considering strong wind events ($>$ 5 m/s), the frictions is determined by the surface waves which are generated in the basin. As demonstrated by Wüest and Lorke (2003), for this range, C_D can be parameterized through the iterative equation,

$$C_D \approx \left(\frac{\kappa}{1} \ln \frac{10g}{C_D w_{10}^2} + K \right)^{-2}, \tag{2.11}$$

in which $K = 11.3$ is the universal constant that has been determined by Smith (1988) and Yelland and Taylor (1996).

For weak wind events ($<$ 5 m/s) the friction is determined by the roughness generated by the surface tension and small-scale capillary waves. However, laboratory experiments conducted by Simon et al. (2002) have shown that the effect is significant for winds $<$ 3 m/s only. Thus, Wüest and Lorke (2003) recommended for w_{10} between 5 m/s and 3 m/s that C_D should be calculated by equation 2.11. Whereas for $w_{10} < 3$ m/s, they recommended the empirical parameterization obtained through laboratory experiments conducted by Simon et al. (2002),

$$C_D \approx 0.0044 w_{10}^{-1.15}. \tag{2.12}$$

Equations 2.11 and 2.12 consider that the wave field is completely developed. As stated by Hasselmann et al. (1973), for small-sized lakes (diameter $<$ 10 km), the wave field stays typically underdeveloped or, in some cases, at young stages. These type of waves extract more momentum for their growth, reducing even more σ_w. As a result, the underdeveloped surface waves in small and mid-sized basins extract a considerable fraction of the momentum transfer, and the C_D is larger than predicted by equations 2.11 and 2.12.

Dividing the buoyancy frequency by the square of the friction wind velocity gives us the densimetric Richardson number,

$$Ri_w = \frac{g' h_i}{\kappa w_*^2}. \tag{2.13}$$

The densimetric Richardson number, Ri_w, can measure the importance of heat convection and mechanical turbulence, in this case, the instability caused by the wind action. When Ri_w is large, the stratification is stronger than the mixing force. In this case, stratification frequency is higher than the frequency related with the wind that blows across the surface of the reservoir. When the stratification is weak and the wind blows with strong intensity, Ri_w can be really small. A detailed classification is presented in the section 2.3, where Ri is explored as part of the generation and disintegration of large internal waves. Note that equation 2.13 is valid just for instability caused by wind action. However,

instability can be caused by other factors, such as gravity currents. Then, in this case, the instability frequency needs to be rewritten. Certainly, the instability of the system can be caused by more than one simple factor. So, if more factors are responsible to cause instability, all factors need to be considered.

Another similarity number is the bulk Froude number, Fr_w. Fr_w also expresses the stability of the system, and can be written as the square root of inverse of Ri_w,

$$Fr_w = \frac{w_*}{\sqrt{g' h_i}}. \tag{2.14}$$

Other two important non-dimensional parameters which measure the mixing in reservoirs and lakes are called the Wedderburn number, W, and the Lake number, L_N. W describes the relationship between the friction velocity of the wind and the baroclinic pressure gradient, representing the importance of the shear velocity as a source of turbulent kinetic energy available for mixing. W can be defined as

$$W = \frac{g' h_e^2}{w_*^2 L}, \tag{2.15}$$

in which h_e is the epilimnion depth and L is the reservoir length aligned with the wind direction. As Talling and Lemoalle (1998) stated out, W is an improvement of Ri_w, where the ratio between the system dimension is not taken into account. Another number that is defined similarly to W is the lake number, L_N. L_N adds the effects of the density distribution in terms of stratification and the bathymetry variation and is defined as

$$L_N = \frac{S_t (H - h_h)}{w_*^2 A_s^{3/2} (H - h_\nu)}, \tag{2.16}$$

in which A_s is the reservoir surface area, h_h is the height from the bottom of the lake to the pycnocline, h_ν is the height of the centre of reservoir volume, and S_t is the Schmidt stability given by

$$S_t = \frac{g}{\bar{\rho}_w} \int_0^H \rho_z (h_\nu - z) A_z \mathrm{d}z, \tag{2.17}$$

where $\bar{\rho}_w$ is the average density of water, and A_z and ρ_z are the area of the reservoir and the water density at depth z. As Robertson and Imberger (1994) stated, values of $L_N \ll 1$ indicate a strong instability in the water column, causing a fully mixed water. $L_N \approx 1$ demonstrates some upwelling of hypolimnetic waters. $L_N > 1$ express a stable system that is not susceptible to mixing. According to Pannard et al. (2011), L_N between 1 – 12 indicates internal wave activity.

As mentioned previously, water motions usually are produced by external forces, except for molecular diffusion. These forces can generate motions in reservoir waters, some of them are presented in Figure 6. Many forces can generate or excite the formation of internal waves in reservoirs. As Spigel and Imberger (1987) stated, internal waves can be generated by any disturbance to a stratified fluid, such as wind action at water surface (SPIGEL; IMBERGER, 1980), turbulence at the base of the mixed layer (KANTHA, 1979), gravity currents (BOOKER; BRETHERTON, 1967), and intrusion from the system boundaries (MANINS, 1976). According to Malone (1978), internal waves are one of the most important processes of vertical mixing in lakes and impoundments, mainly in strong stratification periods.

2.3 Theory of internal waves

Waves can exist not just on a fluid surface but also within a stratified fluid, perturbed on any isopycnal interface. Wave motions can be classified into two modes: barotropic and baroclinic. In the barotropic mode, also called as external, fast, and sinuous mode, the water motion behaves as if the

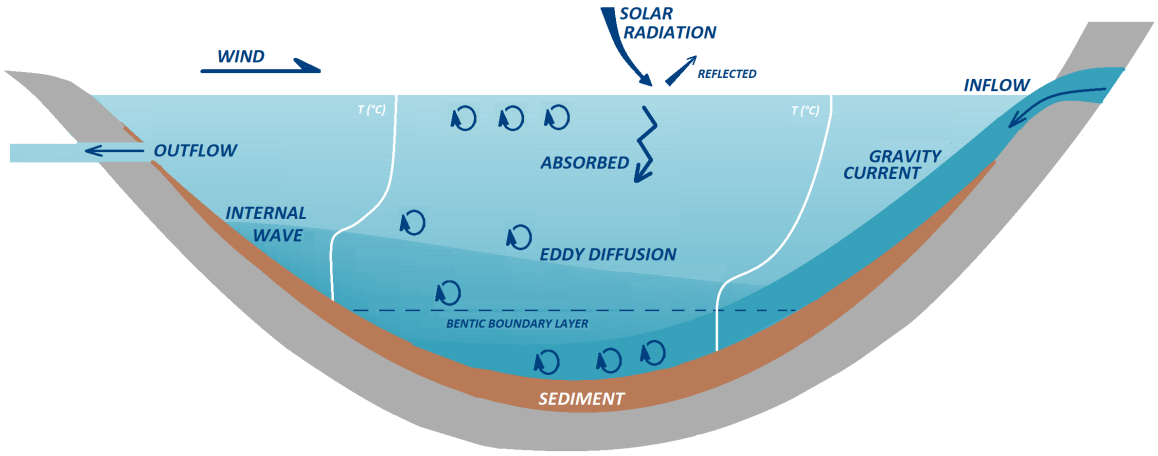

Figure 6 – Schematic overview of mixing process in lakes and reservoirs.

water body is unstratified. In this case, as shown in Figure 7(a), the isopycnals are parallel to isobars, lines of equal pressure. Naturally, this mode has surface waves with higher amplitude than internal waves. Other important characteristics of this mode are that surface and internal waves are created in phase. On the other hand, the baroclinic mode, also called as internal, slow, and varicose mode, has internal waves with larger amplitudes than surface waves. Therefore, the action of internal waves is always related with the baroclinic mode. In this case, isopycnals and isobars are inclined with respect to each other, the angle of the inclination depends on the stratification profile (Figure 7(b)). Other important characteristic is that internal and surface waves have initial opposite phases. Naturally, internal waves have lower velocities, and longer periods than surface waves. The density difference in the interior of the water are very small compared to the water-air density difference. Due to the effect of reduced gravity across the water body, surface waves travel more than 50 times faster than the internal waves. Natural ambient, such as oceans, lakes, pounds, and impoundments, are generally continuously stratified systems, causing another main difference between internal and surface waves. In these environments, internal waves may propagate both vertically and horizontally, whereas surface waves propagate just in the horizontal. Internal waves in a continuously stratified ambient travel horizontally along isopycnals and vertically along the density gradient. As Fjeldstad (1933) stated, internal waves can be simultaneously excited at different depths. This means that its energy may be concentrated in specific depths. As the density difference is not linear, the internal waves in each layer can also present different characteristics, with different propagation phase angle. As the energy needed to increase a water layer in the air is greater than the energy needed to rise a water layer in the lower water density, internal waves are much bigger than surface waves generated by the same energy input.

According to Chakrabarti (2005), the majority of internal waves that are generated in stratified basins such as lakes and reservoirs are not easily visible, even through radar images. They are frequently detected by direct measurements. Generally, this measurement is based on density values. When the ambient is thermal stratified, the estimation of density is provided by temperature measurements. In case of saline stratification, conductivity meters can help on estimation of the density fluctuations. In fresh water thermal stratified lakes and impoundments, as Bryson and Ragotzkie (1960) stated, even in a completely smooth surface and acceptable stratification to suppress turbulence, temperature series can present a periodic oscillation, and consequently indicate an internal wave propagation. According to Hutter, Wang and Chubarenko (2011), isotherms analysis have been the most popular used variable to record internal waves. It should, however, also be emphasized that water velocity measurements have

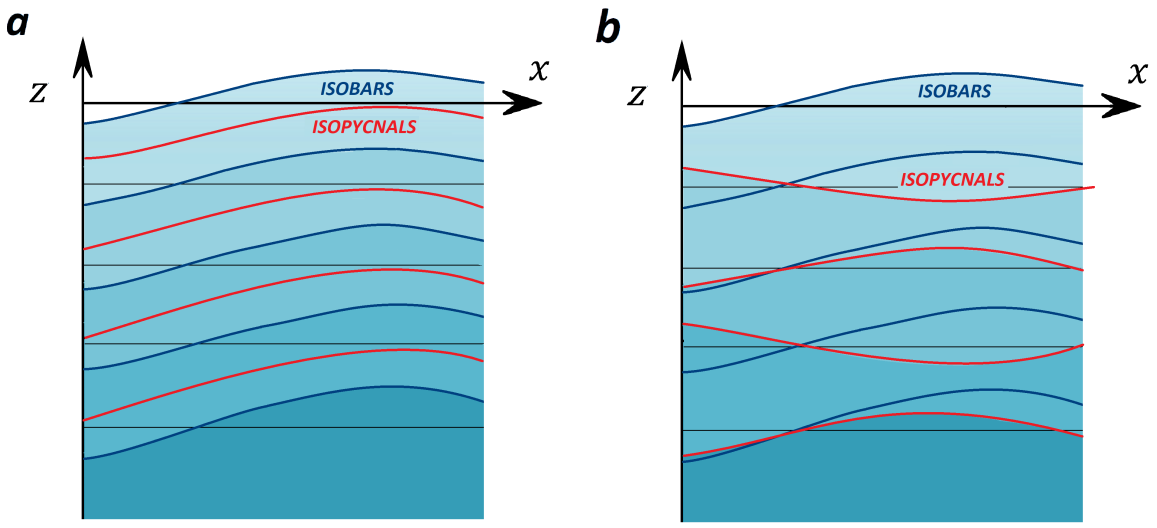

Figure 7 – Distribution of isobars and isopycnals at any depth below the water surface in a shallow system a) Barotropic mode b) Baroclinic mode.

been helpful to identify internal waves. There are other parameters that are periodically affected by internal waves. More types of measurements that help to overcome the difficulty to identify this motion in natural systems is presented in section 2.4, where we describe measurements that can be analyzed through spectral analysis to identify internal waves.

Internal waves are important for many processes in lentic water bodies. They can have several effects on water quality, with chemical and biological consequences. Imberger (1998a) has shown that most part of the momentum and energy that crosses the surface boundary layer is responsible to excite long internal waves. As a consequence, internal waves can increase the transport of nutrients and microorganisms from the hypolimnion to the epilimnion, causing a vertical displacement of the suspended biomass, which may affect light availability. According to Ivey, Winters and Silva (2000), internal waves are responsible for energizing the turbulent benthic boundary layer, and consequently increase mass transport process (e.g., nutrient diffusion), with intrusion from the slope of the reservoir to its centre. As Bruce et al. (2008) stated, large internal waves are responsible for large scale motions in the benthic boundary layer. A research conducted by Umlauf and Lemmin (2005) in Lake Geneva indicated up to 40% of hypolimnetic volume was exchanged following episodes of large internal waves. The aquatic microorganisms distribution may also be affected by internal wave actions, causing an increase in phytoplankton biomass in shallow littoral zones. As Hingsamer, Peeters and Hofmann (2014) pointed out, vertical displacements in isoconcentration of phytoplanktons caused by internal waves have been suggested that phytoplanktons could not regulate their buoyancy to prevent wave-induced vertical displacements. Internal waves can also increase primary production by affecting light availability for photosynthetic microorganisms. Experiments and modelling provided by Evans, MacIntyre and Kling (2008) revealed that internal waves have a strong influence on surface light variation. The effects on photosynthesis may be positive or negative, depending on the relative phase of internal waves displacement and light intensity. The research revealed that large internal waves have a strong potential for internal wave-induced enhancement of photosynthesis. The ecological effects of nutrients, microorganisms, and chemical compound fluxes caused by internal waves have been widely investigated in oceans and in large stratified lakes. In small lakes, the limited surface area reduces the interface through which kinetic energy can be transferred, resulting in a shallow pycnocline and in a weak mixing layer (RUEDA; SCHLADOW, 2009). Thus, the ecological

effects in this kind of environment can be amplified. As Pannard et al. (2011) stated, internal waves generated in small closed basins have been largely ignored, despite the fact that small lentic water bodies may present persistent stratification, and may be affected by low Wedderburn number, W.

According to Pannard et al. (2011), standing internal waves in closed basins may be classified by nodal points on the vertical (V) and horizontal (H) components, VnHm[2], in which n and m are the number of nodes of each component. The vertical mode is related with the stratification patterns. New evidences also suggest that the influence of wind patterns and obstacles may generate different vertical modes. Thus, higher vertical modes can be a result of unequal differences of density between layers, resonance with the wind forcing, and basins with sloping topography, however it is not yet completely understood. V1 mode is characterized by the epilimnion and hypolimnion layer moving in the opposite directions, with shear concentrated in the pycnocline. The second vertical mode (V2) is associated with a change of the metalimnion thickness, a strong tilt of the epilimnion interface, large shear across the base of the epilimnion and a undisturbed hypolimnion. V2 mode is characterized by the epilimnion and hypolimnion moving in the same direction, with a balancing flow in the metalimnion flowing in the opposite direction, creating shear stress at both the top and bottom of the metalimnion. Although higher vertical modes were rarely reported until the end of the 18th century, nowadays it is accepted that high vertical modes are often excited in lentic water bodies. Data from Mortimer (1971) based exclusively in large lakes concluded that higher vertical modes were not frequently observed. Nevertheless, Roget, Salvadé and Zamboni (1997) stated that the formation of higher vertical modes is more evident in small lakes where the metalimnion takes up a relatively larger proportion of the total lake depth than in large closed basins. Hutter, Wang and Chubarenko (2011) showed that second vertical baroclinic modes are not just caused by diffusive metalimnion, but also by the presence of a second pycnocline. In addition, Wiegand and Chamberlain (1987) observed that after a strong wind event, the first vertical mode generated was typically followed by excitation and dominance of a second vertical mode baroclinic wave. Boehrer, Ilmberger and Münnich (2000) reported higher vertical mode due to strong wind events in Lake Constance, where V1H1 mode is dominant. Münnich, Wüest and Imboden (1992) pointed out that wind oscillations also contribute to excite higher vertical baroclinc waves. Although higher internal wave modes have been extensively studied in recent years, the influence of temperature profiles, mean depth, shape, morphology, meteorological conditions, and its resonances on the excitation of higher vertical modes are not well understood yet.

An interesting observation of higher vertical modes is related to the structure of each baroclinic wave. As shown by Salvadè, Zamboni and Barbieru (1988), nodal lines of each baroclinic wave are frequently shifted due to the fact that each baroclinic mode has different vertical boundaries defined by the basin shore. Thus, different baroclinic modes present different nodal positions. As a result, the effect of internal waves may be different along the reservoir depending on the layer depth. Another interesting observation is that higher vertical mode normally carry less energy compared to the fundamental baroclinic mode (V1). This can be interpreted by a process called WKB normalization, an initialism for Wentzel, Kramers, and Brillouin, that was firstly used for a semiclassical calculation in quantum mechanics. According to Sutherland (2010), WKB renormalization is a co-ordinate change procedure that allow the transformation of the structure of internal waves in uniformly stratified fluid to those in non-uniformly stratified fluid. Actually, the WKB is an approximate solution to a time-independent differential equation. This analysis shows that the energy of hydrostatic baroclinic modes at any depth is proportional to the Brunt-Väisälä frequency. Thus, although higher vertical modes present longer periods and higher amplitudes compared to fundamental modes, higher modes normally suggest lower internal wave energy

[2] This nomenclature can be presented in different forms. For example, Sutherland (2010) call as 2–3 modes for what we call V3H2. Hutter, Wang and Chubarenko (2011) call this same internal wave pattern as vertical mode 3 and horizontal mode 2.

due to the density structure. Thus, many scientific papers discuss that normally the wave energy in the bottom of the basin is lower than the energy in the pycnocline, this statement is not necessarily related to the energy dissipation going from the surface downward, but due to the thermal stratification. Even though internal seiches near the bottom may present low energy, large thermal oscillations at depths much deeper than the pycnocline have already been observed by Mortimer (1950). This can explain the eddy diffusion of heat and nutrient content in the benthic boundary layer. The vertical and horizontal modes are completely independent, internal waves can be generated with large range of modes, and some combinations are shown in Figure 8.

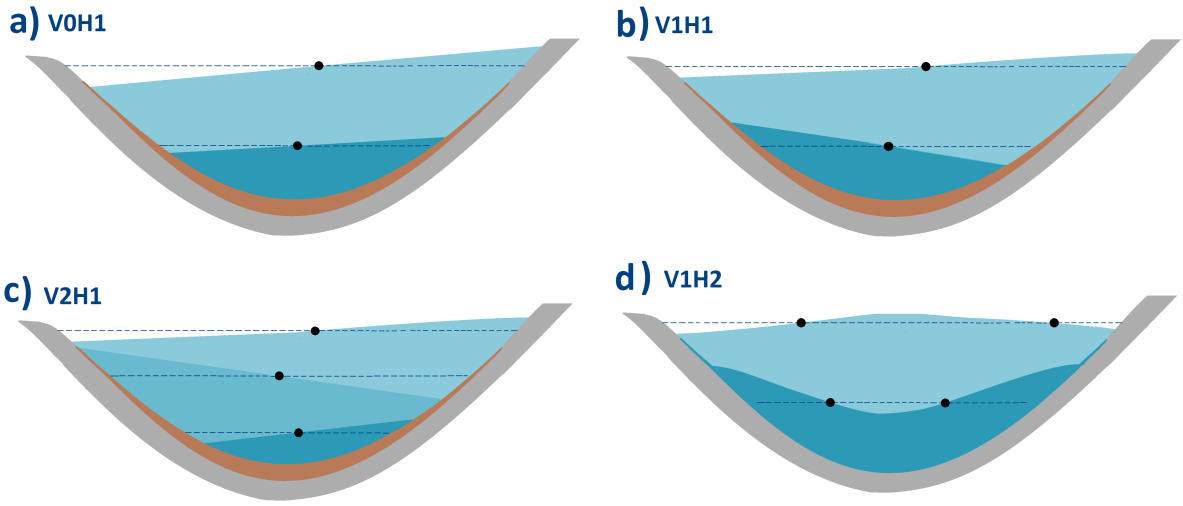

Figure 8 – Schematic view of various internal waves modes in a close basin: a) V0H1, b) V1H1, C) V2H1 and d) V1H2. The $n = 0$ is related to surface (barotropic) mode. The black dots (·) represent nodal points.

As mentioned before, internal waves in lentic water bodies can be generated by many process, such as gravity currents, intrusions, turbulence, diffusion, and the interaction between surface waves and reservoir bathymetry. However, according to Mortimer (1952), the most important source of energy is wind action over the reservoir surface. Lemmin and D'Adamo (1997) observed in Lake Geneva that winds from northeast were responsible to generate a large internal seiche with amplitude of approximately 20 m. The authors also identified that winds from northeast acted normally several hours to days to generate this type of internal wave in Lake Geneva. Lemmin and D'Adamo (1997) compared the results obtained by spectral analysis to different models, which presented a good agreement with the Fourier analysis. Generally, the wind action develops a basin-scale internal standing waves known as internal seiches. Long internal seiches are standing internal waves that have wavelengths comparable to the length of the reservoir. They are capable of reflecting back and forth between the reservoir boundaries without appreciable damping, and commonly they are generated by wind action at the water surface. The wind introduces kinetic energy at the water surface. The transfer of momentum caused by wind stress pushes the surface water to the leeward shore, causing a surface displacement, called as wind set-up. If the wind stress is applied for sufficient time, the horizontal pressure gradient increases, and the hypolimnion water is accelerated towards the upwind direction. Consequently, the hypolimnion and epilimnion layers are tilted, as shown in Figure 8(a). When the wind stops, the tilted layers flow back towards equilibrium. However, momentum is considerable and equilibrium is overshot, resulting in a rocking motion about nodal points. The formation of a long internal wave by wind action is shown in the Figure 9. Balancing the initial forces gives us a relationship between the baroclinic gravitational pressure and the wind-stress

acting through the epilimnion layer. This can be mathematically defined as

$$\frac{\delta\zeta_o}{\delta x} = \frac{w_*^2}{g' h_e}, \tag{2.18}$$

in which ζ is the vertical pycnocline displacement. Equation 2.18 describes the pycnocline slope caused by the internal wave.

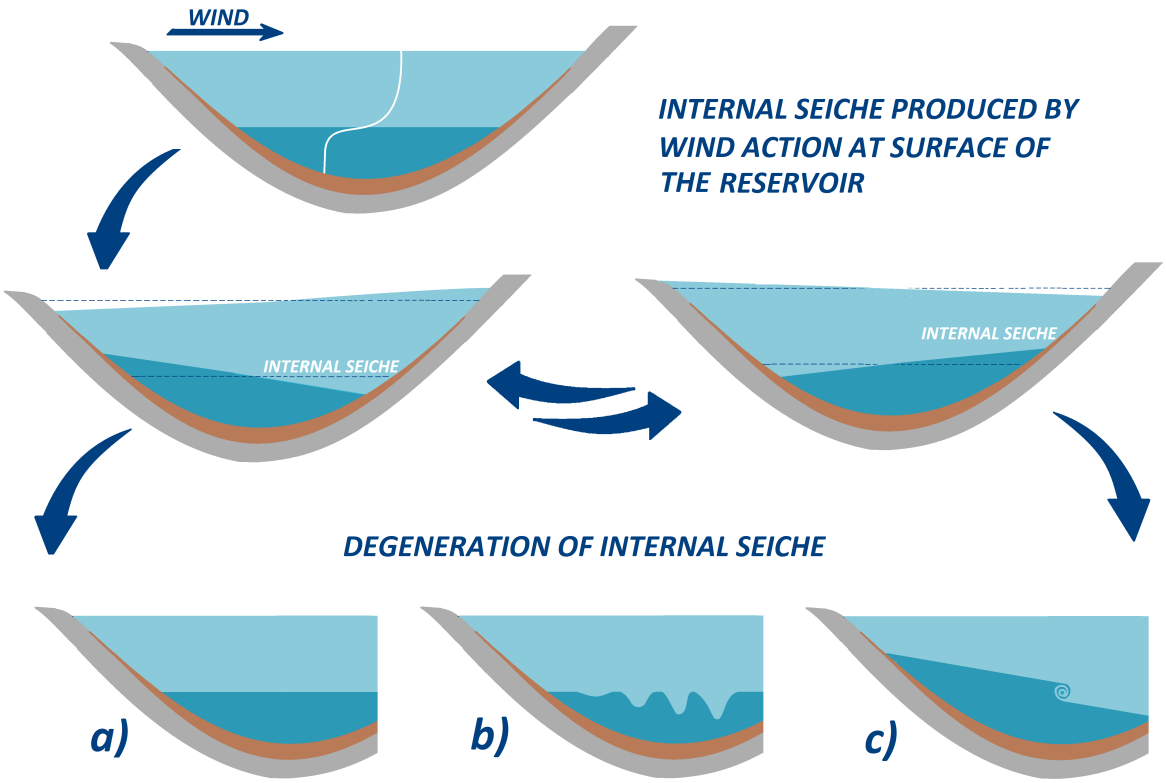

Figure 9 – Internal seiche in a two-layered basin produced by wind stress and the three most common type of degeneration of internal seiches in lakes and reservoirs: a) damped linear waves, b) nonlinear internal wave packet and c) Kelvin-Helmholtz billows. Adapted from Spigel and Imberger (1980)

Internal seiches formed by wind forces are frequently identified in lakes and impoundments and the structure of density stratification is crucial to determine the internal wave patterns. The stability strength depends on the stratification of the system, and instability strength is associated with the wind velocity. According to Roget, Salvadé and Zamboni (1997), internal seiche structure is strongly influenced by wind patterns and the stratification structure, but may be also altered by the complex shape of the reservoir. As aforementioned, one of the most powerful parameters to predict the mixing, and consequently the formation of internal seiches in stratified basins, is the Richardson number (equation 2.13). According to Spigel and Imberger (1980), a prediction of internal seiche generation can be done by comparing the Richardson number with the aspect ratio between the reservoir length that is aligned with the wind, L and the epilimnion thickness, h_e. When $Ri_w < 1$, the instability frequency is higher than the stratification frequency. In spite of baroclinic shear could occur, the intensity of the wind is so strong compared to the stratification that the stratification is broken down by mixing, as shown in Figure 10(a). When $1 < Ri_w < L/(2h_e)\ ((h_e + h_h)/h_h)^{1/2}$, a large interface displacement occurs, and is

accompanied by interface shear and Kelvin-Helmholtz billows. As Bourgault, Galbraith and Chavanne (2016) stated, a Kelvin-Helmholtz billow is a kind of wave that develops when the destabilizing effect overcomes a little the stabilizing density stratification effect, occurring a shear flow effect. In this regime, internal seiches are usually not observed because the instability frequency normally is higher than the Brunt–Väisälä frequency. A complete vertical mixing can occur during a single wind episode and thickness of the metalimnion can be $> 0.3\ h_e$, as presented in Figure 10(b). When $L/(2h_e)\ ((h_e + h_h)/h_h)^{1/2} < Ri_w < L^2/(4h_e^2)\ ((h_e + h_h)/h_h)^{1/2}$, internal seiche is dominant. Although the buoyancy effect is strong compared with the instability caused by wind stress, winds are strong enough to cause significant interface displacements, as shown in Figure 10(c). According to Spigel and Imberger (1980), two-dimensional effects can be disregarded for most of the range of Ri_w in this regime, and a complete vertical mixing is unlikely to occur. When $Ri_w > L^2/(4h_e^2)\ ((h_e+h_h)/h_h)^{1/2}$, the buoyancy dominates all processes. Internal seiches still may be generated, but normally they present short periods and small amplitudes, as presented in Figure 10(d). Although low Ri_w is frequently associated with instability and mixing, the shear flow caused by internal waves in deep water presents instabilities even for large Ri_w. The waves grow by extracting energy from the background shear flow. As the instability grows, linear theory fails to reproduce the real motion. However, as stated by Sutherland (2010), nonlinear simulations have demonstrated that if Ri_w is sufficiently large, the disturbance saturates at finite amplitude. In a weak stratified system, the interface wraps, forming Kelvin-Helmholtz billows, as show in Figure 10(b).

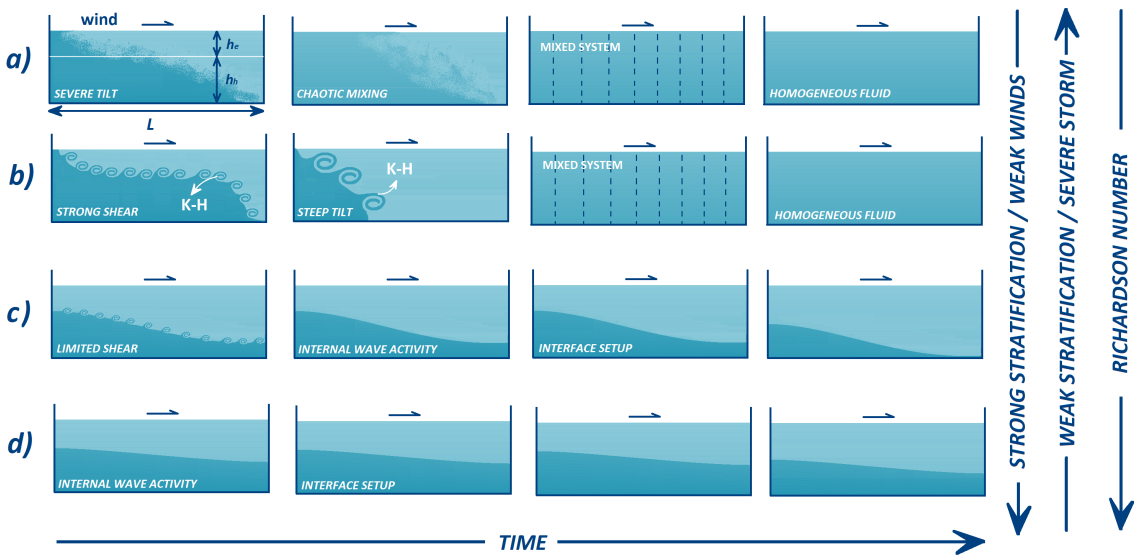

Figure 10 – Sketch of the different regimes of interior mixing and oscillation generated by wind stress in a rectangular reservoir/lake. a) severe vertical mixing, b) large Kevin-Helmholtz billows and severe vertical mixing, c) internal seiches with limited billows, and d) internal seiche rapidly damped.

Higher horizontal modes are not unusual in lakes (HORN; MORTIMER; SCHWAB, 1986). Long standing internal waves can also have higher horizontal modes. A standing wave is basically two opposing waves of equal amplitude, which have central nodes and anti-nodes at the basin walls. A better understanding of the mathematical representation is given in section 3.4. According to Imberger (1994), field studies have shown that the long standing internal waves decay at a rate greater than what can be accounted by internal dissipation. The energy deposited into such long internal waves is eventually transformed through a down-scale energy cascade across the spectrum of internal waves into dissipative

motions over the reservoir topography. This transfer of internal energy is a nonlinear process. Saggio and Imberger (1998) show that the internal waves that were formed after the passage of storms contained higher energy levels than the expected internal seiches. They pointed out that higher frequency waves, identified as nonlinear internal waves, were responsible for the increase of energy. Thus, they observed that the decay times and the time varying spectra suggest that energy is fast transferred within the internal wave spectrum from the internal seiches to high frequency waves. The degeneration of internal seiches occurs primarily as a result of turbulence production in the benthic boundary layer. Although higher frequency waves tend to be nonlinear, their amplitude and wavelength are variable to be considered to explain better the nonlinear behavior. According to Mysak (1984), in long lakes, normally, high frequency waves tend to disappear due to dissipation and dispersion. On the other hand, in shorter lakes, the short waves are seen to travel back and forth along the basin several times. The nonlinearity of high frequency waves is more explored in section 2.5, where the internal wave equation and model discussion are presented. Although, the first horizontal mode internal seiches contain more than 98% of the wave energy, the energy transfer from long waves to shorter waves has important consequences for mixing in stratified closed water bodies since the high frequency waves can shoal and break at basin boundaries, dissipating more than 70% of their energy on first interaction with the basin shore. The disintegration of internal seiches depends on some frequency parameters related with the internal seiches and ambient characteristics, called here as frequency-scales.

2.3.1 Frequency-scales

Many papers that cover this topic use the term "period-scales" to describe the degeneration of long internal seiches. However, since we have introduced many frequency parameters such as Brunt-Väisälä frequency and the square of the vertical shear of the friction velocity of the wind given in frequency units, it is useful to express these variables also in frequency units. Thus, here we call these variables as frequency-scales.

Considering a two-layer rectangular basin, viscous losses occur in the hypolimnion-epilimnion interface and in the benthic boundary layer (Figure 11). According to Spigel and Imberger (1980), the interface displacement decays as $\zeta = \zeta_o \mathrm{e}^{-t\alpha_d f_i}$, in which ζ is the interface displacement at the edge of the reservoir, ζ_o is the initial interface displacement, f_i is the internal seiche frequency, and α_d is the frequency of the energy decay, also known as the e-folding energy decay. This viscous damping is quantified by the frequency-scale associated with the seiche energy and the rate of energy dissipation. The viscous effects can reduce the amplitude of the internal seiches by energy dissipation. According to MacIntyre (2010), the energy dissipation in the interior of the system sometimes is neglected because energy dissipation in the benthic boundary layer is much greater than in the hypolimnion-epilimnion interface. The viscous damping frequency-scale can be written as

$$f_d = \alpha_d, \tag{2.19}$$

in which f_d is the frequency for the wave amplitude decay. The e-folding energy decay, α_d, may be estimated following Batchelor (2000) who estimated the rate of energy dissipation in boundary layer per unit area. As a result, α_d can be written as

$$\alpha_d = \frac{\nu}{h_e}\left(\frac{h_h}{H\delta_b} + \frac{H}{h_h\delta_\rho}\right) \tag{2.20}$$

where $\delta_b = (\nu/\pi f_i)^{1/2}$ is the turbulent boundary layer thickness, ν is the water kinematic viscosity, and δ_ρ is the thickness of the pycnocline. Usually δ_ρ is calculated considering a minimum percentage of the density gradient.

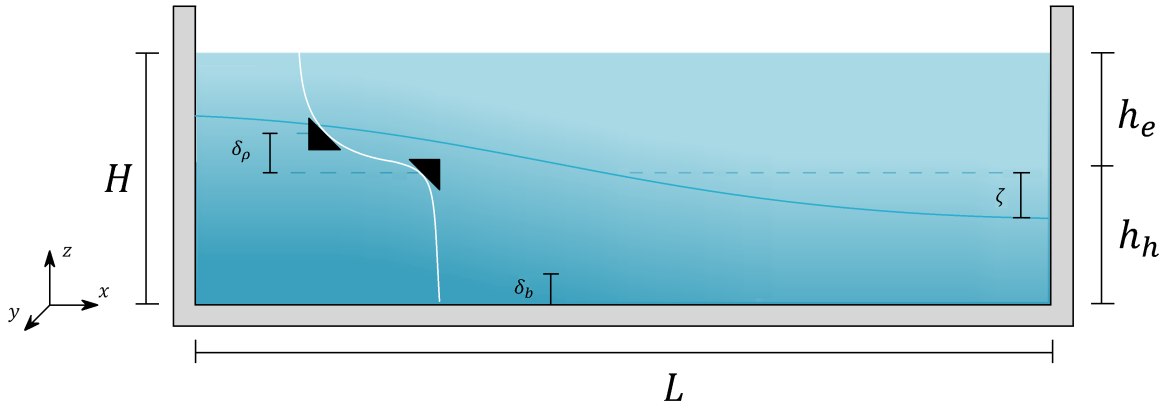

Figure 11 – Schematic view of the model configuration – see text for definition of symbols

Another important frequency-scale is related with the nonlinear effects caused by high frequency internal waves. As Grimshaw (2007) stated, the nonlinear Korteweg-de-Vries (KdV) equation describes propagation of nonlinear internal waves and can be written as

$$\frac{\partial \zeta}{\partial t} + c_p \frac{\partial \zeta}{\partial x} + k_o \zeta \frac{\partial \zeta}{\partial x} + k_u \frac{\partial^3 \zeta}{\partial x^3} = 0, \tag{2.21}$$

in which c_p is the linear long-wave phase speed, and k_o and k_u are the nonlinear and dispersion coefficient, respectively. Considering a two layer system, k_o and k_u are defined as

$$k_o = \frac{3c_p(h_e - h_h)}{2h_e h_h}, \quad k_u = c_p \frac{h_e h_h}{6}. \tag{2.22}$$

Generally for weak nonlinear internal waves, just the dispersion coefficient, k_u, is more significant. Thus, the nonlinear term is responsible for wave steepening. The wave solution steepens ahead of the crest and a hydraulic jump or shock wave is generated. Therefore, the nonlinear and the unsteady term can be balanced to lead a steepening frequency scale for internal seiche of wavelength $\lambda = 2L$, and initial amplitude ζ_o. The nonlinear frequency is given by

$$f_s = \frac{k_o \zeta_o}{L}. \tag{2.23}$$

According to Boegman, Ivey and Imberger (2005a), as the wave steepens, their horizontal length-scales drop due to dispersive effects. Therefore, eventually, high frequency waves develop. When $f_d < f_s$, the internal seiche steepens due to nonlinear effects, and evolves into a train of high frequency waves, as shown in Figure 9(b). This effect has been reported by Stevens (1999) for Sook Lake Reservoir near Victoria, British Columbia, Canada. This criteria is satisfied for most lakes and reservoirs under moderate to strong winds. In a two-layers system, high frequency internal waves always have a depression form in the pycnocline. Other important characteristic is that nonlinear internal waves do not develop when the pycnocline is located at the mid-depth of the system.

On the other hand, if $f_d > f_s$, the internal seiche amplitude is damped before it can steepen and evolve into high frequency waves, as illustrated in Figure 9(a). Generally, for moderated size basins, the viscous damping frequency-scale may varies from 10^{-6} Hz to 10^{-5} Hz. In this case, internal seiche amplitude is not sufficient for high frequency wave production. Using equation 2.19 and 2.23, the higher initial amplitude of internal seiche that is damped before degenerates into high frequency waves is given by

$$\zeta_o = \frac{\alpha_d}{3}\left(\frac{h_e h_h}{h_h - h_e}\right). \tag{2.24}$$

Another important frequency-scale, which is related to the system stability, is called as Kelvin-Helmholtz frequency-scale, f_{kh} (SPIGEL; IMBERGER, 1980). For frequencies higher or equal to f_{kh} Kelvin-Helmholtz billows may be formed. Kelvin-Helmholtz billows are characterized by the iconic billow formation, a partial spiral almost crashing stationary wave. The formation of these billows can occur in a stratified fluid when the velocity shear of each layer causes a shear stress at the interface layer. According to Miles (1961), for a Boussinesq fluid, perturbation increases exponentially if $Ri < 0.25$. As a result, the flow becomes unstable, leading to mixing or Kelvin-Helmholtz billow formations. The mixing process contributes to the pycnocline destruction and the transport of species into the hypolimnion. When Kelvin-Helmholtz billows are developed, a considerable interfacial shear has a maximum value at the nodal point. Considering the Ri criteria, the flow remains stable, without the formation of Kelvin-Helmholtz billows, when $f_{kh} > 4f_i$. The Kelvin-Helmholtz frequency-scale, f_{kh}, is given by

$$f_{kh} = \frac{\zeta_o}{L}\sqrt{\frac{g'}{\delta_\rho}}. \tag{2.25}$$

Note that this Ri is related with the internal seiche velocity, and is not associated directly to the shear created by the wind action. When the internal wave creates a strong shear across the pycnocline, Ri falls below 0.25. In this criteria, if the system is not completely mixed, Kelvin-Helmholtz billows form at the node of the internal seiche, as illustrated in Figure 9(c). Although equation 2.25 just describes the criteria for long internal seiche becoming unstable, the higher frequency waves can also induce local billowing separately. As mentioned before, Kelvin-Helmholtz billows can also be generated before the formation of internal seiches, under the following criteria: $1 < Ri_w < L/(2h_e)\ ((h_e{+}h_h)/h_h)^{1/2}$. According to Likens (2010), the frequency of the most unstable mode is just below the Brunt-Väisälä frequency of the thermocline. After this value the system is susceptible to evolve into a billow and collapses into turbulence. Therefore, the values of Kelvin-Helmholtz frequency-scale in most lakes and impoundments are greater than 3×10^{-4} Hz.

Another frequency-scale is related with supercritical waves. This kind of waves occur in stratified flows at the transition from supercritical to subcritical flow conditions. According to Wood and Simpson (1984), considering a two-layer system, the flow in the epilimnion becomes critical when $Fr_e^2 + Fr_h^2 = 1$, in which Fr_e and Fr_h are the densimetric Froude numbers for epilimnion and hypolimnion flow, respectively. Thus, an internal bore can be developed when the velocity of the surface layer exceeds the internal seiche speed. The frequency at which the flow turns into critical in the region where the velocities are maximum, the centre of the reservoir, is

$$f_b = \frac{4\zeta_o}{f_i h_e \sqrt{H}}\sqrt{\frac{h_e^3 + h_h^3}{h_h^2}}. \tag{2.26}$$

The energy in the initial wave is lost by mixing and enhanced dissipation in the case of ondular bores. According to Horn, Imberger and Ivey (2001), this event just occur when $4f_i < f_b$ and $4f_i > f_s$. In other words, the pycnocline displacement needs to be greater than the epilimnion thickness, corresponding to a upwelling of the pycnocline. Even though this kind of flow is frequently observed in oceans as a result of tidal flow over topographic feature, this frequency is too high to support thermal stratification in closed basins. Generally, the system is mixed before internal bores develops. In conclusion, internal bores are unlikely to occur in lentic water bodies. In addition, The effects of supercritical waves in lakes and impoundments are not well understood. The last regime is a combination of a supercritical flow and Kelvin-Helmholtz billows. When $f_{kh} > 4f_i$ and $f_b > 4f_i$, the layer presents supercritical velocity and shear is sufficient to develop Kelvin-Helmholtz billows. This regime is restricted to conditions of very strong winds.

These frequency-scales can be easily compared to each other. A simple relationship can be obtained using the epilimnion thickness and the initial internal seiche amplitude, ζ_o. Therefore, as demonstrated by Boegman (2009), to simplify the problem we can compare equations 2.15 and 2.18. Thus, the ratio of the initial amplitude of the internal seiche to the pycnocline depth can be written as the inverse form of the Wedderburn number,

$$W^{-1} \sim \frac{\zeta_o}{h_e}. \tag{2.27}$$

The regimes may be classified according to the inverse Wedderburn number and the pycnocline depth. As demonstrated by Horn, Imberger and Ivey (1998), the relationship can be obtained through the frequency-scale and the dispersion relation of internal waves. The dispersion relation is a theoretical expression which represents a solution of the wave evolution, describing the effect of wave dispersion and the frequency wave, f_i. This is explored in the section 3.4, where we present two analytical solution for internal waves. Therefore, from now on, we may assume that f_i is a known variable, which can be compared to the frequency-scales (equations 2.19, 2.23, 2.25, and 2.26) and their regime criteria. Thus, a relationship between the pycnocline depth and the wave internal amplitude may be obtained. As a result each regime can be classified easily through a diagram that is presented in Figure 12. When the reservoir is subject to strong winds or presents a weak stratification, the ratio ζ/h_e decrease, and consequently internal seiches are more susceptible to be damped by viscosity. However, as shown in Figure 12, generally internal seiches are susceptible to evolve into a train of high frequency waves. On the other hand, when the pycnocline is located at the mid-depth of the system, generally internal seiche are damped and high frequency waves are never generated by the disintegration of internal seiches. These regimes were obtained through many experimental and theoretical results obtained by Horn, Imberger and Ivey (1998), Horn, Imberger and Ivey (2001), Boegman, Ivey and Imberger (2005a), Boegman, Ivey and Imberger (2005b).

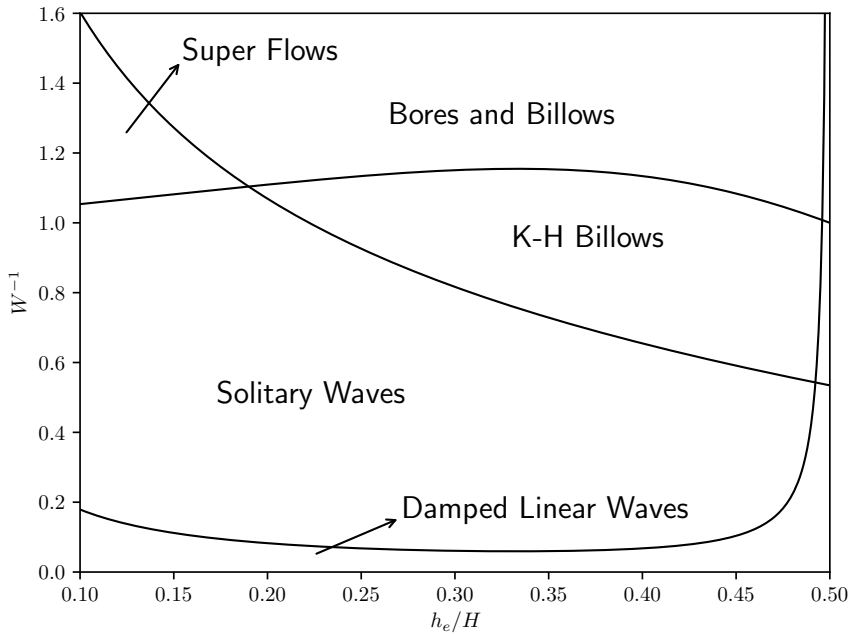

Figure 12 – Analytical regime diagram showing a schematic structure of the degeneration of internal waves in lakes and reservoirs according to frequency scales.

2.4 Spectral Analysis of time series signals

Spectral analysis is one of many statistical techniques used for characterizing and analyzing series of data. In spectral analysis, the time-series is decomposed into sine components using a sum of spectral components. Nowadays there are many spectral-analysis methods like those that are based on Fourier transform and Wavelet transform. Many studies use spectral analysis to identify internal waves in closed basins. As Mortimer (2004) stated that spectral analysis came to revel oscillatory motions that remained hidden in time series measurements, obscured by noises. According to Lin (2012), as spectral-analysis methods transform spatial or temporal patterns into frequency domain, the dominant frequencies of a periodic time series signal can be easily identified. With regard to internal waves, there are many time series measurements that are affected periodically by internal waves, and consequently used to identify internal waves. As stated before, time series of underwater temperature collected in lentic water bodies are more popular variable used to record baroclinic motions. However, water velocity measurements have been also useful to detect baroclinic oscillations. Nonetheless, current meters are much more expensive device to recover water speed in different depths. Thus, normally underwater temperature is used. They are frequently interpolated in space to obtain isotherms, lines that connect points of equal temperature at a given period. According to Lemmin (1987), the linear interpolation used to obtain isotherms does not disrupt the spectral analysis. As Lemmin, Mortimer and Bäuerle (2005) stated, the first vertical mode is often identified using the isotherm located at pycnocline region whilst higher vertical modes generally are identified through more than one isotherm at different depths. As stated before, higher vertical modes can present low levels of energy, and consequently sometimes are not easily detected by spectral analysis.

Although internal seiches have high spectral energy compared to higher horizontal modes, spectral analysis can present little response depending on the location of the temperature sensor within the reservoir. Stations positioned in the middle of the reservoir, a potential nodal point region of internal seiches, show little response of the internal seiche action, but strong response of higher horizontal modes. Another important point is that measurements used to identify internal waves are not influenced just by internal wave motions. For example, temperature measurements can be influenced also by variation of solar radiation, and wind intensity oscillations. Thus, the spectrum needs to be investigated carefully, separating oscillations caused by internal waves from those that are not related to baroclinic motion. Many different variables can help directly and indirectly in the identification of internal waves. Underwater velocities and wind speed are one of many variables that are associated directly with internal waves. Many other variables help to separate internal wave action from oscillatory caused by other factors, such as solar radiation. According to Bernhardt and Kirillin (2013), resonance events between wind intensity and internal seiches may excite internal seiches, and consequently, their intensity may increase strongly. Thus, the internal seiche energy is significantly higher in resonantly forced lakes than in lakes without resonance. However, this type of baroclinic motion is defined as non-free internal seiche since the wind is not just an input of energy to excite waves, but this motion is controlled essentially by wind variations.

In this research we use a spectral analysis based on Fourier transform and Wavelet transform to identify internal waves in closed basins. We now present a detailed description of Fourier and wavelet transforms.

2.4.1 Fourier transform

The Fourier transform is a mathematical technique used to decompose a function of time into a sum of many sine or cosine components of different frequencies, phases, and amplitudes (CHU, 2008). The Fourier transform provides clear information about frequencies, revealing dominant periodicities.

According to Greenberg (2013), the Fourier transform $\mathscr{F}$ of a function $f(m)$ is defined by

$$\mathscr{F}\{f(m)\} = \hat{f}(\omega_t) \equiv \langle f, e^{-i2\pi fm} \rangle = \int_{-\infty}^{+\infty} f(m)\, \mathrm{e}^{-i\omega_t m}\, \mathrm{d}m. \tag{2.28}$$

in which m represents *time* and the transform variable ω_t represent frequency.

Since we have time series of measurements, we focus on a discrete view of the Fourier transform. The discrete Fourier transform (DFT) can be easily obtained from the continuous transformation. The discrete transformation takes M samples in the time domain and converts them into N complex values $\hat{m}(\omega_t)$ in the frequency domain. Thus, equation 2.28 can be rewritten as

$$\mathscr{F}\{f(m)\} = \hat{f}(\omega_t) \equiv \sum_{m=0}^{M-1} f(m)\, \mathrm{e}^{-i\frac{2\pi}{M}\omega_t m}. \tag{2.29}$$

Equations 2.28 and 2.29 show that the Fourier transform is just a convolution between a time function and a series of sine and cosine functions. Although equation 2.29 can be conveniently computed, Cooley and Tukey (1965) implemented a method that explores a symmetry inherent in the DFT, eliminating redundant calculations. The technique, called as fast Fourier transform (FFT), reduces the storage requirements and computation time significantly in the order of $M\log_2 M$ instead of M^2 complex multiplications. The only disadvantage is that M must be a power of two. However there are other techniques based on FFT procedure that does not require that the length of data is a power of two. The FFT breaks up the calculation into two discrete Fourier transforms of length $M/2$, one with even and one with odd subscripts:

$$m = \begin{cases} 2r & \text{for } m \text{ odd} \\ 2r\ +\ 1 & \text{for } m \text{ even} \end{cases}$$

in which $0 < r < M/2$. Thus the fast Fourier transform $\mathscr{F}$ of function $f(m)$ is defined as

$$\mathscr{F}\{f(m)\} = \sum_{r=0}^{(M/2)-1} f(2r)\, \mathrm{e}^{-\frac{4\pi}{M}ikr} + \sum_{r=0}^{(M/2)-1} f(2r+1)\, \mathrm{e}^{-\frac{4\pi}{M}ikr}\, \mathrm{e}^{-\frac{2\pi}{M}i}. \tag{2.30}$$

The number of samples M must be a power of two in equation 2.30. However, when the number of signal points is not a power of two, zero padding can be added in the end of the signal. According to Du and Swamy (2010), the pad-zero method does not increase the true resolution in frequency and does not perturb the transformations. Even though the FFT is one of the most famous algorithms, the method is valid just for stationary time series, signals that have invariant local statistics over the entire duration of the signal. However, many natural time series exhibit a nonlinear and non-stationary behavior. Even though time series may contain dominant periodic signals, their magnitude and frequency may vary over periods of time. The simplest way to analyze non-stationary signals is to compute the mean and variance for different time periods and analyze if the statistics are significantly different. To gain information concerning the frequency domain, Gabor (1946) adapted the conventional FFT to analyze only a section of the signal at each time. The method was named as short-time Fourier transforms (STFT).

The STFT, also called as windowed Fourier transform (WFT), helps overcome the difficulty to analyze non-stationary signals. Depending on the window used, this technique also avoids the leakage problem. Discontinuity involved when the FFT is applied in a signal often causes spectral leakage. The WFT partitions the signal into several equal segments and multiplies each segment by a window function, in which segments are assumed to be stationary. Therefore, the window function g is moved by ς along the time line and the Fourier transform is calculated for each segment, reveling the Fourier spectrum on each segment. This technique decrease spectral variance and also avoids spectral leakage. Thus, the

STFT can be expressed as

$$\mathscr{F}\{f(m)\} = \langle f, g_{m,\omega_t} \rangle = \int_{-\infty}^{+\infty} f(m)\, g(m-\varsigma)\, \mathrm{e}^{-i2\pi\omega_t m} \mathrm{d}m. \tag{2.31}$$

The time-frequency resolution is directly affected by the window function and its size. Currently, there are several types of window functions available, and each of them is suited to a different type of application. Many internal wave studies that use STFT to capture internal wave oscillations in reservoir and lakes use Hamming and Hanning window functions, which are window families known as raised cosine. According to Gao and Yan (2010), Hamming and Hanning window functions are applicable to narrow-band signals. Although, many internal wave studies use these cosine windows, there is not a consensus among the better window to identify internal waves. Some specific application of internal waves have used different windows. For example, Ostrovsky et al. (1996) used a short flat-top window to analyze internal waves on small-scale and Stocker et al. (1987) applied a split cosine bell window to analyze long internal seiches in lakes. According to Smith (2013), although the flat-top window preserves the amplitude of the signal, it squeezes the data, and consequently more data needs to be analyzed. Thus, the flat-top window function is just used to analyze high-frequency internal waves, when the periodic data lasts for long period. Split cosine bell window is also a raised cosine window and does not present a significant difference from results obtained using the Hamming and Hanning windows.

As Nisar, Khan and Tariq (2016) stated, the window size must be chosen carefully, ensuring that the signal remains approximately stationary within the window. Clearly the window frequency also needs to be lower than the frequency range evaluated. For example, the spectral analysis of a thermocline average temperature signal of 20 days cannot be windowed by a window function of 24 h size if there is indication of internal wave action with periods higher than 24 h.

Another technique often used in STFT is known as overlapping process. The overlapping technique consists of overlapping the signal of analyzed segments, so the signal is split up in overlapping segments. Overlap processing is often used because it increases the time-frequency resolution. The best overlap percentage is defined by the window function chosen. Normally, the overlap percentage recommended for wide windows, as Hamming and Hanning window, is 50%. For narrow window functions normally a higher percentage can be used. Heinzel, Rüdiger and Schilling (2002) present the recommended overlap percentage for each window function in details.

Another important preprocessing technique discussed briefly earlier is zero-padding the signal, which means adding additional zeros at the end of the time series. Firstly, the zero-padding technique increases the STFT algorithm performance, since the STFT runs much faster for power of two. Although the zero-padding takes more points in the frequency domain, it does not offer any further information about the individual frequency content, and consequently the real resolution does not increase. However it reduces the space between bins, and consequently avoids the picket fence effect. The picket fence effect, also called as resolution bias error, occurs when the signal frequency is aligned between two bins, reducing the amplitude energy. Therefore, it looks like as the energy is varying at the same time as the frequency is varying. This effect is also a type of spectral leakage. Although the zero-padding can avoid spectral leakage, it can also decrease the energy of the FFT.

Generally, to provide a physical meaning to spectral analysis, the power spectral density is obtained. The PSD measures the signal power per unit bandwidth for a time series, and consequently describes how the signal power is distributed over the frequency domain. The PSD can be obtained though the ratio of sampling frequency and the mean-square power spectrum, which is obtained though the Fourier transform of the auto-covariance function,

$$\phi_{ff}(\omega_t) = \phi^*_{ff} \times T_s \equiv \frac{T_s}{M}|\mathscr{F}\{f(m)\}|^2. \tag{2.32}$$

in which $\phi_{ff}(\omega_t)$ is the PSD of the function $f(m)$, ϕ^*_{ff} is mean-square power spectrum of the function $f(m)$, T_s is the sampling period, and M is the signal length.

Another important spectral analysis with regards to internal waves analysis is the ordinary coherence analysis. Coherence is a method developed to measure the correlation between two or more signals in terms of frequency. The coherence can be obtained using the mean-square power spectrum of two signals and the cross power spectrum, ϕ^*_{fg}. The cross power spectrum is the Fourier transform of the cross-covariance function, given by

$$\phi^*_{fg}(\omega_t) = \sum_{k=-\infty}^{\infty} \frac{1}{M-1} \sum_{m=1}^{M} (f_m - \bar{\mu_f}) \times (g_m - \bar{\mu_g})\, \mathrm{e}^{-i\omega_t k} \qquad \omega_t \in [-1/2, 1/2], \tag{2.33}$$

where $\bar{\mu_f}$ and $\bar{\mu_g}$ are the means of each signals. Thus, the coherence, or mean square coherence, between two signals f and g is given by

$$C_{fg}(\omega_t) = \left| \frac{\phi^*_{fg}(\omega_t)}{\sqrt{\phi^*_{ff}(\omega_t)\ \phi^*_{gg}(\omega_t)}} \right|^2 \qquad \in [0, 1], \tag{2.34}$$

in which ϕ_{fg} is the CPSD of signal $f(m)$ and $g(m)$, and ϕ^*_{ff} and ϕ^*_{gg} are the mean-square power spectrum of functions $f(m)$ and $g(m)$, respectively. The coherence function provides values between 0 and 1, with 1 indicating a perfect linear relationship. Using CPSD we can also obtain the phase shift in frequency domain between time series $f(m)$ and $g(m)$. The phase shift analysis provides the phase lag between two signals in radians for each frequency. This analysis is useful to detect higher baroclinic modes. The phase shift in frequency domain is defined as

$$P_{fg}(\omega_t) = \frac{\mathrm{Re}\left\{\phi^*_{fg}\right\}}{\mathrm{Im}\left\{\phi^*_{fg}\right\}} \qquad \in [\pi, -\pi]. \tag{2.35}$$

Although the STFT technique solves the frequency localization problem, detecting periodic oscillation in a non-stationary signal, the main problem with the STFT is the inconsistent treatment of different frequencies. This problem has to do with the Heisenberg's uncertainly principle. According to Millette (2011), the uncertainly principle is related with time-frequency resolution. As Gubbins (2004) stated, this problem arises from the aliased spectrum that does not fall within the frequency range of the window. Once the window size and type has been selected, the time-frequency resolution is kept constant. Therefore, a satisfactory resolution can just be obtained in the time or frequency domain, but not both. Once the window size is kept fixed, the time-frequency resolution depends just on the window size and type. Thus, part of the problem lies in the fact that at high periods there are few oscillations within the window that frequency localization is lost, whereas at low periods there are many oscillations that the time localization is lost. In addition, there are many windows that needs to be analyzed to obtain a satisfactory result. As mentioned before, the window size need to be selected according the wide range of dominant frequencies. However, in internal waves studies, the range of dominant internal wave periods can vary from seconds to several days. Thus, in some cases, a method of time-frequency localization that does not present a predicted scale frequency, such as wavelet transforms, is more recommended than the Fourier analysis.

2.4.2 Wavelet transform

While STFT gives the same resolution at all frequencies, the wavelet transform uses multi-resolution methods to decompose simultaneously the signal into time and frequency domain. The wavelet

transform, W_x, is just the inner convolution between a wavelet function ψ and a signal f, where $f \in L^2(\mathbb{R})$.

$$W_f(\upsilon, s) \equiv \langle f, \psi_{\upsilon,s} \rangle = \int_{-\infty}^{+\infty} \frac{f(t)}{\sqrt{s}} \psi^* \left(\frac{t-\upsilon}{s} \right) \mathrm{d}t \tag{2.36}$$

The wavelet function is derived from the mother wavelet through translation and scaling. The parameter υ is a translation parameter and is related with the location of the wavelet function as it is shifted through the signal. The parameter s is the scaling parameter, which determines the time-frequency resolution. Large scaling parameters dilate the signal and provide more information about low frequencies, whereas small scaling parameters compress the signal and provide more information about high frequencies. The scaling parameter, s, is responsible to account the Heisenberg's uncertainty principle, and consequently is the reason for wavelet analysis being more powerful than Fourier analysis. By analogy, it looks as though the Fourier windows could change their size during the Fourier transform, and consequently could capture a better time-frequency resolution for each spectrum part. In theory, equation 2.36 measures signal fluctuation in the neighborhood of υ, where the length is proportional to the scaling parameter, s. The asterisk denotes the complex conjugation of the base wavelet function $\psi(n)$.

Although the wavelet function size does not need to be selected in a wavelet analysis, there are many types of wavelet functions. Thus, the wavelet function used in the wavelet transform must be selected considering the time series analyzed. According to Farge (1992), there are many factors that need to be considered, such as the wavelet function orthogonality, the wavelet width, the time series shape, and the function codomain, that can be real or complex. The wavelet can be divided into orthogonal and non-orthogonal wavelet. Orthogonal wavelet transformation has a convolution number at each scale proportional to the wavelet width.

The wavelet functions are also chosen according to the function codomain, real or complex wavelet. A complex wavelet captures better the oscillatory behaviour of a signal, while a real wavelet function usually is used to isolate peaks and identify discontinuities. The wavelet function is also determined according to the e-folding time, a parameter exclusively used for continuous transforms. The resolution of the wavelet transform is related directly with the e-folding time parameter, and is determined by the balance between the width space and Fourier space. The e-folding time measures the wavelet width, relative to the scaling parameter, s. Thus, larger e-folding times imply more spreading of the wavelet power, providing a poorer time resolution and better frequency resolution. The last parameter analyzed to determine the wavelet function is the signal shape. The wavelet function needs to reflect the type of feature which is presented in the signal. As Torrence and Compo (1998) stated out, for sharp signals with jumps and steps, a rectangular function such as the Harr function could be chosen. On the other hand, for smooth signals, a smooth function such as a damped cosine is better suited.

Another application of wavelet analysis is related to the global wavelet spectrum. The global wavelet spectrum is an averaged power spectrum based upon a set of wavelet functions. According to Fernando (2012), the global wavelet spectrum is a smoothed version of the Fourier power spectrum and is an efficient estimator of the true power of a signal. The global wavelet spectrum can be obtained averaging all the local wavelet spectra, equation 2.36.

$$\bar{W_f}^2(\upsilon, s) = \frac{1}{M} \sum_{f=0}^{M-1} |W_f(\upsilon, s)|^2 \tag{2.37}$$

Despite this method being extremely useful to estimate the true power of a time series, it can generate the bias problem. This problem is related to the difference between the global wavelet spectrum and the true Fourier spectrum in terms of energy. At high frequencies, the global wavelet is very broad

in frequency, and consequently all peaks in the spectrum are smoothed. On the other hand, at low frequencies, the wavelet is narrow, therefore the peaks are sharp and they present higher energy. Wu and Liu (2005) reveled that on some occasions the low frequency energy is amplified, and consequently the global wavelet does not work efficiently. He stated out that in these cases the Fourier analysis can be used to achieve the right result. As expected, this bias problem just affects the result when the local wavelet spectra is averaged. Therefore, the wavelet analysis is still better to be suited, used for analyzing non-stationary signals.

To conclude section 2.4, we present a Fourier and wavelet spectral analysis for a stationary and a non-stationery signal. To attach a physical meaning for our example, we consider that the signal is composed by water temperature measurements, which are given in degrees Celsius. The stationary signal is composed of a sum of two cosine waves divided by two, where each cosine waves have amplitude of 2 and 4 °C, and frequency of 0.25 and 0.125 per hour, respectively. The signal is provided with a time step of 30 minutes and has a length of 48 hours. The non-stationary signal is composed of the same cosine waves. However, the fist one, which has an amplitude of 2 °C, occurs during the first 20 hours, while the second cosine wave occurs between 20h30 and the end of the time series, 48 hours. To be more realistic we also added random noise to both signals, as seen in Figure 13(a). The information about the preprocessing was used in this spectral analysis such as an overlapping percentage, window function, wavelet function, and is presented in section 3.3, where the spectral analysis used in this research is shown.

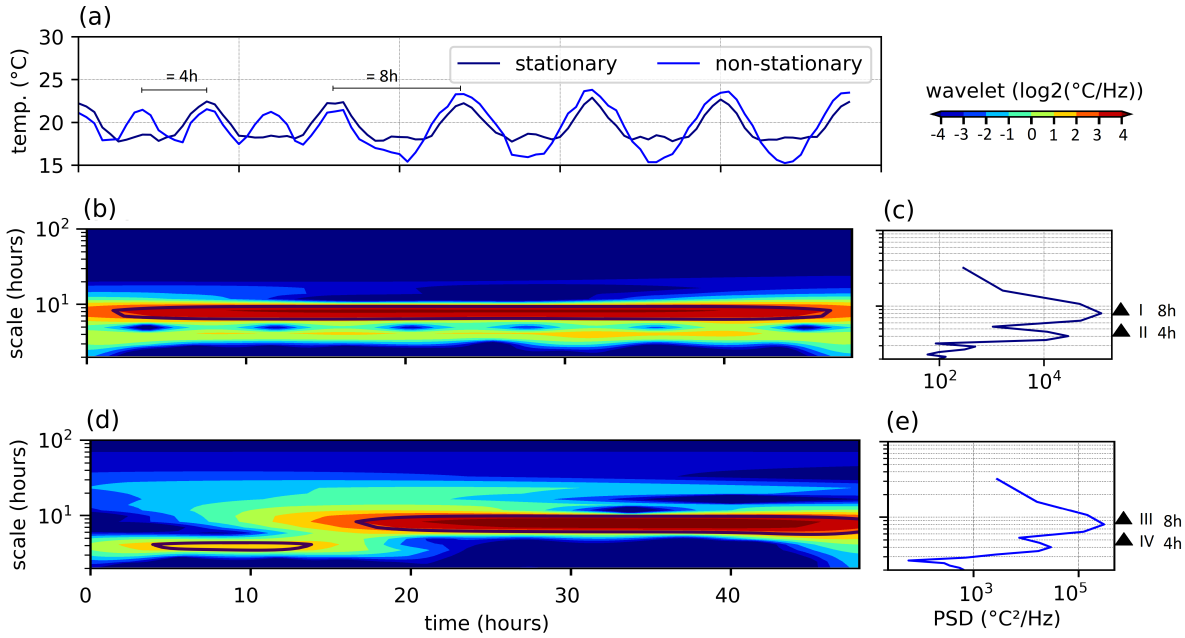

Figure 13 – Spectral analysis of 2 signals, a stationary and a non-stationary signal artificially created. (a) time-evolution of a stationary and a non-stationary signals. (b) wavelet analysis of the stationary signal. (c) the power spectral density of the stationary signal. (d) the wavelet analysis of the non-stationary signal. (e) the power spectral density of the non-stationary signal. The colorbar in the bottom right corner refers for both wavelet color graphs.

As expected, the wavelet and Fourier analysis captured the period peaks of 4h and 8h in both cases, stationary and non-stationary signal. In the stationary case (Figure 13 (b) and (c)) the power spectral density and the wavelet analysis show the peak of 8h (Figure 13 (c): (I)) with higher energy than the 4h peak (Figure 13 (c): (II)) since the 8h oscillations has higher amplitude compared to the 4h ones.

The same peaks are also observed in the non-stationary signal, where (III) peak represents the higher amplitude oscillation with periodicity of 8h and (IV) is the period of 4h, lower amplitude wave. Although both methods has capture the predominant oscillatory motion, the wavelet analysis has the advantage to capture the action period of each frequency. We presented this analysis just for a better visualization of each method discussed. The advantage and further comments about each spectral analysis method is given in section 3.3.

2.5 Modeling

Mathematical models have become an indispensable tool for identifying or simulating internal waves. Many internal wave researches conducted in lentic water bodies uses the combination of spectral analysis and modeling to identify internal waves. In addition, as Imberger (1994) stated, mathematical models are essential to describe and quantify the flux of nutrients, biotas, and contaminant transport influenced by internal waves in stratified basins. All models are based on the solution of the mass-conservation equation and the nonlinear partial differential Navier-Stokes equations. The mass-conservation equation, also called as continuity equation, stats that the mass variation inside a fixed control volume must be equal to the net inflow of mass through the boundary of the control volume. Thus, applying the Reynolds transport and Gauss' theorem and considering a arbitrary control volume, the conservation of mass can be written, in differential form, as

$$\frac{\partial \rho}{\partial t} + \frac{\partial \rho u_i}{\partial x_i} = 0, \tag{2.38}$$

where ρ is the water density and u_i is the velocity vector.

The momentum equations describe the motion of any fluid. These equations express conservation of momentum and may be written as

$$\frac{\partial \rho u_i}{\partial t} + \frac{\partial \rho u_i u_j}{\partial x_j} = \frac{\partial}{\partial x_j}\left(- P + \Lambda \frac{\partial u_k}{\partial x_k}\right) + \rho \left(g_i - \overline{\omega_o j}\ u_k\right) + 2\rho\nu_u \frac{\partial S_{ij}}{\partial x_j}, \tag{2.39}$$

in which P is the total thermodynamic pressure, g is the acceleration due to gravity, S_{ij} is the rate of strain tensor, Λ and ν are viscosity coefficients, and $\overline{\omega_o j} = 2\ \varepsilon\ \sin\overline{\phi}$ is the inertial frequency, where ε is the angular frequency of the earth and $\overline{\phi}$ is the mean latitude of the phenomenon.

The system formed by momentum and mass conservation equations have a inherent nonlinearity and many other inconvenient properties to be solved analytically. The nonlinearity makes many differential equations really complex to be solved or impossible with the present mathematical tools. Therefore, an exact analytical solution for a problem involving equations 2.38 and 2.39 is not available in general form. The significance of nonlinear terms in equation 2.39 can be measured combining two non-dimensional parameters, the nonlinear wave steepening and the linear phase dispersion parameters. This combination give us the Ursell number, U^*:

$$U^* = \frac{\zeta_o \lambda^2}{H^3} \tag{2.40}$$

in which ζ_o is the initial wave height (the difference between the elevations of the wave crest and trough), λ is the horizontal length scale and H is the undisturbed mean water depth. Normally, for long internal waves ($\lambda \gg H$) with small Ursell number ($U^* \ll 100$), the linear wave theory can be applied. However, for fairly long internal waves ($\lambda \gg 7H$), a nonlinear theory is strongly recommended.

Originally, linear internal seiches were modelled considering a rectangular basin with a two-layer density profile. Thus, the first model for internal seiches was developed by Watson (1904). The Watson's

formula was obtained analytically considering the hydrostatic approximation and a simplified case of a rectangular basin with wavelength $\lambda > H$. The Watson's equation considers two homogeneous layers and was tested by Schmidt (1908) and later Mortimer (1952). A better approximation which takes the reservoir shape into account was developed by Defant (1918) for standing surface waves. The Defant's model was developed to calculate the periods and structures of surface standing wave modes. The model presented excellent results in regular lakes. Mortimer (1952) observed isotherm fluctuation corresponding to V1H1 baroclinic mode of 18 h30 $\pm$ 30 min in Lake Windermere. He computed the wave period using Watson's formula and obtained a period of 18 h 48, a maximum error of approximately 5%. Although the Watson's equation presented really good agreement for regular basins, for complex ones the formula did not conform well, giving errors grater than 20% for stratified basins with complex geometry and bathymetry. Mortimer (1952) also analyzed the dynamic of internal seiches with a three layer model considering a rectangular lake of constant length L and depth H. The author concluded for the first time that some features of basin motion could not be explained by a simple two layered model. M. S. Longuet-Higgins set out in an appendix of Mortimer (1952) a three-layer hydrostatic model, which was tested also on Lake Windemere. One year later, Mortimer (1953) developed an adaptation of the one-dimensional model developed by Defant (1918) to identify internal waves. The non-hydrostatic two-layered model in which the discrete momentum and conservation of mass equations are treated along the main axis of the reservoir, at different vertical sections. Mortimer (1953) tested the model in Lake Geneva to identify the first vertical mode (V1), internal seiches considering the shape of the basin. Lemmin and Mortimer (1986) tested Mortimer's model in eight different lakes for which a two-layered approximation to density distribution was adequate. Lammel (1984) tested Mortimer's model in Kochelsee and observed a good agreement (within $\pm$ 10%) between Mortimer's model and the observed basin-mode period, obtained through the prominent peaks in energy spectra. Another two-layered internal wave model was developed by Schwab (1977). Schwab model is a two-layered model, assuming a uniform equivalent depth. This model is commonly called a two layer equivalent depth model (TEDM). The TEDM has both layers with constant depth and the computation domain is bounded by the pycnocline shore. He observed that the periods obtained in Lake Ontario fell into two categories, Kelvin and Poincaré-type internal waves. Although the model uses the hydrostatic approximation, observational evidences from Lake Ontario agreed well with the results obtained from the model. Schwab extended his two-layer model with uniform equivalent depth to a variable depth bottom layer, neglecting the Earth rotation. Schwab modified model is called the two-layer variable depth model (TVDM). Horn, Mortimer and Schwab (1986) compared the results of the Mortimer and Schwab model in Lake Zurich. They concluded that the periods and structure of internal waves are well modeled by the TVDM and also, a little less accurately by the Mortimer model.

Increased computing power has allowed the development of complex models of internal seiches. Many sophisticated models have been developed since the late 19th century, improving descriptions of stratification, the generalization to arbitrary bathymetry and consider the nonlinear effects. Nowadays, there are countless different models, using different approximations. Hydrodynamic models used to model large scale phenomena often neglect non hydrostatic pressure, and subsequently vertical momentum changes, considering that the horizontal length scales are larger than the vertical length scales. However, according to Wadzuk and Hodges (2004), the hydrostatic approximation may be problematic since non-hydrostatic pressure plays an important role in internal wave evolution. As evidenced by Horn et al. (2002), many times the hydrostatic approximation fails at open boundaries and at steep slopes with strong vertical velocities. Although non-hydrostatic models represent better the real stratified environment, the solution of the governing equations considering the non-hydrostatic pressure is much more complex and has a high computational cost, limiting its use in large scale systems. In addition, according to Long (1972), long internal seiches that are damped by viscous effects may be often considered linear. In this situation, non-hydrostatic pressure does not significantly affect the motion of internal waves, and consequently a

hydrostatic approximation is valid. Thus, even though a large number of studies currently uses complex models to quantify the biochemical flux in stratified basins affected by internal waves, simpler models are yet an interesting option to model the internal wave evolution and their effects on biochemical fluxes. Cuypers et al. (2011) used a two-dimensional linear and hydrostatic seiche model to analyze the impact of internal seiches on the spatial distribution of cyanobacteria in Lake Lac du Bourget, France. The distribution was well represented by the model, which identified that V1H1 internal wave mode was responsible for the vertical displacements of the biomass peak in the water column in Lake Lac du Bourget. Motivated by the limitation of nonlinear models caused by high computational cost, Wadzuk and Hodges (2004) studied the difference between hydrostatic and non-hydrostatic models and the scale for which non-hydrostatic pressure impacts internal waves patterns. As Wadzuk and Hodges (2004) pointed out, with some limitations, even internal waves with non-hydrostatic behavior can be detected using hydrostatic models. However, hydrostatic models cannot model the wave breaking, and consequently energy dissipation. One important aspect needs to be carefully analyzed, the energy dissipation may still appear in some hydrostatic numerical models as numerical dissipation, this numerical diffusion of mass and momentum may present an incorrect evolution of internal waves and its energy. As Wadzuk and Hodges (2003) stated, hydrostatic models often predict a high steepening, creating a weakened pycnocline. So a careful analyses of numerical results needs to be conducted to predict the real evolution of internal waves.

Another term in the momentum equation that is usually neglected is the Coriolis force term, the angular speed of the earth term in equation 2.39 is proportional to the Coriolis force and is responsible for deflecting internal seiches, giving rise to wave propagating phases. This term is often neglected for small scales processes or processes that occur near the equator. The Earth's rotation may have significant effects with respect of internal waves, to generate internal Kelvin and Poincaré waves in basins with more than 5 km in the mid latitudes, large closed basin near the equator, and small basins in the Arctic. Many authors use the expression "small basin" to neglect the Coriolis term. However, as stated by Bäuerle (1994), the Earth rotation may affect the dynamic of internal seiches even in basins of fairly small size lake. Thus, in spite of the fact that the spatial scale of the motion is not so large, the temporal scale of the motion is relatively large, sometimes much larger than the inertial period. Bäuerle (1994) identified Poicaré baroclinic oscillations in the Lake Uberlingen, a small portion of the Upper Lake Constance, which has width of just few kilometers. Internal Kelvin waves are large-scale waves that are affected by Earth's rotation and have higher amplitude at the boundary, decaying exponentially with distance from the lakeshore, where the wave is trapped. As a result this motion normally presents higher velocities close to the shore and smaller ones in the interior of the basin. The pressure balances the Coriolis force, driving the wave along the horizontal boundaries, clockwise in the Southern Hemisphere. Poincaré waves are also large-scale waves, but they are not trapped at boundaries. This type of waves develops from crosswise seiching, which becomes deflected by Coriolis force (WÜEST; LORKE, 2003). They are frequently observed by a counter-clockwise direction in the south hemisphere and greater transverse velocities. To identify when the Coriolis force can affect the propagation of internal waves, Antenucci and Imberger (2003) suggest the computation of the Burger number, Bu. The Burger number is defined as the ratio of the internal Rossby radius of deformation to a length scale L', the horizontal half length of the basin. The Bu can be written as

$$Bu_i = \frac{Ld}{L'} \equiv \frac{2c_p}{\omega_o j L_p}, \tag{2.41}$$

in which Ld is the Rossby deformation radius, c_p is the non-rotating internal wave velocity, and L_p. Thus, Bu varies in a determined lake with season as the stratification increase and decrease. If $Bu \ll 1$, the Coriolis acceleration play an important role in the dynamic of internal waves, changing the internal wave velocity and the lateral distribution of the wave energy (FORCAT et al., 2011). Bauerle (1985) modeled

Table 1 – Rossby deformation radius, Ld, and Burger numbers, Bu, for some lakes and reservoirs.

Basin	Latitude	L'(m)	Ld (m)	Bu	Source
Lake Mono	38° 01' N	4000	8261	2.07	MacIntyre et al. (2009)
Lake Babine	54° 45' N	3000	1600	0.53	Farmer (1978)
Lake Kinneret	32° 50' N	7500	4185	0.56	Antenucci, Imberger and Saggio (2000)
Lake Zurich	47° 13' N	15000	2155	0.14	Horn, Mortimer and Schwab (1986)
Alpnacher See	46° 57' N	1750	376	0.22	Münnich, Wüest and Imboden (1992)
Sau Reservoir	41° 58' N	350	925	2.64	Vidal et al. (2005)

with the TEDM model the Lake Geneva. The author observed the formation of an V1H1 internal Kelvin wave with period of 78h. The amphidromic system showed a clearly counter-clockwise rotation, indicating a Kelvin-type wave for north hemisphere. Bauerle (1985) also obtained V1H10 and V1H11 modes, but with some nodes presenting apposite amphidromic phase, which indicate a mixed behaviours between Kelvin and Poicaré waves. In table 1 we summarized some different values of Bu obtained from some internal wave studies performed in different basins.

As observed, the influence of earth rotation does not depend only on the basin spatial scale, but also the internal wave temporal evolution. Works focusing on the influence of Earth rotation on internal wave patterns have also been published about Lake Constance (Germany, Switzerland, Austria) and Lake Biwa (Japan), see Imberger [3].

As seen before, despite the density gradients in nature are always continuous, many studies use homogeneous layers to describe the system and the internal wave evolution. The stratification is generally continuous, and its structure varies seasonally, with consequent seasonal effects on the evolution of internal waves. Generally, continuous stratified environments can present internal waves in different depths. Since the system presents continuous vertical density variation, waves can travel horizontally along isopicnals and vertically along the density gradient. However, a layered model simplifies the mathematics involved and the computational coast. As Simmons et al. (2011) stated, the two-layer model is particularly useful to detect the first vertical internal wave mode, offering significant reduction of parameters. The two-layer model yields only the first vertical baroclinic mode, neglecting all others. Although this simplification eliminates higher vertical baroclinic waves, the fundamental vertical mode (V1) is much more frequently observed in lakes and reservoirs. The higher layer model also is useful to detect higher vertical internal wave modes. The real advantage of the layered-model is that we can make the irrotational flow assumption, and consequently we can define a velocity potential, reducing the number of variables or adding new equations to the problem.

In spite of the fact that the layered-model predicts good results in many situations, in continuous stratified environment the flow is always rotational, mainly for baroclinic modes. The curl of each term of the momentum equations, the vorticity equation can be written as

$$\frac{\partial \Omega_k}{\partial t} + u_j \frac{\partial \Omega_k}{\partial x_j} = (\Omega_j + 2\overline{\omega_o j})\frac{\partial u_k}{\partial x_j} + \varepsilon_{ijk}\frac{\partial}{\partial x_j}\left(\frac{1}{\rho}\frac{\partial P}{\partial x_i}\right) + \nu\frac{\partial \Omega_k}{\partial x_j}, \tag{2.42}$$

where vorticity is produced by the baroclinic effect, the second term on the right-hand-side of equation 2.42. The first term on the right-hand-side of equation 2.42 is called as vortex stretching and tilting and is responsible to amplify the vorticity, really important to turbulent analysis. The last term accounts for diffusion of vorticity due to the viscous effects. As we can note, for a inviscid flow, this term can be neglected. We presented this analysis to understand all errors involved in our models due to simplifications. Note that the irrotational assumption is much more aggressive for internal waves (baroclinic mode) than

[3] Appt, Imberger and Kobus (2004) and Shimizu and Imberger (2009)

for barotropic flows. Even in an inviscid flow, under a baroclinic wave action, the second term on the right-hand-side produces vorticity.

2.6 Experimental analysis of internal waves

Laboratory experiments help to overcome the difficulty to interpret a naturally occurring phenomena in the environment. Although laboratory experimental analysis contains an element of abstraction, they frequently allow us to examine a specific phenomena without considering other effects. Thus, a specific effect can be better explored in the laboratory than in natural environment, where the complexity is far greater.

dimensional analysis and similarity is an important technique that can be used, but not restrict, for correlating the physical characteristics of flow in the real dimensions to laboratory experiments dimension, which frequently is conduced on a smaller scale.

2.6.1 Dimensional analysis & similarity

Dimensional analysis explains how and when laboratory experiments reproduce the real process that occurs in nature and is often applied for developing scaling laws. This analysis is a technique by which physical processes are combined with rigorous mathematical description. The dimensional analysis provide the combination of non-dimensional physical parameters that are relevant in physical motion of internal waves. We shall not prove any theorem in this section. We also do not present any step to determine the functional dependence of variables. Proofs and 'step-by-step' processes can be found in many fluid mechanic books.

The dimensional analysis here is based on the Buckingham's theorem, also called Π-Theorem. According to Kundu and Cohen (2002), the Buckingham's theorem states that, in a problem with n dimensional variables, the n variables can be combined into $n - r$ independent dimensionless parameter group Π, in which r is the number of independent dimensions. Therefore, we have

$$f(q_1, q_2, q_3, ..., q_n) = g(\Pi_1, \Pi_2, \Pi_3, ...\Pi_{n-r}) = 0. \tag{2.43}$$

Thus, it does not depend upon the choice of the fundamental quantities and their units. As stated by Barenblatt (1987), if there is a physical law that be written as a relationship between dimensional variables and several dimensional governed parameters, the relation can be reduced through dimensionless products of quantities, in which the number of products is equal to the difference between the total number of governing parameters and those with independent dimensions. Obviously, when internal wave motions are described by Π-groups, all processes with same values are physically indistinguishable. For example, we do not need to have the same density difference in laboratory experiments as that observed in nature. However, we need to have the same ratio between the Brunt-Väisälä frequency and the "shear" frequency. Thus, we do not necessarily need to input energy in form of wind (or any shear velocity at water surface). As seen before, this ratio is called the Richardson number, and it is often a Π-group in the dimensional analysis for stratified flows. We can represent the natural environment in laboratory experiments by keeping all the Π-products invariant in both problems. However, often we have problems handling this. For example, Fr and Reynolds number are essentially variant, which means that is impossible to keep them simultaneously invariant.

One of the advantages of dimensional analysis is the reduction of variables. However, for a reliable representation of the natural environment, the identification of all physical variables, which influence

the motion of internal waves, is essential for a better representation in laboratory-scales. According to Hutter, Chubarenko and Wang (2014), for many barotropic and baroclinic motions in large-scales (in time or space-scales), the effect of Earth rotation are often not negligible. This implies that the dynamic of internal waves in laboratories also needs to reproduce the rotation effect in the laboratory tank, in which the rule of similitude requires a relatively fast rotation of the tank. Such apparatus are really expensive. In addition, the rotation frame would increase complexity to measure some parameters in the tank. As a result, this analysis is still little explored in terms of internal waves investigation.

2.6.2 Wavemaker

In laboratory experiments, internal waves can be generated in several different ways. The best-known techniques are related to disturbances caused by different sources. As stated by Sutherland (2010), convection, imbalance of large-scale flows, gravity currents, and oscillatory motion caused by solid bodies are some of the many sources of disturbance that can excite internal waves in laboratory experiments. With regards to the generation of internal waves by solid bodies, Yeung and Nguyen (1999) studied the formation of internal waves in a two-layer system for a steadily translating source. To explain the wave patterns, Ten and Kashiwagi (2004) examined the generation and evolution of linear internal waves for two different configurations of a vertically oscillating box-shaped wavemaker. In the first configuration, the wavemaker was positioned on the surface of the lighter fluid. In the second configuration, the wavemaker was positioned both in the lighter and heavier fluid. Many other experiments were conducted to study the formation of nonlinear internal waves using solid bodies wave-makers. Many experimental studies have described how to generate solitary internal waves in tanks using some wave-making mechanism. Walker (1973) used a vertically oscillating wavemaker at the interface between two fluids, whilst Mercier, Vasseur and Dauxois (2011) used a horizontally translating ship-shaped model moving on the free surface.

Another common source of internal waves in two layer stratified fluids confined in a closed rectangular tank is to tilt the tank. When the tank is tilted, the denser layer flows towards the bottom of the tank, whilst the lighter layer is forced toward the top of the tank. Therefore, the inclination creates a long interfacial wave that moves forth and back. The initial angle of the tilt determines the energy input. This technique was used in many experiments executed to create shear flow in stratified fluid and is described in details by Thorpe (1968). Although this is a really good option to create baroclinic motion without any surface perturbation, the tank must be closed. For a free-surface rectangular tank, the tilt creates surface waves that suppress any baroclinic motion. Thus, one option for rectangular tanks that are not closed is the generation of internal waves by gravity currents. Such currents do not create barotropic waves since there is no perturbation of the free surface. However, there are many techniques to generate internal waves by gravity currents, each method describes the generation of different types of internal waves. A common internal wave generated by gravity currents is that formed in a two-layer system under the influence of subcritical flows. According to White and Helfrich (2008), gravity currents flowing through stratified fluids may generate long-internal waves ahead of the gravity current. Despite this being an important result in internal wave theory, this technique is not necessarily related to the formation of basin-internal seiches. Since we are interested in low-frequency internal seiches, we describe the technique called here *lock-exchange release* to produce laboratory gravity currents that are sources for long-internal seiches. The only disadvantage is that the energy input can not be changed for a specific density profile. As demonstrated by Bueno et al. (2017), the gravity current speed is a function of the gravity current density. Thus, the energy transferred to internal wave generation will be always related to the density stratification. A short theory of gravity currents produced by lock-exchange release is presented here.

In a lock-exchange release experiment, fluids of different densities are separated in two compartments by a vertical sliding gate, as illustrated in Figure 14(a). Although several researches have studied partial-depth release, the present research deals just with full-depth release, which means that the depths of both fluids are equal. The experiment begins when the gate is vertically removed, leaving the locked fluids to flow. Therefore, the dense gravity current travels horizontally along the bottom of the thank, whereas the lighter fluid flows in the opposite direction along the free surface (Figure 14(b)).

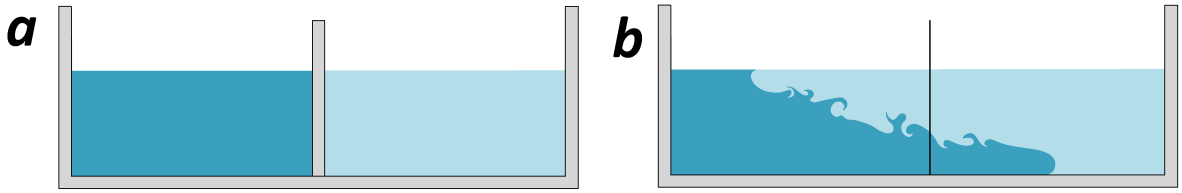

Figure 14 – (a) Sketch of the lock-exchange initial condition for a full-depth release in a rectangular channel. (b) Sketch of the gravity currents produced by lock-exchange. The lower boundary condition is rigid and the upper is free.

The gravity current velocity have been largely studied since 1960s. Benjamin (1968) developed the energy-conserving theory for gravity currents, neglecting the dissipation due to turbulence and viscous stresses. He considered the propagation of a two-dimensional gravity current into a homogeneous ambient in a rectangular channel. For Boussinesq currents and using the Benjamin's energy-conserving theory, Benjamin (1968) predicted $Fr_H \equiv S_p/\sqrt{g'H} = 0.5$, in which S_p is the gravity current speed and H is the channel depth, equation 2.14. Based on several experiments, Keulegan (1953) observed a small increase in Fr_H for higher Reynolds number, $Re = S_p H/\nu$. Based on Keulegan work, Bar (1967) extend Benjamin's analysis to account the bottom stress, which, as expected, decreases Fr_H. He observed $Fr_H \approx 0.49$ and $Fr_H \approx 0.59$ for heavier and lighter gravity current, respectively. Barr also observed that the variation of Fr_H is most pronounced for Re from 200 to 1000. For $Re \geq 1,000$, Fr_H does not significantly increase. Finally, although effects of non-conservation of energy may play a important role in the dynamic of gravity currents, as stated by Shin, Dalziel and Linden (2004), for a total-depth lock-exchange release, the Beijamin's energy-conserving theory seems to describe the experiments satisfactorily. Thus, we can assume that the gravity current velocities are constant.

Here we summarized some aspects about gravity current speed. The kinetic energy from the gravity currents is responsible to transfer energy for the formation of internal seiches in this experiments. The gravity current speed is an important factor for the initial energy of the internal seiche. The gravity current velocity can be compared similarly to the wind stress, which are the instability force responsible for the formation of internal seiche in many closed basins. Therefore, the gravity current reflects at end wall of the tank, and consequently, transfer energy for the generation of the long internal seiche. The energy transferred is proportional to the gravity current speed. In spite of the fact that we are interested just on the gravity current velocity, there are many other consequences and analysis for gravity currents. For a theoretical understanding of gravity currents, we recommend Simpson (1999).

2.6.3 Stratifying agent

Another important aspect of internal wave experiments is related to the stratifying agent. As aforementioned, one of the most common cases of stratification in lentic water bodies is caused by temperature differences, phenomenon known as thermal-stratification. However, in laboratory experiments it is difficult to control the heat transfer and provide a good analysis of thermal stratification. Thus, many

laboratory studies conduct salinity stratification experiments to compare and analyze thermal stratification environments, considering that the density difference is the most relevant property to analyze stratified flows. However, even though the same density difference can be achieved using salinity and thermal stratifying agents, the stratified analysis can present different results due to physical and chemical properties, which can affect the stratified flow and mixing. As Jackson and Rehmann (2014) stated out, the mixing caused by internal waves can be affected since the differential diffusion of temperature and salinity across a sheared density interface are different. In addition, Hebert and Ruddick (2003) shown that dyes used frequently in experimental analysis of stratified flows can affect the evolution of internal wave breaking since the dye can affect the water molecular diffusivity. However, according to Jackson and Rehmann (2014), the difference of molecular diffusivity is not so important compared to stratification in lakes and reservoirs. Thus, for internal wave evolution, the buoyancy term is much more significant than the water molecular diffusivity.

2.7 Internal wave: A historic view

2.7.1 Historical review

The theory of internal waves is derived from Stokes (1847) that described the case of two fluids with different densities, a simple two layer system. Internal waves were just noticed in field observations when the investigations of vertical distribution of temperature became common. Thus, the first publication about field observations about internal seiches in heterogeneous lakes was published by Thoulet (1894 apud MORTIMER, 1952). Although he noticed an oscillation with higher amplitude in just some isotherms, he did not explain these oscillations. Watson (1903) also observed these oscillations in a field campaign in Lake Loch Ness. Watson (1903) gave the first correct interpretation of internal waves, concluding that this temperature oscillation was caused by a uninodal baroclinc internal wave in Lake Loch Ness. Motivated by his earlier observations, Watson (1904) developed the first equation to determine the internal wave period, a hydrostatic solution for a rectangular basin, that is known as Watson's equation. He observed that the periods of these oscillations found fair agreement between the observed and calculated periods. In those early years, Wedderburn and collaborators[4] provided guidelines to spread the knowledge about internal seiches in stratified basins, that he denominated internal seiches as "temperature seiches". Although Wedderburn have notable improvements in theory and observations of internal seiches in closed basins, many limnologists disbelieved that internal waves could be important or even exist within thermal stratified lakes. The phenomenon was doubted until 1952, when finally Mortimer (1952) demonstrated their universality and importance in details. He investigated the formation of large internal seiches generated by wind forcing in Lake Windermere analyzing a long time series of measurements with moored thermistor chains. Under the isotherms analysis, Mortimer (1952) observed a V1H1 baroclinic wave of periods of 18h to 19h that was well represented by the Watson's formula (maximum error of 5%). He concluded that the main effect of the wind action in stratified basins is to generate internal seiches. In association with M. S. Longuet-Higgins, Mortimer (1952) developed a hydrostatic three-layer model for a rectangular basin of a constant length and depth. Although the three-layer model was useful to describe the evolution of internal waves in some situations, high vertical modes were not often reported in lentic water bodies until the 19th century. Heaps (1961) identified other modes of oscillation in the lower depths of the lake below the pycnocline. However, as Münnich, Wüest and Imboden (1992) reported, the observation was rare and uncertain. Mortimer (1955) identified the formation of Kelvin and Poicaré waves in large closed basins where the Earth's rotation becomes important. Kelvin

[4] Wedderburn and Williams (1911), Wedderburn (1912), Wedderburn and Young (1915)

waves also were identified in other lakes, such as Lake Ontario (CSANADY; SCOTT, 1974), and Lake Onega (BELETSKY; FILATOV; IBRAEV, 1994). Thorpe (1971) was the first limnologist to detect internal surges, asymmetrical nonlinear wave components, in Lake Loch Ness. He observed that energy is fast transferred within the internal wave spectrum from the internal seiches to a progressive nonlinear internal wave. Hunkins and Fliegel (1973) demonstrated that the non stationary solution of Korteweg-de Vries equation provides good results compared to internal surges observed in Seneca Lake, results that did not match with the linear theory. Hunkins and Fliegel (1973) identified many internal surges in Seneca Lake during summer and fall when the lake was stratified. Similar important observations of internal surges in other lakes were provided by Farmer (1978), Mortimer and Horn (1982), and Boegman et al. (2003).

Nowadays, most of internal waves research use spectral analysis to help identifying internal waves in closed basins. The spectral analysis can provide a real view of oscillations, avoiding a misinterpretation of temperature-time series. Although the first published work on the FFT algorithm was formulated by Cooley and Tukey (1965), the first paper in the context of internal waves was written by Phillips (1971) just few years later. Mortimer and Horn (1982) used the Fourier transform to analyze the temperature fluctuation at 2 different depths, 14 m and 30 m, in Lake of Zurich. To identify the internal surges, they confronted the spectrum with the first 5 internal modes obtained using the modified Defant's two layer model. Lemmin (1987) used the Fourier transform to analyze the isotherm-depth fluctuation. He stated that the FFT technique was used to determine the number of standing wave modes, the depth variation of each mode, and the energy distribution. At earlier times, all identification of internal waves were based purely by spatial pattern analysis and internal waves modelling. The second vertical mode in lakes and impoundments has been largely observed when spectral analysis started to be used in internal waves investigation. Lemmin (1987) detected the second vertical mode through spectral analysis and a 3-layers model based in the model developed by Mortimer (1952). He concluded that the second vertical mode can also exist when the first vertical mode is the dominant dynamic feature and when the metalimnion is not thicker than the epilimnion and hypolimnion layers. However, he observed that despite the second vertical mode is not unlikely to occur, the detection of this high vertical mode is a harder task.

Wavelet transform has become intensively used since its inception in the 1980s. However, this technique in the context of internal waves investigation in lentic water bodies has not been reported until the end of the 20th century. One of the first publication was provided by Stevens et al. (1996), which studied the wind action effect in the formation of internal waves in a long narrow stratified lake using the wavelet spectral analysis. The study concluded that long internal seiches decay at a rate higher than observed by a simple internal dissipation, the same behaviour was observed by Imberger (1994). Antenucci, Imberger and Saggio (2000) used continuous wavelet transform to investigate the formation and evolution of Kelvin and Poincaré waves in the large Lake Kinneret, located in Israel. Bernhardt and Kirillin (2013) studied the formation of internal seiches during summer stratification in 2010 in the temperate Lake Arendsee, a small lake located in Germany. Bernhardt and Kirillin (2013) used a model based on a three-layer density stratification model and the wavelet analysis on 6 month time series of isotherms and wind speeds to identify internal seiches, similar work done by Guyennon et al. (2014), which applied wavelet transform to temperature and wind data time series to identify internal waves in Lake Como, Italy. Nowadays, internal wave researchers have used use wavelet transform to identify internal waves applying the spectral wavelet analysis in synthetic-aperture radar (SAR) images. Although this technique has been explored in ocean, there are no evidences that this technique can be used to identify internal waves in closed basins, since its amplitude in closed basins are not as higher as in the ocean.

2.7.2 State of the art

Nowadays, many researchers are investigating the physical, chemical, and biological effects of internal seiches in lakes and reservoirs. Recent research has addressed the importance of the mixing caused by internal waves. Bernhardt and Kirillin (2013) focused in the impact on mixing caused by internal waves. They identify the presence of long internal seiches, affected by earth's rotation, in the small, 3 km long, ellipse-shaped temperate Lake Arendsee, located in Germany. They concluded that internal seiches may have important ecological implications, driving nutrients from the littoral zone to the thermocline and triggering biological production in the metalimnion. Bogucki and Redekopp (1999) explored the sediment resuspension in benthic boundary layer caused by internal waves. They presented evidence that benthic stimulation leading to episodes of re-suspension occurs mainly with the appearance of energetic long internal waves. Internal waves create complex unsteady force that presses the bottom boundary layer and, as a result, play a important role in triggering significant resuspension events which occurs intermittently in time and space. In another study, Bogucki and Redekopp (2008) presented evidences that the second vertical mode plays also an important role in the sediment resuspension. Cuypers et al. (2011) studied the impact of internal waves on the spatial distribution of a type of cyanobacteria that can produce microcystins, a dangerous hepatoxin that threatens human and animal health. They concluded that internal seiches have the major impact on the vertical and horizontal distribution of this bacteria in an alpine lake. In addition, they discovered that internal waves can also influence the growth of this species by a direct impact on light availability. Other researches also demonstrated the influence of internal seiches on the spatial distribution of microalgae in the epilimnetic layer of basins (GAEDKE; SCHIMMELE, 1991) and impoundments (MARCE et al., 2007). Although since 1900s internal waves in large lentic water bodies have been explored extensively by many researchers, the influence of these waves in small and dendritic reservoirs is poorly explored. According to Downing et al. (2006), the internal motions of small lentic water bodies are poorly studied compared with large lakes. One of the smallest lakes where internal wave has been investigated is Lake Frain, Michigan. LaZerte (1980) investigated internal seiches in Lake Frain, which has a maximum depth of 9.1 m and surface area of 0.07 km^2. They observed excitation of second, third, and six vertical mode, concluding that fundamental and higher vertical modes are responsible by the major hydrodynamics processes within the water body. Therefore, internal seiches strongly influence water quality, altering the physical, chemical, and biological processes in closed water basins.

3 Methods

"[...] All scientific ideas were born
in a dramatic conflict between reality
and our attempts to understand it."
A. Einstein

In this research we analyze the formation, evolution and degeneration of internal seiches in reservoirs and lakes. To identify internal wave pattern and its periodicity we used spectral analysis and modeling. For a better analysis, we studied internal seiches in a small, dendritic reservoir located in Brazil – Vossoraca Reservoir and in Harp Lake, a small non dendritic lake located in north-central Labrador, Canada. We compared some results with laboratory experiments conducted in a range of different density differences and pycnocline depth. We analyzed parameters and stratification structures obtained from Vossoroca Reservoir, Harp Lake, and experiments, highlighting the main parameters to identify internal waves and their patterns in closed basins.

3.1 Site description & data collection

3.1.1 Vossoroca reservoir

Vossoroca Reservoir (25° 49' 31" S, 49° 3' 60" W) is a small and dendritic-shaped reservoir located 30 km from Curitiba, capital of Paraná state in southern Brazil. The reservoir presents a shoreline development index of 6.2 and has two long narrow arms 300 m wide. The longest arm is oriented in a northwest-southeast direction and has a length of 3.25 km. The second arm is oriented northeast-southwest direction and has a length of 2.72 km. The reservoir, shown in Figure 15, has a volume of 35.7 10^6 m^3, a maximum depth of 17 m, and an average depth of approximately 6 m. The wind action over the reservoir during the period of observations was dominated essentially by northeasterly winds with a average magnitude lower than 3.6 m/s, Figure 15(b). The strongest wind events (5.5 to 7.3 m/s) were identified in northeast-southwest direction just 2% of the whole period, lasting only a few minutes. The wind action in Vossoroca reservoir is characterized by diurnal periods. As stated by Münnich, Wüest and Imboden (1992), diurnal periods of wind are important for wind forced oscillations and higher vertical modes generation. The vertical temperature structure of Vossoroca Reservoir corresponds to a holomictic lake, presenting uniform temperature from top to bottom during winters, which allows the reservoir waters to completely mix. Mixing periods start after April, but the system is completely unstratified at the end of May. Around September, a gentle stratification again develops and, consequently, the reservoir is stratified for nine months. During summer, the temperature difference between the hypolimnion and epilimnion is approximately 10 °C. The relatively simple bathymetry of Vossoroca Reservoir and the constant wind direction lend itself well to standing internal waves activity. As a response to the breeze forcing against the stratification structure, an energetic fundamental internal seiche has been previously identified in Vossoroca reservoir during late spring by Bueno and Bleninger (2017). Now we extend the analysis to higher vertical modes and higher frequency waves. We also use different techniques, including wavelet transform and multi-layer models to identify the formation and structure of internal waves, including the presence of higher vertical modes. For Vossoroca reservoir, we also used a three-dimensional thermal stratification numerical model implemented in Delft3D-FLOW to analyze the internal wave patterns.

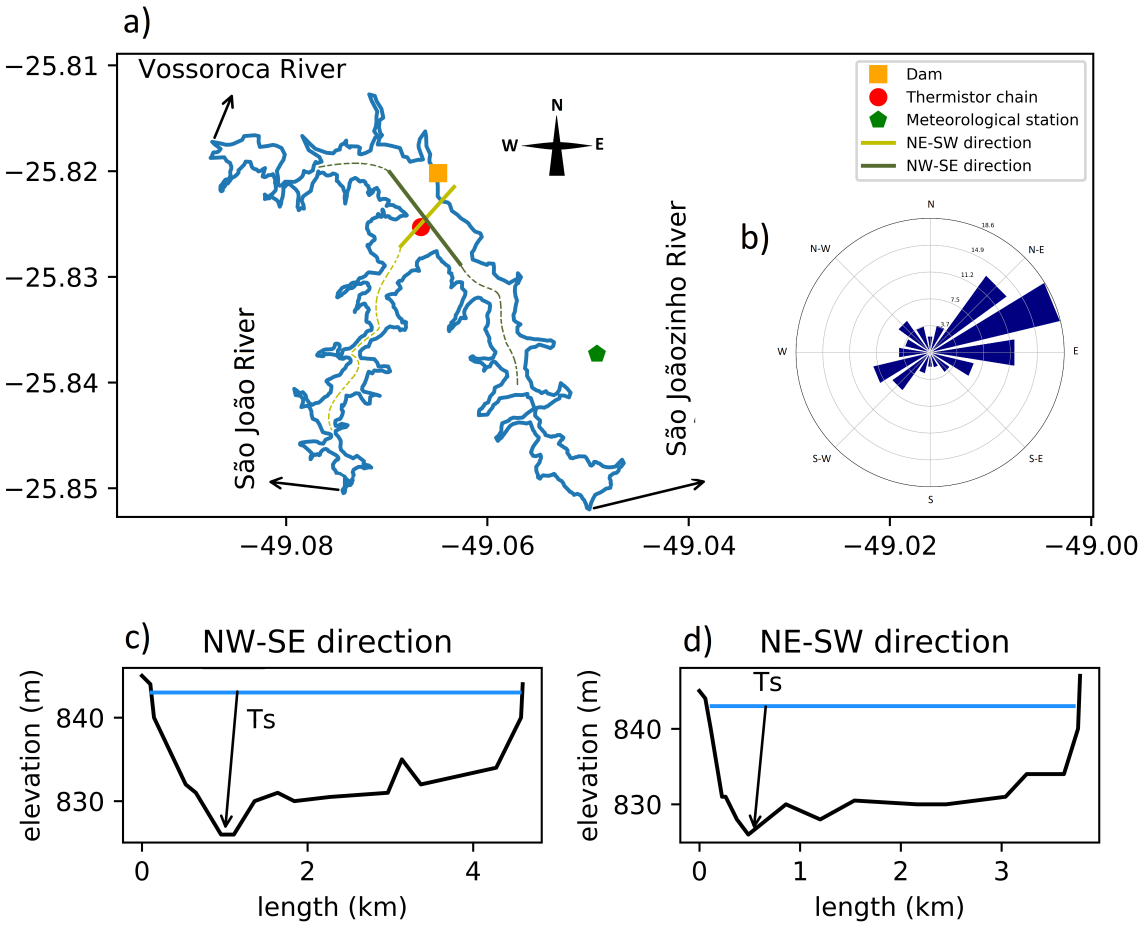

Figure 15 – (a) Map of Vossoroca reservoir, indicating the location of the thermistor chain, meteorological station, elevation water station, and dam. (b) Wind rose showing wind speed and direction from data between 20 May 2012 and 1 February 2013. (c) Bathymetric profile of the reservoir crossing the northwest – southeast direction and (d) the northeast – southwest direction, indicating the thermistor chain location Ts.

Water temperature, water level, solar radiation, wind speed and direction were recorded during 2012 and 2013. Wind direction and velocity were measured by Young wind monitor with accuracy of ± 2° and ± 0.3 m/s, respectively. Solar radiation was measured by a Campbell Scientific CMP3-L Pyranometer with accuracy of ± 1 W/m^2. The meteorological station was deployed at the reservoir shore, 2.4 km from the dam and 10 m above the reservoir lake on the meteorology platform, as shown in Figure 15. The meteorological station recorded solar radiation, wind speed and direction at 30-min intervals.

A thermistor chain was deployed at the north portion of the reservoir 440 m from the dam, at the deepest location (Figure 15). According to Mannich (2013), the chain position was chosen based on the location of highest temperature gradient during different seasons of the year. The chain was equipped with seven thermistor LM 35 with accuracy of ± 0.1 °C (after the final calibration) and range of 10 to 55 °C. The thermistors were placed at water depths of 1 m, 3 m, 5 m, 7 m, 9 m, and 11 m. The seventh sensor was fixed 1 m above the bottom of the reservoir. The thermistors were adjusted to record temperature every 10-min.

3.1.2 Harp Lake

We compare the results obtained from Vossoroca reservoir with results obtained from Harp Lake, which has been monitored by personnel of the Ontario Ministry of the Environment's Dorset Environmental Science Centre (DESC) (YAN; STRUS, 1980; YAN; PAWSON, 1997; YOUNG; LOEW; YAN, 2009). Harp Lake (45° 22' 45" N, 79° 08' 08" W) is a small square-shaped lake located in north-central Labrador, Canada. The lake, shown in Figure 16, is a oligotrophic lake, presenting low primary production, as a result of low nutrient content. The lake has a volume of 95.07 10^5 m^3, a maximum depth of 37.5 m, and an average depth of approximately 13.30 m. The Harp Lake presents a shoreline development index of 1.7. The northwest-southeast and northeast-southwest length are approximately 1100 m (Figure 16(c)) and 1180 m (Figure 16(d)), respectively. The lake has five inlet streams (HP3, HP3A, HP4, HP5, HP6A) and one outlet (HPFO), where each of the six streams and the lake's outlet is monitored for discharge flow rates and sampled fortnightly for water chemistry. The wind does not present a dominant direction as observed in Vossoroca reservoir. The wind has an average magnitude of 3.0 m/s, Figure 16(b). The strong wind events were identified in southwest direction with magnitude up to 5.4 m/s. The vertical temperature structure of Harp Lake corresponds to a dimictic lake, a holomictic lake that is covered by ice during the winter. Stratified periods start after April, but the system is most stratified in July, when the temperature difference between the hypolimnion and epilimnion is approximately 20 °C. Around September, a thin layer of ice begin to form above the water surface. Around February, the ice layer thickness reaches approximately 40 cm. Some recent research have studied the formation of internal waves in ice-covered lakes (BOUFFARD et al., 2016). As stated by Bouffard and Boegman (2012), observations of internal waves activity in ice–covered lakes is not linked directly to wind forcing. Basically, the generation of internal waves is due to oscillations of ice cover, resulting from changes in atmospheric pressure and wind forcing. As our goals in this study is to compare results between Vossoroca Reservoir and Harp Lake, the consideration of internal waves in ice-covered lakes is beyond the scope of this study. Thus, we did not investigate the internal wave activity in winter period since formed in ice-covered period may be excited by different sources, and not necessarily due to the wind action at the water surface.

Water temperature, solar radiation, wind speed and direction were recorded between 2010 and 2015. The wind information was measured by RM Young wind monitor model 05103 with wind direction and speed accuracy of ± 3° and ± 0.3 m/s, respectively. The solar radiation was measured by Kipp & Zonen Solar Radiation CMP6 Sensors with accuracy of 5 to 20 $\mu V/W/m^2$. The meteorological station was located 600 m from the thermistor chain (floater) and 10 m above the lake (Figure 16). The meteorological station recorded solar radiation, wind speed and direction at 1 hour intervals.

One thermistor chain was deployed at the center of the lake, at the deepest region of the lake (Figure 16). The chain was equipped with 28 thermistors (Campbell Scientific custom thermistor string of model 109 temperature probe) with accuracy of ± 0.1 °C. The thermistors were placed every 1 m, from 10 cm below the water surface. Differently from Vossoroca reservoir, all thermistor were fixed in the floater. Since the variation of surface water at Harp lake is small and the depth in the thermistor chain region reach at least 37 m, the last sensor has never reached the reservoir bottom. In Figure 17, we present a schematic configuration of the thermistor chain deployed in (a) Harp Lake and (b) Vossoroca Reservoir. The thermistors were adjusted to have sampling frequency of 1 hour.

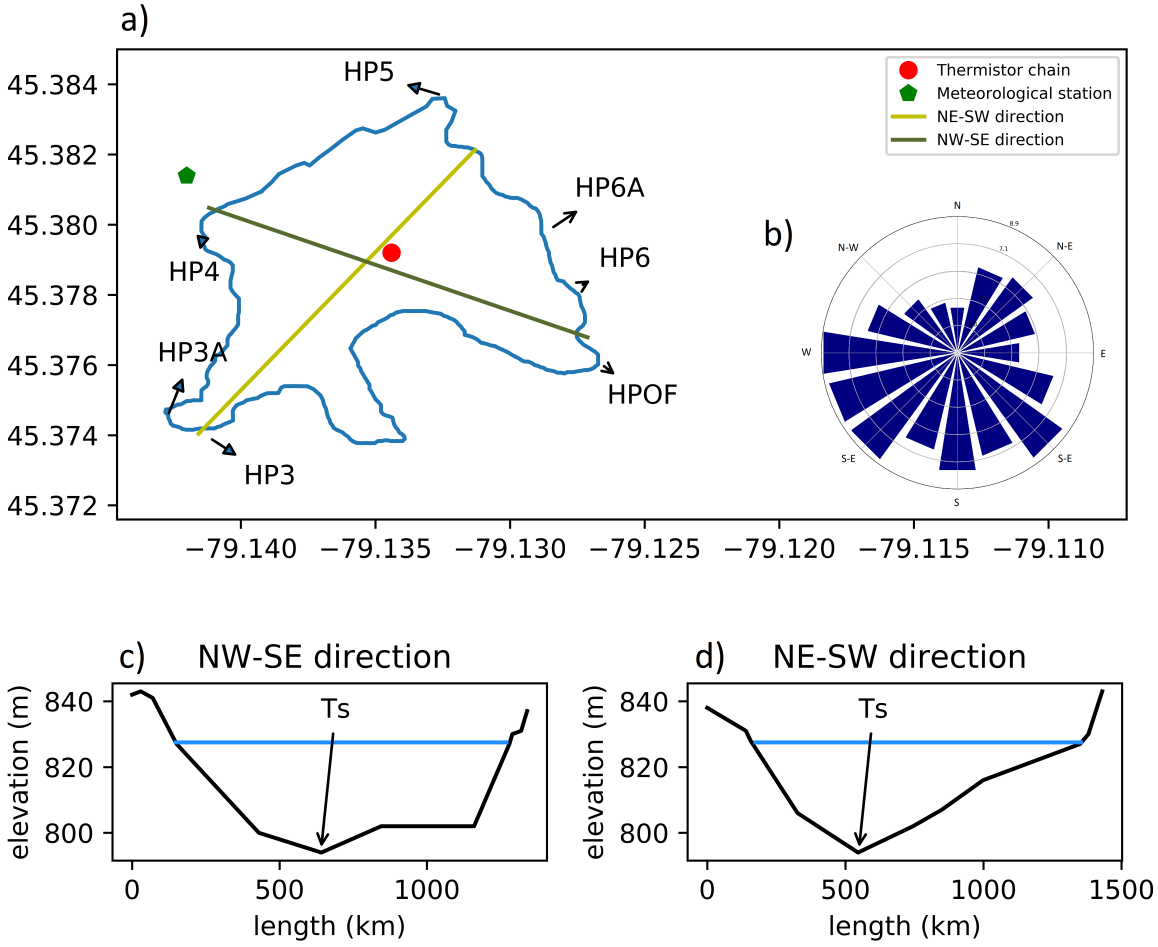

Figure 16 – (a) Map of Harp Lake, indicating the location of the thermistor chain, meteorological station, and inlet and outlet streams. (b) Wind rose showing wind speed and direction from data between 14 July 2010 and 19 October 2015. (c) Bathymetric profile of the lake crossing the northwest – southeast direction and (d) the northeast – southwest direction, indicating the thermistor chain location Ts.

3.2 Data treatment & Characteristic parameters

We calculated density profiles based on the last version of the equation of state proposed by Commission et al. (2015), presented in details in appendix A. The seasonal density stratification is essentially due to temperature. Thus, we neglected the contribution of salinity to density since the temperature contribution is much higher in fresh water bodies. Moreover, we also ignored the effect of pressure on water density since we considered the flow as incompressible. These hypotheses have been used by many internal waves researches conducted in closed basins of fresh water (e.g. Mortimer (1979)). Even though the equation of state is essentially formulated for ocean water, the formulation of pure water developed by Wagner and Pruß (2002) is valid for fresh water basins. Although the equation of state considers just the effect of pressure, salinity, and temperature, as Wüest and Lorke (2003) stated, water density is not determined only by the variables of the equation of state, but also by dissolved particles. However, as stated by Ollinger (1999 apud HUTTER; WANG; CHUBARENKO, 2011), dissolved organic matter found on fresh lakes may influence water density only when temperatures are near 4 °C.

To find the pycnocline depth, we used the approach proposed by Read et al. (2011), equation 2.4.

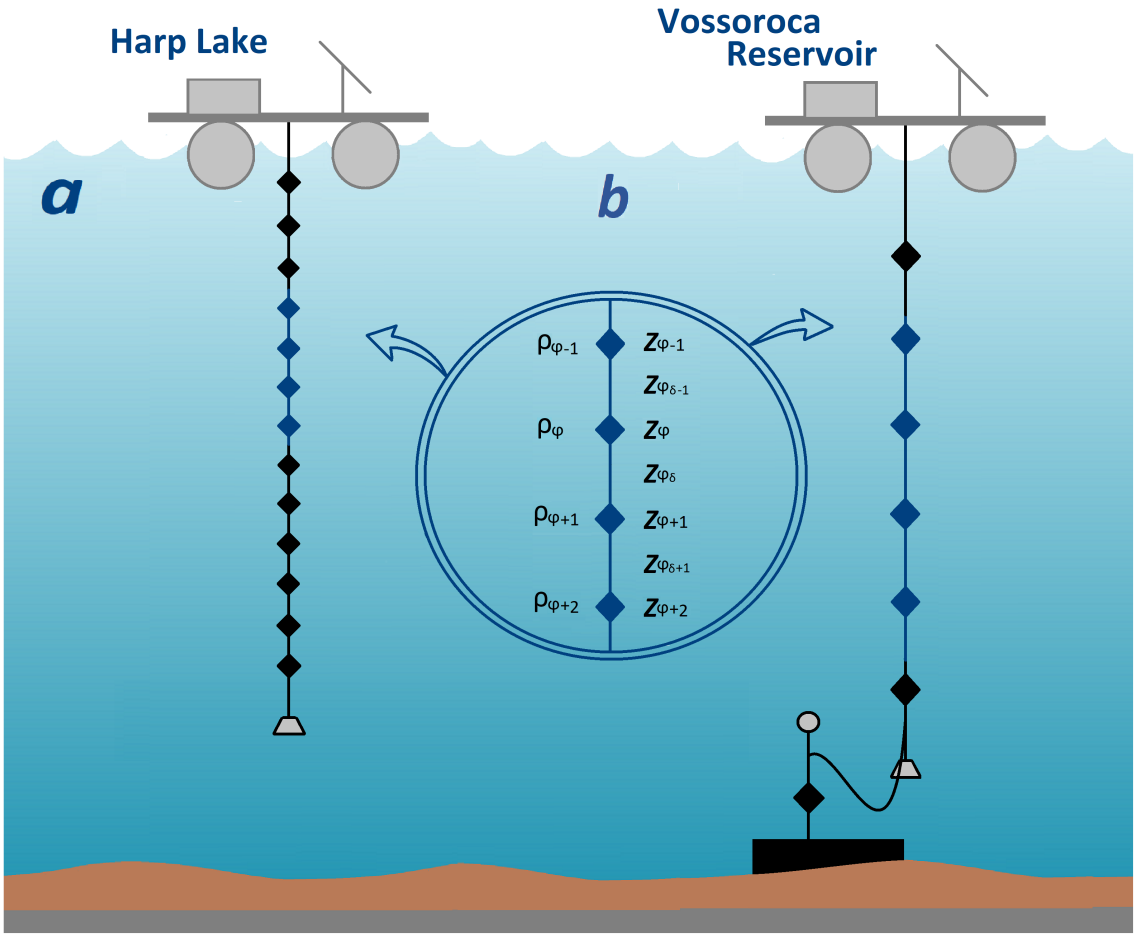

Figure 17 – Schematic configuration of the thermistor chain deployed in (a) Harp Lake and (b) Vossoroca Reservoir and the schematic algorithm used to determine the pycnocline depth. The sketch of Harp Lake and Vossoroca reservoir present different scale unit in this figure. We also simplified the number of sensor in Harp Lake.

The technique used for each basin is shown in Figure 17. We also compared pycnocline depth obtained in Vossoroca reservoir by the Read et al. (2011) algorithm to CTD profiles (YSI CastAway CTD), which were obtained during sporadic campaigns, once or twice a month from February 2012 to February 2013. The YSI CastAway CTD has a sampling rate and sensor response of 5 Hz with 1 m/s and accuracy of ± 0.05 °C. It uses a six electrode flow-through conductivity cell with zero external field coupled with a rapid response thermistor to attain high measurement accuracies. We calculated the metalimnion thickness also using an approach proposed by Read et al. (2011). The technique estimates the metalimnion thickness based on derivatives of discrete density measurements. We calculated the metalimnion thickness by subtracting equation 2.6 from equations 2.5 and considering a density gradient threshold $\delta_{min} = 0.1$.

To obtain different isotherms and other important parameters, we firstly interpolated temperature profiles linearly in a grid of 10 cm. According to Lemmin (1987), the linear interpolation does not disrupt any analysis of the internal wave pattern. The algorithm implemented to obtain isotherms finds the region of the required temperature and, subsequently, defines the depth by doing a linear interpolation between the grid values. We just analyzed isotherms that did not reach the surface water or the basin bottom, since, after that, this interface no longer exists and, physically, cannot represent an internal wave propagation. Although Bryson and Ragotzkie (1960) have demonstrated, using a series of

bathythermograph casts at one location near the lake shore, that this phenomenon could be related to breaking of internal waves, our observation points are distant from the basin shore to present internal wave breaking, as shown in Figures 15 and 16. Certainly, as stated by Boegman, Ivey and Imberger (2005a), an irregular bathymetry (slopes, shelves, and ridges) excites internal wave breaking. However, the relatively simple bathymetry of Vossoroca Reservoir and Harp Lake makes this phenomenon essentially due to diurnal temperature oscillation caused by solar radiation. Thus, for that reason, we did not include in our analysis isotherms that reached the bottom or surface boundaries.

From the density profiles we calculated the Brunt–Väisälä frequency, given in equation 2.7. The wind stress at the water surface, σ_w, was calculated using the wind-drag formula (equation 2.10). The surface drag coefficient C_D, which depends on the wind speed and the surface wave development state, was obtained through equation 2.11 and 2.12. The wind effect was characterized through the square of the vertical shear of the horizontal wind velocity at the water surface, also called wind instability frequency, S, given in equation 2.8. To measure the importance of heat convection and mechanical turbulence, we calculated the ratio between the Brunt–Väisälä frequency and the wind instability, ratio known as densimetric Richardson number, Ri_w. As demonstrated by Spigel and Imberger (1980), the Ri_w is one of the most powerful parameter to identify the formation of long internal waves in lentic water bodies. We used equation 2.13 to obtain the densimetric Richardson number along the water column. In addition, we also look at Ri_w in the thermocline region to analyze the formation of internal fundamental seiche (V1H1), procedure explained in section 2.3. We compared the Ri_w at the thermocline to the aspect ratio between the reservoir length of the intersection between the boundaries wall and the pycnocline shore L_p and the epilimnion thickness h_e to analyze the formation of internal seiches (Figure 10). The characteristic temperature, density, Brunt–Väisälä frequency, and Richardson number for 19 October 2012 at midday in Vossoroca Reservoir are presented in Figure 18.

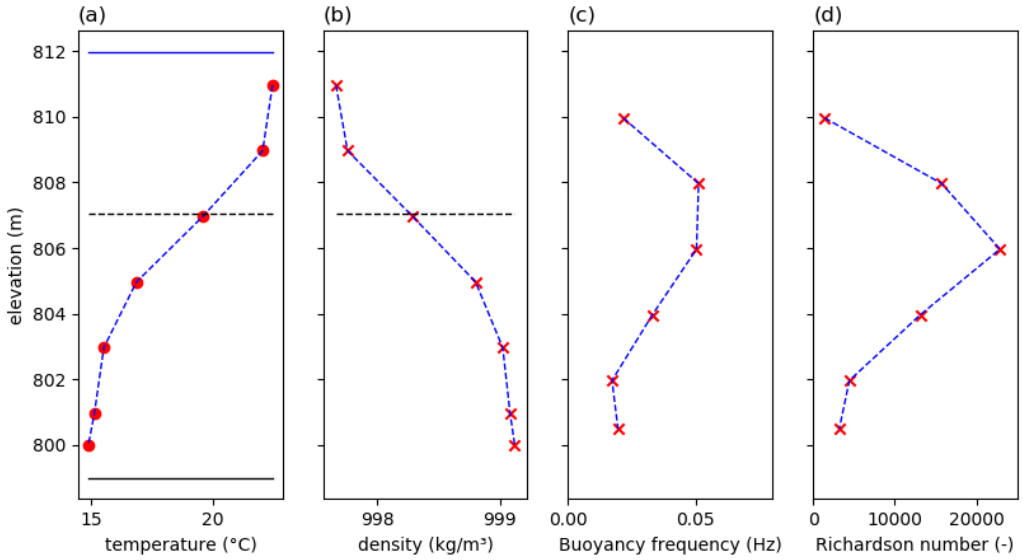

Figure 18 – Characteristic profiles of (a) temperature, (b) density (c) Brunt–Väisälä frequency, and (d) Richardson obtained from Vossoroca Reservoir in 19 October 2012 at midday. In figure (a) the blue and black horizontal lines indicate the surface and the bottom of the reservoir, respectively. The horizontal dashed lines indicate the thermocline/pycnocline location. Red dots on the temperature profile shows the location of the temperature sensors.

To describe the importance of the shear velocity as a source of turbulent kinetic energy available

for mixing during an internal wave event, we computed the Wedderburn number, W. As stated by Boegman (2009), the inverse Wedderburn number and the ratio between the pycnocline and the total depth are important parameters to describe the degeneration of long internal waves. Thus, we computed W using equation 2.15. Therefore, we compared $1/W$ to the ratio of pycnocline and the total depth (h_e/H) to classify the degeneration of long internal waves. To establish the criteria for each regime, we obtained the relationship between the frequency-scales (equations 2.19, 2.23, 2.25, and 2.26) and the internal wave frequency f_i, obtained using the analytical model described below in section 3.4. Thus, we obtained a diagram similar to Figure 12, and as a result we could identify when internal seiches were more susceptible to be damped by viscosity or to evolve into a train of high frequency waves.

3.3 Spectral analysis

To highlight the periodic evolution in meteorological and temperature data, we used two spectral analysis for identification of internal waves. The spectral analysis of isotherms were used to determine the number of standing wave modes, the depth variation of each mode, its energy distribution, and the presence of higher vertical modes. Although spectral analysis of isotherms gives a strong sign for baroclinic motion, it does not prove their existence. Thus, we perform spectral analysis for meteorological data to remove other factors that could influence the isotherm fluctuations. The spectral analysis of solar radiation may show influence of solar energy on diurnal temperature variations. In addition, wind spectra can present evidences of baroclinic motions on inertial and diurnal periods. As stated by Bernhardt and Kirillin (2013), wind oscillations at diurnal and inertial periods and their resonance events can strongly increase the intensity of the baroclinic motions, exciting often higher vertical internal wave modes and forced oscillations. A windowed Fourier transform, also called as short-time Fourier transform (STFT), with segment overlapped was used to identify high energy peaks, which could be correlated with internal waves action. Moreover, in some cases we also analyzed the ordinary coherence and phase between two or more isotherms to measure the vertical internal wave structure. In addition, we also used the wavelet transform to have a better representation of high- and low- frequency components since, according to Niu (2017), the Wavelet transform is not dependant on window function and its size. Moreover, Wavelet analysis improve the frequency-time resolution due to the time-frequency localization method.

The spectral analysis was applied to the time series of wind speed, solar radiation and the depth of different isotherms. The choice of isotherms series rather than the temperature variation at fixed depths was made because it better represents the physics of the wave motion. For the model results, we also used more horizontal points to improve the description of the internal wave pattern. Spectral densities were obtained for two different periods, from June 2012 to February 2013 and from January to March 2014. These spectral analysis were compared with the internal wave characteristic, obtained by lab experiments, and analytical and numerical models used in this work.

Power spectral densities were applied to overlapping data segments using the Hamming window function. Then, firstly, we obtained the traditional FFT, which provided time-averaged pictures of the frequency distribution. We used four different window sizes (5 days, 1 day, 12 hours, and 1 hour) to analyze the spectrum. This technique was used to improve the confidence interval for the spectral power at short time periods. The overlap percentage was defined according to the function chosen. As recommended by Heinzel, Rüdiger and Schilling (2002), for Hamming, we used 50%. In addition, to increase spectral resolution, we also zero-padded signals to the next higher power of two, except when the next power of two was at least 20% greater than the original signal length. In this case, we truncated the signal to the last power of two for STFT calculation since the zero-padding technique can affect significantly the spectral energy. Finally, through the ratio of sampling frequency and the mean-square power spectrum, which

is obtained through the Fourier transform of the auto-covariance function, the power spectral density (PSD) was obtained using equation 2.32.

We obtained the coherence of isotherms and meteorological data to identify energetic peaks in the temperature spectrum that were not correlated with periodic oscillations in solar radiation. We also used the coherence of wind speed and isotherms to identify resonance between wind-forced oscillations and free internal seiches. Therefore, we compute the coherence between two signals using the mean-square power spectrum of these signals and the cross power spectrum (equation 2.34). To analyze the presence of internal waves in the Delft3D-FLOW model, we also applied coherence analysis between model and field observation isotherms. This technique was also used to identify the formation of non-free internal waves, internal seiches driven by the wind action. Finally, we computed the phase shift in frequency domain between two isotherms (equation 2.35). Since density interfaces are out of phase in comparison with each other in baroclinic motion, we use the phase shift to identify higher vertical modes. To identify internal waves in the Delft3D-FLOW we also calculated the phase shift in frequency domain between isotherm in different basin region. Many studies have observed the phase shift between isotherms using direct time-series comparison. For example, Stocker et al. (1987) observed hourly averaged isotherms fluctuations in different locations of Lake Lugano (Switzerland and Italy) to confirm the presence of higher horizontal internal seiche modes. Pannard et al. (2011) observed through the deviation from the mean of different isotherms the presence of higher vertical modes in Lake Bromont (Canada). Even though we could detect the phase shift between two time series by a direct comparison between then, for long signals the phase obtained for each frequency component helped to overcome the difficulty to identify these angular deviation. This spectral analysis also avoids wrong interpretation of variations in other frequencies that could not be correlated to internal wave actions.

Although we used four different window sizes to improve the confidence level of the STFT, the spectrum has energy peaks in different scales. As our data is non stationary in frequency content and the frequency peaks are not predetermined, we used a method of time-frequency localization to improve the temporal resolution. Therefore, to minimize this problem, we applied the wavelet transform to the data. The wavelet transform provides a two-dimensional contour graph of the three-dimensional surface, in which the colored surface represents the wavelet energy. Since this color surface graph just can be analyzed individually each signal, we just applied the wavelet technique in the isotherms data, in which are the most important data to internal waves identification. As Torrence and Compo (1998) stated out, this spectral analysis solves the variations of frequency content with time, improving the temporal resolution.

In this work, we used only the continuous wavelet transform (CWT). That does not mean that the time series used was continuous. The CWT, just like a discrete wavelet transform, can be applied in a discrete time series. This analysis is sometimes called as discrete time continuous wavelet transform (DT-CWT). The main difference between DT-CWT and discrete wavelet transform (DWT) in the wavelet analysis context is related with the number of samples skipped in the wavelet analysis, during the convolution calculation and when the wavelet function is dilated. Although a continuous analysis requires more computation and computer memory, DT-CWT is often easier to interpret, making all information more visible. Despite of the fact that DT-CWT could be calculated using equation 2.36, we obtained the wavelet transform in Fourier space using the concepts of the discrete Fourier transform (DFT). This technique has been described in details by Torrence and Compo (1998). He pointed out that the calculation in Fourier space is considerably faster than in real space. The computation is not based on a direct convolution, but on a convolution by means of multiplication in Fourier space. We explored a faster way to compute and reuse the fast Fourier transform algorithm, used to compute the STFT. So using equation 2.29 and applying the convolution theorem, the wavelet transform was written as the

inverse Fourier transform of the product:

$$W_f(\upsilon, s) = \sum_{k=0}^{N-1} \hat{f}_t \hat{\psi}(s\omega_t) e^{i\omega_t \upsilon \Delta t}, \tag{3.1}$$

in which $\hat{\psi}(s\omega_t)$ is the Fourier transform of ψ, and ω_t is the angular frequency, defined as

$$\omega_t = \begin{cases} +\dfrac{2\pi k}{N\Delta t} & k \leq N/2, \\ -\dfrac{2\pi k}{N\Delta t} & k > N/2. \end{cases}$$

So using equation 3.1 and the fast Fourier algorithm, we obtained the CWT at all υ simultaneously. From the wavelet transform, we obtained the wavelet power spectrum as the square of the modulus of the wavelet transform, $|W_f(\upsilon, s)|^2$. However, as the inverse Fourier transform in equation 3.1 assumes the signal is cyclic, distortion could be identified on spectrum borders, and consequently spectral leakage could occur. To minimize the distortion problem, we padded zeros at the end of the signal, similar technique used for STFT.

To compare different wavelet power spectra, we normalized the wavelet power spectrum by a common normalization. Thus, we normalized the frequency scale s to have energy unit and applied the normalization parameter on equation 3.1. It shows that the expected value for the wavelet transform is given by $|W_f(\upsilon, s)|^2 = \sigma^2$ at all υ and s, in which σ is the variance. Therefore, wavelet power spectrum was normalized by $|W_f(\upsilon, s)|^2/\sigma^2$.

In this research, we use the Morlet basic wavelet function since, according to Stevens (1999), Morlet basis function has a simple waveform structure, the best form to internal waves analysis. The analytic Morlet wavelet consists of a plane wave modulated by a Gaussian function and is defined in the Fourier domain as

$$\hat{\psi}(s\omega_t) = \sqrt{2\pi} U(s\omega_t) e^{-(s\omega_t - k_\psi)^2/2}, \tag{3.2}$$

in which $U(s\omega_t)$ is the Heavyside step function and $k_\psi = 6$ is the wave-vector. According to Farge (1992), if we take $k_\psi = 6$ for $s\omega_t > 0$ and $\hat{\psi} = 0$ for $s\omega_t \ll 0$, we can ensure admissibility. In other words, we ensure that errors will be in the same order of typical computer round-off errors. Therefore, to ensure admissibility we use the Heavyside step function and make $k_\psi = 6$ when Heavyside step function gives zero.

The wavelet function does not change significantly the energy and the energy location, it can just change the time-frequency resolution. Thus, we also tested the derivative of a Gaussian wavelet function. The same feature appear in both plots, however, the derivative of a Gaussian wavelet function gives us sharper energy peaks in time direction and more elongated in the scale direction. The derivative of a Gaussian function improves the time localization, losing frequency resolution. On the other hand, Morlet function is really well localized in frequency, providing a good frequency resolution, but poorer time resolution. We did not used the global wavelet spectrum due to spectral distortion that can be caused at low frequencies, problem mentioned in section 2.4.2.

The spectra analysis of numerical and measured data were carried out in Python, using some pre-implemented functions to speed up the algorithm. To determine the internal seiche patterns, we performed spectral analysis for different isotherms representing different regions of the system. We plotted, together with the power spectral density, the predicted internal seiches periodicity for different vertical and horizontal modes obtained by analytical models used. We present in the next section (section 3.4) a detailed description of each model used in this research.

3.4 Modeling

We used in this work two analytical internal wave models and one three-dimensional numerical thermal stratification model. The first one, a non-hydrostatic linear internal wave model with free surface was based on the analytical model described by Buick (1997). The second one, a multi-layer hydrostatic linear model with free surface and shallow water assumption based on Mortimer (1952) three-layer model. For each model we also computed the wind fetch based on the geographic wind direction and the reservoir length. We also computed the deviation caused by Earth rotation for cases when $Bu > 1$. Therefore, we corrected the angular frequency based on technique for shallow water influenced by rotation proposed by Sutherland (2010). As mentioned before, if the wind stress is applied for sufficient time, the setup height at the lake end can increase and, consequently internal waves can develop. We also checked the model sensitivity. Since the model results are based on specific parameters, we varied slightly some parameter to see how the internal wave periods and structure reacts to such variation. This analysis has been recommend by Hutter, Wang and Chubarenko (2011). Therefore, we compared the wind stress and the direction of the wind to identify the direction and the predicted periodicity of internal seiches. We computed the mean internal seiche period averaging all the fetch vectors within 20 degree from the main wind direction, considering the pycnocline shore. We also used a three-dimensional thermal stratification model implemented in Delft3D-FLOW and developed by Polli et al. (2017). The model uses a finite-difference method in which simulates the hydrodynamic processes considering an incompressible fluid, under the shallow water and the Boussinesq assumptions. We used the three-dimensional numerical model to identify the internal wave patterns along the reservoir. Finally, we forced the three-dimensional thermal model with different winds to see how the body system would respond under different wind events, changing the direction and intensity.

3.4.1 Two-layer non-hydrostatic linear model

To improve the analytical two-layered linear model provided by Buick (1997), we consider the presence of the top free surface, considering that the rigid lid approximation is no longer valid to a system with free surface even for baroclinic mode. As Kodaira et al. (2016) stated, in laboratory experiments, the Boussinesq and the rigid lid approximation are often violated. In addition, we continue considering only gravity waves and neglecting the effect of surface tension since the surface tension just affect waves with small wavelength. The reference coordinate is placed at interface between the epilimnion and hypolimnion layer, where the x-axis is drawn horizontally, as shown in Figure 19(a).

The z-axis is drawn vertically and the positive branch points upward. The horizontally and vertical velocity of the upper and lower fluids along these axes are denoted by u_e, w_e and u_h, w_h, respectively. Assuming that the flow is irrotational and inviscid, the epilimnion layer velocity potential ϕ_e and the hypolimnion layer velocity potential ϕ_h that satisfy the mass-conservation equation can be expressed, respectively, as

$$\phi_e = (C_1 \cosh(k(z - h_e)) + C_2 \sinh(k(z - h_e))) \cos(kx) \sin(\omega t), \tag{3.3}$$

$$\phi_e = (C_3 \cosh(k(z + h_h)) + C_4 \sinh(k(z + h_h))) \cos(kx) \sin(\omega t), \tag{3.4}$$

in which C_1, C_2, C_3, C_4 are unknown constants, k is the wavenumber, and ω is the angular frequency.

Any small-amplitude wave can be well represented by a superposition of sinusoidal functions. The wave evolution may be described by tracking the individual progress of each sine wave. The advantage to represent disturbances as sine waves is that sinusoidal function may be expanded as Taylor series and each term is a solution for the Laplace equation (equations B.3 and B.4) without yielding any limitation

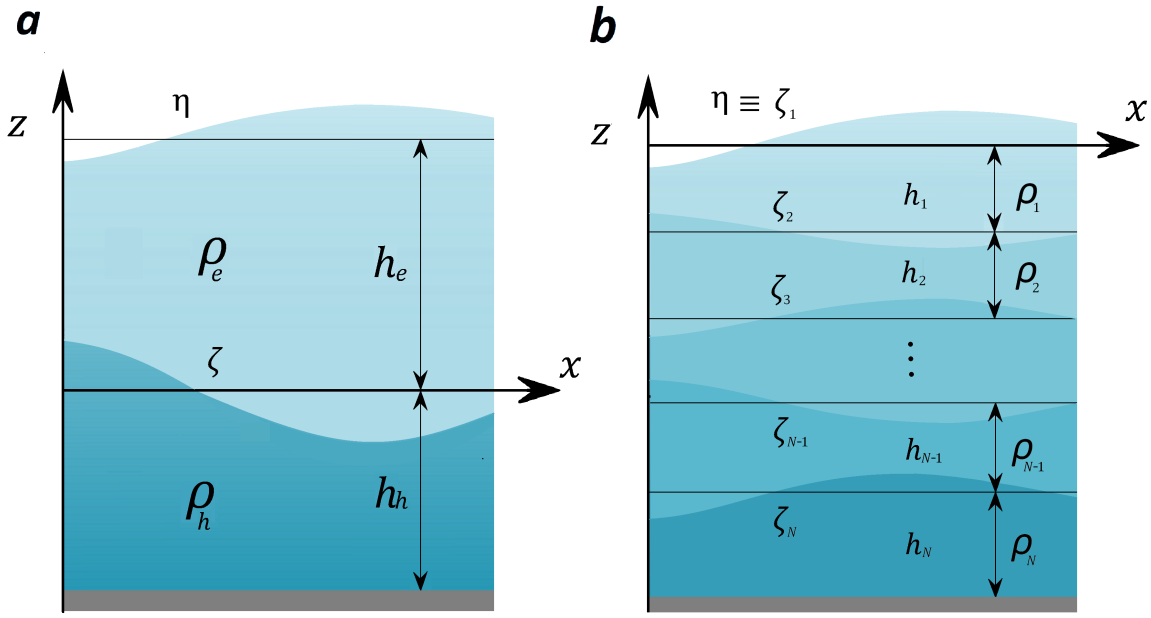

Figure 19 – Schematic view of a a) 2-layer system and b) N-layer system in a rectangular lake.

of the wave form. Thus, the displacements caused by surface and internal waves are given by a wave of sinusoidal shape, expressed in the forms:

$$\eta(x,t) = a\cos(kx)\cos(\omega t) \tag{3.5}$$

and

$$\zeta(x,t) = b\cos(kx)\cos(\omega t), \tag{3.6}$$

in which a and b are surface and internal waves amplitude, respectively. The complete solution to obtain the dispersion relation is presented in appendix B. Here we summarized the result, presenting just the final result for internal seiches. Thus, the velocity potentials (equations 3.3 and 3.4) and the interfaces disturbance (equations 3.5 and 3.6), satisfy the six linearized boundary conditions, three kinematic, two dynamic, and one rigid-bottom boundary condition. Substitution of equations 3.3 – 3.6 into the boundary conditions gives a biquadratic equation, which can be solved with an auxiliary variable $\omega^* = \omega^2$

$$\omega^4\left(\frac{\gamma\tanh(kh_e)\tanh(kh_h)+1}{k\tanh(kh_h)}\right) - \omega^2\left(\frac{g(\tanh(kh_e)+\tanh(kh_h))}{\tanh(kh_h)}\right) - (\gamma-1)g^2k\tanh(kh_e) = 0. \tag{3.7}$$

Thus, the dispersion relation becomes

$$\omega^2 = \frac{g}{2(\gamma T_e T_h + 1)}\left((T_e+T_h) \pm \sqrt{(T_e+T_h)^2 + 4T_hT_e(\gamma T_eT_h - 1)(\gamma-1)}\right), \tag{3.8}$$

in which h_e and h_h are the epilimnion and hypolimnion thickness, respectively. H is the total depth, $T_e = \tanh kh_e$, $T_h = \tanh kh_h$, and $\gamma = \rho_e/\rho_h$, where ρ_e and ρ_h are the epilimnion and the hypolimnion density, respectively. The ω^2 give us two real roots representing the wave direction. The minus sign in equation 3.8 represents the baroclinic mode, whilst barotropic is defined by the positive argument. From 3.8, the fundamental internal seiche period for first vertical mode and m horizontal mode is given by

$$T_{1,m} = \frac{2\pi}{\sqrt{\omega(m)}}. \tag{3.9}$$

For standing waves, the lakeshore adds a new boundary condition to the system. The wall boundary condition is similar to the rigid bottom boundary condition (equation B.9). However, in this case, the horizontal velocity must vanish. Thus, the wall boundary condition at the reservoir gives us the relationship between the wavenumber, $k(m)$, and the basin length of the intersection between the boundaries wall and the pycnocline shore with the wind direction, the wave propagation direction L_p. Thus, considering

$$\underset{\sim}{\nabla}\phi_i \cdot \underset{\sim}{\hat{n}}|_{x=L} = 0, \tag{3.10}$$

we have

$$k_m = \frac{m\pi}{L_p}, \tag{3.11}$$

where m is related with the internal wave horizontal mode (H), in which $m = 1$ is the fundamental horizontal mode, H1. L_p was obtained considering the mean wind direction and mean pycnocline depth. The result was interpolated considering the slope of the lake shore. For great slope, generally the L_p can be approximated by the length of the reservoir at the surface depth, $L_p \approx L$. When this approximation is applied for any lake, the internal wave period can be somewhat smaller than the period for the full basin domain.

3.4.2 Multi-layer hydrostatic linear model

We now relax the two-layer approximation, creating a multi-linear model. It is theoretically straightforward to extend the concepts of two-layer non-hydrostatic linear model, presented in section 3.4.1, to waves in a fluid with multi-interfaces. Therefore, to simplify our problem, we introduce new assumptions. We consider that just basin-scale internal seiches are generated in our system. In other words, we consider the shallow-water assumption ($H \ll \lambda$). In addition, we consider a complete hydrostatic model, neglecting the vertical velocities. In this new concept, the unsteady Bernoulli equation is no longer used just as boundaries conditions, but now it is a part of our system of differential equations. Thus, we have a system formed by mass-conservation and momentum equation for x-direction. Based on Mortimer (1952) work, we extended the number of layers and created a multi-layered model, schematically shown in Figure 19(b). The inviscid, linearized momentum equation for x-direction becomes

$$\frac{\partial u_j}{\partial t} + \frac{1}{\rho_j}\frac{\partial P_j}{\partial x} = 0, \tag{3.12}$$

in which the j subscript denotes the layer number that varies between 1 to N, where N is the maximum layer number. Since we consider just basin-scale waves, we can express the total pressure as the hydrostatic pressure. Therefore, the pressure can be easily expanded for N layers as

$$\begin{aligned} P_j(z) = P_o + \sum_{k=1}^{j-1}\left(\rho_k g(H_k + (\zeta_k + \zeta_{k+1})(-1)^{k+1})\right) + \\ \rho_j g\left(\sum_{k=j}^{N}(H_k + (\zeta_k + \zeta_{k+1})(-1)^{k+1}) + z - H\right), \end{aligned} \tag{3.13}$$

in which P_o is the atmospheric pressure, P_j is the total pressure at a specify depth z within the local layer j, H is the total depth of the system, H_k is the total depth until layer j, ζ_j is the interfacial displacement of layer j, except for ζ_1 that represents the surface displacement. Substitution of equation 3.13 into the momentum equation 3.12 gives

$$\frac{\partial u_j}{\partial t} = -g\sum_{k=1}^{N}\left(\frac{\rho_{k(j)}}{\rho_j}\frac{\partial}{\partial x}(\zeta_k + \zeta_{k+1})(-1)^{k+1}\right), \tag{3.14}$$

where $\rho_{k(j)}$ is the density of the layer k when $k < j$ whilst for $k > j$, the $\rho_{k(j)}$ assumes the value of j.

The linearized mass-conservation equation can be obtained with the same procedure described in equation B.12. Thus, expanding the mass conservation in Taylor series and linearizing ($a_j \ll \lambda$), we obtain

$$\frac{\partial}{\partial t}((\zeta_j + \zeta_{j+1})(-1)^{k+1}) + H_j \frac{\partial u_j}{\partial x} = 0, \tag{3.15}$$

in which equation 3.15 represents the mass conservation of j layer. Note that the ζ_1 represents the surface wave η. Combining equations 3.12 and 3.15 to eliminate u gives us the wave equation:

$$\frac{\partial^2}{\partial t^2}(\zeta_j + \zeta_{j+1}) = -gH_j \sum_{k=1}^{N} \left(\frac{\rho_{k(j)}}{\rho_j} \frac{\partial^2}{\partial x^2}(\zeta_k + \zeta_{k+1}) \right). \tag{3.16}$$

Note that the wave equation 3.16 is a second order partial differential equation system. We can simplify the equation 3.16 by assuming that $\zeta_j + \zeta_{j+1} \equiv f(x,t) = X(x)\cos(\omega\, t)$. Thus, the wave equation reduces to a second-order linear ordinary differential equation, which is a classical Sturm-Liouville eigenvalue problem. The general eigenfunction of this Sturm-Liouville problem for N layers is given by

$$\det\left[\underset{\sim}{A}\right] = \begin{vmatrix} H_1 - \beta & H_1 & \dots & H_1 & H_1 \\ H_2\gamma_{1,2} & H_2 - \beta & \dots & H_2 & H_2 \\ \vdots & \vdots & & \vdots & \vdots \\ H_{N-1}\gamma_{1,N-1} & H_1 & \dots & H_{N-1} - \beta & H_{N-1} \\ H_N\gamma_{1,N} & H_N\gamma_{2,N} & \dots & H_N\gamma_{N-1,N} & H_N - \beta \end{vmatrix} = 0, \tag{3.17}$$

in which β represents the eigenvalues, $\gamma_{kj} = \rho_k/\rho_j$, in which $k < j$, and

$$\underset{\sim}{A} = H_j \frac{\rho_{k(j)}}{\rho_j}.$$

Finally, combining the horizontal eigenvalue problem with the phase speed ($c_n = \sqrt{g\beta_n}$) yields the dispersion relation

$$\omega_{n,m}^2 = g\beta_n k^2. \tag{3.18}$$

Substitution of the lateral boundary condition, equation 3.11, and the simple wave relation into equation 3.18, we obtain the internal wave period, $T_{n,m}$, given by

$$T_{n,m} = \frac{2L_p}{m\sqrt{g\beta_n}}. \tag{3.19}$$

Thus, for a N-layer problem, we have n-solutions where each solution represents one different vertical mode. Since we consider the effect of the water surface, $n = 1$ gives us only one solution, which represents the pure barotropic wave mode propagating in an unstratified fluid. In our analysis we just considered the first three baroclinic modes. For the first vertical baroclinic mode, we used the pycnocline depth (equation 2.4) to divide the basin into two different layers. In this analysis we called each layer as epilimnion and hypolimnion, neglecting the presence of the metalimnion thickness. For the second vertical baroclinic mode, we computed the three layers system considering the metalimnion boundaries as part of each interface using equation 2.5 and 2.6. Finally, for the third vertical mode we used the pycnocline and the metalimnion boundaries to create a four layer system. As mentioned before, since the model results are based on arbitrary threshold values, often different choices can be made. Thus, we varied slightly the density and the thickness of each layer to see how the internal seiche patterns reacted under some variations. The parameter modification was done considering a change of a single parameter for each test. As done by Hutter, Wang and Chubarenko (2011), we did not keep a consistent modification,

since our aim was to test the model sensitivity to the change of a single parameter. Therefore, although physically a change in the epilimnion thickness would involve a change of mean epilimnion density, we did not consider this change in the model sensitivity analysis.

3.4.3 Interfacial waves influenced by Earth rotation

Now we consider an interfacial wave under the influence of Coriolis force. We again assume the shallow water assumption and the hydrostatic approximation. In addition, since we consider the influence of rotation, the y-component needs to be included in the differential system. Therefore, including the effect of rotation and the hydrostatic pressure assumption, the x- and y-momentum equations, equation 3.12, becomes

$$\frac{\partial u}{\partial t} + g' \frac{\partial \zeta}{\partial x} - v\overline{\omega_o j} = 0 \tag{3.20}$$

and

$$\frac{\partial v}{\partial t} + g' \frac{\partial \zeta}{\partial y} + u\overline{\omega_o j} = 0, \tag{3.21}$$

in which $\overline{\omega_o j} = 2\ \varepsilon\ \sin\overline{\phi_o}$ is the inertial angular frequency, $\varepsilon = 7.27\ 10^{-5}$ rad/sec is the angular frequency of the Earth, and $\overline{\phi_o}$ is the mean latitude of the basin.

In addition, the system is formed by the linearized form of the interfacial kinematic boundary condition and mass conservation equation. Integrating the mass conservation equation over the entire depth and combing the both equations, we have

$$\frac{\partial \zeta}{\partial t} + \bar{H}\left(\frac{\partial u}{\partial x} + \frac{\partial y}{\partial y}\right) = 0, \tag{3.22}$$

in which

$$\bar{H} \equiv \frac{h_e h_h}{he + h_h}.$$

The three coupled differential equations 3.20, 3.21, and 3.22 may be solved taking a general solution in the form of an exponential function for x-y components and time. After some algebra, we obtain the dispersion relation for shallow water waves affected by Earth rotation, which can be written as

$$\omega^2 = \bar{H} g'(k_x^2 + k_y^2) + \omega_o^2 \tag{3.23}$$

in which k_x and k_y are the wavenumber for x- and y-component, respectively. For a negligible rotating system, equation 3.23 becomes equivalent to equation 3.18. Therefore, the rotating effect increases the wave frequency, and consequently its period decreases. As we can note, the Earth rotation effect increases for higher baroclinic mode. Our aim here is not provide a comprehensive understanding of hydrodynamics of internal waves affected by Coriolis force on Vossoroca Reservoir and Harp Lake. Actually, our goal is just to demonstrate at what level Earth rotation may affect internal waves, avoiding the complex classification and comparison of different inertial waves that are formed in these basins.

3.4.4 Delft3D-FLOW model

The linear internal wave patterns in Vossoroca reservoir were also modeled with simulations of the heat transport by direct wind and solar radiation inputs using the Delft3D-FLOW software, Polli et al. (2017). The Delft3D-FLOW, developed by Hydraulics (2003), is a hydrodynamic simulation program based on the Navier-Stokes equations using the Boussinesq and hydrostatic pressure assumptions, appropriate for shallow water approximation. The software includes the effect of tides, wind, bathymetry,

density currents, waves, river entrance and turbulence. The developed model uses an implicit finite difference scheme for numerical solution, and operates on rectangular grid with 15 m × 15 m squared cells and 20 fixed layers, as shown in Figure 20. The depth of each layer was defined in the center of each square cell, whereas the velocity field was defined in the middle of the cell side.

Figure 20 – Vossoroca reservoir model grid.

A constant temperature was used as initial condition for the unstratified period, 12 July 2012. We used a time step of 3 seconds to simulate the whole period since the Courant number needed to be within the Courant–Friedrichs–Lewy condition to assure numerical stability. Firstly we simulated the model with the real wind information to obtain a complete knowledge of internal wave patterns in each region of the basin. We also compared the model results obtained in the region of the mooring to spectral analysis of the real data. In a second step, we modified the wind speed and direction to see how the internal seiche structure reacted under some wind variations. We applied a constant wind of 3.5 m/s at 220° from the North during 2 days, 11/09/2012 to 12/09/2012. In a second modification period, we kept a constant wind intensity of 5 m/s also at 220° from the North during 2 days, 17/09/2012 and 18/09/2012. Finally we applied during 26/09/2012 and 27/09/2012 a constant wind intensity of 4 m/s at 140° from the North of Vossoroca Reservoir.

3.5 Laboratory experiments

The study of interfacial seiche propagation was simplified by consideration of this process in a rectangular tank. In this case, all secondary effect was removed, so specific effects of internal wave evolution could be better explored. As mentioned before, in lakes and reservoirs, the wind stress increases the horizontal pressure gradient, and consequently the water is accelerated toward the upwind end, tilting the pycnocline. The instability force, responsible to tilt initially the pycnocline in laboratories, can be produced by many sources such as solid bodies and disturbances effects, simulating the wind action at water surface. We focus our investigation on interfacial waves generated by gravity currents. We generated long internal seiches through a experiment known as lock exchange release. The stratification profiles were obtained through a salinity stratification of two-layers. The internal seiche displacement was compared to the values obtained in Harp Lake and Vossoroca reservoir through non-dimensional parameters.

3.5.1 Experimental Setup

The laboratory experiments were carried out in a rectangular acrylic tank 200 cm long, 10 cm wide, and 50 cm high. Initially the channel was filled with fresh water to 20 cm high and a waterproof gate was placed in a specific position, according to the required pycnocline depth (Figure 21). The pycnocline depth was defined according to the ratio h_e/H. According to a geometric analyze, a symmetric lock exchange release results in system with ratio $h_e/H = 0.5$. As observed, the ratio h_e/H decreases when we increase the length of the dense water compartment for an asymmetric lock exchange release. We carried out 15 laboratory experiments covering a range of density difference 0.5 kg/m^3 $\leq \Delta\rho \leq$ 10 kg/m^3. Since most lake and reservoirs presents $h_e < h_h$, we used ratio $h_e/H = 0.25$, 0.4, and 0.5. Horn, Imberger and Ivey (2001), Stashchuk, Vlasenko and Hutter (2005) and Ulloa et al. (2015) have conducted similar laboratory experiments. However they carried out experiments in closed tanks. For this reason, they considered the rigid-lid approximation in both horizontal boundaries. Although this approximation is valid for most cases where the Boussinesq approximation is applicable, Michallet and Barthelemy (1998) showed that in laboratory experiments the assumption of small density variation is often violated. Thus, even though any surface wave were detected in our experiment, the closed upper boundary can present strong shear at the upper fluid layer, affecting the interfacial wave patterns.

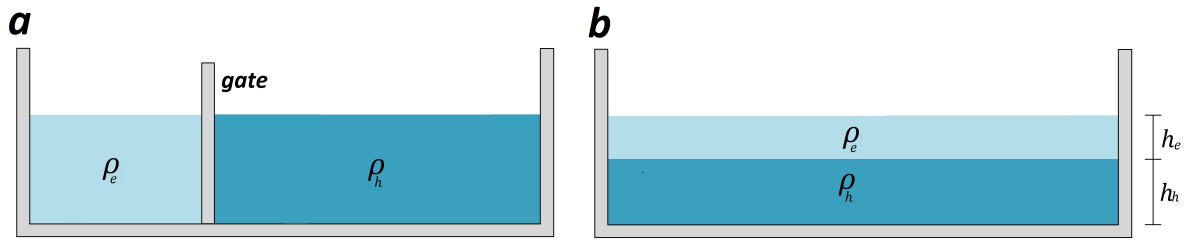

Figure 21 – (a) Sketch of the asymmetric lock-exchange release experiment for a final ratio $h_e/H = 0.4$. (b) Sketch of the final two-layer system after the internal seiche degeneration.

After the compartments division, sodium chloride (NaCl) was added to one compartment until a required water density was obtained. Since the stratification was based only on salinity, density measurements were obtained by electrical conductivity measurements. We used a conductivity meter MARCONI MA-521, with accuracy of ± 1% and precision of 0.001 for 0–2 μS/cm, 0.01 for 0–20 μS/cm, and 0.1 for 0–200 μS/cm. The conductivity meter used accept three cell constants: $K = 0.1$, $K = 1$ and $K = 10$. We used just one conductivity probe since the conductivity range used in this research is ideal for a conductivity probe with a cell constant of $K = 10$, which covers a range of 1–200 mS/cm. The conductivity meter was calibrated daily through a standard solution with electrical conductivity of 149.6 μS/cm at 25 °C. We did not used the approach proposed by Fofonoff and Millard (1983) to convert electrical conductivity to salinity since the algorithm has a minimum range of approximately 32 mS/cm for a water temperature near to 17 °C. Thus, we used a simple linear relationship between water density and electrical conductivity. Since in our laboratory experiment case the stratification was purely caused by salinity, the temperature did not affect the density stratification. As observed by Fofonoff and Millard (1983), there is a strong nonlinearity on density-temperature relationship, as seen in Figure 22(a). However, the relationship between electrical conductivity and water density has a linear trend (Figure 22(b)).

Although water temperature did not affect directly density stratification profiles in our laboratory experiments, the water temperature always affects the electrical conductivity. As mentioned in section 2.1.1, the relationship between temperature and conductivity follows an extremely nonlinear behavior. Since the electrical conductivity depends on both ion concentration and temperature, the influence of

temperature must be reduced. Thus, we calculated conductivity based on a reference temperature of 25 °C. Therefore, we used equation 2.2 and a temperature correction factor, f_{25}, for nonlinear correction as a function of sample temperature at a reference temperature of 25 °C. The f_{25} were obtained based on tables of Mattler-Toledo AG, Analytical (2013). We compute the f_{25} using a third order polynomial equation, which best fitted in the values tabulated by Mattler-Toledo AG, Analytical (2013), Figure 22(c). The temperature of samples were obtained using an analogue thermometer with resolution of ± 1 °C and temperature range of −10 °C to 50 °C.

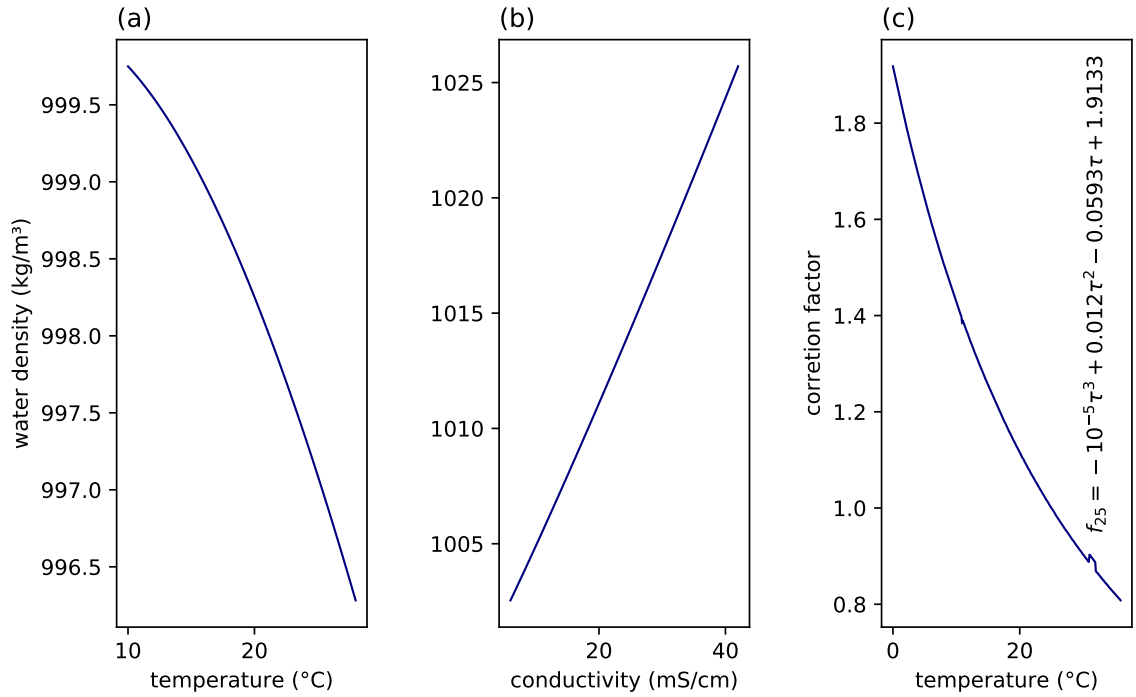

Figure 22 – (a) Relationship between fresh water density and temperature. (b) Relationship between water density at 14 °C and electrical conductivity. The Relations were obtained though the equation of state proposed by Commission et al. (2015) and the conductivity ratio to salinity conversion presented by Fofonoff and Millard (1983) considering the incompressibility assumption. (c) Relationship between temperature correction factor and temperature for nonlinear correction at 25 °C based on tables presented by Mattler-Toledo AG, Analytical (2013).

To reduce the influence of temporal factors, we daily computed the linear relationship between electrical conductivity, water density, and sodium chloride (NaCl) concentration. Since we did not used pure water, sodium chloride was not the only source of ions in the fluid. The tap water used contain ions from other places, such as pipes and due to water treatment. This effects influences the background density temporally, so the background density of one day was significantly different from another. We collected the data from the experiments during 10 days. For each day we calibrated the conductivity-density curve using seven samples with the water density range required for each day. In appendix subsection D.1.1 we present a comprehensive summary of daily calibration of water density and electrical conductivity. Based on the calibration data, we also obtained daily a relationship between sodium chloride (NaCl) concentration and water density. The density-NaCl concentration curve was used to estimate the amount of NaCl required to obtain a specific stratification.

Instantly after the NaCl addition, dye was added into the fluid located at dense water compart-

Table 2 – Experimental parameters used to each experiment run (1–24).

Run	$\Delta\rho$ **(kg/m^3)**	h_e/H (–)	**Run**	$\Delta\rho$ **(kg/m^3)**	h_e/H (–)	**Run**	$\Delta\rho$ **(kg/m^3)**	h_e/H (–)
E.1	~ 6.5	0.50	**E.6**	~ 9.5	0.45	**E.11**	~ 14.0	0.30
E.2	~ 6.0	0.50	**E.7**	~ 7.0	0.40	**E.12**	~ 7.0	0.25
E.3	~ 3.0	0.50	**E.8**	~ 6.5	0.40	**E.13**	~ 6.5	0.25
E.4	~ 1.0	0.50	**E.9**	~ 4.0	0.40	**E.14**	~ 2.0	0.25
E.5	~ 13.0	0.45	**E.10**	~ 1.0	0.40	**E.15**	~ 0.5	0.25

ment for a better visualization of the internal wave patterns. Before removing the gate, we measured the electrical conductivity in different regions and depths of the system. Using the conductivity-density relationship, presented in appendix subsection D.1.1, we confirmed the homogeneity for each compartment and the water density values. We also checked the value of water density for each compartment by tanking a sample of water that was analyzed through a pycnometer.

The experiment started when the gate was vertically removed, the dense water flows along the bottom of the tank, whilst the lighter surrounding fluid propagates in the opposite direction along the upper boundary, as illustrated schematically in Figure 14. We used three cameras to recover the propagation of the gravity currents and the internal seiche evolution (Figure 23). Two cameras were placed at positions 100 cm and 200 cm to recover the experiment in front face view. The first and second camera were positioned at a distance of 1.00 m and 0.30 m from the front face of the channel, respectively. Camera 1 was used mainly to recover the basin-internal seiche evolution through overview of the flow. and to measure the interfacial displacement at stations 2 and 3. Camera 2 was employed to recover in details the internal wave displacement at end wall of the tank, in front of station 1. A third camera was added 50 cm above the tank to recover the experiment in top plan view. Camera 3 helped to recover the propagation of the light and heavier gravity current, and subsequently it was utilized to obtain gravity current velocities.

The front speed of the gravity currents and the internal seiche displacements were measured using the open source physics tool Tracker Video Analysis and Modelling Tool (BROWN, 2017). The Tracker software was built on the OSP code library Java framework and allows the analysis of particles in motion frame by frame. We used the 4.9.8 version, which was run in Linux system. The videos from camera 2 were used to measure the internal wave displacement. We submitted the videos from camera 2 to a sharpen filter to highlight the pycnocline before using the Tracker Video Analysis and Modelling Tool. To overcome the difficulty to track the vertical internal wave displacement, we added two black strips, creating a vertical slot at the end wall of the tank (station 1), as shown in Figure 23(b). A second and third station was deployed on the middle and 0.50 m from the left end-wall of the thank, respectively. The videos from camera 3 were used to measure the front speed of the gravity currents. One thin black line was drawn at the bottom of the tank to help to overcome the difficulty to track a straight horizontal line, Figure 23(a).

We conduced a total of 15 laboratory experiments covering a range of density differences of $0.50\ \text{kg/m}^3 \leq \Delta\rho \leq 10.00\ \text{kg/m}^3$, varying the ratio h_e/H from 0.25 to 0.5. The density values used were chosen based on values of Richardson and Reynolds numbers. Large Re number were used to apply the inviscid analysis, since at large Re numbers, the viscosity approaches zero. We used the same background water density for all 15 experiments, epilimnion layer formed with just tap water. The difference between each experiments is due to temporal change in the background density of tap water. Table 2 shows the full list of the initial experimental conditions and the dimensionless parameters: h_e/H, Ri, and Re numbers. In appendix D we present a comprehensive summary of all laboratory experiments.

We analyzed the evolution of internal waves, detecting visual instabilities. We also computed the

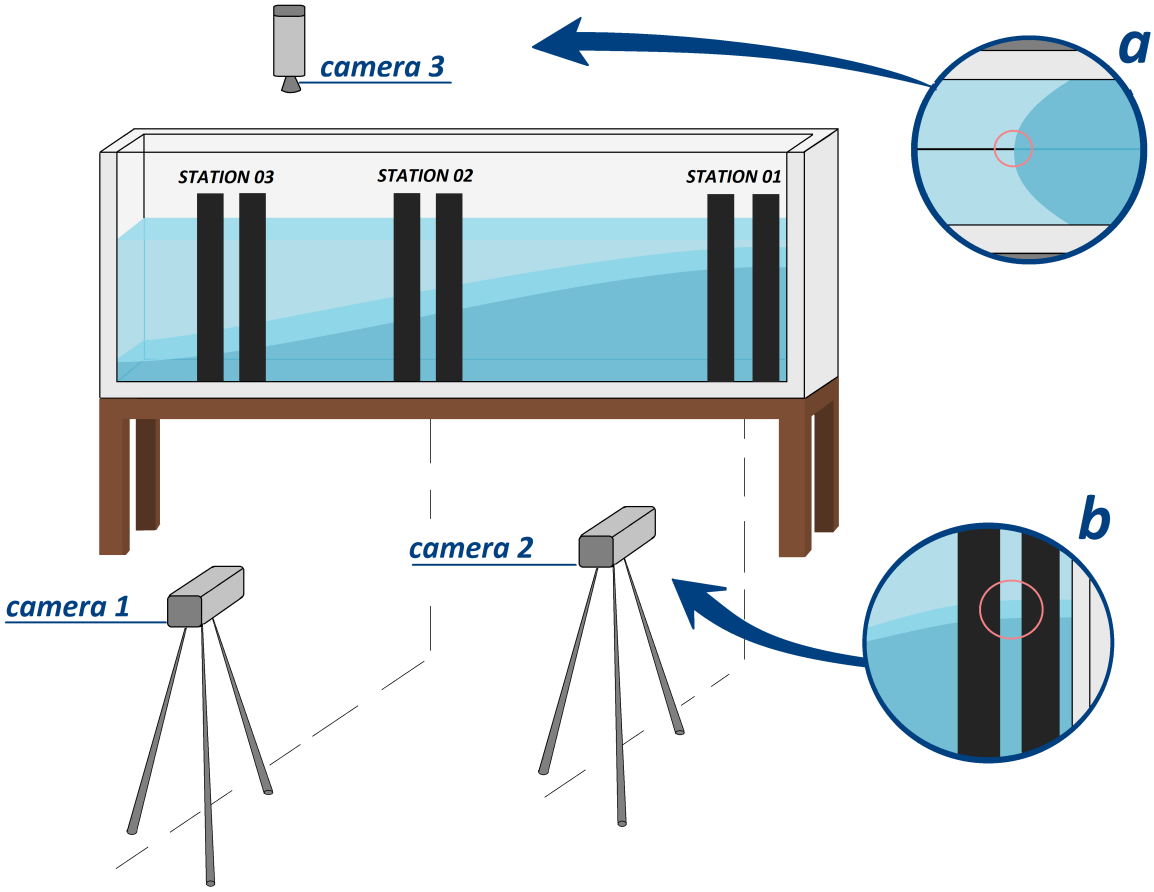

Figure 23 – Three-dimensional view: experimental set-up and apparatus. (a) view from camera 3 that recover the propagation of the gravity current before the reflection in the end wall of the tank. The red circle denotes the region where the target are is defined to tracker the propagation of gravity current. (b) view from camera 2 that recover the interfacial displacement due to internal seiche action. The red circle denotes the target area.

Brunt–Väisälä frequency, equation 2.7. To measure the importance of heat convection and mechanical turbulence, we calculated the densimetric Ri number at the pycnocline region, given in equation 2.13. We computed the value of the maximum and the minimum Ri number for each density structure considering the formation of large internal seiche, according to criteria for case c in Figure 10(c). To describe the importance of the shear velocity as a source of turbulent kinetic energy, we computed the W number, defined in equation 2.15. Similarly, as we have done with field data in section A to describe the degeneration of long internal seiches, we compared the ratio of pycnocline and the total depth (h_e/H) to the inverse W number. Since our internal seiches were not formed by the wind stress applied on water surface, we obtained the inverse W number through the idealized equation 2.27. This approximation has been used in many internal wave scientific laboratory studies (e.g., Horn, Imberger and Ivey (2001); Stashchuk, Vlasenko and Hutter (2005); Ulloa et al. (2015)) and is better explained by Boegman (2009). We measured the interfacial wave amplitude using the Digimizer image analysis software (MEDCALC, 2009). The Digimizer software is an open source image processing program designed for scientific multidimensional images, allowing a precise measurement and many preprocessing functions. To establish a criteria for each disintegration regime, we also used the frequency-scale equations (equations 2.19, 2.23, 2.25, and 2.26) and the internal seiche frequency obtained through equation 3.8 and the boundary condition 3.11.

Finally we also applied the spectral analysis on interfacial displacement series obtained from station 1, 2 and 3 for each laboratory experiment. We compared each spectrum with results obtained in different stations and tests. In addition, we tried to identify differences between each frequency spectrum and disintegration pattern of long internal seiches. Finally, we computed the theoretical period of internal waves using the two-layer non-hydrostatic linear model described in section 3.4.1. Thus, we compared results obtained from spectral analysis and modeling.

4 Results and Discussion

This chapter presents results of data analyses obtained from field monitoring and laboratory experiments, as well as results from comparisons and improvements made on internal wave theory to detect and predict internal wave activity in small stratified freshwater basins along the year seasons. We divide this chapter into three main sections. In section 4.1, we show the field monitoring results from Vossoroca reservoir and Harp lake, highlighting only one period of each basin. Based on similar analyses of these periods, we present a comprehensive summary of all analyzed periods. In addition, we applied the three-dimensional thermal stratification model implemented in Delft3D-FLOW by Polli et al. (2017) to detect the fundamental internal seiches observed in some periods. Based on results summarized in section 4.1, in section 4.2 we perform a comprehensive analyses of both cases, including an analyses of different meteorological and stratification conditions. Moreover, we compare theoretical with measured results, identifying well-matched and non-well-matched variables. Based on this analyses we refine the theory to better predict internal wave of different modes under different conditions.

In section 4.3 we present a comprehensive analyses of laboratory experiments, similar to those described in section 4.2 for field data. In addition, we use spectral analysis and laboratory experiments to investigate the influence of thermistor chain location on internal wave amplitude. Finally, in section 4.4, we extend the analyses present in section 4.2 by adding the laboratory experiment results, obtained in section 4.3. Thus, we reconstruct the amplitude of internal seiches, based on the decay of the vertical interfacial displacement observed through laboratory experiments. Finally, we correlate all result with linear and nonlinear solutions.

4.1 Case study

In this section we present the analyses of one only period of each basin. We show the excitation of internal waves in early spring in the Southern Hemisphere, during the month of September 2012 in Vossoroca reservoir. We choose this period based on previously detection of baroclinic motion during this extend of time, Bueno and Bleninger (2017) and Bueno and Bleninger (2018). In addition, we had already some simulations of the three-dimensional thermal stratification model implemented in Delft3D-FLOW run for September, 2012. In appendix C, we present a comprehensive summary of analyzed periods from 2012 to 2013 for Vossoroca reservoir. Although we perform an analyses of several period from Autumn and summer seasons between 2012 and 2014 for Harp Lake, we show results from September 16 to October 20, 2013. We selected this period for any specific reason since this is the first study of internal waves in Harp Lake.

4.1.1 Vossoroca Reservoir

Firstly, we extracted one sub-period from September 2012. The selected period is comprised between September 15 and 25, 2012. Although the first half of September has presented a strong oscillation of the thermocline, seen in Figure 24 (a), the system presented low Ri_w, with daily wind events < 1 m/s. The powerful variation is associated to low thermal stratification, $\Delta T << 4$ °C. Although during the selected sub-period the temperature difference increased to $\Delta T \approx 8$ °C, the wind event presented peaks $>> 5$ m/s and mean daily wind speed of 1.3 m/s (Figure 24 (b)). Since the increase of the thermal stratification was compensated by the mean daily wind rise, the daily Ri decreased in the sub-period,

declining the daily Ri from 10^6 to 10^3. Even though we detected lower Ri in the second period, the system presented weaker thermocline fluctuation compared to the first period of September. According to classification proposed by Spigel and Imberger (1980), the first period could be susceptible to excite linear internal seiches of small amplitude, whilst the second one, present a Ri number which indicates the dominance of basin-scale internal wave activity of high amplitude.

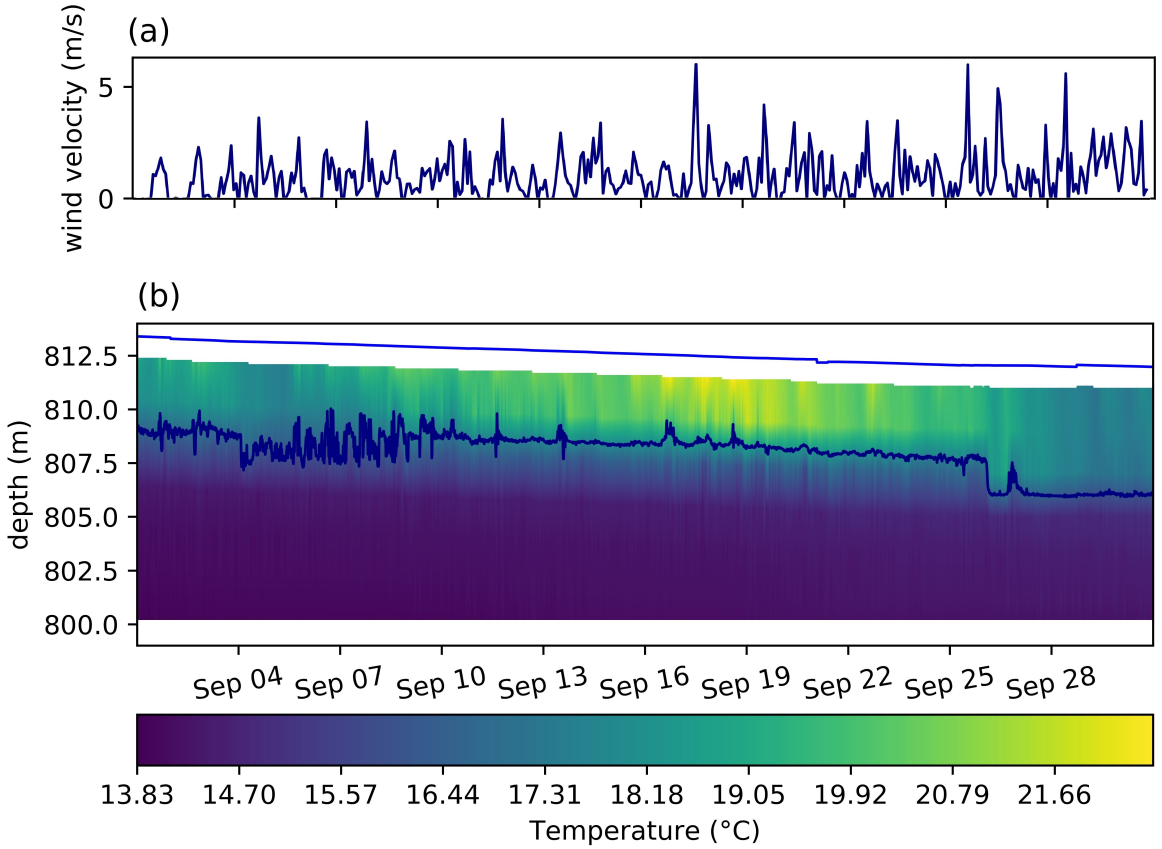

Figure 24 – Temporal analyses of Vossoroca reservoir during September 2012 (Voss. Res.; 01/09 – 29/09) (a) Wind speed time series and (b) the thermal structure.

Thus, the period from 15th to 25th of September 2012 was chosen based on the lower daily Ri compared to the first half of September, but apparently soft thermocline. The spectral analyses (Figure 25 (a)) shows that the most energetic peaks, as expected, are not located at the thermocline, which is represented approximately by the 18 °C isotherm. The most energetic frequency spectrum occurs in the 16 °C isotherm. The mean 16 °C isotherm was located at approximately 2 m below the thermocline. Although the coherence between the 16 °C isotherm and the wind intensity is notable low ($<<$ 10%), the high frequency band is energetic, indicating that the wind resonance may amplify internal seiches. The resonance phenomenon is discussed in details in the general analysis, in section 4.2. However, since the power spectral density of the wind is low at fundamental internal wave period, the internal wave is not forced by the wind-driven fluctuation.

The multi-layer hydrostatic linear model with free surface and shallow water assumption was applied to predict the first three vertical internal wave modes (Figure 25). The non-hydrostatic internal wave model does not present a distinct solution compared to the V1H1 obtained through the hydrostatic model. In addition, the first two modes, V1H1 and V2H1, were not strongly influenced by the Coriolis acceleration, since their frequencies are not close or greater than the inertial frequency. The V3H1 mode,

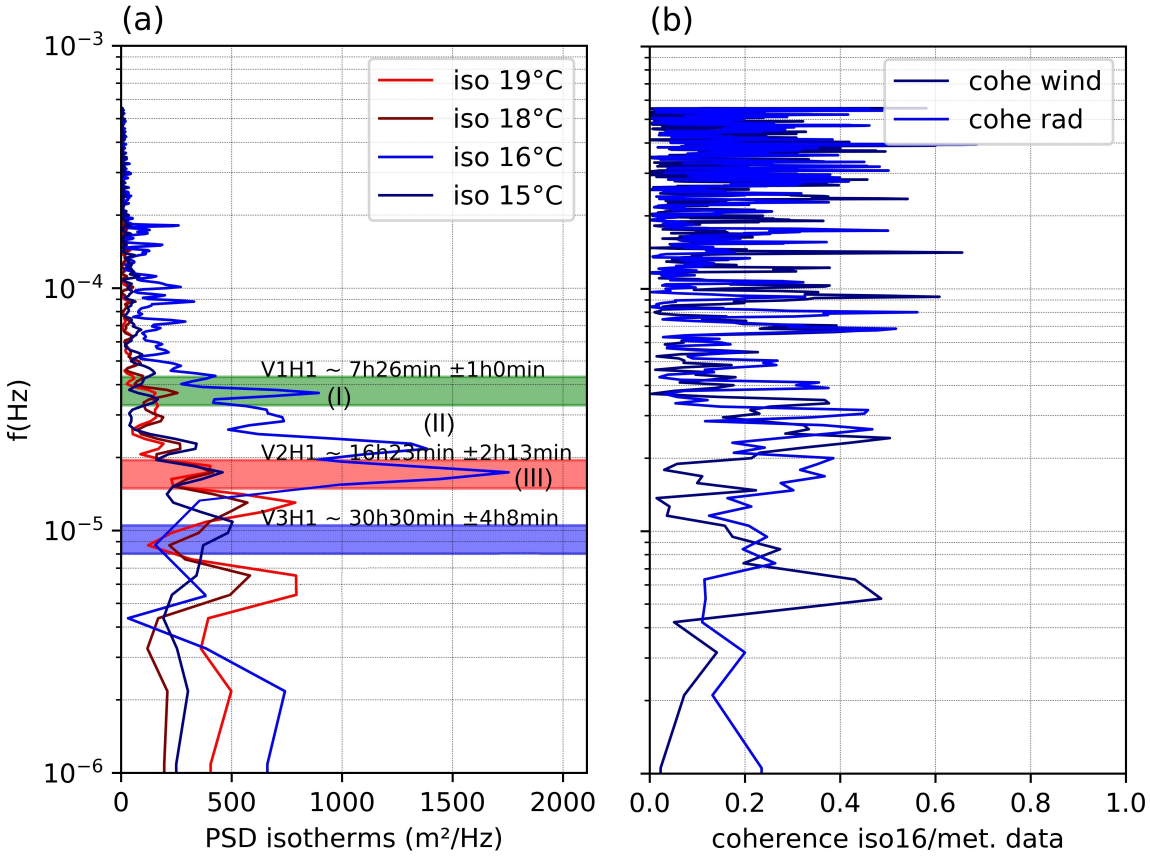

Figure 25 – (a) Power spectral density of the isotherms of 19 °C, 18 °C, 16 °C, and 15 °C (Voss. Res.; 15/09 – 25/09). (b) Coherence between 16 °C isotherm and meteorological data, solar radiation and wind speed.

that has periodicity of $\approx$ 30 h 30 $\pm$ 4 h, is accelerated by Coriolis force and presents a correction to $\approx$ 20 h 30 $\pm$ 1 h. The range compression is caused by the fact that Coriolis correction is greater in the maximum periods than in the minimum ones. Although this is an interesting observation, the V3H1 does not match with any energetic peak, which indicates that V3 or higher vertical modes were not excited during this period.

The model predicted period ranges that matched well with energetic peaks observed through the spectral analyses of the 16 °C isotherm. The V2H1 period suggests that the periodicity of approximately 16 h 30, Figure 25 (a) – peak (III) represents the propagation of the second vertical baroclinic wave mode. This period of September was also analyzed by Bueno and Bleninger (2018) considering just a power spectral analyses of the mean thermocline depth. Bueno and Bleninger (2018) used a two-layer non-hydrostatic model with rigid-lid assumption at lake surface, which can just predict the periodicity of fundamental baroclinic wave. However, considering the energetic observed peak in the mean thermocline depth ($\approx$ 15 h) and the calculated period for V1H1 mode, they suggested the excitation of a higher baroclinic wave. As observed in Figure 26 (a), the phase analyses suggests that a higher baroclinic wave was generated during this period, giving more credibility to the assumption made by Bueno and Bleninger (2018). The phase analyses shows that the 19 °C and 16 °C isotherms are out of phase in respect to each other. 24 h fluctuation was observed with higher energy, but low compared to frequencies where internal wave was identified, in 19 °C isotherm. This suggests that the variation is caused essentially by solar radiation. The low energy peak probably is due to the strong wind events in that periods, which

decreases the water temperature fluctuation at the basin surface.

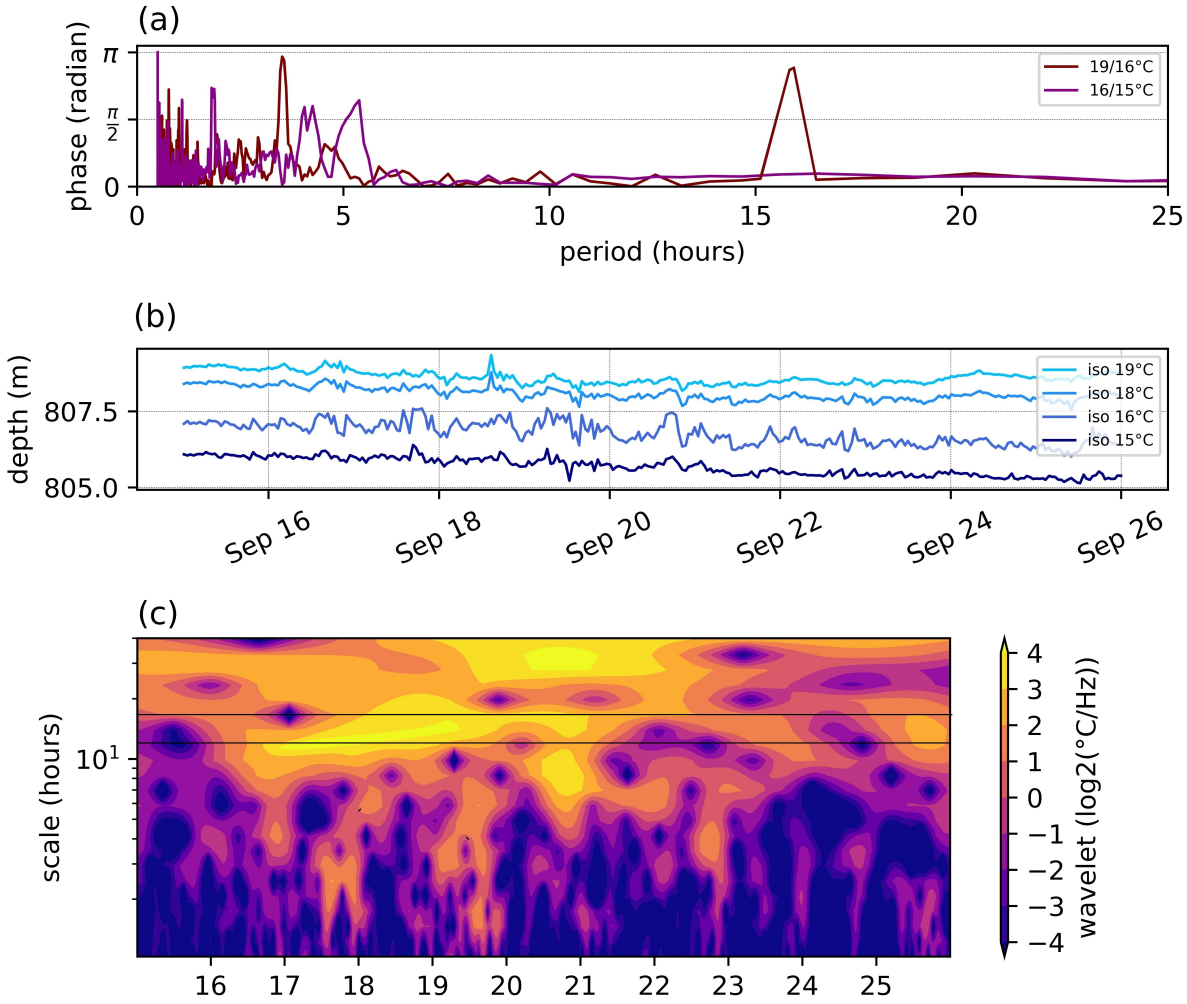

Figure 26 – (a) Spectral phase analyses, (b) isotherms series, (c) wavelet analyses of the 16 °C (Voss. Res.; 15/09 – 25/09). The black horizontal lines represent the range of periods of the V2H1 baroclinic mode obtained through the hydrostatic linear internal wave model.

Even though both isotherms are 90° out of phase, strong fluctuation is observed just on 16 °C isotherm. Since the 16 °C isotherm is below the thermocline and the water density difference is lower, the same energy input makes the 16 °C isotherm has greater amplitude (Figure 26 (b)). The variation due to internal seiche activity presented a total vertical displacement of ≈ 1.0 m in the 16 °C isotherm, 6% of the total depth excluding the small effect on the 19 °C isotherm. The wavelet analyses, seen in Figure 26 (c), shows that the V2H1 internal seiche was generated on the end of day 16. The internal wave action lasted for four days and was completely damped on September 20. The internal seiche was generated by northeast powerful wind events of 6 m/s and strong thermal stratification, $\Delta T \approx 8$ °C. As observed by Boehrer, Ilmberger and Münnich (2000), strong wind events were also responsible to generated second vertical baroclinic mode in Lake Constance. In addition, Münnich, Wüest and Imboden (1992) pointed out that the excitation of higher vertical modes is quite common in thermal stratified small basins, especially for winds with regular periodicity, normally exciting internal waves with period close to 24 h. Although the generated V2 mode did not present periodicity near to the diurnal period, it

presented regular resonant diurnal winds that matched with the internal seiche period of mode 2 during those days.

The energetic peak of 13 h (Figure 25 (a) – peak (II)), probably is due to the degeneration of the most energetic peak, which in this case is the identified V2H1 internal wave. Through the wavelet analyses (Figure 26 (c)), we observe that the 13 h oscillation acts during the same interval of the V2H1 internal wave and present the same characteristics, which indicates that the 13 h fluctuation is caused by the basin-scale degeneration of mode V2. The third most energetic peak on the spectrum, as observed in Figure 25 (a) – peak (I), matches with a V1H1 internal wave with modeled period of 7 h 30. However, differently from the second peak, this one is not so clear. This fluctuation could be correlated to the resonance of the V2H1 mode, but may also represents a V1H1 internal seiche that is quickly damped. Thus, the second vertical mode would be followed by excitation and dominance of a fundamental internal seiche. Therefore, it is hard to infer any conclusion, even because Wiegand and Chamberlain (1987) indicates that V1H1 modes may be followed by excitation of higher baroclinic wave, but did not mention the opposite situation. Thus, for any further conclusion we need most evidences of those type of excitation, since this type of energy transference has never been reported earlier.

We also ran the Delft3D-FLOW heat transport model. As we can observed in Figure 27, the three-dimensional thermal stratification model captured the most energetic frequencies observed in the wavelet analyses of field data. Although the numerical model smoothed the most energetic oscillations, the main features still remained in the spectral analyses. The wavelet analysis show that the high frequency spectra is completely ignored, indicating that although low frequency internal wave may be detected depending on the internal wave amplitude, high frequency internal wave are not represented, neglecting completely the degeneration of the basin-scale internal wave.

4.1.2 Harp Lake

Firstly, we extracted one sub-period from the main one, comprised between September 16 and October 20, 2013. We selected the period from 25th of September to 4th of October since it presented low Ri due to the strong wind events, with mean wind speed > 3.5 m/s and peaks that reached almost 6 m/s, as shown in Figure 28 (a). The wind presented a mean homogeneous duration of 11h blowing 169° North. The thermal stratification was practically constant during the whole main period, $\Delta T \approx 15$ °C. The strong wind events decreased the Ri from 10^6 to 10^3, which apparently leaded to an increase of instability, as seen in Figure 28 (b). According to criteria established by Spigel and Imberger (1980), the reduction of Ri value leads to a region between the formation of basin-scale internal waves of small amplitude and the dominance of internal seiche. Although it is not a full proof of their existence, this theory gives indication of their generation. As we will discuss in section 4.2, more analysis need to be conduced to better predict the internal seiche occurrence since Ri does not account the complexity of wind patterns.

Considering the sub-period, we detected two strong disturbance events mainly in the 8 °C isotherm, located approximately 1 m below the mean thermocline elevation ($\approx$ 821 m), as shown in Figure 29 (a). The first event occurred between September 28 and 30, whilst the second and stronger one was detected in the last five days of the analyzed sub-period, from 1st to 5th of October, 2013. Both disturbances are clearly due to homogeneous wind events (Figure 29 (b)). The first one presents mean wind intensity of 2.7 m/s, whereas the second one a mean wind speed of 3.5 m/s. Both periods present low Ri and, according to Spigel and Imberger (1980), were susceptible to internal seiche formations. Although the Ri does not account the wind direction to analyze the excitation of internal waves, the period presents homogeneous wind events, with mean wind direction to 120° and 270° North, re-

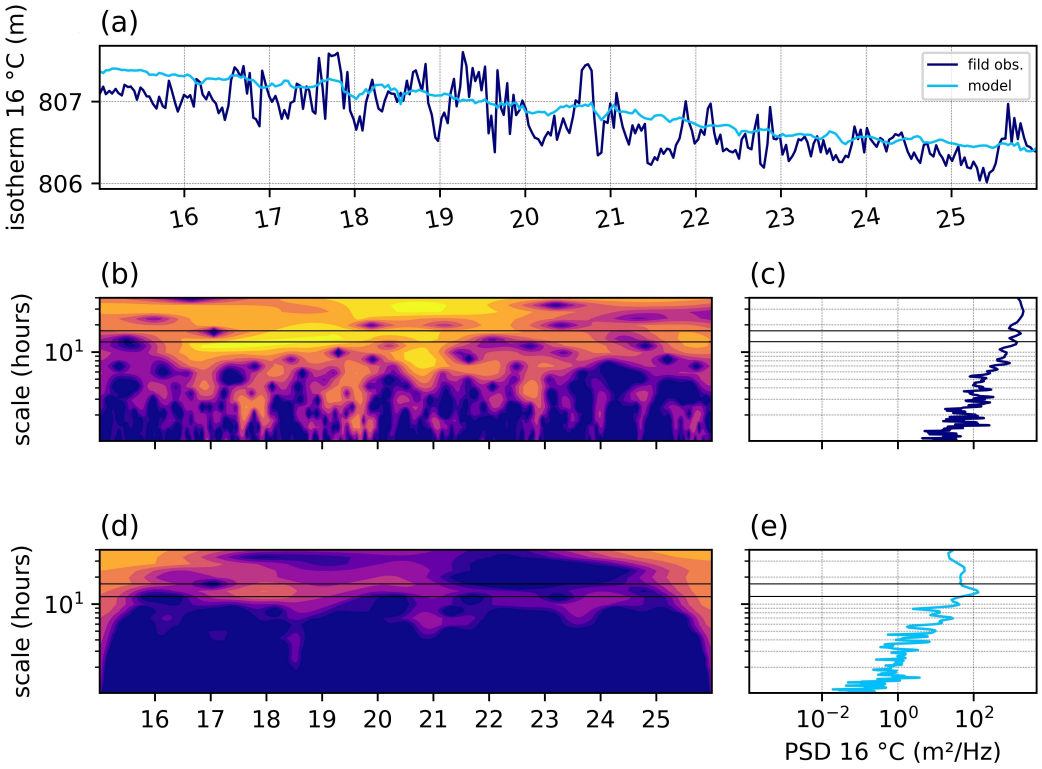

Figure 27 – A modeling and field observation comparison of the 16 °C isotherm (Voss. Res.; 15/09 – 25/09). (a) 16 °C isotherm. The spectral analyses of the 16 °C isotherm: (b) and (d) wavelet analyses and (c) and (e) PSD analyses. The black horizontal lines represent the range of periods of the V2H1 baroclinic mode obtained through the hydrostatic linear internal wave model.

spectively. Stronger wind events provided higher oscillations, with vertical displacement reaching 1.2 m, whilst the first period presented isotherm oscillation with 0.6 m variation. The linear theory, detailed by Boegman, Ivey and Imberger (2005a), underestimated the amplitude of the oscillations, mainly for mode V2. According to equation 2.15, the initial amplitude of internal seiches would be 0.5 and 0.6 m for first and second mode, respectively. Although the nonlinear solution have improved the results, see tests F.11 and F.16 in Appendix C, the amplitude growth probably have an important contribution due to the resonance phenomenon.

Figure 30 (a) shows results of the multi-layer hydrostatic linear model with free surface and the power spectral density of some isotherms, including the 8 °C isotherm. Clearly the fluctuation observed in Figure 29 (b) in the 8 °C isotherm has a dominant periodicity. Actually we detected two energetic peaks (Figure 30 (a)), a peak (I) of 5 h 30 and a peak (II) of 4 h 30, which match with modeled periodicity of mode V1 and V2. Both modes showed similar results considering the model sensibility. This occurs since the thermal structure of Harp Lake in this period presents a thin metalimnion, as shown in Figure 30 (b). The temperature profile is really different from stratified period of Vossoroca reservoir that presents thicker metalimnion ($\approx$ 4 m) with an almost linear stratification between thermocline and the reservoir bottom (Figure 18).

The 4 h 30 peak (Figure 30 (a) – peak (I)), has lower spectral energy compared to the peak (II), that has periodicity of 5 h 30. It indicates that the 4 h 30 fluctuation occurred between September 28 and 30 due to wind event of 2.7 m/s. All analyzed isotherms oscillated in phase with each other in these

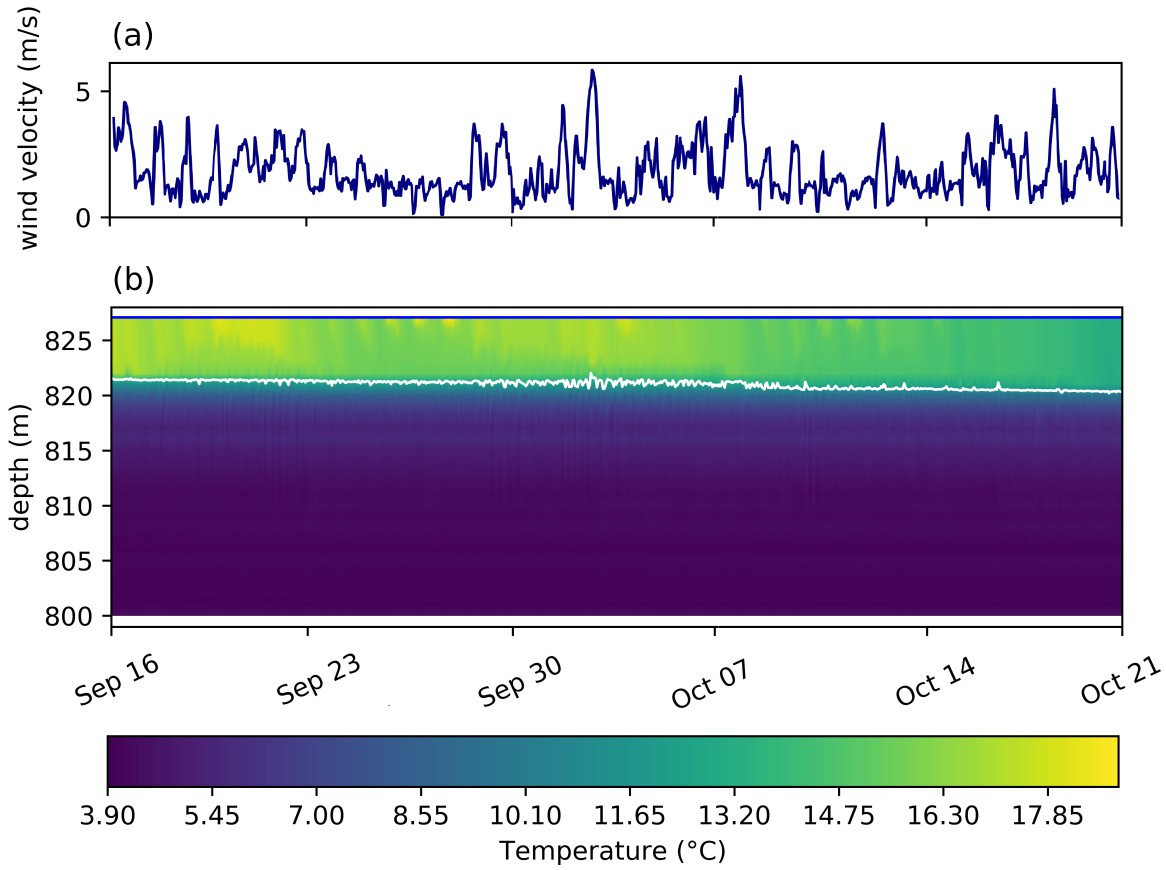

Figure 28 – Temporal analyses of Harp Lake during Autumn 2013 (Harp Lake; 16/09 – 20/10) (a) Wind speed time series and (b) the thermal structure.

periodicities, with exception of the 8 °C and 12 °C isotherms (Figure 30 (b)). The phase analyses suggests that higher baroclinic internal wave was exited in both periods. The out-of-phase structure may also be observed through Figure 29 (b) from 1st to 5th of October. However, the detection of the out-of-phase structure is harder for the first period, since the internal seiche amplitude is lower. In both periods the V2H1 mode was more pronounced below the thermocline, in the 8 °C isotherm, and barely detectable at the 10 °C isotherm. It suggests that a V2H1 internal seiche mode was excited two times during the analyzed sub-period. The occurrence of V2 mode in Harp Lake is discussed in details in section 4.2 since, as stated by Roget, Salvadé and Zamboni (1997), higher baroclinic modes are more dominant in lakes with diffusive metalimnion, which is not the case of Harp Lake, as seen in Figure 30 (c). To finish the detailed procedure of internal seiche detection, we shows schematically how the second vertical mode affects the vertical temperature profile, as shown in Figure 30 (d). We choose two periods representing 2 h interval, that is approximately half of the internal seiche period. As we can see, at 821 m elevation the water became warmer, which means that the 12 °C isotherm eroded during this interval due to the passage of an internal wave. However, 2 m bellow that point, the water became colder due to the elevation of the 8 °C isotherm, that was caused by the oscillation of the second interface, clearly out-of-phase with the 12 °C isotherm. This motion occurs repeatedly, as illustrated schematically in Figure 30 (e), until the complete internal seiche dissipation.

To highlight the out of phase nature of the second vertical mode, we applied a bandpass butterworth filter of $\approx$ 1/5 h^{-1} – 1/3 h^{-1}, which are based on the internal seiche period and the sensibility

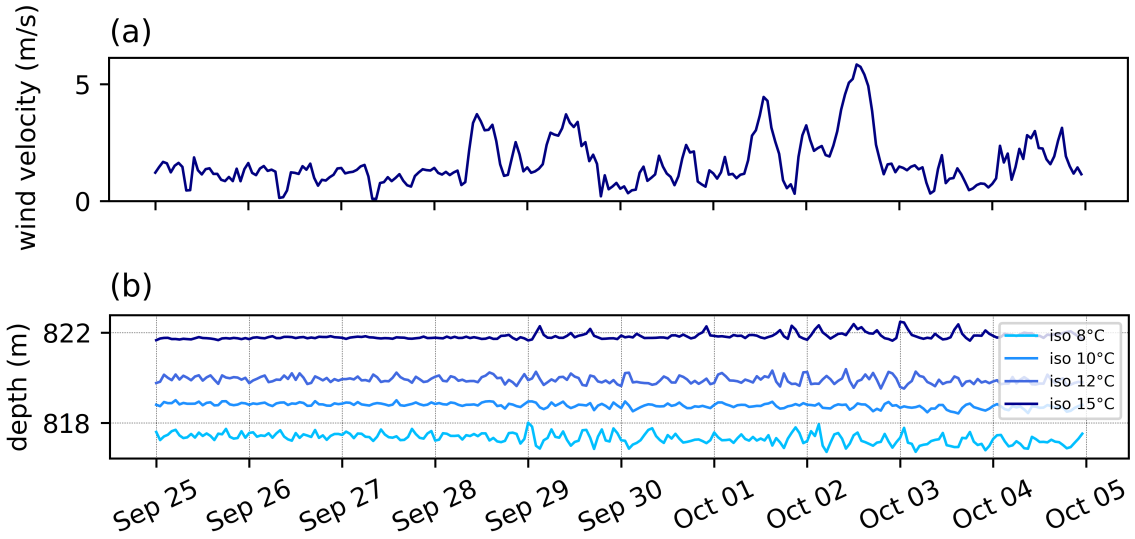

Figure 29 – (a) Isotherms series, (b) Wind speed time series (Harp Lake; 25/09 – 04/10).

analyses, to 12 °C and 8 °C isotherms, Figure 31. The strong variation has initial amplitude > 0.4 m and is excited during 2nd October. The behavior persists until the end of the analyzed period, which suggests that the second mode lasts for more than four days.

4.2 Overall Results

In this section we present a comprehensive analyses of internal seiche formation based on analyzed periods, that are summarized in appendix C. Before introduce the internal waves analyses, we present a description of meteorological and stratification conditions along the year for each basin.

4.2.1 General Comparison

The meteorological conditions and its variation have important influence on the internal wave dynamic in stratified water basins. Vossoroca reservoir and Harp Lake present distinct meteorological conditions, including the seasonal variation. Firstly, the Vossoroca reservoir is a shallow and small basin, with significant water level change. Since Vossoroca reservoir is not a deep basin, the hypolimnion is small and strongly controlled by the solar radiation, as shown in Figure 32 (a). The stratification is almost linear during most part of the year, with lower temperature difference in winter, with exception of July that most of time the system is completely mixed. The Harp lake is much deeper and the hypolimnion presents small temperature change during seasons, as shown in Figure 32 (b). During winter the system presents inverse temperature stratification, which indicates that the hypolimnion is warmer than the lake surface. In most part of the Spring, the system is practically mixed or present small stratification. The strongest thermal stratification in Harp Lake occurs during Summer and Autumn. In vossoroca reservoir the most stratified periods occurs during Summer and Spring. In Autumn the system presents high temperature from bottom to bed, and consequently shows a weaker thermal stratification.

The Vossoroca reservoir presents almost constant winds events during different seasons of the year, with peak wind speed of 6 m/s and mean wind events of 2.5 m/s. Because the Vossoroca reservoir is a

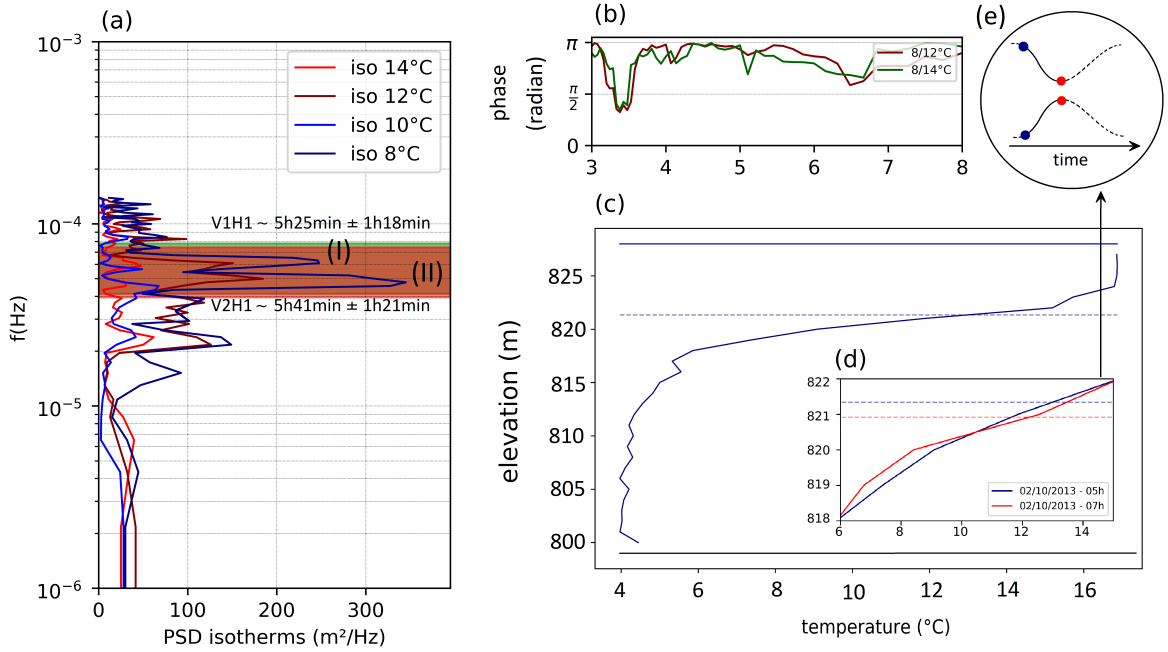

Figure 30 – (a) Power spectral density of the isotherms of 15 °C, 12 °C, 10 °C, and 8 °C, (b) spectral phase analyses (Harp Lake; 25/09 – 05/10), (c) Vertical temperature profile obtained from Harp Lake in 2nd of October 2013 at 5 a.m., (d) Zoom-in view of the temperature profile with a second profile 2 h late, and (e) a sketch of the V2 mode presented in (d).

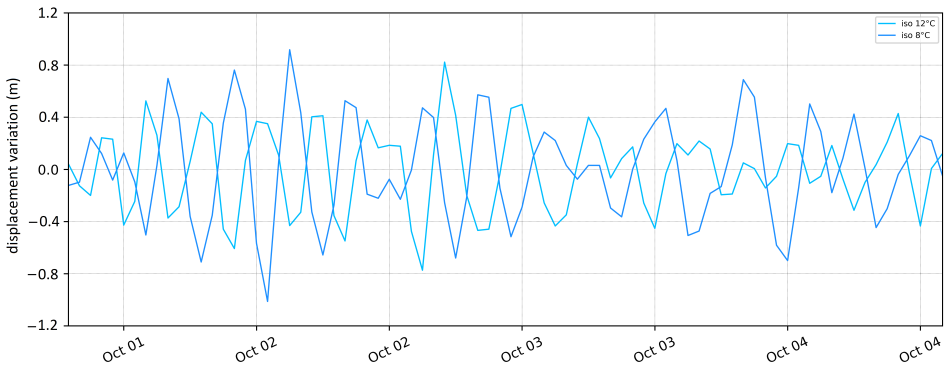

Figure 31 – Time series of filtered vertical displacements of the 12 °C and 8 °C isotherms, approximately at 6 and 8 m below the surface, respectively.

valley dammed reservoir, winds are oriented upward and downward in valley direction. Vossoroca reservoir presents wind events in four main direction, which are essentially the four reservoir arms direction. Harp Lake presents mean wind of 3 m/s with heterogeneous direction. The strongest wind events reach frequently 8 m/s and is more susceptible to be generated during summer.

Based on the meteorological conditions, we obtained the theoretical parameters that describe the formation and degeneration of internal seiches during different seasons along the year. Based on values of Ri and criteria established by Spigel and Imberger (1980), the internal seiche dominance changes abruptly along the year and for different basins. The thermal stratification is really strong during the summer, presenting high Brunt-Väisälä frequency in the thermocline ($N \approx 0.038$ /s). The stable condition

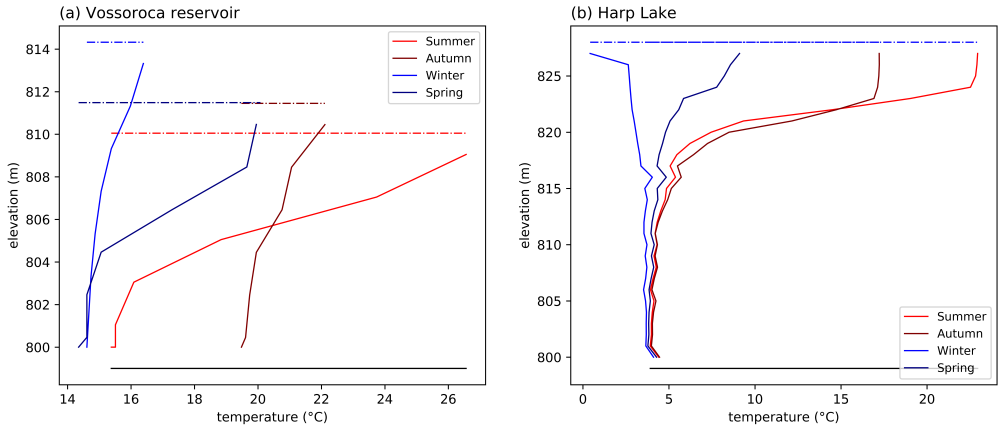

Figure 32 – Vertical temperature profile interpolated linearly between thermistors for each season and basin. (a) Vossoroca reservoir; Summer (13/12/2012), Autumn (15/04/13), Winter (14/06/12), and Spring (13/10/12). (b) Harp Lake; Summer (21/08/13), Autumn (02/10/13), Winter (02/01/13), and Spring (02/05/13).

in Summer hinders the dominance of large amplitude internal seiches in Vossoroca reservoir (Figure 33 (a)). The lower Ri in Harp Lake summers, according to the theory, allows the dominance of internal seiche for at least half of the period. Although in Autumn the thermal stratification in Harp Lake is weaker compared to Vossoroca reservoir, the wind tends to be lighter, leading to a increase of the Ri and preventing internal seiche dominance, as shown in Figure 33 (b).

In Vossoroca reservoir, after the summer period, the stratification gets weaker, increasing the probability to internal wave activity. According to theoretical results, 55 % of the autumn period is dominated by internal seiche activity. However, the system is more susceptible to excite internal waves during the winter, when the system has low Ri. 60 % of winter presents the dominance of internal seiches. However, during July the reservoir is completely mixed (Figure 33 (a)).

As aforementioned, we individually analyzed several periods, which are summarized in appendix C, table 3. The theoretical results of the basin-scale internal wave degeneration for all these analyzed periods show that the W varies between 0.23 and 104, and indicates that frequently when internal seiches are excited, probably will evolve into high frequency waves, as seen in Figure 33 (c)[1]. The small stratification observed during the stratified winter period in Vossoroca reservoir leads to high instability, in which supports the formation of high amplitude internal seiche. During this period we identified $W \approx 0.24$, that was the lowest mean value observed for all analyzed periods. In addition, Figure 33 (c) shows that the thermocline in Vossoroca reservoir is most of time located between 0.3 and 0.5 of the total depth, without any relationship between seasons. Whilst, the thermocline in Harp Lake takes up a relatively small proportion of the total lake depth, and is strongly influenced by seasons. In Summer, Harp Lake presents high temperature difference between surface and lake bottom, and consequently the thermocline is shallow, located ≈ 0.1 of the total depth, 50 % shallower compared to Autumn, as shown in Figure 33 (c).

[1] All curves of Figure 33 (c) is derived from equations 2.19, 2.23, 2.25, and 2.26. They are a function of system variables, such as water density and theoretical internal seiche velocity. For both basins, the blue curve, that divides the regimes of damped linear waves and solitary waves, is more affected by this variables. Thus, the thickness of this curve in Figure 33 (c) indicates the variability of the regime for different periods and basins. Generally, for Vossoroca reservoir, the area of damped linear wave regime is greater than for Harp lake. Other lines (red and black one) present difference between all periods lower than 5 %, thus we did not account the variable changes through the line thickness.

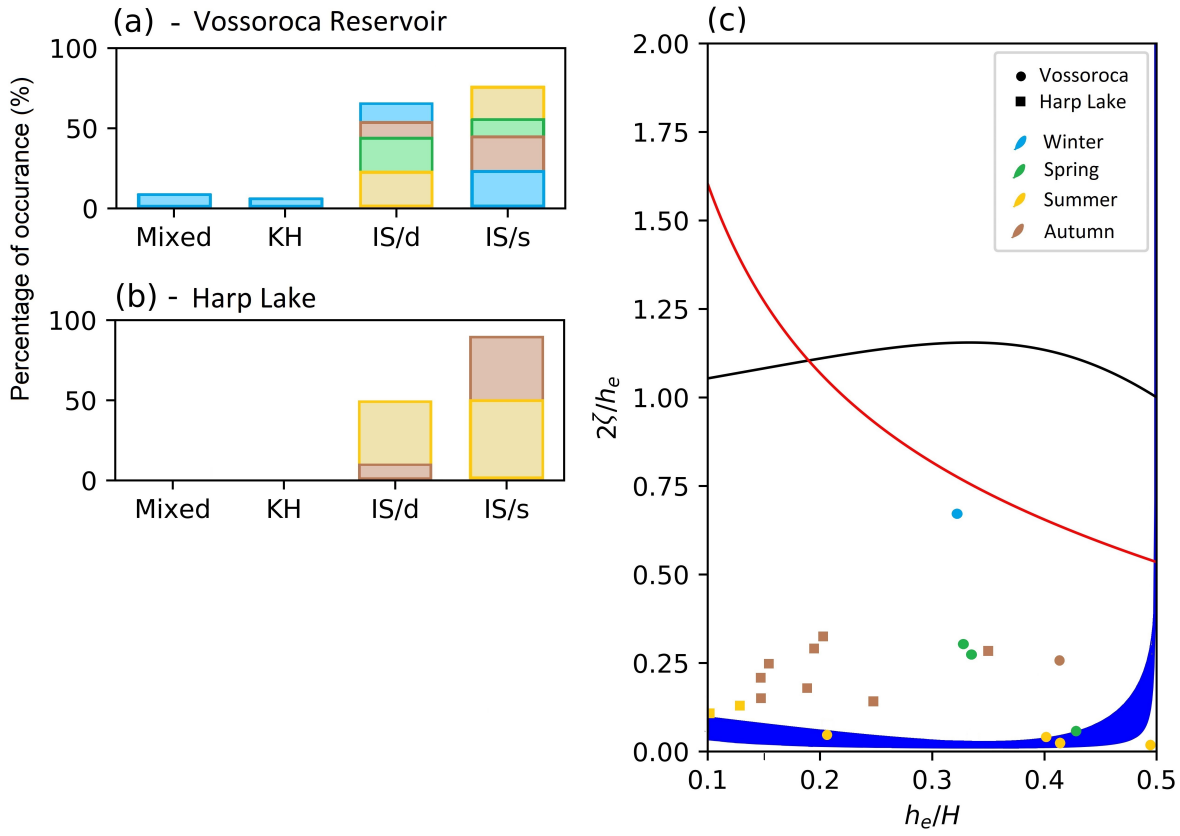

Figure 33 – Regimes of interior mixing and oscillation generated by wind stress in (a) Vossoroca reservoir and (b) Harp Lake for different seasons. Each basin is divided into four regimes, as established by Spigel and Imberger (1980): Mixed; With presence of intense instability, including Kelvin-Helmholtz billows (KH); Internal seiche dominance (IS/d); and small internal seiche activity (IS/s). (c) Analytical regime of degeneration of internal seiches and period analyzed, in which blue curve is given by nonlinear and damping frequency, red curve is derived from nonlinear and Kelvin-Helmholtz frequency, and black curve counts the two later and the bore frequency.

Internal seiche periods, detected through spectral analyses, are plotted against the theoretical internal seiche periods (Figure 34). We used the non-hydrostatic linear internal wave model with free surface, described in section 3.4.1, and the multi-layer hydrostatic linear model with free surface and shallow water assumption, described in section 3.4.2. Both models presented same results for fundamental internal seiche mode, with the advantage that the multi-layer could capture higher vertical modes. Thus, for our analysis, we used just results obtained through the multi-layer hydrostatic linear model with Coriolis correction, discussed in section 3.4.3. The standard error for fundamental internal seiche modes is approximately 1 h, which indicates good agreement between the two-layer model prediction and the observed results.

The error increased considerably for higher vertical modes, ≈ 3.5 h. Such error may be predicted by the sensibility analyses, which for second vertical mode indicates a difference of $\approx$ 4 hours for a variation of 0.75 m in the metalimnion thickness. Clearly, for higher baroclinic mode, the parameters is more sensitive. For example, the V2H1 period is fairly sensitive to the metalimnion thickness. This conclusion agreed well with results obtained by Münnich, Wüest and Imboden (1992) that concluded that the percentage error in thickness becomes larger for small layer thickness. As stated by Hutter, Wang

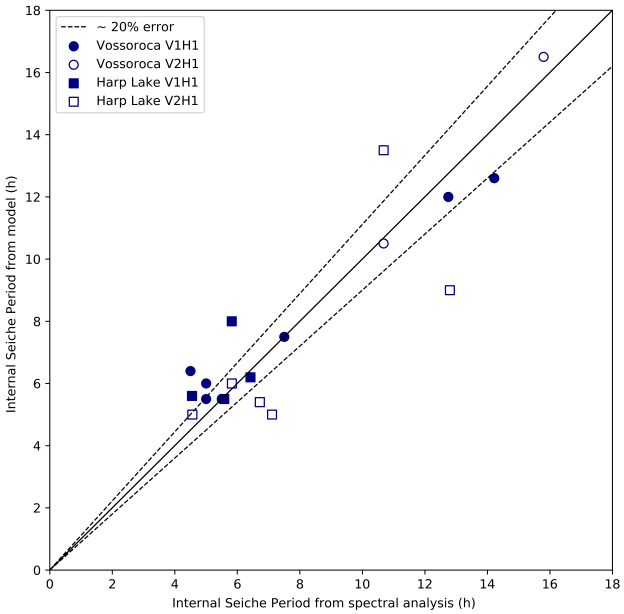

Figure 34 – Comparison between internal seiche periods obtained through spectral analyses and the analytical 1D hydrostatic model.

and Chubarenko (2011), the variables used to model the environment are somewhat subjective, mainly for higher vertical modes. This may also be seen in the fundamental internal seiche mode. Although the sensibility is lower for V1H1 internal seiche, results from Vossoroca reservoir present higher error compared to Harp Lake results, 1.1 h and 0.8 h, respectively. This increase of error can be explained by the measured thermocline depth. A 1 m change in the thermocline depth in a shallow water basin, such as in Vossoroca reservoir, affects much more the parameters than in a deep lake.

The spectral energy of the vertical displacement of the most energetic isotherm, that is oscillating-displaced due to internal seiche activity, represents the basin-scale internal wave amplitude when is normalized by the frequency resolution of the spectrum-analyses. The wave amplitude is directly associated to the daily Ri of the analyzed period at the thermocline depth. The overall results, mainly for V1H1 internal seiche mode observed in Vossoroca reservoir, show an inversely proportional relationship between internal wave amplitude and the Ri. This suggests that internal seiches with higher amplitude were generated during periods of higher instability, which may be due to low stratification or strong wind events (Figure 35). In addition, results from Vossoroca reservoir suggest that internal wave amplitude grows exponentially with the decrease of Ri, indicating that stronger wind events can lead to baroclinic motion with higher amplitude. This is true unless the Ri reaches a critical value, $Ri_c \sim L/2h_e$. In this case, as stated by Spigel and Imberger (1980), interface shear, Kelvin Helmholtz billows, and rapid deepening accompany large interface displacements may cause a complete vertical mixing during a single wind episode. This type of regime has been observed during the transition between mixed and low stratified periods in Vossoroca reservoir, which was observed in the beginning of May.

In this stage we cannot infer any conclusion about the relationship between basin-scale internal wave and Ri for second vertical mode in Vossoroca reservoir. Since fundamental internal seiches are dominant in Vossoroca reservoir, we detected only two occurrence of V2H1 mode ($<$ % 20 of all analyzed periods). Both V2H1 mode values fitted well in the log-regression, with just slight lower amplitude.

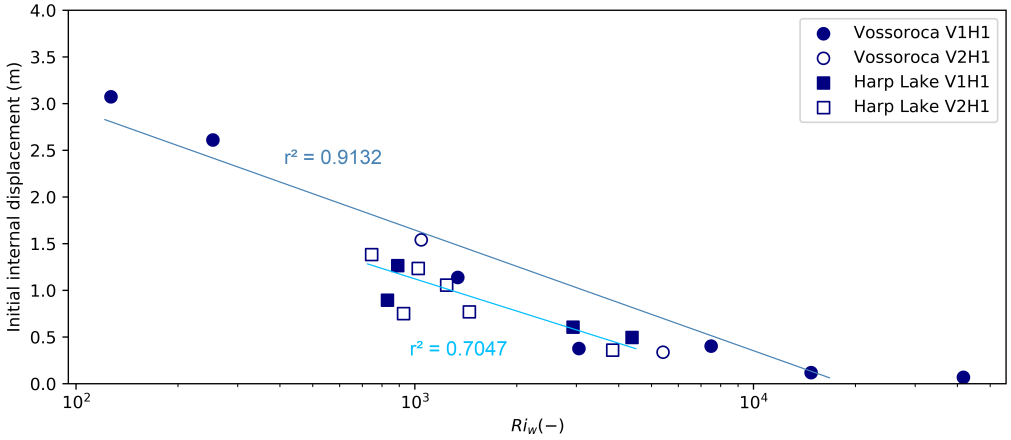

Figure 35 – Peak of the spectral thermal of the most energetic isotherm versus the daily Ri.

However, it is difficult to conclude that this mode has lower amplitudes. This error could be generated since we used the daily Ri at the thermocline depth, which is expected that fits better in results of mode V1H1. In addition, another conclusion with respect to the generation of higher baroclinic mode is that V2 mode is not directly related to the Ri, since in both basins the Ri does not present any relationship between the excitation of V1 and V2 modes. In other words, both modes were generated in the same range of Ri (Figure 35).

Internal seiches detected in Harp Lake apparently presented lower amplitude compared to Vossoroca reservoir, as shown in Figure 35. This contradicts the prediction described by Imberger (1985), that points out that the interfacial displacement is $\sim L/2Ri$. Since the variation of the epilimnion thickness between the two basins is negligible and the Ri is not significantly different, the amplitude of internal seiche should be in the same order of magnitude, considering equation 2.27. Actually, although Figure 35 gives the impression that internal seiches excited in Vossoroca reservoir present higher amplitude compared to those formed in Harp Lake, the vertical displacement obtained through spectral analysis represents essentially the variation of temperature in the thermistor chain location. As discussed before, the direct comparison of internal wave displacement between both basins is not recommended at this time, and is better explored in section 4.4. Nevertheless, the results follow a poorer inverse behavior, with r^2 lower than those found from Vossoroca reservoir (Figure 35). It indicates that this difference must not be caused just by the location of the thermistors, but must be caused by other parameters that the Ri neglects.

A complex parameter that is parametrized to obtain the Ri, is the wind intensity. The Ri, as defined by equation 2.13, just contemplates one single value that is derived from the mean wind speed, neglecting other wind components, such as fluctuation, direction, and duration of the wind. Based on correlation between wind peaks and thermal variation due to internal seiche passage, we observed that the wind peak does not show any directly correlation to the wave amplitude. It means that these events could support internal wave activity, but is not responsible to its growth in height (Figure 36 (a)). On the other hand, the mean wind speed presents a strong correlation to the internal seiche amplitude (Figure 36 (b)). Results from Vossoroca reservoir, including both modes, V1H1 and V2H1, follow a strong linear-trend. However, for Harp Lake, the trend is slightly disrupted. It suggests that the same parameter that influences the relationship between Ri and the thermal displacement (Figure 35), probably appears here (Figure 36 (b)). It suggests that the disturbance probably is hidden in the mean wind intensity.

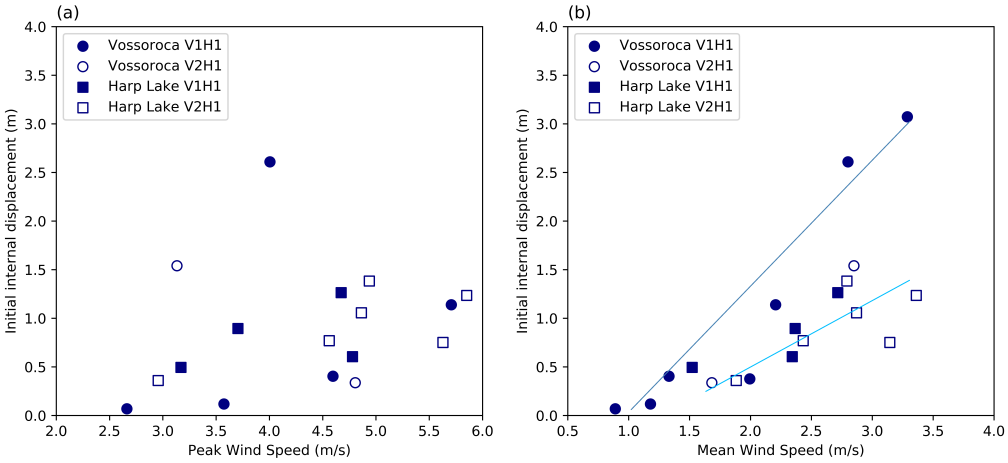

Figure 36 – Spectral thermal variations versus (a) the peak wind events and (b) the mean wind intensity.

Recently, Gaudard et al. (2017) pointed out that some filtering implementation in the friction velocity of the wind, w_*, can significantly improve the accuracy of some models to predict internal seiches in deep lakes. Valerio et al. (2017) and Stevens and Imberger (1996) found that the response of a stratified basin to wind depends on the strength, duration and homogeneity of the wind field.

Schwefel et al. (2016) sugested a parametrization based on the duration of the wind events. Essentially, they recommended that wind stress lasting less than one-fourth of the internal wave period should be filtered. Gaudard et al. (2017) recommended the fallowing parametrization:

$$\Psi_{dur} = \min\left\{\sqrt{\frac{4T_{wind}}{T_{n,1}}}, 1\right\}, \tag{4.1}$$

in which T_{wind} is the wind event duration and $T_{n,1}$ is the theoretical internal seiche period of vertical mode n. Gaudard et al. (2017) defined the duration of wind event as periods with mean wind speed equal to at least 1.5 times the overall average, which depends essentially on the analyzed period. However, in order to avoid a subjective analyses of the wind duration, we calculated the event based on the values of W. We filtered just consecutive wind events when $W < 32$. This values is not universal, nor critical, but chosen just to describe periods of consecutive wind intensity. Note that this value does not represent the criteria for internal seiche formation, that according to linear theory described by Imberger and Patterson (1989), generally is approximately 1, though Stevens and Lawrence (1997) have reported internal seiche activity in Brenda Mines Pit-Lake when $W > 50$.

The filtered Richardson number, Ri_{dur}, that is based essentially on the friction velocity, that is responsible to excite internal seiches, is defined as $Ri_{dur} = Ri_w \Psi_{dur}$, in which Ψ_{dur} is the duration coefficient and varies between zero to one, as defined in equation 4.1. This coefficient reduces the effective wind speed available for internal seiche generation. However, the filtering processes is just used to compute the wind energy availability to excite internal seiches, and does not represent a global reduction of the wind strength.

Since Harp lake has stronger wind events compared to Vossoroca reservoir, frequently Ri_{dur} is equal to the standard Ri, which indicates that $\Psi_{dur} \approx 1.0$. With regards to the analyzed periods, we observed that most of time $\Psi_{dur} = 1.0$ (Figure 37 (a)). This suggests that the wind duration is not a problem to excite internal seiche in Harp Lake, actually we observed frequently wind events with duration > 8 h, which is approximately 2 times greater than the fundamental internal seiche period. On the other

hand, since the duration of the wind events varies from 0.25 h to 9 h in Vossoroca reservoir, frequently $Ri_{dur} < Ri$. The duration filter applied in Vossoroca results reduced slightly the energy transport into internal seiche, leading to a better log-regression between basin-scale internal wave amplitude and Ri_{dur} with $r^2 = 0.9365$ (Figure 37 (a)). Although Gaudard et al. (2017) observed lower Ψ_{dur} in winter due to the increase of the internal seiche periodicity, since in our cases the wave period did not strongly varied, we observed reduction of energy transport during summer because the winds speed tends to be higher in winter. We observed the increase of mean wind stress from 0.95 mPa to 1.67 mPa in Vossoroca reservoir, whilst in Harp Lake the mean wind stress varied from 2.00 mPa to 2.40 mPa.

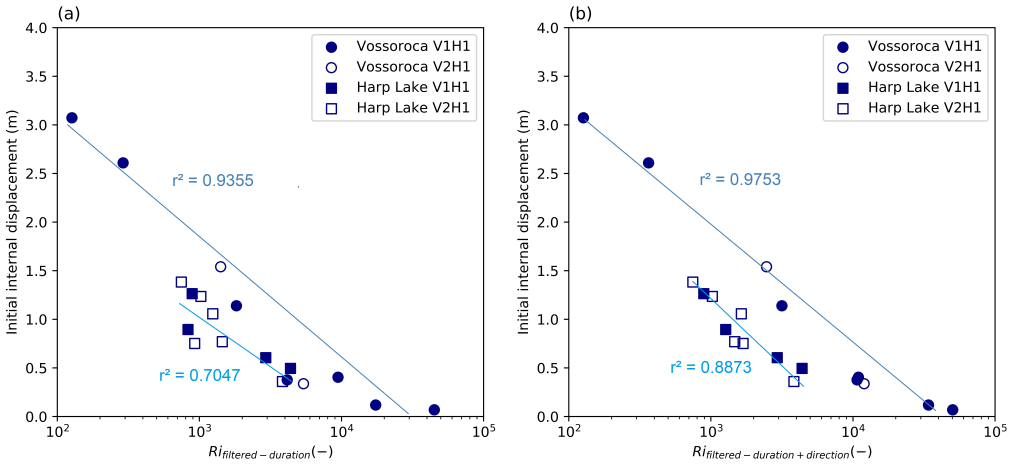

Figure 37 – Peak of the spectral thermal variations versus the filtered Richardson: counting the contribution of (a) wind duration and (b) wind duration and direction.

Wind with heterogeneous direction may also be incapable to generate internal seiches. Despite the fact that Vossoroca reservoir is a valley dammed reservoir, since the wind events are relatively weak and nonconstant, the direction is not completely homogeneous. In addition, we observe in Vossoroca reservoir that winds events often with opposite directions to the last event, generally in the valley direction. On the other hand, although Harp Lake presents strong wind events, sometimes it behaves in a heterogeneous way, which indicates that the direction during this event may not be capable of causing basin-scale internal wave. As a further improvement, we added a new coefficient Ψ_{dir} based on the direction and duration of the wind event in the standard Richardson number, Ri. Ψ_{dir} was estimated exactly in the same way of Ψ_{dur}, with exception that a new condition was imposed on the wind duration estimation. Ψ_{dir} was estimated as the fraction of the time that wind direction was in the same a quarter of a circle. This procedure was performed to obtain the new filtered Richardson number, Ri_{dir}. All information is summarized in appendix C, Table 5. The filtering implementation improved the log-linear regression for both basins (Figure 37 (b)). However, in Harp Lake, the improvement was much more evidenced, mainly because the wind direction play a major role in Ri. A further improvement is explored in section 4.3.2 and 4.4, when we perform an analyze to calculate the internal wave amplitude decay based on the station location. Although apparently it would just influence the difference between each basin, depending on amplitude decay rate, it can influence differently periods of the same basin.

Another critical issue is: in which condition higher baroclinic modes could be generated in stratified water basins. Salvadè, Zamboni and Barbieru (1988) reported higher baroclinic mode with large oscillations at depth much deeper than the thermocline. In that circumstances, Salvadè, Zamboni and Barbieru (1988) pointed out that the V2 mode was excited due to the presence of a chemocline, commonly observed where local conditions favor the development of photosynthetic sulfur bacteria, representing a

transition between rich-oxygen to anoxic regions. This is not apparently the case of V2 mode detected in Harp Lake, since the second vertical mode was observed through temperature measurements and near the thermocline. Although higher baroclinic mode may be associated to the density structure, other factors could favor the excitation of higher vertical modes. As suggested by Hutter, Wang and Chubarenko (2011), higher vertical modes are dominant in lakes with diffusive matalimnion, characteristic of shallow basins. However, V2H1 internal seiche mode is apparently dominant during all analyzed period in Harp Lake. On the other hand, Vossoroca reservoir, where the metalimnion takes up a relatively larger proportion of the total reservoir depth, presents dominant fundamental internal seiche activity. Hamagami et al. (2011) have also reported the dominance of V1H1 internal waves in a shallow water basin ($\approx$ 3 m depth), Shikinawa Lake. Although this suggests that in Vossoroca reservoir, and extremely shallow water basins, the lack of water depths may increase the probability to excite fundamental basin scale internal waves, we did not observe any correlation between the formation of V2 mode and total water depth.

Münnich, Wüest and Imboden (1992) suggested that the potential for resonance with the diurnal component of the wind is an important condition to favor the excitation of V2H1 internal seiche. As stated by Boegman (2009), when the forcing frequency matches one of the natural frequency of the basin scale internal wave mode, resonant amplification may occur. Since Harp lake is a small water basin, the theoretical internal seiche period tend to be relatively short, $\approx$ 3 h, and does not match with any energetic wind frequency. However, the theoretical internal wave period of V2H1 mode often matches one energetic frequency component of the wind, that has period $\approx$ 6 h and 12 h. Then, we observe the formation of the second vertical internal seiche mode repetitively in Harp Lake. Whereas, in Vossoroca reservoir, V1H1 mode period often matches one of those energetic wind period, the semidiurnal component of the wind, and consequently the fundamental internal seiche period is dominant in Vossoroca reservoir.

Note that the potential for resonance with the diurnal component of the wind is not just important to excite higher vertical modes, but to amplify any internal wave mode already generated. Although Hutter, Wang and Chubarenko (2011) poited out that the daily wind circle enable the increase of internal wave amplitude as its period is near resonance, we concluded that not just the daily wind, but more importantly for small stratified water basin, the semidiurnal wind and higher frequency components may also cause resonance, which leads to a increase of the internal wave amplitude (Figure 38). This phenomena has been observed in both basins, Vossoroca reservoir and Harp Lake.

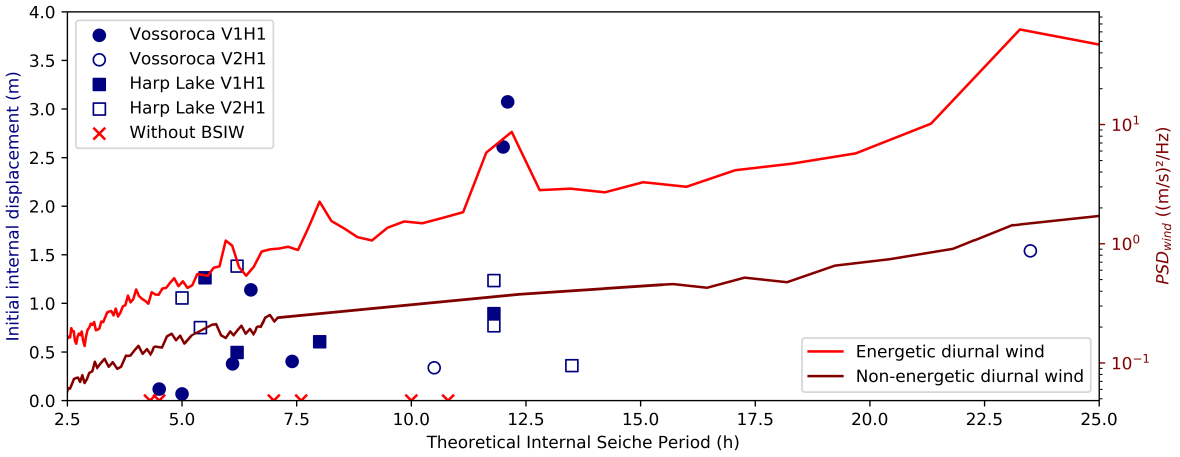

Figure 38 – Thermal variation energy for both modes and basins versus the theoretical internal seiche period. The right axis represents the power spectral density of the wind intensity for a arbitrary period of Harp Lake, including one energetic and non-energetic diurnal wind period.

Note that although the wind variation often presents diurnal and higher frequency components due to the solar radiation, their energies may vary according to basin and periods (Figure 38). We did not detected any signal of internal seiche activity, or presented insignificant amplitude that could barely be detected, for periods with small energetic wind components. Thus, we can conclude that the potential for resonance with the diurnal component of the wind is one important factor to generate internal seiches, and consequently is crucial to excite higher vertical baroclinic modes in Harp Lake.

To finish this section, in Figure 39 we compare conditions to internal seiches generation, as proposed by Spigel and Imberger (1980), with the degeneration of basin-scale internal waves detailed by Horn, Imberger and Ivey (2001).

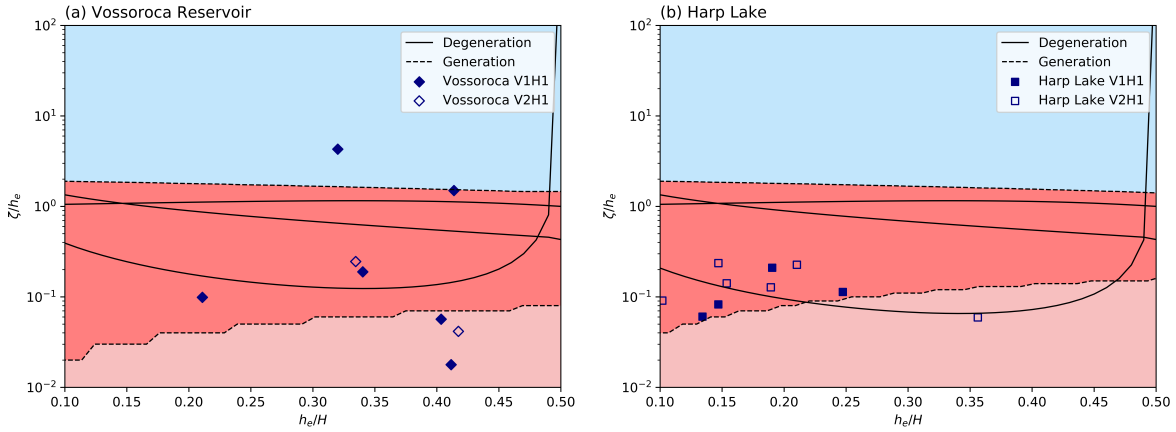

Figure 39 – Analytical regime diagram showing a schematic structure of the generation and degeneration of basin-scale internal waves in (a) Vossoroca Reservoir and (b) Harp Lake. The Figure shows three generation regimes: Internal seiche rapidly damped (light red region), Internal seiche with limited billows (red region), and large Kelvin-Helmholtz billows (light blue region).

According to the classification proposed by Spigel and Imberger (1980), fundamental baroclinic motions with high amplitudes are more susceptible to be excited in Vossoroca reservoir. In addition, for both basins, the decrease of the epilimnion thickness favor the occurrence of basin-scale internal wave. However, this was just observed in Harp Lake, where internal waves were excited mainly when $h_e/H < 0.25$. It may be mentioned that Harp lake is much deeper than Vossoroca reservoir, and normally presents shorter epilimnion than hypolimnion layer. Thus, we did not observe a correlation between the epilimnion thickness and the internal wave occurrence. However, on the other hands, the majority of analyzed periods fitted in the internal wave condition proposed by Spigel and Imberger (1980), as evident in Figure 39.

The study of degeneration of basin-scale internal waves is a far more challenging task since the phenomenon is complex to be detected through a single thermistor chain. Thus, our analysis with regards to the internal wave degeneration is essentially based on the theories already described in the literature, see section 2.3.1.

As discussed before, the greatest variation between different basins is related to the regimes of damped linear wave and nonlinear waves, blue line in Figure 33 (c). We observed that all the identified internal waves fall into these two degeneration categories, except for winter periods observed in Vossoroca reservoir. In addition, since the length of the Harp Lake is smaller compared to Vossoroca reservoir, the basin-scale internal waves are more susceptible to be degenerated into nonlinear internal waves. We cannot

infer any conclusion about the degeneration of the second vertical mode, since this theory describes only the wave degeneration in a two-layer system. Here, it may be mentioned that this analyses is based only in theory. A complete analyses must be verify the degeneration patterns through direct measurements, which was impossible with just one thermistor chain.

4.3 Laboratory Experiments

In this section, we explore the excitation and evolution of internal seiches in a controlled two-layer system maintained by saline stratification. First, we perform a similar analysis to that carried out for field data in section 4.2.1, describing the relationship between mechanical turbulence, produced by the instability force, and the internal seiche amplitude, which was obtained through a normalization of the power spectral density peak of the interfacial vertical displacement with the frequency resolution. Finally, in the end of this section, we analyze the internal seiche displacement decay based on longitudinal distance from the interfacial wave node.

4.3.1 Experimental analyses

Similar to field data analysis (Figure 34) we evaluated the theoretical periods of internal seiches, obtained through the 1D multi-layer hydrostatic linear model, to experimental periods (Figure 40 (a)). The experimental period was obtained from the time series of the interface displacement, that was estimated through the open source physics tool Tracker Video analyses and Modelling Tool (BROWN, 2017) from video recorded at station 1, see Figure 23.

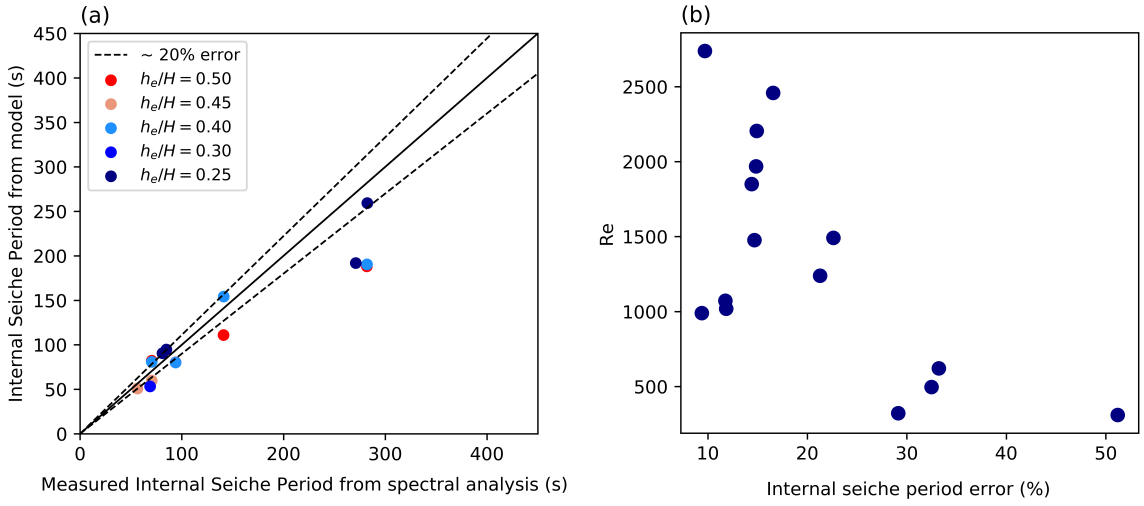

Figure 40 – (a) Comparison between internal seiche periods obtained through spectral analyses and the analytical 1D hydrostatic model for experimental data. (b) Reynolds number, Re, against the error percentage of the internal seiche period.

The error rate increases exponentially as the stratification becomes weaker for all ratio h_e/H. As observed in Figure 40 (a), the model underestimated the internal wave periodicity as the phase velocity becomes lower. However, with respect to field analysis (Figure 34), we detected no correlation between error and the internal wave periodicity. Since viscous effects influence the vorticity diffusion, and consequently the internal wave evolution, we observe an inversely correlation between error and the Reynolds Number, as shown in Figure 40 (b). This suggests that viscous effects turn out to be important,

and cannot be neglected in such case. However, for field observation, the mean Re, that in our cases is $\approx 5 \times 10^5$, is much greater than Re for our laboratory experiments, which suggests that errors in the field analysis (Figure 34) is not caused by viscous effects. As we observed in Figure 40 (b), $Re < 750$ presents error > 30 % on the internal seiche period estimation.

In addition, with regards to ratio h_e/H, the shallowest pycnocline, $h_e/H = 0.25$, exhibits average error of ≈ 25 %, greater than the mean error for $h_e/H > 0.3$, that is ≈ 17 %. As aforementioned, and will be further discussed, the $h_e/H = 0.25$ presents several problems. The pycnocline reaches the surface of the thank due to the strong instability caused by the gravity current and the thin first layer. The interface suffers an abrupt deceleration, that influences directly the internal wave periodicity.

Before discussing the internal seiche evolution and the relationship with the salinity-driven convection and mechanical turbulence, we further investigate the instability frequency, since this disturbed process is completely distinct from the instability caused by the wind forcing. In our laboratory experiments, internal seiches were generated by gravity currents, in which the flow occurs essentially due to the density difference between the current and the ambient. According to Bar (1967), considering the energy-conserving theory proposed by Keulegan (1957), the Fr, equation 2.14, must be constant along the channel for a saline gravity current.

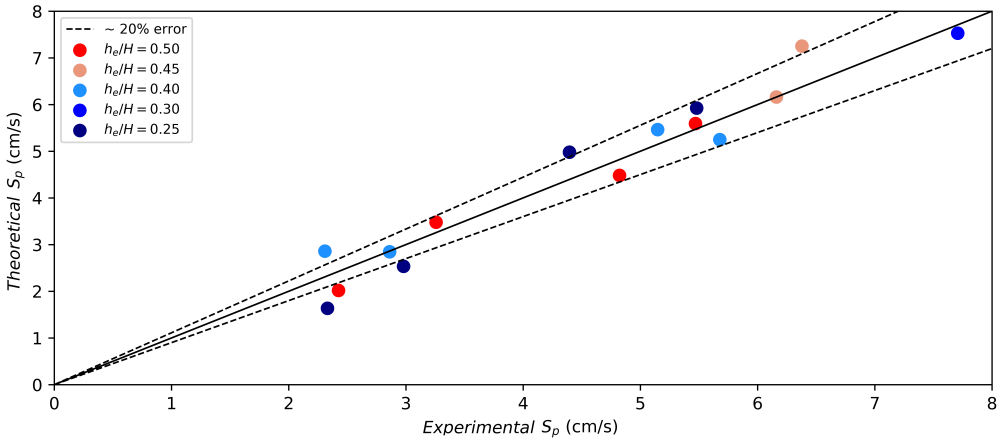

Figure 41 – Comparison between theoretical gravity current velocity from Bar (1967) and experimental gravity current speed.

The result obtained in laboratory experiments, $\bar{Fr} = 0.47 \pm 0.04$, presents good agreement with theoretical result proposed by Bar (1967), which found $\bar{Fr} = 0.49$ (Figure 41). Experiments conduced with ratio $h_e/H = 0.5$ show $\bar{Fr} = 0.49 \pm 0.05$. However, when we decreased the ratio h_e/H to 0.25, $\bar{Fr}$ increased to 0.51 ± 0.11. Since the denser gravity current did not reach the constant-velocity phase, and most of the energy was transfered from the disturbances generated in the lock region to the gravity current, the density current was accelerated, and consequently added error to the speed front estimation.

Although, through the principle of energy conservation, the Ri should be equal for all cases, the gravity current energy is not transfered as a whole to generate the initial interface displacement. To analyze this, the interfacial wave amplitude was estimated through a band-pass Butterworth filter considering the modeled interfacial period and the video recorded from camera 2, as seen in Figure 42.

As a matter of fact, the vertical velocity feels a extra force due to the reduced gravity. Thus, the duration and amplitude of internal seiche is directly influenced by the system stratification and gravity current velocity, as shown in Figure 43 (a). The disadvantage of this analyses is that we cannot control the

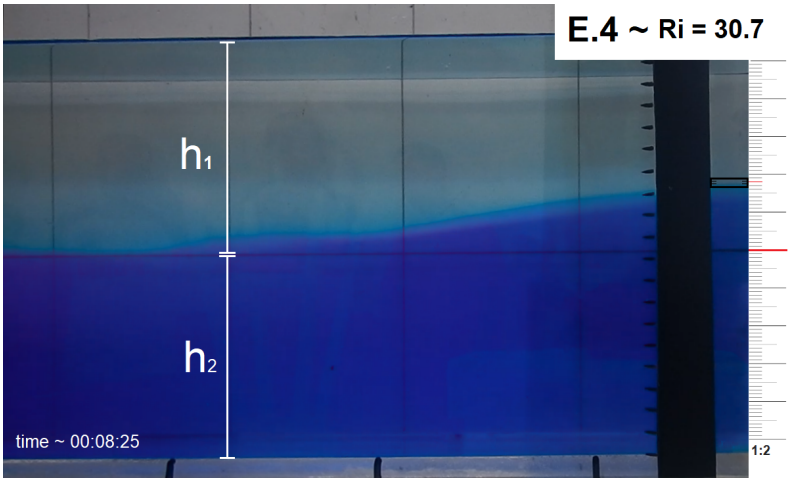

Figure 42 – Video image showing the basin-scale internal wave generated in run E.4 at the end wall of the tank, station 1. The E.4 was performed with h_1 and $h_2 = 10$ cm.

instability frequency, since it is associated invariantly to the density difference. In addition, the analyses cannot be done immediately after the lock-exchange release, since the interfacial layer is first forced by gravity current.

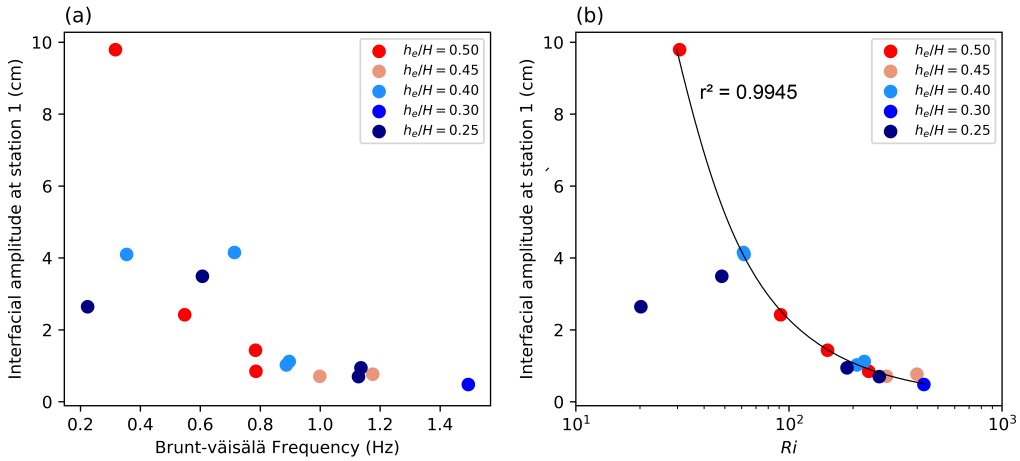

Figure 43 – Peak of the spectral interface displacement at station 1 (a) versus the Brunt-Väisälä frequency, and (b) versus the Richardson number.

The salinity-driven convection and mechanical turbulence, measured by Ri, indicates an inverse correlation to the basin-scale internal wave amplitude with $r^2 = 0.9945$, excluding the tests with ratio $h_e/H = 0.25$ (Figure 43 (b)). The correlation is similar to that found in field analyses (Figure 37). However, Figure 37 suggests that when $Ri \approx 100$, the relation fits well in a linear regression. In other words, the internal wave amplitude grows linearly as the Ri decreases at around $Ri \approx 100$.

Although results with ratio $h_e/H = 0.25$ presented good agreement for $Ri > 100$, for $Ri < 100$, the values did not fit in the linear regression. As mentioned earlier, for cases with $h_e/H = 0.25$, the interface reaches the tank surface, specially for lower Ri, due to the strong stability and tiny upper layer. This phenomenon limits the internal seiche growth.

4.3.2 Energy cascade

Here we analyze the displacement decay along the longitudinal main axis based on the power spectral density analysis. The vertical displacement recorded in each station for experiments with ratio $h_e/H = 0.5$ was submitted to the spectral analyses based on Fourier transform and converted to amplitude through a normalization with frequency resolution (Figure 44). As the density difference between upper and lower layer decreases, the internal wave period rises. The increase of the period is due to the reduced gravity, since it gets lower, the internal wave motions become slower, increasing the internal wave periodicity. As suggested early in Figure 43, the internal wave amplitude, obtained through station 1, is inversely proportional to the density difference (Figure 44). Part of spectral energy of the variation of the pycnocline is felt with lower energy in station 3, located at 1/4 of the tank length. However, at station 2, located exactly in the middle of the tank, the energy of fundamental horizontal mode ($\lambda = 2L$) is barely felt. This suggests, as expected, that in the middle of the tank the vertical displacement is minimum due to proximity of the basin-scale internal wave node.

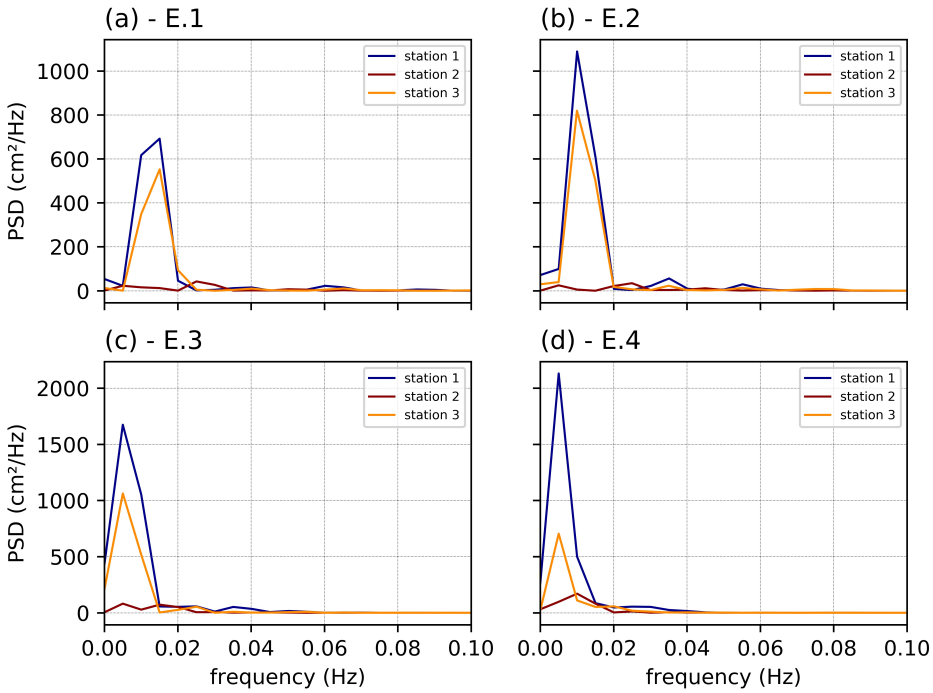

Figure 44 – Power Spectral density of the vertical interfacial displacement for experiments ran with $h_e/H = 0.5$ in all three stations: (a) E.1, (b) E.2, (c) E.3, and (d) E.4.

The four two-layer experiments conduced with ratio $h_e/H = 0.5$ (Figure 44) presented $\Delta\rho \approx 7$ kg/m^3, 5 kg/m^3, 3 kg/m^3, and 1 kg/m^3 for experiments E.1, E.2, E.3, and E.4, respectively. The first three laboratory experiments show a similar behavior along the tank, a decreasing growth in amplitude. However, for the laboratory experiment with $\Delta\rho \approx 1$ kg/m^3, which presents low Ri, the spectral energy rises increasing with the distance of the internal wave node (Figure 45). In this case, the interface is curved up- and downward at the basin end, depending on the wave phase. It suggests that the tilt of the interface along the tank does not follow a linear solution, as described by Antenucci, Imberger and Saggio (2000), considering a low Ri number.

According to Shintani et al. (2010), finite amplitude effects must be taken into account when $W < 3$. The curvature of the interfacial displacement, that is assumed to be infinitesimally small by the linear Wedderburn number scaling, leads to a upwelling to the free surface at $W \approx 0.9$, rather than

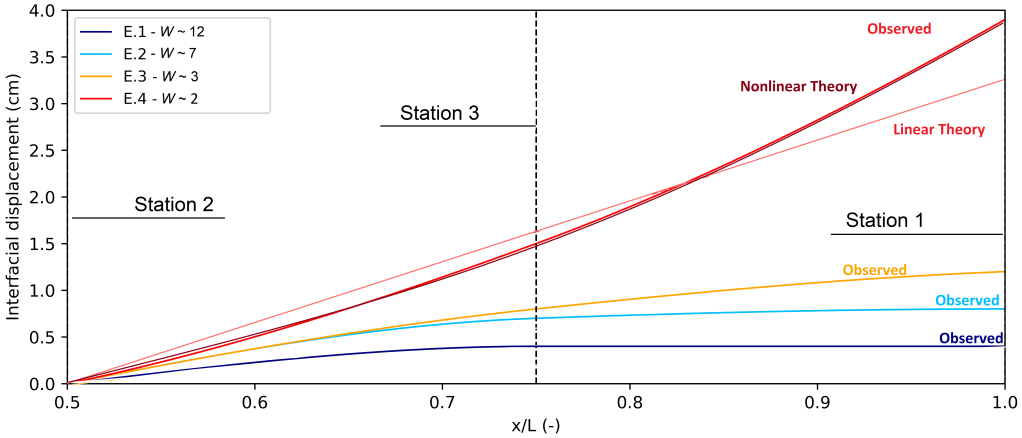

Figure 45 – Longitudinal shapes of the spectral energy distribution for experiments with ratio $h_e/H = 0.5$. Curves were obtained through spline interpolation between each station value.

$W = 0.5$ as described by linear approach. Thus, in E.1, the internal wave amplitude rose more than 5 % in the end of the tank, whilst at station 3 the amplitude slightly decreases compared to the linear theory, as shown in Figure 45 and 46. For simplification we neglected the small vertical variation at $x/L = 0.5$. The solution conforms well with results obtained by Shintani et al. (2010) from numerical simulations.

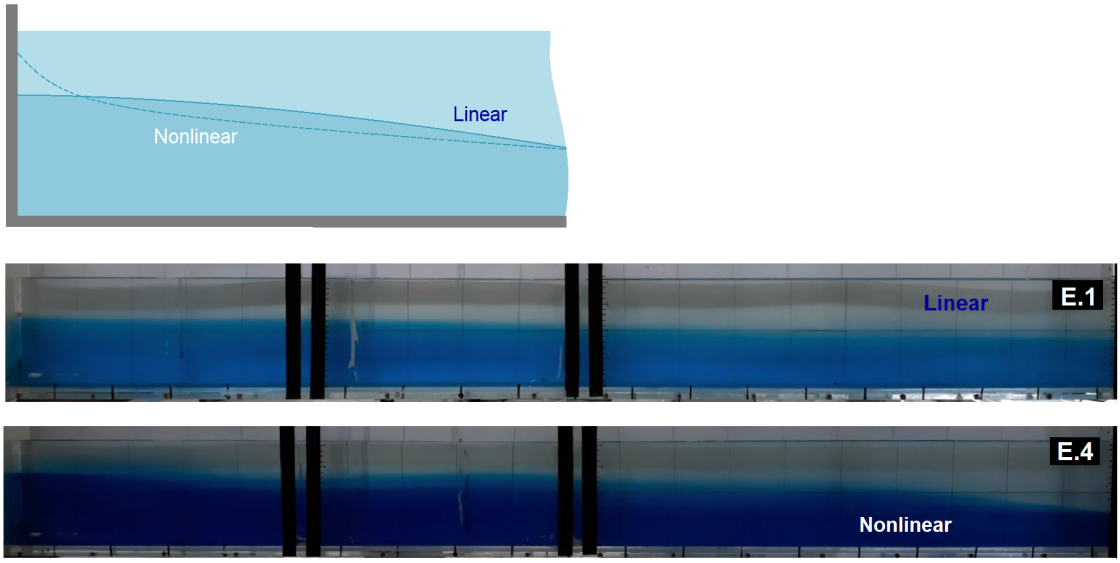

Figure 46 – Screenshots of experiments E.1 and E.4 to characterize the longitudinal shape of the interfacial waves.

Shintani et al. (2010) showed, based on numerical simulation and two experiments, that

$$W = \frac{8}{9}\tan\left(\frac{\pi}{2}\left(1 - \frac{b_i}{h_e}\right)^{1/0.57}\right)^{1/0.81} + \frac{8}{9}, \tag{4.2}$$

in which equation 4.2 accounts the nonlinear effects, and consequently describes the upward curvature of the interface.

The error in the linear solution is not limited to $W < 3$ but also to $W \gtrsim 3$. Although, in E.2 and E.3, the linear theory predicts lower internal seiche amplitude, the most notable interfacial variation is observed from $x/L = 0.5$ to 0.75 of the tank length. The variation is much higher than the value predicted by linear theory, described by Antenucci, Imberger and Saggio (2000). In this case, the amplitude does not grow linearly with the distance of the internal wave node, but grows rapidly in the first 0.5 meter, presenting approximately constant vertical displacement after the third fourth of the tank, mainly for $W \geq 7$ (Figure 47). For E.3, that has $W \approx 3$, the nonlinear effect did not tilt the interface upward at $x/L = 1$, however the internal wave amplitude continues growing after $x/L = 0.75$. It suggests that the internal wave amplitude does not vary linearly along the tank. The basin-scale internal wave shape is influenced by W and nonlinear effects. Thus, we conclude that, although linear theory predicts well the internal wave amplitude when $W \approx 12$, the internal seiche displacement is not properly modeled far from the shoreline. The nonlinear theory also presents some inconsistence for $W \geq 3$, but describe well the upwelling of the interface at the tank end, which is more evident for $W \ll 3$.

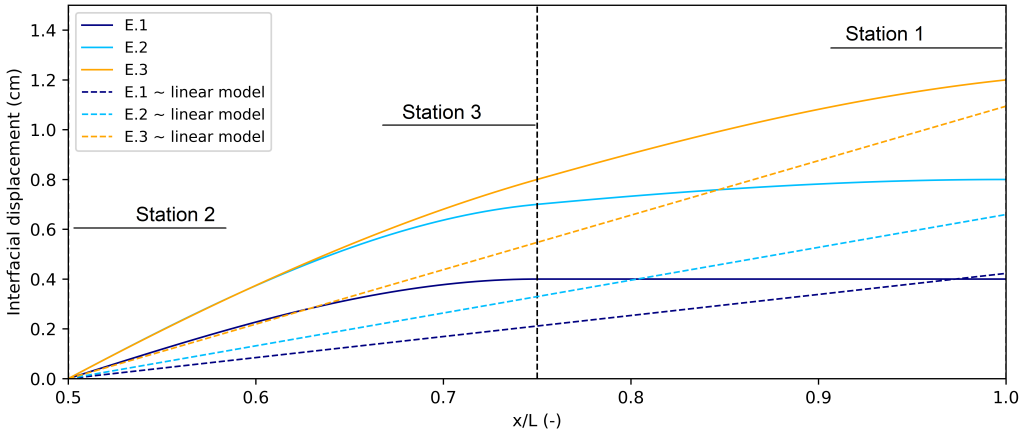

Figure 47 – Longitudinal shape of the vertical interfacial displacement for experiments E.1, E.2, and E.3.

4.4 Foundations and Connections

In this section we present a combined analysis of the laboratory experiments with field results. Firstly, we parametrized the Ri, that for field analysis we used the filtered Ri_{dir}, to h_e^2/L_p, in which h_e is the epilimnion thickness and L_p is the basin length of the intersection between the boundaries wall and the pycnocline shore in the instability direction. As expected, L_p for laboratory experiments are exactly equal to the tank length, L. Thus, the parametrization of Ri is plotted against the initial internal seiche amplitude, Figure 48.

The parametrization considers the difference between the basin lengths, making a comparison among each analyses possible. For low Ri values, the results did not fit well in the linear regression. The results that most deviated from the linear theory are those found in Vossoroca stratified winter, when Ri are really low and internal amplitude are great. In these circumstances, the system may present low W, and consequently the nonlinearity becomes stronger, causing a curvature of the interfacial displacement, which causes an increase of internal wave amplitude. However, it can be suppressed by the proximity of the internal wave with the stratified basin surface. This is exactly what happened in the laboratory experiments with $h_e/H = 0.25$ and low W, and is plotted in figure 48.

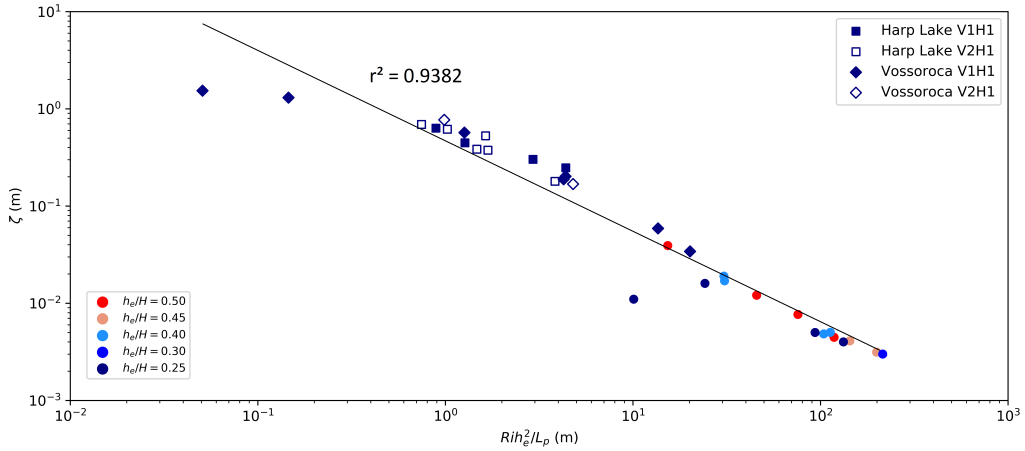

Figure 48 – Parametrization of Ri (Rih_e^2/L_p) as a function of initial internal seiche amplitude.

The W may be obtained dividing the Rih_e^2/L_p by h_e. Normalizing the internal wave amplitude by h_e, we observe that the ratio ζ_o/h_e increases exponentially as the W decreases (Figure 49 (a)). However, since the internal wave is unstable and internal wave displacement approach to the basin surface, basin-scale internal seiche can steepen into high-frequency internal waves, increasing the mixing. Part of energy is dissipated and the internal wave amplitude gets smaller than predicted by nonlinear and linear theories. This was observed for $W < 0.7$ in two periods that was analyzed during winter in Vossoroca reservoir and two laboratory experiments, as shown in Figure 49 (a). The linear and nonlinear solution are obtained through a normalization of equations 2.27 and 4.2, respectively.

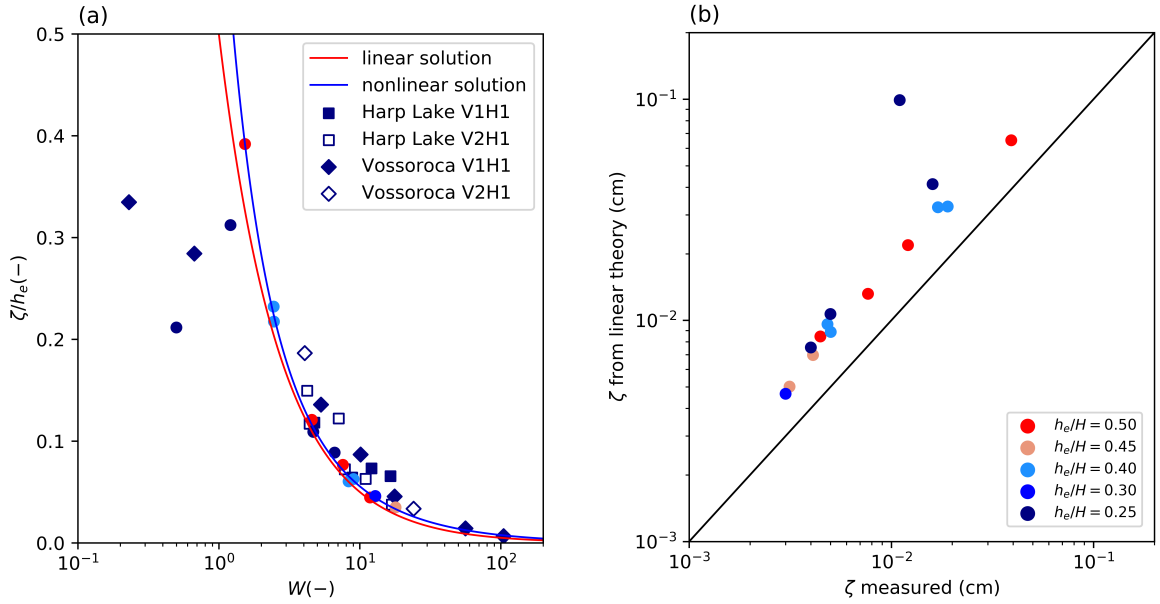

Figure 49 – (a) Vertical displacements of the interface at upwind side together with linear and nonlinear theory as a function of the effective Wedderburn number, W. (b) Linear solution error against the ratio ζ_o/h_e for laboratory experiments.

The linear solution has lower agreement with the measured interfacial displacement considering

the laboratory experiments for higher amplitude waves, presenting poorer results for lower W. In other words, as the ζ_o/h_e increases, the nonlinear advection terms begin to play an important role, and consequently the internal wave amplitude deviates from the linear theory (Figure 49 (b)). The nonlinear solution, given by equation 4.2, shows good agreement with results obtained by laboratory experiments with error lower than 5%, except for $h_e/H = 0.25$, that presented error $\approx 20\%$ (Figure 50). This increase of error for ratio $h_e/H = 0.25$ is related to the instability caused by the presence of high frequency internal waves and the proximity of the interfacial displacement to the water surface, as discussed in section 4.3.1.

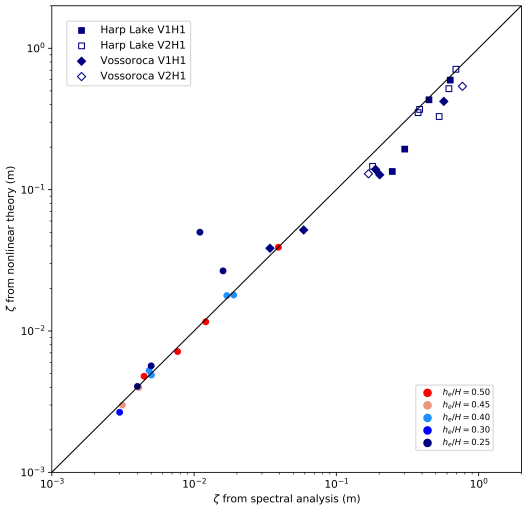

Figure 50 – Internal seiche amplitude obtained through nonlinear solution against the real amplitude.

Another relevant observation is related to higher W. The linear and nonlinear solution underestimated the internal wave amplitude for field observation. As suggested in section 4.2.1, the growth in amplitude is due to the resonance effect caused by the wind forcing frequency. Both mathematical descriptions, linear and nonlinear theories, underestimate the amplitude of the basin-scale internal seiche (Figure 50). For both basins and modes, the initial amplitude was approximately 30% greater than that predicted by the linear and nonlinear theory, except for $W < 1$, that, as discussed before, presented an amplitude reduction due to instabilities and the proximity with the lake surface. Although we do not observe a clear evidence that resonance occurs exactly when internal seiche periodicity matches an frequency of the wind component, we observe that the integration of the power spectral density of the wind velocity of higher frequencies are directly proportional to the growth of amplitude due to resonance effect, as shown in Figure 51. It suggests that the wind fluctuations with higher frequency than the internal seiches are responsible to the amplitude growth due to resonance effects. This conclusion agrees well with laboratory results conduced by Boegman and Ivey (2012), considering that both basins are relatively shallow, $H/L \ll 1$, the resonant bandwidth shift is positive with maximum amplification occurring for forcing frequencies higher than the internal wave frequency.

To finish our analysis we outline important points in regard to the classification of internal waves through the relationship between the friction velocity of the wind and the baroclinic pressure gradient, representing the importance of the shear velocity as a source of turbulent kinetic energy available for mixing, which is represented by the non-dimensional parameter W. For high W, $\gg 12$, we observe the formation of small amplitude internal seiches (Figure 52 (a)). The interfacial displacement presents good

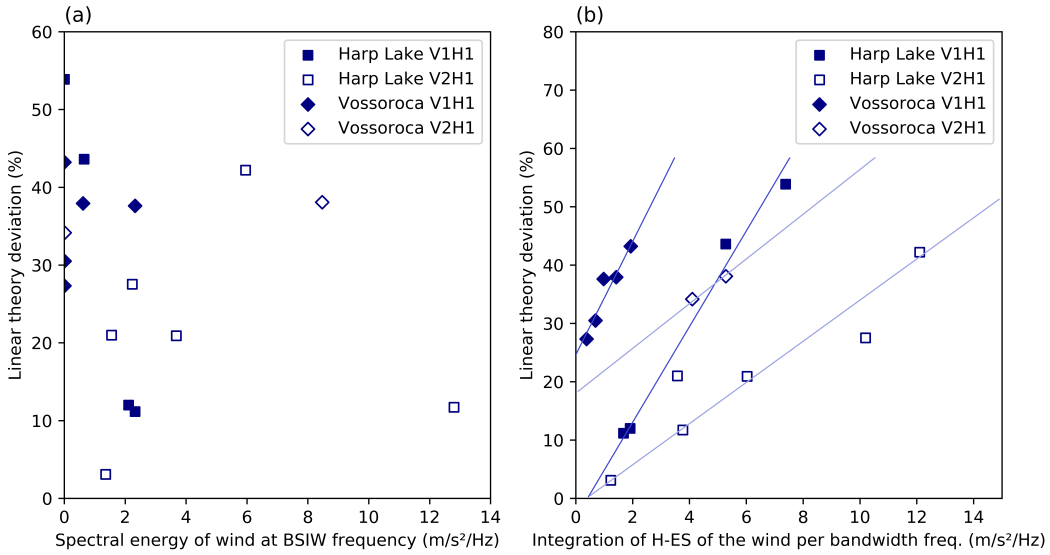

Figure 51 – Amplitude growth due to resonance effect against (a) the peak of the power spectral density of the wind intensity at the internal seiche period and (b) the sum of the power spectral density of the wind speed for frequency higher than the internal seiche frequency normalized by bandwidth frequency of the wind intensity.

agreement with linear theory, except when resonance between internal seiche modes and wind forced oscillations play important role in the amplitude growth. In such cases, we observed an increase of approximately 30% on the internal wave amplitude compared to linear solution. It is hard to measure the difference between errors associated to the effect of position of temperature measurements and resonance effects. However, apparently the position for station is not so determinant for $W \gg 12$, except if the station is deployed in the first one third distance from the wave node.

For $W < 12$ and > 3, the linear theory predicted well the interfacial displacement and the position of thermistor chain does not perturbed the amplitude estimation, Figure 52 (b). The internal seiches are characterized by constant variation along the basin and abrupt variation just near the wave node, mainly in the first one third distance from the wave node. Although we detected for laboratory experiments that the location of thermistor chain is important even near the basin shore for $W \approx 3$, field observations predicted well the internal wave amplitude even in Harp Lake. In addition, for $W \approx 3$, the greater errors were observed due to nonlinear steepening, except for periods with resonance effects.

For $W < 3$, the linear theory fails strongly to observe the amplitude growth, however, when $W \ll 1$, the growth is fallowed by strong instabilities that stop their complete development. Thus, the linear and nonlinear theories overestimate the amplitude of the basin-scale internal waves. This has been observed experimentally, by experiment E.14, and through field observations in Vossoroca reservoir, during periods of Winter, F.6 and F.7, see Table 5 in appendix C and Table 11 in appendix D.

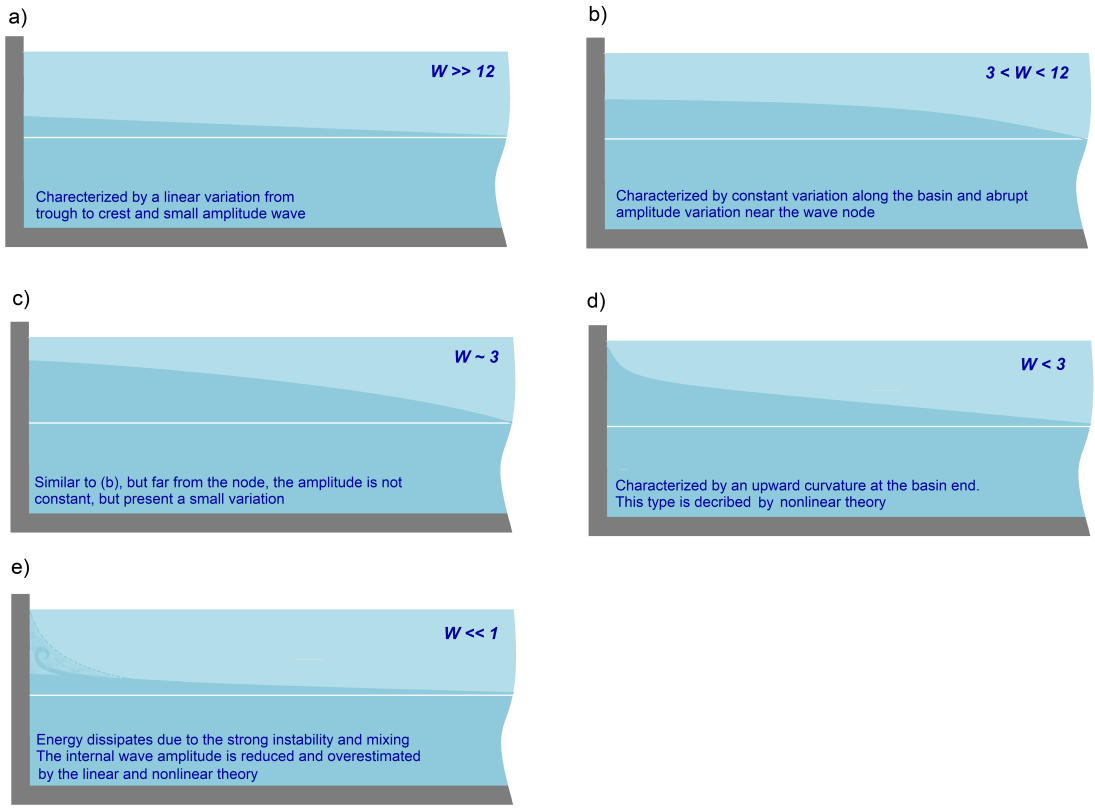

Figure 52 – Sketch of the different regimes of internal wave generation due to wind stress in a rectangular two-layer stratified basin.

5 Conclusion

In this concluding chapter we summarize the research questions and the general conclusion based on the findings of this master thesis. In addition, the research limitation and recommendation for future studies, which include the avenues to be explored for future developments about internal seiches in lakes and reservoirs, are summarized in the end of this chapter.

5.1 Research Objectives

This master thesis verified the importance of the shear velocity as a source of turbulent kinetic energy available for mixing during internal wave events considering small stratified basins. We compared the results with linear and nonlinear theories, as discussed by Spigel and Imberger (1980) and Shintani et al. (2010), respectively. We observed that although both mathematical descriptions presented good agreement with the observed results, for some conditions we detected a strong deviation between theoretical and experimental results. The error associated to nonlinear terms have been extensively discussed by various authors, and we observed that the linear solution underestimated the internal wave amplitude when $W \approx 3$, as expected by Shintani et al. (2010).

However, we observed through laboratory experiments and field observations that for $W < 1$ and $h_e/H < 0.25$, the analytical mathematical models strongly overestimated the interfacial displacement, presenting errors much greater than those due to nonlinear terms. This suggests that turbulent kinetic energy available is also used to produce mixing and billows, extracting energy that would be used to the internal wave growth. This suggests that there is a critical value of W, probably between 0.8 and 1, which represents the maximum internal seiche amplitude before instabilities start to play a crucial role in the internal wave evolution.

In addition, considering $W > 3$ detected in field observations, we observed that the mathematical solutions underestimated (around $0-40\%$) the internal seiche amplitude, depending on the spectral wind intensity. The resonance phenomenon have been reported early in large lakes, with positive contribution made by Mortimer (1953) and Münnich, Wüest and Imboden (1992), that pointed out that the daily wind circle enable the increase of internal wave amplitude as its period is near resonance. However, we observed that the wind resonance in small stratified basins is more associated to energy of the wind frequencies lower than the frequency of the internal seiche. This phenomenon have been studied experimentally by Boegman and Ivey (2012), and evidenced in our analysis through field observations in shallow and small stratified lakes.

We studied the longitudinal evolution of the internal seiche. We observed that not just the interfacial amplitude of the internal wave depends on the turbulent kinetic energy available for mixing, but also the longitudinal evolution of the wave. We suggest that the greater longitudinal variation occurs when $W \approx 3$, which presents waveform quite similar to that predicted by nonlinear theory and discussed by Shintani et al. (2010). However, for $W \approx 1$, the internal wave instabilities may develop, and just small amplitude internal seiche may be excited, presenting form similar to waves generated when $W \gg 12$. We observed that between this range, $3 < W < 12$, internal seiches amplitude just present strong interfacial variation within the first one third distance from the wave node.

Moreover, we classified the regimes of generation and degeneration that should occur in Vossoroca

reservoir and Harp Lake based essentially on regimes described by Spigel and Imberger (1980) and Boegman, Ivey and Imberger (2005a). We observed that most of time high amplitude internal waves are damped by viscous or degenerate into a high-frequency internal waves, in which for small basins the probability of nonlinear degeneration is much higher than large lakes. In addition, although small amplitude internal waves generally is damped before it can steepen and evolve into high frequency waves, we observe that even small amplitude waves may steepen and evolve into nonlinear internal waves.

Finally, it may be mentioned that although some other observations and analysis have been already conduced for other authors, a complete analyses of the shear velocity as a source of turbulent kinetic energy available for mixing, using several periods along the year of two small basins and laboratory experiments, have never been reported in the literature. In addition, we applied some recent techniques to better represent and explore the internal seiche propagations. We observed that the internal wave analysis improved through the filtering processes, applied to Ri as discussed by Gaudard et al. (2017), and better computed the wind energy availability to excite internal seiches.

5.2 Research Limitation

Our analysis are essentially based on underwater temperature obtained from only one thermistor chain. The study of the degeneration of basin scale internal waves is a far more challenging task, and just can be satisfactorily conduced through a longitudinal observation of the isotherm fluctuation. In this study we just observed the regimes of degeneration based on theoretical solutions of a two-layer system, as described by Boegman, Ivey and Imberger (2005a), and consequently we could not infer any conclusion about the degeneration of the second vertical mode and experimental results. Thus, to have a comprehensive analysis about the disintegration of basin-scale internal waves, we recommend the implementation of more thermistor chains along a main lake axis.

In addition, although Hutter, Wang and Chubarenko (2011) have pointed out that isotherms analysis have been the most popular used variable to record internal waves, vertical profiles of currents may also help on internal wave investigation.

Here, it may be mentioned the limitation of the analytical and linear models. In our models the length of two opposite interface shore (the interface with the bottom profile), L_p, and the interface depth was obtained considering the mean wind direction and a general 1D topography. However the values of these variables, used to model the internal seiche formation, are somewhat subjective, since the slope of the basin shore may be different depending on the regions. A more realistic procedure certainly requires a 3D topography. The 3D topography also would help in the identification of separated basins, in which may also excite higher horizontal modes, as observed by Roget, Salvadé and Zamboni (1997). Even though the model predicted the periodicity of internal waves with relatively good agreement, it neglects the instabilities, degenerations, topography features, and variation of stratification.

With respect to laboratory experiments, although we obtained good results, the shear velocity as a source of turbulent kinetic energy available for mixing depended essentially on the salinity stratification. In other words, we could not keep the instability frequency for a range of stratification. Thus, we needed to account how much of energy was transferred to the interface between heavier and lighter fluid to generate the interfacial displacement. The gravity current technique applied here could reproduce well the internal waves, but it produces strong turbulence that is much greater than in nature. Thus, the mixing analysis were compromised since is hard to separate the mixing into those from gravity current and internal waves motion.

5.3 Recommendation and Future Investigations

There are several lines of research arising from this work which should be pursued.

In particular, we investigated the internal wave patterns excited under a wide range of W. Since we observed a critical value near $W \approx 1$, which would represent the maximum internal seiche amplitude before instabilities start to play a crucial role in the internal wave evolution, future studies might predict the exact critical value of W, running several experiments for $W \approx 1$.

Another area for further research that have been highlighted by this study is the occurrence of nonlinear degeneration of basin-scale internal waves in small stratified basins. Thus, this brings attention to a deeply investigation of the degeneration of basin-scale internal wave in small lakes. In addition, since nonlinear internal waves tend to be excited due to the degeneration of basin-scale internal waves in small lakes, nonlinear internal waves in small stratified basins need to be better investigated, since, according to Droghei et al. (2016), nonlinear internal waves are responsible to a significant influence water quality, affecting directly the sediment resuspension and water mixing. Although the degeneration of basin-scale internal wave have been studied by many authors, the establishment of a theory for multi-layer system have been completed neglected.

Finally, even though there are many studies that have been conduced to evaluate the influence of internal wave activity on water quality, new studies might be conduced using this classification based on the importance of the shear velocity as a source of turbulent kinetic energy available for mixing, which are more detailed than the general lake water mixing theory presented by Spigel and Imberger (1980).

Bibliography

ALFORD, M. H.; PEACOCK, T.; MACKINNON, J. A.; NASH, J. D.; BUIJSMAN, M. C.; CENTURIONI, L. R.; CHAO, S.-Y.; CHANG, M.-H.; FARMER, D. M.; FRINGER, O. B. et al. The formation and fate of internal waves in the south china sea. *Nature*, Nature Publishing Group, v. 521, n. 7550, p. 65, 2015.

ALLOWAY, B.; AYRES, D. C. *Chemical principles of environmental pollution*. [S.l.]: CRC press, 1997.

ANTENUCCI, J. P.; IMBERGER, J. The seasonal evolution of wind/internal wave resonance in lake kinneret. *Limnology and oceanography*, Wiley Online Library, v. 48, n. 5, p. 2055–2061, 2003.

ANTENUCCI, J. P.; IMBERGER, J.; SAGGIO, A. Seasonal evolution of the basin-scale internal wave field in a large stratified lake. *Limnology and oceanography*, Wiley Online Library, v. 45, n. 7, p. 1621–1638, 2000.

APPT, J.; IMBERGER, J.; KOBUS, H. Basin-scale motion in stratified upper lake constance. *Limnology and Oceanography*, Wiley Online Library, v. 49, n. 4, p. 919–933, 2004.

BAR, D. Densimetric exchange flow in rectangular channels. *La Houille Blanche*, EDP Sciences, n. 6, p. 619–632, 1967.

BARENBLATT, G. I. *Dimensional analysis*. [S.l.]: CRC Press, 1987.

BARRON, J. J.; ASHTON, C. The effect of temperature on conductivity measurement. *TSP*, v. 7, n. 73, p. 1–5, 2005.

BATCHELOR, G. K. *An introduction to fluid dynamics*. [S.l.]: Cambridge university press, 2000.

BAUERLE, E. Internal free oscillations in the lake of geneva. In: GAUTHIER-VILLARS. *Annales Geophysicae*. [S.l.], 1985. v. 3, n. 2, p. 199–206.

BÄUERLE, E. Transverse baroclinic oscillations in lake überlingen. *Aquatic sciences*, Springer, v. 56, n. 2, p. 145–160, 1994.

BELETSKY, D.; FILATOV, N.; IBRAEV, R. Hydrodynamics of lakes ladoga and onega. *Water Quality Research Journal of Canada*, v. 29, n. 2-3, 1994.

BENJAMIN, T. B. Gravity currents and related phenomena. *Journal of Fluid Mechanics*, Cambridge University Press, v. 31, n. 2, p. 209–248, 1968.

BERNHARDT, J.; KIRILLIN, G. Seasonal pattern of rotation-affected internal seiches in a small temperate lake. *Limnology and Oceanography*, Wiley Online Library, v. 58, n. 4, p. 1344–1360, 2013.

BIRGE, E. A. The work of the wind in warming a lake. *Trans. Wis. Acad. Sci. Arts Lett.*, v. 18, p. 341–391, 1916.

BOEGMAN, L. Currents in stratified water bodies 2: Internal waves. *Encyclopedia of inland waters*, Academic Press, v. 1, p. 539–558, 2009.

BOEGMAN, L.; IMBERGER, J.; IVEY, G. N.; ANTENUCCI, J. P. High-frequency internal waves in large stratified lakes. *Limnology and oceanography*, Wiley Online Library, v. 48, n. 2, p. 895–919, 2003.

BOEGMAN, L.; IVEY, G.; IMBERGER, J. The degeneration of internal waves in lakes with sloping topography. *Limnology and oceanography*, Wiley Online Library, v. 50, n. 5, p. 1620–1637, 2005.

BOEGMAN, L.; IVEY, G.; IMBERGER, J. The energetics of large-scale internal wave degeneration in lakes. *Journal of Fluid Mechanics*, Cambridge University Press, v. 531, p. 159–180, 2005.

BOEGMAN, L.; IVEY, G. N. The dynamics of internal wave resonance in periodically forced narrow basins. *Journal of Geophysical Research: Oceans*, Wiley Online Library, v. 117, n. C11, 2012.

BOEHRER, B.; ILMBERGER, J.; MÜNNICH, K. O. Vertical structure of currents in western lake constance. *Journal of Geophysical Research: Oceans*, Wiley Online Library, v. 105, n. C12, p. 28823–28835, 2000.

BOGUCKI, D. J.; REDEKOPP, L. G. A mechanism for sediment resuspension by internal solitary waves. *Geophysical Research Letters*, Wiley Online Library, v. 26, n. 9, p. 1317–1320, 1999.

BOGUCKI, D. J.; REDEKOPP, L. G. Climate of long internal waves and resuspension on the coastal shelf. *Oceanologia*, -, v. 50, n. 1, p. 5–21, 2008.

BOOKER, J. R.; BRETHERTON, F. P. The critical layer for internal gravity waves in a shear flow. *Journal of Fluid Mechanics*, Cambridge University Press, v. 27, n. 3, p. 513–539, 1967.

BOUFFARD, D.; ACKERMAN, J. D.; BOEGMAN, L. Factors affecting the development and dynamics of hypoxia in a large shallow stratified lake: hourly to seasonal patterns. *Water Resources Research*, Wiley Online Library, v. 49, n. 5, p. 2380–2394, 2013.

BOUFFARD, D.; BOEGMAN, L. Basin-scale internal waves. In: *Encyclopedia of lakes and Reservoirs*. [S.l.]: Springer, 2012. p. 102–107.

BOUFFARD, D.; ZDOROVENNOV, R. E.; ZDOROVENNOVA, G. E.; PASCHE, N.; WÜEST, A.; TERZHEVIK, A. Y. Ice-covered lake onega: effects of radiation on convection and internal waves. *Hydrobiologia*, Springer, v. 780, n. 1, p. 21–36, 2016.

BOURGAULT, D.; GALBRAITH, P.; CHAVANNE, C. Generation of kelvin-helmholtz billows and internal solitons at geophysical fronts. In: *EGU General Assembly Conference Abstracts*. [S.l.: s.n.], 2016. v. 18, p. 7099.

BROWN, D. *Tracker Video Analysis and Modeling Tool*. 2017.

BRUCE, L. C.; JELLISON, R.; IMBERGER, J.; MELACK, J. M. Effect of benthic boundary layer transport on the productivity of mono lake, california. *Saline systems*, BioMed Central, v. 4, n. 1, p. 11, 2008.

BRYSON, R. A.; RAGOTZKIE, R. A. On internal waves in lakes. *Limnology and Oceanography*, Wiley Online Library, v. 5, n. 4, p. 397–408, 1960.

BUENO, R.; BLENINGER, T. Verificação da ocorrência de ondas internas no reservatório do vossoroca. In: *XXII Simpósio Brasileiro de Recursos Hídricos*. Florianópolis-SC, Brazil: [s.n.], 2017.

BUENO, R.; BLENINGER, T. Wind-induced internal seiches in vossoroca reservoir, pr, brazil. *RBRH*, SciELO Brasil, v. 23, 2018.

BUENO, R.; MARCON, L.; WOSIACKI, L.; ROMERO, M.; MANNICH, M.; BLENINGER, T. Correntes de gravidade e de intrusão produzidas pelo experimento lock-exchange. In: *XXII Simpósio Brasileiro de Recursos Hídricos*. Florianópolis-SC, Brazil: [s.n.], 2017.

BUERK, D. G. *Biosensors: Theory and applications*. [S.l.]: Crc Press, 1995.

BUICK, J. M. *Lattice Boltzmann methods in interfacial wave modelling*. (Doctoral dissertation) — University of Edinburgh, 1997.

CHAKRABARTI, S. *Handbook of Offshore Engineering (2-volume set)*. [S.l.]: Elsevier, 2005.

CHU, E. *Discrete and continuous fourier transforms: analysis, applications and fast algorithms*. [S.l.]: Crc Press, 2008.

COMMISSION, I. O. et al. The international thermodynamic equation of seawater–2010: calculation and use of thermodynamic properties. corrections – 2015. Unesco, 2015.

COOLEY, J. W.; TUKEY, J. W. An algorithm for the machine calculation of complex fourier series. *Mathematics of computation*, JSTOR, v. 19, n. 90, p. 297–301, 1965.

CRAIG, H. Standard for reporting concentrations of deuterium and oxygen-18 in natural waters. *Science*, American Association for the Advancement of Science, v. 133, n. 3467, p. 1833–1834, 1961.

CSANADY, G.; SCOTT, J. T. Baroclinic coastal jets in lake ontario during ifygl. *Journal of Physical oceanography*, v. 4, n. 4, p. 524–541, 1974.

CUSHMAN-ROISIN, B.; BECKERS, J.-M. *Introduction to geophysical fluid dynamics: physical and numerical aspects*. [S.l.]: Academic Press, 2011. v. 101.

CUYPERS, Y.; VINÇON-LEITE, B.; GROLEAU, A.; TASSIN, B.; HUMBERT, J.-F. Impact of internal waves on the spatial distribution of planktothrix rubescens (cyanobacteria) in an alpine lake. *The ISME journal*, Nature Publishing Group, v. 5, n. 4, p. 580, 2011.

DEFANT, A. Neue methode zur ermittlung der eigenschwingungen (seiches) von abgeschlossenen wassermassen (seen, buchten usw). *Ann. Hydrogr*, v. 46, p. 78–85, 1918.

DENNY, M. W.; GAINES, S. D. *Encyclopedia of tidepools and rocky shores*. [S.l.]: Univ of California Press, 2007.

DOWNING, J.; PRAIRIE, Y.; COLE, J.; DUARTE, C.; TRANVIK, L.; STRIEGL, R.; MCDOWELL, W.; KORTELAINEN, P.; CARACO, N.; MELACK, J. et al. The global abundance and size distribution of lakes, ponds, and impoundments. *Limnology and Oceanography*, Wiley Online Library, v. 51, n. 5, p. 2388–2397, 2006.

DROGHEI, R.; FALCINI, F.; CASALBORE, D.; MARTORELLI, E.; MOSETTI, R.; SANNINO, G.; SANTOLERI, R.; CHIOCCI, F. The role of internal solitary waves on deep-water sedimentary processes: the case of up-slope migrating sediment waves off the messina strait. *Scientific reports*, Nature Publishing Group, v. 6, p. 36376, 2016.

DU, K.-L.; SWAMY, M. N. *Wireless communication systems: from RF subsystems to 4G enabling technologies*. [S.l.]: Cambridge University Press, 2010.

EKMAN, V. W. On dead water. *Sci. Results Norw. Polar Expedi. 1893-96*, v. 5, n. 15, p. 152, 1904.

EVANS, M. A.; MACINTYRE, S.; KLING, G. W. Internal wave effects on photosynthesis: Experiments, theory, and modeling. *Limnology and Oceanography*, Wiley Online Library, v. 53, n. 1, p. 339–353, 2008.

FARGE, M. Wavelet transforms and their applications to turbulence. *Annual review of fluid mechanics*, Annual reviews 4139 El Camino Way, PO Box 10139, Palo Alto, CA 94303-0139, USA, v. 24, n. 1, p. 395–458, 1992.

FARMER, D. M. Observations of long nonlinear internal waves in a lake. *Journal of Physical Oceanography*, v. 8, n. 1, p. 63–73, 1978.

FERNANDO, H. J. *Handbook of Environmental Fluid Dynamics, Volume Two: Systems, Pollution, Modeling, and Measurements*. [S.l.]: CRC press, 2012. v. 2.

FJELDSTAD, J. E. *Interne wellen*. [S.l.]: Grøndahl & søns boktrykkeri, I kommission hos Cammermeyers boghandel, 1933.

FOFONOFF, N. P.; MILLARD, R. Algorithms for the computation of fundamental properties of seawater. Unesco, 1983.

FORCAT, F.; ROGET, E.; FIGUEROA, M.; SÁNCHEZ, X. Earth rotation effects on the internal wave field in a stratified small lake. *limnetica*, v. 30, n. 1, p. 0027–42, 2011.

GABOR, D. Theory of communication. part 1: The analysis of information. *Journal of the Institution of Electrical Engineers-Part III: Radio and Communication Engineering*, IET, v. 93, n. 26, p. 429–441, 1946.

GAEDKE, U.; SCHIMMELE, M. Internal seiches in lake constance: influence on plankton abundance at a fixed sampling site. *Journal of plankton research*, Oxford University Press, v. 13, n. 4, p. 743–754, 1991.

GAO, R. X.; YAN, R. *Wavelets: Theory and applications for manufacturing*. [S.l.]: Springer Science & Business Media, 2010.

GAUDARD, A.; SCHWEFEL, R.; VINNÅ, L. R.; SCHMID, M.; WÜEST, A.; BOUFFARD, D. Optimizing the parameterization of deep mixing and internal seiches in one-dimensional hydrodynamic models: a case study with simstrat v1. 3. *Geoscientific Model Development*, Copernicus GmbH, v. 10, n. 9, p. 3411–3423, 2017.

GORHAM, E.; BOYCE, F. M. Influence of lake surface area and depth upon thermal stratification and the depth of the summer thermocline. *Journal of Great Lakes Research*, Elsevier, v. 15, n. 2, p. 233–245, 1989.

GOVORUSHKO, S. M. *Natural processes and human impacts: interactions between humanity and the environment*. [S.l.]: Springer Science & Business Media, 2011.

GRAY, J. R. Conductivity analyzers and their application. *Environmental instrumentation and analysis handbook*, Wiley Online Library, p. 491–510, 2005.

GREENBERG, M. D. *Foundations of applied mathematics*. [S.l.]: Courier Corporation, 2013.

GRIMSHAW, R. *Solitary waves in fluids*. [S.l.]: WIT Press, 2007. v. 47.

GUBBINS, D. *Time series analysis and inverse theory for geophysicists*. [S.l.]: Cambridge University Press, 2004.

GUYENNON, N.; VALERIO, G.; SALERNO, F.; PILOTTI, M.; TARTARI, G.; COPETTI, D. Internal wave weather heterogeneity in a deep multi-basin subalpine lake resulting from wavelet transform and numerical analysis. *Advances in Water Resources*, v. 71, p. 149 – 161, 2014.

HAMAGAMI, K.; MORI, K.; IGUCHI, S.; HIRAI, Y. Response characteristics of internal wave to wind stress in a shallow closed water body. *Journal of the Faculty of Agriculture, Kyushu University*, Citeseer, v. 56, n. 1, p. 123–128, 2011.

HASSELMANN, K.; BARNETT, T. P.; BOUWS, E.; CARLSON, H.; CARTWRIGHT, D. E.; ENKE, K.; EWING, J. A.; GIENAPP, H.; HASSELMANN, D. E.; KRUSEMAN, P.; MEERBURG, A.; MüLLER, P.; OLBERS, D.; RICHTER, K.; SELL, W.; WALDEN, H. Measurements of wind-wave growth and swell decay during the joint north sea wave project (jonswap). v. 8, p. 1–95, 01 1973.

HAYNES, W. M. *CRC handbook of chemistry and physics*. [S.l.]: CRC press, 2014.

HEAPS, N. Seiches in a narrow lake, uniformly stratified in three layers. *Geophysical Journal International*, Blackwell Publishing Ltd Oxford, UK, v. 5, n. 2, p. 134–156, 1961.

HEBERT, D.; RUDDICK, B. R. Differential mixing by breaking internal waves. *Geophysical research letters*, Wiley Online Library, v. 30, n. 2, 2003.

HEINZEL, G.; RÜDIGER, A.; SCHILLING, R. Spectrum and spectral density estimation by the discrete fourier transform (dft), including a comprehensive list of window functions and some new at-top windows. 2002.

HERMAN, S. L. *Electronics for electricians*. [S.l.]: Cengage Learning, 2011.

HINGSAMER, P.; PEETERS, F.; HOFMANN, H. The consequences of internal waves for phytoplankton focusing on the distribution and production of planktothrix rubescens. *PloS one*, Public Library of Science, v. 9, n. 8, p. e104359, 2014.

HORN, D.; IMBERGER, J.; IVEY, G. The degeneration of basin-scale internal waves in lakes. In: *Thirteenth Australasian Fluid Mechanics Conference*. Monash University: [s.n.], 1998. p. 863–866.

HORN, D.; IMBERGER, J.; IVEY, G. The degeneration of large-scale interfacial gravity waves in lakes. *Journal of Fluid Mechanics*, Cambridge University Press, v. 434, p. 181–207, 2001.

HORN, D.; IMBERGER, J.; IVEY, G.; REDEKOPP, L. A weakly nonlinear model of long internal waves in closed basins. *Journal of Fluid Mechanics*, Cambridge University Press, v. 467, p. 269–287, 2002.

HORN, W.; MORTIMER, C. H.; SCHWAB, D. J. Wind-induced internal seiches in lake zurich observed and modeled. *Limnology and oceanography*, Wiley Online Library, v. 31, n. 6, p. 1232–1254, 1986.

HUNKINS, K.; FLIEGEL, M. Internal undular surges in seneca lake: A natural occurrence of solitons. *Journal of geophysical research*, Wiley Online Library, v. 78, n. 3, p. 539–548, 1973.

HUTTER, K.; CHUBARENKO, I. P.; WANG, Y. *Physics of Lakes: Volume 3: Methods of Understanding Lakes as Components of the Geophysical Environment*. [S.l.]: Springer Science & Business Media, 2014.

HUTTER, K.; WANG, Y.; CHUBARENKO, I. P. *Physics of Lakes, volume 2: lakes as oscillators. Advances in geophysical and environmental mechanics and mathematics*. [S.l.]: Springer, 2011.

HYDRAULICS, W. D. . *User Manual of Delft3D-FLOW—Simulation of Multi-dimensional Hydrodynamic Flows and Transport Phenomena, Including Sediments*. 2003. 497 pp. p.

IMBERGER, J. The diurnal mixed layer1. *Limnology and oceanography*, Wiley Online Library, v. 30, n. 4, p. 737–770, 1985.

IMBERGER, J. Transport processes in lakes: A review. Elsevier Science, 1994.

IMBERGER, J. Flux paths in a stratified lake. *Physical processes in lakes and oceans*, Wiley Online Library, p. 1–17, 1998.

IMBERGER, J. *Physical processes in lakes and oceans*. [S.l.]: American Geophysical Union, 1998. v. 54.

IMBERGER, J.; PATTERSON, J. C. Physical limnology. *Advances in applied mechanics*, Elsevier, v. 27, p. 303–475, 1989.

IVEY, G.; WINTERS, K.; SILVA, I. D. Turbulent mixing in a sloping benthic boundary layer energized by internal waves. *Journal of Fluid Mechanics*, Cambridge University Press, v. 418, p. 59–76, 2000.

JACKSON, P. R.; REHMANN, C. R. Experiments on differential scalar mixing in turbulence in a sheared, stratified flow. *Journal of Physical Oceanography*, v. 44, n. 10, p. 2661–2680, 2014.

JI, Z.-G. *Hydrodynamics and water quality: modeling rivers, lakes, and estuaries*. [S.l.]: John Wiley & Sons, 2017.

KANTHA, L. H. On generation of internal waves by turbulence in the mixed layer. *Dynamics of Atmospheres and Oceans*, Elsevier, v. 3, n. 1, p. 39–46, 1979.

KELL, G. S. Density, thermal expansivity, and compressibility of liquid water from 0. deg. to 150. deg.. correlations and tables for atmospheric pressure and saturation reviewed and expressed on 1968 temperature scale. *Journal of Chemical and Engineering Data*, ACS Publications, v. 20, n. 1, p. 97–105, 1975.

KEULEGAN, G. An experimental study of the motion of saline water from locks into fresh water channels. *Nat. Bur. Stand. Rept. Technical Report*, v. 5168, 1957.

KEULEGAN, G. H. The motion of saline fronts in still water. *Nat. Bur. Stand. Rept.*, v. 5831, 1953.

KNUDSEN MARTIN E FORCH, C. *Hydrographical tables*. [S.l.]: GECGAD, 1901.

KODAIRA, T.; WASEDA, T.; MIYATA, M.; CHOI, W. Internal solitary waves in a two-fluid system with a free surface. *Journal of Fluid Mechanics*, Cambridge University Press, v. 804, p. 201–223, 2016.

KUNDU, R. K.; COHEN, I. M. *Fluid mechanics*. [S.l.]: Academic press, 2002.

LAMMEL, K. Der geschichtete kochelsee unter windlast: Erste datenauswcrtung und ergebnisse. *Dtsch. Gewaesserkd. Mitt*, v. 28, p. 44–49, 1984.

LAMONT, G.; LAVAL, B.; PAWLOWICZ, R.; PIETERS, R.; LAWRENCE, G. A. Physical mechanisms leading to upwelling of anoxic bottom water in nitinat lake. In: UNIVERSITY OF DELAWARE, NEWARK, DELAWARE, EEUU. *17th ASCE Engineering Mechanisms Conference*. [S.l.], 2004. v. 8.

LAZERTE, B. D. The dominating higher order vertical modes of the internal seiche in a small lake. Wiley Online Library, 1980.

LEMMIN, U. The structure and dynamics of internal waves in baldeggersee. *Limnology and Oceanography*, Wiley Online Library, v. 32, n. 1, p. 43–61, 1987.

LEMMIN, U.; D'ADAMO, N. Summertime winds and direct cyclonic circulation: observations from lake geneva. In: SPRINGER. *Annales Geophysicae*. [S.l.], 1997. v. 14, n. 11, p. 1207–1220.

LEMMIN, U.; MORTIMER, C.; BÄUERLE, E. Internal seiche dynamics in lake geneva. *Limnology and Oceanography*, Wiley Online Library, v. 50, n. 1, p. 207–216, 2005.

LEMMIN, U.; MORTIMER, C. H. Tests of an extension to internal seiches of defant's procedure for determination of surface seiche characteristics in real lakes. *Limnology and oceanography*, Wiley Online Library, v. 31, n. 6, p. 1207–1231, 1986.

LIKENS, G. E. *Lake ecosystem ecology: A global perspective*. [S.l.]: Academic Press, 2010.

LIN, H. *Hydropedology: Synergistic integration of soil science and hydrology*. [S.l.]: Academic Press, 2012.

LONG, R. R. The steepening of long, internal waves. *Tellus*, Wiley Online Library, v. 24, n. 2, p. 88–99, 1972.

MACINTYRE, S. The surface mixed layer in lakes and reservoirs. *Biogeochemistry of Inland Waters*, Academic Press, p. 207, 2010.

MACINTYRE, S.; CLARK, J. F.; JELLISON, R.; FRAM, J. P. Turbulent mixing induced by nonlinear internal waves in mono lake, california. *Limnology and Oceanography*, Wiley Online Library, v. 54, n. 6, p. 2255–2272, 2009.

MACINTYRE, S.; JELLISON, R. Nutrient fluxes from upwelling and enhanced turbulence at the top of the pycnocline in mono lake, california. In: *Saline Lakes*. [S.l.]: Springer, 2001. p. 13–29.

MALONE, T. C. *The 1976 Ceratium tripos bloom in the New York Bight: Causes and consequences*. [S.l.]: US Department of Commerce, National Marine Fisheries Service, 1978.

MAMAEV, O. A simplified relationship between density, temperature and salinity of sea water. *Izv. Akad. Nauk SSSR, Ser. Geofiz*, n. 2, p. 309–311, 1964.

MANINS, P. Intrusion into a stratified fluid. *Journal of Fluid Mechanics*, Cambridge University Press, v. 74, n. 3, p. 547–560, 1976.

MANNICH, M. *Estimativa de emissão de gases do efeito estufa em reservatórios e lagos – contribuições para o monitoramento e modelagem 1D – vetical*. (Doctoral dissertation) — Graduate Program in Water Resources and Environmental Engineering of the Federal University of Paraná., 2013.

MARCE, R.; FEIJOO, C.; NAVARRO, E.; ORDONEZ, J.; GOMA, J.; ARMENGOL, J. Interaction between wind-induced seiches and convective cooling governs algal distribution in a canyon-shaped reservoir. *Freshwater biology*, Wiley Online Library, v. 52, n. 7, p. 1336–1352, 2007.

Mattler-Toledo AG, Analytical. *A guide to conductivity measuremnt: Theory and practice of conductivity applications*. Schwerzenbach, Switzerland: [s.n.], 2013.

MCDOUGALL, T. J.; R., J. D.; R., F.; G., W. D. Computationally efficient 25-term expressions for the density of seawater in terms of potential temperature and conservative temperature. *Ocean Science Discussions*, 2010b.

MEDCALC, S. Digimizer 3.6. 0. *Gent, Belgium*, 2009.

MERCIER, M.; VASSEUR, R.; DAUXOIS, T. Resurrecting dead-water phenomenon. *arXiv preprint arXiv:1103.0903*, 2011.

MICHALLET, H.; BARTHELEMY, E. Experimental study of interfacial solitary waves. *Journal of Fluid Mechanics*, Cambridge University Press, v. 366, p. 159–177, 1998.

MILES, J. W. On the stability of heterogeneous shear flows. *Journal of Fluid Mechanics*, Cambridge University Press, v. 10, n. 4, p. 496–508, 1961.

MILLERO, F. J.; POISSON, A. International one-atmosphere equation of state of seawater. *Deep Sea Research Part A. Oceanographic Research Papers*, Elsevier, v. 28, n. 6, p. 625–629, 1981.

MILLETTE, P. A. The heisenberg uncertainty principle and the nyquist-shannon sampling theorem. *arXiv preprint arXiv:1108.3135*, 2011.

MORTIMER, C. The resonant response of stratified lakes to wind. *Schweizerische Zeitschrift für Hydrologie*, Springer, v. 15, n. 1, p. 94–151, 1953.

MORTIMER, C. *Some effects of the earth's rotation on water movements in stratified lakes*. [S.l.: s.n.], 1955.

MORTIMER, C. Strategies for coupling data collection and analysis with dynamic modelling of lake motions. *Developments in Water Science*, Elsevier, v. 11, p. 183–222, 1979.

MORTIMER, C. H. The use of models in the study of water movement in stratified lakes: With 6 figures in the text and on 2 folders. *Internationale Vereinigung für theoretische und angewandte Limnologie: Verhandlungen*, Taylor & Francis, v. 11, n. 1, p. 254–260, 1950.

MORTIMER, C. H. Water movements in lakes during summer stratification; evidence from the distribution of temperature in windermere. *Philosophical Transactions of the Royal Society of London B: Biological Sciences*, The Royal Society, v. 236, n. 635, p. 355–398, 1952.

MORTIMER, C. H. Large-scale oscillatory motions and seasonal temperature changes in lake michigan and lake ontario. 1971.

MORTIMER, C. H. *Lake Michigan in motion: Responses of an inland sea to weather, earth-spin, and human activities*. [S.l.]: Univ of Wisconsin Press, 2004.

MORTIMER, C. H.; HORN, W. Internal wave dynamics and their implications for plankton biology in the lake of zurich. *Vier. Natur. Gesell. Zurich*, v. 127, p. 299–318, 1982.

MÜNNICH, M.; WÜEST, A.; IMBODEN, D. M. Observations of the second vertical mode of the internal seiche in an alpine lake. *Limnology and oceanography*, Wiley Online Library, v. 37, n. 8, p. 1705–1719, 1992.

MYSAK, L. A. Nonlinear internal waves. In: *Hydrodynamics of Lakes*. [S.l.]: Springer, 1984. p. 129–152.

NANSEN, F. *Farthest North: The epic adventure of a visionary explorer*. [S.l.]: Harper and Brothers, 1897. v. 1.

NISAR, S.; KHAN, O. U.; TARIQ, M. An efficient adaptive window size selection method for improving spectrogram visualization. *Computational intelligence and neuroscience*, Hindawi Publishing Corporation, v. 2016, 2016.

NIU, G. *Data-Driven Technology for Engineering Systems Health Management*. [S.l.]: Springer, 2017.

OLLINGER, D. *Modellierung von Temperatur, Turbulenz und Algenwachstum mit einem gekoppelten physikalisch-biologischen Modell*. (Doctoral dissertation) — University of Heildelberg, 1999.

OSBORNE, P. L. *Tropical ecosystems and ecological concepts*. [S.l.]: Cambridge University Press, 2000.

OSTROVSKY, L.; KAZAKOV, V.; MATUSOV, P.; ZABORSKIKH, D. Experimental study of the internal wave damping on small-scale turbulence. *Journal of physical oceanography*, v. 26, n. 3, p. 398–405, 1996.

PANNARD, A.; BEISNER, B. E.; BIRD, D. F.; BRAUN, J.; PLANAS, D.; BORMANS, M. Recurrent internal waves in a small lake: Potential ecological consequences for metalimnetic phytoplankton populations. *Limnology and Oceanography: Fluids and Environments*, Wiley Online Library, v. 1, n. 1, p. 91–109, 2011.

PANNARD, A.; BORMANS, M.; LAGADEUC, Y. Phytoplankton species turnover controlled by physical forcing at different time scales. *Canadian Journal of Fisheries and Aquatic Sciences*, NRC Research Press, v. 65, n. 1, p. 47–60, 2008.

PERKIN, R.; WALKER, E. Salinity calculations from in situ measurements. *Journal of Geophysical Research*, Wiley Online Library, v. 77, n. 33, p. 6618–6621, 1972.

PHILLIPS, O. On spectra measured in an undulating layered medium. *Journal of Physical Oceanography*, v. 1, n. 1, p. 1–6, 1971.

POLLI, B. A.; BERNARDO, J. W. Y.; HILGERT, S.; BLENINGER, T. Three dimensional heat transport modeling in vossoroca reservoir. In: *EGU General Assembly Conference Abstracts*. [S.l.: s.n.], 2017. v. 19, p. 17811.

PRUPPACHER, H. R.; KLETT, J. D. Microphysics of clouds and precipitation. *Nature*, Nature Publishing Group, v. 284, n. 5751, p. 88–88, 1980.

READ, J. S.; HAMILTON, D. P.; JONES, I. D.; MURAOKA, K.; WINSLOW, L. A.; KROISS, R.; WU, C. H.; GAISER, E. Derivation of lake mixing and stratification indices from high-resolution lake buoy data. *Environmental Modelling & Software*, Elsevier, v. 26, n. 11, p. 1325–1336, 2011.

ROBERTSON, D. M.; IMBERGER, J. Lake number, a quantitative indicator of mixing used to estimate changes in dissolved oxygen. *International Review of Hydrobiology*, Wiley Online Library, v. 79, n. 2, p. 159–176, 1994.

ROGET, E.; SALVADÉ, G.; ZAMBONI, F. Internal seiche climatology in a small lake where transversal and second vertical modes are usually observed. *Limnology and oceanography*, Wiley Online Library, v. 42, n. 4, p. 663–673, 1997.

RUEDA, F.; SCHLADOW, G. Mixing and stratification in lakes of varying horizontal length scales: Scaling arguments and energy partitioning. *Limnology and Oceanography*, Wiley Online Library, v. 54, n. 6, p. 2003–2017, 2009.

SAGGIO, A.; IMBERGER, J. Internal wave weather in a stratified lake. *Limnology and oceanography*, Wiley Online Library, v. 43, n. 8, p. 1780–1795, 1998.

SALVADÈ, G.; ZAMBONI, F.; BARBIERU, A. Three-layer model of the north basin of the lake of lugano. In: *Annales geophysicae. Atmospheres, hydrospheres and space sciences*. [S.l.: s.n.], 1988. v. 6, n. 4, p. 463–474.

SCHMIDT, W. Stehende schwingungen in der grenzschicht zweier flussigkeiten. *SB Akad. Wiss. Wien, Ia*, v. 117, p. 91–102, 1908.

SCHWAB, D. J. Internal free oscillations in lake ontario. *Limnology and oceanography*, Wiley Online Library, v. 22, n. 4, p. 700–708, 1977.

SCHWEFEL, R.; GAUDARD, A.; WÜEST, A.; BOUFFARD, D. Effects of climate change on deepwater oxygen and winter mixing in a deep lake (lake geneva): Comparing observational findings and modeling. *Water Resources Research*, Wiley Online Library, v. 52, n. 11, p. 8811–8826, 2016.

SERREZE, M. C.; BARRY, R. G. *The Arctic climate system*. [S.l.]: Cambridge University Press, 2014.

SHIMIZU, K.; IMBERGER, J. Damping mechanisms of internal waves in continuously stratified rotating basins. *Journal of Fluid Mechanics*, Cambridge University Press, v. 637, p. 137–172, 2009.

SHIN, J.; DALZIEL, S.; LINDEN, P. Gravity currents produced by lock exchange. *Journal of Fluid Mechanics*, Cambridge University Press, v. 521, p. 1–34, 2004.

SHINTANI, T.; FUENTE, A. de la; FUENTE, A. de la; NIÑO, Y.; IMBERGER, J. Generalizations of the wedderburn number: Parameterizing upwelling in stratified lakes. *Limnology and Oceanography*, Wiley Online Library, v. 55, n. 3, p. 1377–1389, 2010.

SIMMONS, H.; CHANG, M.-H.; CHANG, Y.-T.; CHAO, S.-Y.; FRINGER, O.; JACKSON, C. R.; KO, D. S. Modeling and prediction of internal waves in the south china sea. *Oceanography*, JSTOR, v. 24, n. 4, p. 88–99, 2011.

SIMON, A.; KOCSIS, O.; STIPS, A.; WÜEST, A. Momentum and turbulent kinetic energy balance in the surface boundary layer of developing waves. *J. Geophys. Res*, 2002.

SIMPSON, J. E. *Gravity currents: In the environment and the laboratory*. [S.l.]: Cambridge university press, 1999.

SMITH, S. *Digital signal processing: a practical guide for engineers and scientists*. [S.l.]: Newnes, 2013.

SMITH, S. D. Coefficients for sea surface wind stress, heat flux, and wind profiles as a function of wind speed and temperature. *Journal of Geophysical Research: Oceans*, Wiley Online Library, v. 93, n. C12, p. 15467–15472, 1988.

SPIGEL, R. H.; IMBERGER, J. The classification of mixed-layer dynamics of lakes of small to medium size. *Journal of physical oceanography*, v. 10, n. 7, p. 1104–1121, 1980.

SPIGEL, R. H.; IMBERGER, J. Mixing processes relevant to phytoplankton dynamics in lakes. *New Zealand Journal of Marine and Freshwater Research*, Taylor & Francis, v. 21, n. 3, p. 361–377, 1987.

STASHCHUK, N.; VLASENKO, V.; HUTTER, K. Numerical modelling of disintegration of basin-scale internal waves in a tank filled with stratified water. *Nonlinear Processes in Geophysics*, v. 12, n. 6, p. 955–964, 2005.

STEVENS, C.; IMBERGER, J. The initial response of a stratified lake to a surface shear stress. *Journal of Fluid Mechanics*, Cambridge University Press, v. 312, p. 39–66, 1996.

STEVENS, C.; LAWRENCE, G.; HAMBLIN, P.; CARMACK, E. Wind forcing of internal waves in a long narrow stratified lake. *Dynamics of atmospheres and oceans*, Elsevier, v. 24, n. 1-4, p. 41–50, 1996.

STEVENS, C. L. Internal waves in a small reservoir. *Journal of Geophysical Research: Oceans*, Wiley Online Library, v. 104, n. C7, p. 15777–15788, 1999.

STEVENS, C. L.; LAWRENCE, G. A. Estimation of wind-forced internal seiche amplitudes in lakes and reservoirs, with data from british columbia, canada. *Aquatic Sciences*, Springer, v. 59, n. 2, p. 115–134, 1997.

STOCKER, K.; HUTTER, K.; SALVADÈ, G.; TROSCH, J.; ZAMBONI, F. Observations and analysis of internal seiches in the southern basin of lake of lugano. In: *Annales geophysicae. Series B. Terrestrial and planetary physics*. [S.l.: s.n.], 1987. v. 5, n. 6, p. 553–568.

STOKES, G. G. On the theory of oscillatory waves. *Trans Cambridge Philos Soc*, v. 8, p. 441–473, 1847.

SUTHERLAND, B. R. *Internal gravity waves*. [S.l.]: Cambridge University Press, 2010.

TAIT, P. *Voy. Challenger Rep. 2 (Phys. and Chem.). IV. Report on some of the physical properties of fresh and sea water*. [S.l.]: London: HMSO, 1888.

TALLING, J. F.; LEMOALLE, J. *Ecological dynamics of tropical inland waters*. [S.l.]: Cambridge University Press, 1998.

TAYLOR, H. R. *Data acquisition for sensor systems*. [S.l.]: Springer Science & Business Media, 1997. v. 5.

TEN, I.; KASHIWAGI, M. Hydrodynamics of a body floating in a two-layer fluid of finite depth. part 1. radiation problem. *Journal of Marine Science and Technology*, Springer, v. 9, n. 3, p. 127–141, 2004.

THORPE, S. A method of producing a shear flow in a stratified fluid. *Journal of Fluid Mechanics*, Cambridge University Press, v. 32, n. 4, p. 693–704, 1968.

THORPE, S. Asymmetry of the internal seiche in loch ness. *Nature*, Springer, v. 231, n. 5301, p. 306–308, 1971.

THOULET, J. *Contribution a l'Etude des lacs des Vosges*. [S.l.: s.n.], 1894.

TORRENCE, C.; COMPO, G. P. A practical guide to wavelet analysis. *Bulletin of the American Meteorological society*, v. 79, n. 1, p. 61–78, 1998.

ULLOA, H. N.; WINTERS, K. B.; FUENTE, A. de la; NIÑO, Y. Degeneration of internal kelvin waves in a continuous two-layer stratification. *Journal of Fluid Mechanics*, Cambridge University Press, v. 777, p. 68–96, 2015.

UMLAUF, L.; LEMMIN, U. Interbasin exchange and mixing in the hypolimnion of a large lake: The role of long internal waves. *Limnology and Oceanography*, Wiley Online Library, v. 50, n. 5, p. 1601–1611, 2005.

VALERIO, G.; CANTELLI, A.; MONTI, P.; LEUZZI, G. A modeling approach to identify the effective forcing exerted by wind on a prealpine lake surrounded by a complex topography. *Water Resources Research*, Wiley Online Library, v. 53, n. 5, p. 4036–4052, 2017.

VIDAL, J.; CASAMITJANA, X.; COLOMER, J.; SERRA, T. The internal wave field in sau reservoir: Observation and modeling of a third vertical mode. *Limnology and oceanography*, Wiley Online Library, v. 50, n. 4, p. 1326–1333, 2005.

WADZUK, B. M.; HODGES, B. Comparing hydrostatic and non-hydrostatic navier stokes models of internal waves. In: *ASCE Engineeri Mechanics Conference, July*. [S.l.: s.n.], 2003. v. 16.

WADZUK, B. M.; HODGES, B. R. *Hydrostatic and non-hydrostatic internal wave models*. [S.l.], 2004.

WAGNER, W.; PRUSS, A. The iapws formulation 1995 for the thermodynamic properties of ordinary water substance for general and scientific use. *Journal of physical and chemical reference data*, NIST, v. 31, n. 2, p. 387–535, 2002.

WALKER, L. R. Interfacial solitary waves in a two-fluid medium. *The Physics of Fluids*, AIP, v. 16, n. 11, p. 1796–1804, 1973.

WATSON, E. Movements of the waters of loch ness, as indicated by temperature observations. *The Geographical Journal*, JSTOR, v. 24, n. 4, p. 430–437, 1904.

WATSON, E. R. Internal oscillation in the waters of loch ness. *Nature*, v. 69, p. 174, 1903.

WEDDERBURN, E. Temperature observations in loch earn; with a further contribution to the hydrodynamical theory of the temperature seiche. *Earth and Environmental Science Transactions of The Royal Society of Edinburgh*, Royal Society of Edinburgh Scotland Foundation, v. 48, n. 3, p. 629–695, 1912.

WEDDERBURN, E. M.; WILLIAMS, A. The temperature seiche. part ii. hydrodynamical theory of temperature oscillations in lakes. *Earth and Environmental Science Transactions of The Royal Society of Edinburgh*, Royal Society of Edinburgh Scotland Foundation, v. 47, n. 4, p. 628–634, 1911.

WEDDERBURN, E. M.; YOUNG, A. W. Temperature observations in loch earn, part ii. *Earth and Environmental Science Transactions of The Royal Society of Edinburgh*, Royal Society of Edinburgh Scotland Foundation, v. 50, n. 4, p. 741–767, 1915.

WETZEL, R. G. *Limnology: lake and river ecosystems*. [S.l.]: Gulf Professional Publishing, 2001.

WHITE, B. L.; HELFRICH, K. R. Gravity currents and internal waves in a stratified fluid. *Journal of Fluid Mechanics*, Cambridge University Press, v. 616, p. 327–356, 2008.

WIEGAND, R. C.; CHAMBERLAIN, V. Internal waves of the second vertical mode in a stratified lake. *Limnology and oceanography*, Wiley Online Library, v. 32, n. 1, p. 29–42, 1987.

WOOD, I.; SIMPSON, J. Jumps in layered miscible fluids. *Journal of Fluid Mechanics*, Cambridge University Press, v. 140, p. 329–342, 1984.

WU, S.; LIU, Q. Some problems on the global wavelet spectrum. *Journal of Ocean University of China. JOUC*, Springer Science & Business Media, v. 4, n. 4, p. 398, 2005.

WÜEST, A.; LORKE, A. Small-scale hydrodynamics in lakes. *Annual Review of fluid mechanics*, Annual Reviews 4139 El Camino Way, PO Box 10139, Palo Alto, CA 94303-0139, USA, v. 35, n. 1, p. 373–412, 2003.

YAN, N.; PAWSON, T. Changes in the crustacean zooplankton community of harp lake, canada, following invasion by bythotrephes cederstroemi. *Freshwater Biology*, Wiley Online Library, v. 37, n. 2, p. 409–425, 1997.

YAN, N.; STRUS, R. Crustacean zooplankton communities of acidic, metal-contaminated lakes near sudbury, ontario. *Canadian Journal of Fisheries and Aquatic Sciences*, NRC Research Press, v. 37, n. 12, p. 2282–2293, 1980.

YELLAND, M.; TAYLOR, P. K. Wind stress measurements from the open ocean. *Journal of Physical Oceanography*, v. 26, n. 4, p. 541–558, 1996.

YEUNG, R.; NGUYEN, T. Waves generated by a moving source in a two-layer ocean of finite depth. *Journal of engineering mathematics*, Springer, v. 35, n. 1, p. 85–107, 1999.

YOUNG, J. D.; LOEW, E. R.; YAN, N. D. Examination of direct daytime predation by coregonus artedi on bythotrephes longimanus in harp lake, ontario, canada: no evidence for the refuge hypothesis. *Canadian Journal of Fisheries and Aquatic Sciences*, NRC Research Press, v. 66, n. 3, p. 449–459, 2009.

APPENDIX A – Equations of State

Oceanographic models represent better the real environment though the practical salinity S_p and potential temperature θ. For a better representation, Commission et al. (2015) recommends a computationally efficient 25-term expressions for water density in terms of potential and conservative temperature. However, since we consider the system incompressible, there is not any adiabatic movement $\theta \approx \tau$. This approximation is easily observed through Poisson's equation.

The 25-term expressions for water density in terms of potential expression for water density has been proposed by McDougall et al. (2010b) and may be written explicitly as the ratio of two polynomials of (S_A, θ, p)

$$\rho(S_p, \tau, p) \simeq \hat{\rho}(S_A, \theta, p) \equiv \frac{a_0 + 2a_1 p + a_2 p^2}{b_0 b_1 + b_2 p + b_3 p^2 + b_4 p^3} \tag{A.1}$$

where the coefficients a_0, a_1, a_2, b_0, b_1, b_2, b_3, and b_4 are the following functions of salinity (S_A) and temperature (θ)

$$\begin{aligned}
a_0 &= c_1 + c_2\theta + c_3\theta^2 + c_4\theta^3 + c_5 S_A + c_6 S_A\theta + c_7 {S_A}^2, \\
a_1 &= 0.5(c_8 + c_9\theta^2 + c_10 S_A), \\
a_2 &= c_{11} + c_{12}\theta^2, \\
b_0 &= c_{13} + c_{14}\theta + c_{15}\theta^2 + c_{16}\theta^3 + c_{17}\theta^4, \\
b_1 &= c_{18} S_A + c_{19} S_A\theta + c_{20} S_A\theta^3 + c_{21} {S_A}^{1.5} + c_{12} {S_A}^{1.5}\theta^2, \\
b_2 &= c_{23}, \\
b_3 &= c_{24}\theta^3, \\
b_4 &= c_{25}\theta,
\end{aligned} \tag{A.2}$$

and the coefficients c_1 to c_{25} are

$$\begin{aligned}
c_1 &= 9.9984277040408688\ 10^{2} \\
c_2 &= 7.3539907257802000\ 10^{0} \quad \theta \\
c_3 &= -5.2725024846580537\ 10^{-2} \quad \theta^2 \\
c_4 &= 5.1051405427900501\ 10^{-4} \quad \theta^3 \\
c_5 &= 2.8372074954162994\ 10^{0} \quad S_A \\
c_6 &= -5.7462873738668985\ 10^{-3} \quad S_A\theta \\
c_7 &= 2.0165828404011005\ 10^{-3} \quad {S_A}^2 \\
c_8 &= 1.1506680128760695\ 10^{-2} \quad p \\
c_9 &= 1.2026027029004581\ 10^{-7} \quad p\theta^2 \\
c_{10} &= 5.5361909365048466\ 10^{-6} \quad pS_A \\
c_{11} &= -2.7563156404651928\ 10^{-8} \quad p^2 \\
c_{12} &= -5.8834769459933364\ 10^{-12} \quad p^2\theta^2 \\
c_{13} &= 1.0000000000000000\ 10^{0} \\
c_{14} &= 7.2882773179945397\ 10^{-3} \quad \theta \\
c_{15} &= -4.4270423575705795\ 10^{-5} \quad \theta^2 \\
c_{16} &= 4.8218167574165732\ 10^{-7} \quad \theta^3 \\
c_{17} &= 1.9666437776499541\ 10^{-10} \quad \theta^4 \\
c_{18} &= 2.0192201315731156\ 10^{-3} \quad S_A \\
c_{19} &= -7.8386667410747671\ 10^{-6} \quad S_A\theta \\
c_{20} &= -2.7493971171215844\ 10^{-10} \quad S_A\theta^3 \\
c_{21} &= 4.6614419029016429\ 10^{-6} \quad {S_A}^{1.5} \\
c_{22} &= 1.5182712637288295\ 10^{-9} \quad {S_A}^{1.5}\theta^2 \\
c_{23} &= 6.4146293567422886\ 10^{-6} \quad p \\
c_{24} &= -9.5362845886397360\ 10^{-17} \quad p^2\theta^3 \\
c_{25} &= -9.6237455486277320\ 10^{-18} \quad p^3\theta
\end{aligned}$$

The c's coefficients are dimensionless when the normalizing values of S_A, θ and p are taken to be 1 g/kg, 1 K (≡ -272.15°C) and 1 dbar respectively. Simplifying equations A.2 and A.1 according to assumptions of incompressibility and neglecting the influence of salinity, as commented in subsection , equations A.2 and A.1 become

$$\rho(z) = f(\tau(z), p = \text{constant}) = \frac{a_0^* + 2a_1^* p + a_2 p^2}{b_2 p + b_3 p^2 + b_4 p^3} \tag{A.3}$$

where the coefficients a_0 to b_4 are the following functions of just the potential temperature (θ), where coefficients denoted by * are modified coefficients from equations A.2 due to the assumptions made.

$$\begin{aligned}
a_0^* &= c_1 + c_2\theta + c_3\theta^2 + c_4\theta^3, \\
a_1^* &= 0.5(c_8 + c_9\theta^2), \\
a_2 &= c_{11} + c_{12}\theta^2, \\
b_0 &= c_{13} + c_{14}\theta + c_{15}\theta^2 + c_{16}\theta^3 + c_{17}\theta^4, \\
b_2 &= c_{23}, \\
b_3 &= c_{24}\theta^3, \\
b_4 &= c_{25}\theta,
\end{aligned} \tag{A.4}$$

APPENDIX B – Wave dispersion solution

B.1 Two-layer non-hydrostatic model with free surface

The displacement of the free surface and the interface are given, respectively, by waves of sinusoidal shape with wavenumber k and angular frequency ω

$$\eta(x,t) = a\cos(kx)\cos(\omega t), \tag{B.1}$$

$$\zeta(x,t) = b\cos(kx)\cos(\omega t). \tag{B.2}$$

According to Kelvin's circulation theorem, since we assume that each layer has homogeneous density, the viscous effects are ignored, and the Coriolis force neglected, the result motion for each layer is irrotational. Thus, we can define a independent velocity potentials in each layer and rewrite equation 2.38 as the Laplace equation for each layer

$$\frac{\partial^2\phi_e}{\partial x^2} + \frac{\partial^2\phi_e}{\partial z^2} = 0, \tag{B.3}$$

$$\frac{\partial^2\phi_h}{\partial x^2} + \frac{\partial^2\phi_h}{\partial z^2} = 0, \tag{B.4}$$

where equation B.3 refers to the mass conservation in the epilimnion layer and equation B.4 refers to the mass conservation in the hypolimnion layer. For a cosine dependence, the velocities potential ϕ_e and ϕ_h that satisfy the Laplace equations B.3 and B.4 are, respectively, in the form

$$\phi_e(x,z,t) = f_e(z)\cos(kx)\sin(\omega t), \tag{B.5}$$

$$\phi_h(x,z,t) = f_h(z)\cos(kx)\sin(\omega t). \tag{B.6}$$

Substitution of equation B.5 and B.6 into the Laplace equations gives us second-order linear homogeneous differential equation with two linearly independent solutions. Thus, the general solution can be written in forms

$$f_e(z) = C_1\cosh(k(z-h_e)) + C_2\sinh(k(z-h_e)), \tag{B.7}$$

$$f_h(z) = C_3\cosh(k(z+h_h)) + C_4\sinh(k(z+h_h)), \tag{B.8}$$

where the constants C_1, C_2, C_3, and C_4 can be determined from the boundary conditions.

At the bottom the vertical velocity must vanish. So the boundary condition at bottom is given by

$$\underset{\sim}{\nabla}\phi_h \cdot \underset{\sim}{\hat{n}}|_{z=-h_h} = 0. \tag{B.9}$$

Applying the general solution B.5 in the bottom condition B.9 gives that $C_4 = 0$. We can obtain C_3 using the kinematic boundary condition at the interface. Note that now the interface may be moving or deforming in some way. Thus, the boundary condition must be satisfied on such wave moving, so in this case

$$\underset{\sim}{\nabla}\phi_h \cdot \underset{\sim}{\hat{n}}|_{z=\zeta} = \underset{\sim}{u}_{int} \cdot \underset{\sim}{\hat{n}}|_{z=\zeta}, \tag{B.10}$$

where u_{int} represents the interface velocity, differently of the fluid particles velocity $\underset{\sim}{u}$. Thus, the kinematic boundary condition at the interface for the hypolimnion layer can be expressed as

$$\left.\frac{\partial \phi_h}{\partial z}\right|_{z=\zeta} - \left.\frac{\partial \zeta}{\partial x}\frac{\partial \phi_h}{\partial x}\right|_{z=\zeta} = \frac{\partial \zeta}{\partial t}. \tag{B.11}$$

To linearize equation B.11 we can write it in non-dimensional form, where variables denoted by * are the non-dimensional variables,

$$\left.\frac{\partial \phi_h^*}{\partial z^*}\right|_{z=\zeta} = \frac{\partial \zeta^*}{\partial t^*} + \frac{b}{\lambda}u^*\left.\frac{\partial \phi_h^*}{\partial x^*}\right|_{z=\zeta}. \tag{B.12}$$

For small-amplitude waves, linear waves, $b \ll \lambda$. Thus, the nonlinear convective term can be neglected. Note that the left-hand side is evaluated at $z = \zeta$, where ζ is a function of x and t. So, we can simplify the term expanding in a Taylor series around $z = 0$ and neglecting the higher order terms. Thus, the kinematic boundary condition at the interface for hypolimnion fluid particles becomes

$$\left.\frac{\partial \phi_h}{\partial z}\right|_{z=0} \approx \frac{\partial \zeta}{\partial t}. \tag{B.13}$$

As kinematic boundary condition just describe the motion properties without any consideration of acting forces, the equation B.13 can be rewritten easily to obtain the kinematic boundary conditions for epilimnion layer, at the surface and the interface

$$\left.\frac{\partial \phi_e}{\partial z}\right|_{z=h_e} \approx \frac{\partial \eta}{\partial t}, \tag{B.14}$$

$$\left.\frac{\partial \phi_e}{\partial z}\right|_{z=0} \approx \frac{\partial \zeta}{\partial t}. \tag{B.15}$$

Applying the general solution B.5 in the kinematic boundary conditions B.13 give us the value of C_3. Thus, finally, the velocity potential ϕ_h becomes

$$\phi_h(x,z,t) = \left(\frac{b\omega}{k\cosh(kh_h)}\right)\cosh(k(z+h_h))\cos(kx)\sin(\omega t). \tag{B.16}$$

Applying the kinematic boundary condition B.14 and B.15 in the general solution 3.3 give us the values of C_1 and C_2. Thus, finally, the potential velocity ϕ_e can be written as

$$\phi_e(x,z,t) = \frac{\omega}{k}\left(\left(\frac{a\cosh(kh_e)-b}{\sinh(kh_e)}\right)\cosh(k(z-h_e)) + a\sinh(k(z+h_e))\right)\cos(kx)\sin(\omega t). \tag{B.17}$$

The last two boundary condition come from the momentum equation and are known as dynamic boundaries conditions. From equation 2.39, applying the inviscid and irrotational assumptions, we obtain

$$\rho\frac{\partial}{\partial t}\left(\frac{\partial \phi}{\partial x_i}\right) + \rho\frac{\partial}{\partial x_i}\left(\frac{u_j u_j}{2}\right) = -\frac{\partial P}{\partial x_i} + \frac{\partial}{\partial x_i}(g_i x_i). \tag{B.18}$$

Taking just the vertical direction of equation B.18 and integrating with respect to z, we have

$$\rho\frac{\partial \phi}{\partial t} + \rho\left(\frac{u^2+w^2}{2}\right) + P + \rho g z = F(t), \tag{B.19}$$

where the equation B.19 is known as the unsteady Bernoulli equation, and is constant along a streamline, where the pressure is also constant. The $F(t)$ can be absorbed by the potential velocity, since it is just a function of t. We can apply the equation B.19 at reservoir surface ($z = \eta$). Thus, firstly, we write equation B.19 in non dimensional form to linearize the momentum equation

$$\rho^* \frac{\partial \phi^*}{\partial t^*}\bigg|_{z=h_e+\eta} + \frac{a}{\lambda}\rho^* \left(\frac{u^{*2} + w^{*2}}{2}\right)\bigg|_{z=h_e+\eta} + \rho^* g^* z^* = 0. \tag{B.20}$$

Again, for small-amplitude waves, $a \ll \lambda$, the non linear kinetic energy term can be neglected in equation B.20. To simplify more, we can expand the equation in a Taylor series around $z = h_e$ and neglect the higher order terms. Thus, we have

$$\rho \frac{\partial \phi}{\partial t}\bigg|_{z=h_e} + \rho g \eta \approx 0. \tag{B.21}$$

Selecting the fluid surface as the streamline and neglecting the "air layer", gives

$$\frac{\partial \phi_e}{\partial t}\bigg|_{z=h_e} = -g\eta. \tag{B.22}$$

Substitution of equations B.1 and B.16 into equation B.22 gives the relationship between the surface and internal wave amplitude,

$$\frac{b}{a} = \cosh(kh_e) - \frac{kg}{\omega^2} \sinh kh_e. \tag{B.23}$$

Finally, substitution of equation B.23 into the dynamic boundary condition at the interface give us the dispersion relation. The dynamic boundary condition at interface can be obtained similarly. However, when the streamline is selected, the upper layer is not neglected. Thus, from equation B.21, we have

$$\frac{\rho_e}{\rho_h} \frac{\partial \phi_e}{\partial t}\bigg|_{z=0} = \frac{\partial \phi_h}{\partial t}\bigg|_{z=0} + \frac{\Delta\rho}{\rho_h} g\zeta. \tag{B.24}$$

Substitution of equations B.2, B.16, B.17, and B.23 into equation B.24 gives a biquadratic equation,

$$\omega^4 \left(\frac{\gamma \tanh(kh_e)\tanh(kh_h) + 1}{k \tanh(kh_h)}\right) - \omega^2 \left(\frac{g(\tanh(kh_e) + \tanh(kh_h))}{\tanh(kh_h)}\right) - (\gamma - 1)g^2 k \tanh(kh_e) = 0. \tag{B.25}$$

Finally, the final solution is given by

$$\omega^2 = \frac{g}{2(\gamma T_e T_h + 1)} \left((T_e + T_h) \pm \sqrt{(T_e + T_h)^2 + 4T_h T_e(\gamma T_e T_h - 1)(\gamma - 1)}\right) \tag{B.26}$$

APPENDIX C – Complete field analysis

This appendix gives a comprehensive summary of all analyzed periods, including information when internal baroclinic motion, V1H1 and V2H1 internal seiche modes, were excited in Vossoroca reservoir and Harp Lake. Table 3 shows all preliminary information about all analyzed period, including the excited internal wave mode detected and the theoretical period obtained through the multi-layer hydrostatic linear model with Coriolis correction, described in section 3.4.2 and 3.4.3.

Table 3 – Preliminary information about each analyzed periods.

Num.	Basin	Season	Month	Year	Period	Mode	Wave Period (h)	
							V1H1	V2H1
F.1	Vossoroca	Summer	12	2012	04/dez–07/dez	V1H1	7.4	9.1
F.2	Vossoroca	Summer	12	2012	11/dez–15/dez	V1H1	6.1	8.5
F.3	Vossoroca	Summer	12	2012	11/dez–15/dez	V1H1	4.5	5.8
F.4	Vossoroca	Summer	12	2012	16/dez–21/dez	V1H1	5.0	10.7
F.5	Vossoroca	Spring	9	2012	15/sep–25/sep	V1H1	6.5	8.5
F.6	Vossoroca	Autum	4	2013	10/apr–16/apr	V1H1	12.0	13.7
F.7	Vossoroca	Winter	8	2012	01/aug–09/aug	V1H1	12.1	13.2
F.8	Harp	Summer	6	2012	05/jun–09/jun	V1H1	6.2	16.6
F.9	Harp	Autum	9	2014	13/sep–20/sep	V1H1	5.5	6.0
F.10	Harp	Autum	10	2014	13/oct–20/oct	V1H1	8.0	8.5
F.11	Harp	Autum	9	2013	25/sep–04/oct	V1H1	6.0	8.2
F.12	Vossoroca	Spring	11	2012	11/nov–22/nov	V2H1	5.4	10.5
F.13	Vossoroca	Spring	9	2012	15/sep–25/sep	V2H1	8.3	23.5
F.14	Harp	Summer	6	2014	26/jun–30/jun	V2H1	4.9	13.5
F.15	Harp	Autum	9	2012	01/sep–08/sep	V2H1	5.2	11.8
F.16	Harp	Autum	9	2013	25/sep–04/oct	V2H1	5.7	8.0
F.17	Harp	Autum	9	2012	24/sep–30/sep	V2H1	5.3	5.4
F.18	Harp	Autum	9	2014	01/sep–09/sep	V2H1	4.9	5.0
F.19	Harp	Autum	9	2014	21/sep–25/sep	V2H1	5.1	6.2
F.20	Vossoroca	Summer	2	2013	05/feb–11/feb	-	10.0	11.4
F.21	Vossoroca	Summer	2	2013	12/feb–20/feb	-	7.0	13.7
F.22	Vossoroca	Winter	8	2012	14/aug–21/aug	-	7.6	18.4
F.23	Harp	Summer	6	2014	04/jun–12/jun	-	4.5	11.1
F.24	Harp	Summer	7	2014	17/jul–26/jul	-	4.3	10.5
F.25	Harp	Autum	10	2014	25/oct–30/oct	-	10.8	10.9

Table 4 shows some information about the density structure of the analyzed periods where internal seiches were identified. The ρ_e, ρ_m, and ρ_h are the epilimnion, metalimnion, and hypolimnion density, respectively. The h_e, h_m, and h_h are the epilimnion, metalimnion, and hypolimnion thickness, respectively. Finally g' is the reduced gravity, considering a two-layer system. These parameters were used to calculate the internal seiche periods and other important parameters to describe basin-scale internal

wave evolution.

Table 4 – Mean layers thickness and density considering a two- or three-layer system, depending on the mode detected through spectral analysis.

Num.	h_e **(m)**	h_m **(m)**	h_h **(m)**	ρ_e **(kg/m^3)**	ρ_m **(kg/m^3)**	ρ_h **(kg/m^3)**	g' **(m/s^2)**
F.1	4.02	-	7.81	997.16	-	998.89	0.0229
F.2	4.13	-	6.94	997.08	-	998.87	0.0176
F.3	4.13	-	6.94	997.08	-	998.87	0.0176
F.4	5.19	-	5.74	997.1	-	998.83	0.0170
F.5	4.13	-	6.94	997.08	-	998.87	0.0103
F.6	4.59	-	7.74	997.87	-	998.27	0.0036
F.7	4.59	-	10.76	998.95	-	999.25	0.0029
F.8	3.77	-	24.33	998.66	-	999.91	0.0123
F.9	5.35	-	22.75	998.92	-	999.94	0.0100
F.10	6.95	-	21.15	999.48	-	999.95	0.0046
F.11	5.92	-	22.18	998.93	-	999.94	0.0283
F.12	1.98	6.08	4.84	997.52	998.26	999.09	0.0154
F.13	2.07	5.46	3.54	996.91	998.16	999.02	0.0176
F.14	0.7	5.23	22.17	997.22	998.61	999.96	0.0269
F.15	2.9	4.92	20.28	997.71	998.74	999.94	0.0118
F.16	4.07	3.58	20.45	998.88	999.39	999.96	0.0283
F.17	5.51	2.95	19.64	999.06	999.48	999.94	0.0086
F.18	1.76	5.22	21.12	997.88	998.84	999.96	0.0204
F.19	4.41	3.00	20.69	999.12	999.54	999.96	0.0082

Table 5 shows the mean wind intensity w for each period where basin-scale internal wave were excited, the standard Richardson number, Ri, and the filtered Ri, Ri_{dur} and Ri_{dir}. In addition, we present the filtering parameters, Ψ_{dur} and Ψ_{dir}. Finally, we present the Wedderburn number, W.

Table 5 – The mean wind speed for each period and calculated non-dimensional parameters.

Num.	w **(m/s)**	Ri	Ψ_{dur}	Ψ_{dir}	Ri_{dur}	Ri_{dir}	W
F.1	1.33	7500	0.79	0.69	9458	10917	10.13
F.2	1.99	3051	0.74	0.29	4151	10680	17.64
F.3	1.18	14793	0.85	0.44	17424	34007	56.18
F.4	0.89	41671	0.93	0.83	45050	50388	104.61
F.5	2.21	1339	0.74	0.42	1823	3159	5.30
F.6	2.80	253	0.87	0.70	290	364	0.67
F.7	3.29	126	1.00	1.00	127	127	0.24
F.8	1.52	4380	1.00	1.00	4381	4381	16.51
F.9	2.72	890	1.00	1.00	890	891	4.76
F.10	2.34	830	1.00	0.65	831	1270	8.83
F.11	2.37	2932	1.00	1.00	2932	2932	12.11
F.12	1.68	5409	1.00	0.45	5409	11994	24.08
F.13	2.85	1045	0.74	0.42	1413	2466	4.07

Table 5 – The mean wind speed for each period and calculated non-dimensional parameters.

Num.	w **(m/s)**	Ri	Ψ_{dur}	Ψ_{dir}	Ri_{dur}	Ri_{dir}	W
F.14	1.88	3838	1.00	1.00	3839	3839	10.98
F.15	2.43	1449	1.00	0.99	1449	1472	7.83
F.16	3.36	1024	1.00	1.00	1024	1024	4.23
F.17	3.14	927	1.00	0.55	927	1685	16.87
F.18	2.87	1242	1.00	0.76	1242	1638	7.08
F.19	2.79	746	1.00	1.00	746	746	4.41

Table 6 shows the Peak of the Power Spectral Density (PSD) of the most energetic isotherm, where internal seiche was detected, and the experimental and theoretical amplitude, considering linear and non-linear results. The experimental amplitudes were obtained through the normalization of the peak of the PSD[1]. The linear amplitude is calculated through the relation with wedderburn number, equation 2.27 with a parametrization proportional to 1/2. Finally, the non-linear amplitude solution of the upwelling height was estimated by the empirical fitting function, equation **??**.

Table 6 – PSD analysis and basin-scale internal wave amplitude of field analysis.

Num.	PSD **(m^2/Hz)**	**Total vertical displacement (cm)**		
		Experimental	**Linear Theory**	**Non-linear Theory**
F.1	220	40	23	26
F.2	160	38	23	28
F.3	75	12	7	10
F.4	105	7	5	8
F.5	1750	114	79	84
F.6	1532	261	686	–
F.7	2125	307	1972	–
F.8	276	50	11	27
F.9	180	126	56	119
F.10	360	89	39	87
F.11	247	61	17	39
F.12	510	34	11	26
F.13	1600	154	51	108
F.14	87	36	13	29
F.15	400	77	34	74
F.16	343	124	49	104
F.17	127	75	30	70
F.18	251	106	31	65
F.19	344	138	67	142

[1] The correlation between PSD and the experimental amplitude is not proportional since ζ is obtained through a normalization considering the frequency resolution, in which was obtained through the length of the applied window in the FFT

APPENDIX D – Complete experimental data

This appendix gives a comprehensive summary of the data collected as part of experimental runs. We divided the presentation in two sections. In section D.2 we presents the data collected during the full-depth lock-exchange release experiment, which is described in section 3.5.1. In section D.2, we present the data collected during and after the passage of the long-internal seiche.

D.1 Lock-exchange release experiments

D.1.1 Calibration of conductivity-density relationship

The calibration of conductivity-density-sodium chloride concentration relationship was done daily, during five days of laboratory experiments. For each day we calibrated the conductivity-density curve and the density-sodium chloride concentration curve using samples with the water density range required for each day of experiment runs. The number of samples used to calibrate the curves was chosen based on the density range required and in the quality of the early sample measurements. We used to calibrate the system tap water, sodium chloride, an analytical balance with 0.1 mg resolution, a pycnometer of 50 ml and a conductivity meter MARCONI MA-521 with accuracy of ±1% and precision of 0.1 μS/cm. Table 7 presents all parameters for curves calibration and Figure 53 shows the calibration values in scatter graphs.

Table 7 – Water density calibration parameters. σ_{25} was obtained using equation found in figure 22–c and the variables σ_τ and τ.

Cal.	**Day**	C**NaCl**	σ_τ	**Pycnometer (50 ml)**		τ	σ_{25}
		(g/m^3)	**(mS/cm)**	M_{pic} **(g)**	$\rho_{\mathbf{H_2O}}$ **(kg/m^3)**	**(°C)**	**(mS/cm)**
C.1	A	0.0	4.84	50.2189	1004.38	19.6	4.84
C.2	A	4176.7	7.07	50.3454	1006.91	20.3	7.07
C.3	A	5560.0	9.11	50.4272	1008.54	19.9	9.11
C.4	A	6612.3	11.74	50.5551	1011.10	19.7	11.74
C.5	A	8594.5	14.84	50.5889	1011.78	19.7	14.84
C.6	A	10274.0	19.09	50.5973	1011.95	19.5	19.09
C.7	B	0.0	5.11	50.26	1005.20	19.0	5.11
C.8	B	0.0	5.11	50.2643	1005.29	19.0	5.11
C.9	B	2502.1	6.11	50.3669	1007.34	20.1	6.11
C.10	B	3137.1	6.75	50.3977	1007.95	20.4	6.75
C.11	B	3581.3	7.37	50.4265	1008.53	20.4	7.37
C.12	B	3930.0	7.89	50.4634	1009.27	19.9	7.89
C.13	C	0.0	4.16	50.2395	1004.79	19.5	4.79
C.14	C	2141.3	4.77	50.2879	1005.76	19.7	5.49
C.15	C	3997.9	6.76	50.4029	1008.06	19.9	7.78
C.16	C	5961.3	10.72	50.4992	1009.98	20.4	12.34

Table 7 – Water density calibration parameters. σ_{25} was obtained using equation found in figure 22–c and the variables σ_τ and τ.

Cal.	**Day**	C**NaCl**	σ_τ	**Pycnometer (50 ml)**		τ	σ_{25}
		(g/m^3)	**(mS/cm)**	M_{pic} **(g)**	$\rho_{\mathbf{H_2O}}$ **(kg/m^3)**	**(°C)**	**(mS/cm)**
C.17	C	9274.6	18.03	50.5271	1010.54	19.9	20.76
C.18	C	10260.4	20.41	50.5916	1011.83	19.0	23.50
C.19	D	0.0	3.79	50.2837	1005.67	20.1	4.36
C.20	D	1610.0	4.05	50.3333	1006.67	19.9	4.66
C.21	D	2387.1	4.37	50.3528	1007.06	20.4	5.03
C.22	D	2387.1	4.37	50.3528	1007.06	20.4	5.03
C.23	E	0.0	5.16	50.2226	1004.45	19.0	5.94
C.24	E	0.0	5.16	50.2362	1004.72	20.0	5.82
C.25	E	3922.1	12.02	50.4321	1008.64	19.0	13.84
C.26	E	3922.1	11.98	50.4431	1008.86	20.4	13.39
C.27	E	3922.1	12.20	50.4566	1009.13	19.0	14.04
C.28	E	8750.0	19.09	50.623	1012.46	19.6	21.70
C.29	E	8750.0	19.35	50.6506	1013.01	19.7	21.95
C.30	E	10654.6	19.88	50.6639	1013.28	19.5	22.65
C.31	E	9655.8	20.01	50.6677	1013.35	19.7	22.70
C.32	E	8750.0	19.41	50.6682	1013.36	20.3	21.75
C.33	E	10094.2	20.06	50.6696	1013.39	19.5	22.85
C.34	E	9655.8	22.00	50.6801	1013.60	19.6	25.01
C.35	E	9655.8	21.60	50.682	1013.64	19.0	24.87
C.36	E	10094.2	21.55	50.7003	1014.01	19.7	24.45
C.37	E	10654.6	21.65	50.7012	1014.02	20.4	24.21
C.38	E	10094.2	21.95	50.749	1014.98	20.1	24.69
C.39	E	10654.6	22.02	50.7642	1015.28	19.7	24.98

Linear equations were obtained for each experiment day (A to E), using the values from C.1 to C.39. We applied the ordinary least squares (OLS) method, the beat linear unbiased estimator (BLUE), in order to obtain the linear regression. For each experiment day, we obtained two linear regression equations, presented in Table 8. The first one was used to predict water density ρ through water conductivity σ_{25}, mainly used to estimate water density within the stratified tank. The second linear regression equation was used to predict the NaCl concentration through required water density, used mainly in the determination of NaCl to achieve the density difference required.

Table 8 – Linear regression equations with the Pearson product-moment correlation coefficient r^2 for each day (A–E): water density ρ in kg/m^3 Vs water conductivity σ_{25} in mS/cm and NaCl concentration C_{salt} in kg/m^3 Vs water density ρ in kg/m^3.

Day	equation (ρ x σ_{25})	r^2	equation (ρ x C_{salt})	r^2
A	$\rho = 0.53432\ \sigma_{25} + 1003.17$	0.84	$C_{salt} = 1133.3965\ \rho$ -1137851	0.93
B	$\rho = 1.44105\ \sigma_{25} + 998.05$	0.97	$C_{salt} = 1035.3074\ \rho$ -1040635	0.98
C	$\rho = 0.32248\ \sigma_{25} + 1004.48$	0.85	$C_{salt} = 1399.7805\ \rho$ -1406398	0.95
D	$\rho = 2.03145\ \sigma_{25} + 996.95$	0.91	$C_{salt} = 1706.8225\ \rho$ -1716525	1.00
E	$\rho = 0.51004\ \sigma_{25} + 1001.73$	0.98	$C_{salt} = 1088.2817\ \rho$ -1093497	0.97

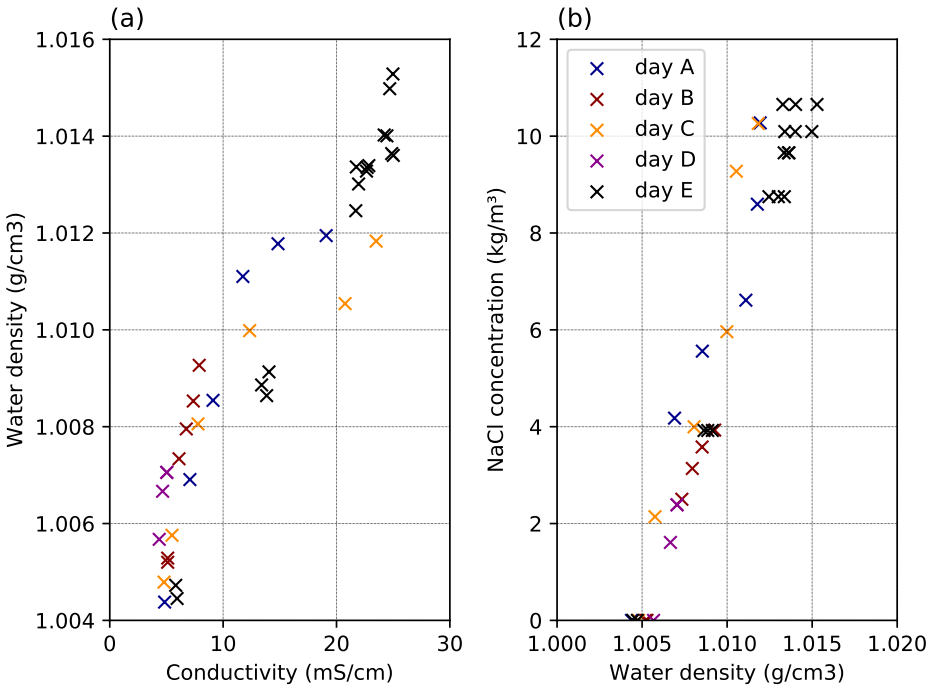

Figure 53 – (a) Scatter graph of conductivity in mS/cm and NaCl concentration in kg/m^3 for five days of calibrations (day A to E). (b) Scatter graph of conductivity in mS/cm and water density in kg/m^3 for five days of calibrations (day A to E).

D.1.2 Lock-exchange Experiment

Table 9 shows initial parameters of each experimental run during the *lock-exchange* release part. The initial water density, ρ_i, for each layer was measured through conductivity measurements. The volume of lock exchange release for denser, L_1, and lighter fluid, L_2, was chosen based on the h_e/H required.

Table 9 – Initial parameters for lock-exchange release and the non-dimensional parameter Re.

Run	ρ_i **(kg/m^3)**		**Lock Volume (cm)**		Re
	ρ_e	ρ_h	L_e	L_h	
E.1	1005.29	1012.93	100	100	4918
E.2	1005.64	1010.53	100	100	3702
E.3	1005.29	1008.23	100	100	2478
E.4	1005.71	1006.70	100	100	1242
E.5	1006.12	1019.04	90	110	6085
E.6	1005.73	1015.01	90	110	4900
E.7	1005.00	1012.28	80	120	3692
E.8	1005.65	1012.37	80	120	4922
E.9	1005.83	1007.80	80	120	2476
E.10	1005.08	1007.06	80	120	1241
E.11	1006.42	1020.36	60	140	4975
E.12	1005.04	1011.08	50	150	4291
E.13	1005.52	1014.10	50	150	4079
E.14	1005.83	1007.39	50	150	1291

Table 9 – Initial parameters for lock-exchange release and the non-dimensional parameter Re.

Run	ρ_i (kg/m^3)		Lock Volume (cm)		Re
	ρ_e	ρ_h	L_e	L_h	
E.15	1005.27	1005.92	50	150	1242

Table 10 presents some measured variables of each experimental run. The front velocity of the dense gravity currents were recorded through camera 3 (Figure 23) and measured by the open source physics tool Tracker Video Analysis and Modelling Tool (BROWN, 2017). One thin black line was drawn at the bottom of the tank to help to overcome the difficulty to track a straight horizontal line, as shown in Figure 23(a). The theoretical front speed was calculated through equation 2.14, with exception that w_* was replaced by the front velocity and h_i by the total depth, H. The theory imply that, according to Bar (1967), the dense front has $\bar{Fr} = 0.49$.

Table 10 – Lock-exchange experiment: a comparison between theoretical and experimental results.

Run	g'(m/s)	N (Hz)	S_p (cm/s)		$\bar{Fr}$
			Theoretical	Experimental	
E.1	0.0740	0.7857	5.47	5.60	0.45
E.2	0.0475	0.7838	4.82	4.48	0.49
E.3	0.0286	0.5476	3.26	3.48	0.43
E.4	0.0096	0.3166	2.43	2.02	0.55
E.5	0.1243	1.1754	6.38	7.25	0.40
E.6	0.0897	0.9983	6.16	6.16	0.46
E.7	0.0706	0.8964	5.15	5.47	0.43
E.8	0.0651	0.8869	5.68	5.25	0.50
E.9	0.0192	0.7137	2.86	2.85	0.46
E.10	0.0193	0.3540	2.31	2.86	0.37
E.11	0.1339	1.4941	7.71	7.53	0.47
E.12	0.0586	1.1360	4.39	4.98	0.41
E.13	0.0829	1.1279	5.48	5.92	0.43
E.14	0.0152	0.6068	2.98	2.54	0.54
E.15	0.0063	0.2240	2.33	1.64	0.65

D.2 Internal Seiche experiments

Table 11 shows some non-dimensional and internal seiche parameters, including theoretical and experimental basin-scale internal wave period and phase velocity. The theoretical internal seiche period $T_{1,1}$ and phase speed, c_p, were calculated using the two-layer non-hydrostatic linear model, described in section 3.4.1, and the spectral analysis. We applied the short-time Fourier transform (STFT) to time-series of the interfacial displacement from station 3, obtained from the Tracker Video Analysis and Modelling Tool, to identify the experimental internal seiche period $T_{1,1}$, and consequently the phase speed c_p. The Richardson number, Ri, was obtained though equation 2.13, considering a parametrization with the front velocity of the gravity current, S_p.

Table 11 – Non-dimensional and internal seiche parameters

Run	Hydrostatic Linear Model		Spectral Analysis		Ri	W
	c_p (cm/s)	$T_{1,1}$ (s)	c_p (cm/s)	$T_{1,1}$ (s)		
E.1	4.871	82	5.677	70	236.51	11.83
E.2	4.972	80	4.257	94	151.70	7.59
E.3	3.605	111	2.838	141	91.38	4.57
E.4	2.124	188	1.419	282	30.68	1.53
E.5	7.857	51	7.095	56	398.53	17.93
E.6	6.671	60	5.676	70	286.99	12.92
E.7	4.990	80	4.257	94	225.65	9.03
E.8	4.943	81	5.676	70	208.17	8.33
E.9	2.591	154	2.834	141	61.14	2.45
E.10	2.101	190	1.419	282	61.62	2.47
E.11	7.511	53	5.813	69	429.50	12.89
E.12	4.419	91	4.938	81	187.22	4.68
E.13	4.218	95	4.718	85	265.23	6.63
E.14	2.083	192	1.476	271	48.43	1.21
E.15	1.542	259	1.417	282	20.20	0.51

Table 12 shows the Peak of the Power Spectral Density (PSD) of the pycnocline and the experimental and theoretical amplitude, considering linear and non-linear results. The experimental amplitudes were obtained through the normalization of the peak of the PSD[1]. The linear amplitude is calculated through the relation with wedderburn number, equation 2.27 with a parametrization proportional to 1/2. Finally, the non-linear amplitude solution of the upwelling height was estimated by the empirical fitting function defined by equation 4.2.

Table 12 – PSD analysis and basin-scale internal wave amplitude of experimental analysis.

Run	PSD Stations (cm^2/Hz)			Total vertical displacement (cm)		
	1	2	3	Exp.	Linear	Non-linear
E.1	700	550	11	0.89	0.96	0.90
E.2	1100	800	27	1.53	1.43	1.40
E.3	1700	1050	82	2.42	2.32	2.43
E.4	2100	750	15	7.84	7.83	10.00
E.5	590	–	–	0.63	0.60	0.55
E.6	820	–	–	0.82	0.80	0.75
E.7	1050	–	–	1.00	0.98	0.94
E.8	800	–	–	0.97	1.05	1.02
E.9	2500	–	–	3.71	3.59	4.02
E.10	1850	–	–	3.48	3.56	4.16
E.11	420	–	–	0.55	0.53	0.50
E.12	360	–	–	1.09	1.13	1.18
E.13	250	–	–	0.89	0.81	0.81

[1] The correlation between PSD and the experimental amplitude is not proportional since ζ is obtained through a normalization considering the frequency resolution, in which was obtained through the length of the applied window in the FFT

Table 12 – PSD analysis and basin-scale internal wave amplitude of experimental analysis.

Run	*PSD* Stations (cm^2/Hz)			Total vertical displacement (cm)		
	1	**2**	**3**	**Exp.**	**Linear**	**Non-linear**
E.14	1100	–	–	3.12	5.32	5.00
E.15	650	–	–	2.12	10.00	5.00